Universidade do Minho
Escola de Engenharia

Arthur da Silva Rebouças

Design of ductile moment-resisting steel-timber joints using the component method

March 2026

Design of ductile moment-resisting steel-timber joints using the component method
Arthur da Silva Rebouças
UMinho | 2026

UFPB

Fundação
para a Ciência
e a Tecnologia

Universidade do Minho
Escola de Engenharia

Arthur da Silva Rebouças

Design of ductile moment-resisting steel-timber joints using the component method

Doctoral thesis

Civil Engineering

Work performed under the supervision of:
Jorge Manuel Branco
Paulo José Brandão Barbosa Lourenço
Hidelbrando José Farkat Diógenes

March 2026

Copyright and Terms of Use for Third Party Work.

This dissertation reports on academic work that can be used by third parties as long as the internationally accepted standards and good practices are respected concerning copyright and related rights.

This work can thereafter be used under the terms established in the license below.

Readers needing authorization conditions not provided for in the indicated licensing should contact the author through the RepositóriUM of the University of Minho

License granted to users of this work:



Atribuição-NãoComercial-SemDerivações
CC BY-NC-ND

https://creativecommons.org/licenses/by-nc-nd/4.0/

ACKNOWLEDGMENTS

This research was conducted at the Civil Engineering Department of the University of Minho, Portugal, under the supervision of Professor Paulo Lourenço and Professor Jorge Branco. It was also conducted at the Civil Engineering Department of the Federal University of Paraíba, Brazil, under the supervision of Professor Hidelbrando Diógenes. The Portuguese Foundation for Science and Technology (Fundação para a Ciência e a Tecnologia, FCT) financially supported this work under grant number SFRH/BD/06301/2021, for which I am grateful. This work would not have been possible without the financial support of this institution. I would also like to acknowledge the Institute for Sustainability and Innovation in Structural Engineering (ISISE) and the Postgraduate Program in Civil and Environmental Engineering of UFPB (PPGECAM) for providing facilities and resources. Additionally, I would like to thank the Federal Institute of Education, Science, and Technology of Rio Grande do Norte, for their support during my leave of absence for my doctoral studies.

Above all, I would like to thank my supervisors for their essential assistance and encouragement. To my supervisor, Professor Jorge Branco, I am grateful for his scientific guidance, patience, and for sharing his knowledge and opportunities. I also acknowledge my supervisor at UFPB, Professor Hidelbrando Diógenes, for his support during the co-supervision period, his clarifications and teachings on modelling, and for the warm welcome in João Pessoa. I must also thank my supervisor, Professor Paulo Lourenço, for all his support and assistance. I am thankful to all of them for the opportunities to participate in workshops and conferences during this period.

My special thanks go to the technicians from the LEST laboratories at the University of Minho, especially António Matos, Marco Jorge, and Luciano, for their support, good advice, and training over the years. I would like to thank the friends and colleagues I had the pleasure of meeting during my PhD, including Manuel, Zabih, Aiuba, Claudinha, Adilson, Thaís, Raul, Carolina, Alejandro, and many others. Special thanks to my friends Carol, Daniel, Marina, and Victor for all their help, input, and support during this journey. I would also like to give special thanks to the friends in Guimarães who became family to us in Portugal: Isis, Bruno, Martin, Adriana, Manu, Nuno, and Mateus. The moments we shared were very special.

Finally, I would like to dedicate this work to my family: my wife, Thaís, and my son, Théo, for embarking on this dream with me. Without your love and support, it would have been impossible. I also dedicate this work to my mother, Leide, to Maria, and to my mother-in-law, Socorro. I will be eternally grateful to you. -

STATEMENT OF INTEGRITY

I hereby declare having conducted this academic work with integrity. I confirm that I have not used plagiarism or any form of undue use of information or falsification of results along the process leading to its elaboration.

I further declare that I have fully acknowledged the Code of Ethical Conduct of the University of Minho.

University of Minho, March 31, 2025



Arthur da Silva Rebouças

ABSTRACT

The construction sector ranks among the most energy-intensive industries, playing a significant role in global CO2 emissions. Within this sector, timber emerges as a material with substantial potential to mitigate these emissions. During their growth, trees absorb carbon dioxide from the atmosphere and store it in their biomass, allowing this carbon to remain sequestered throughout the building's service life. Recent advancements in engineered wood products have broadened the possibilities for constructing buildings with timber structures, leading to a significant increase in the number of mass timber buildings over the past decade, particularly those up to eight stories high. However, notable limitations persist. In mid- and high-rise timber structures, systems with cross-laminated timber (CLT) or glued-laminated timber (GLT) truss systems are still necessary, where vertical and diagonal elements are connected using dowelled slotted-in steel plate joints. While effective, these structural systems impose architectural constraints, especially regarding large openings. Alternative structural systems, such as moment-resisting timber frames (MRTF), have been proposed, but their effectiveness hinges on achieving connections with adequate moment resistance, rotational stiffness, and ductility.

Recognizing the importance of moment-resisting timber joints in the advancement of timber buildings, as well as the necessity for joints with sufficient ductility to aid in the redistribution of internal forces, prevent sudden brittle failures, and enhance structural robustness, this thesis delves into the structural behavior of moment-resisting steel-timber joints. These joints feature timber connected to a steel plate (end-plate) through bonded-in rods and are coupled to a steel link. The primary objective is to propose a comprehensive yet straightforward design procedure using the component method to estimate the moment resistance, initial rotational stiffness, and rotational capacity of these joints. The research methodology involves understanding and proposing formulations for components where wood and steel interact, adapting and evolving analytical models to determine rotational stiffness, and improving the accuracy of the component method for this type of joint. Distinguishing itself from previous studies, this research examines joints with multiple bonded-in rod arrangements, specifically two and four rows, stiffened end-plates, and the coupled behavior of various components. Analytical predictions are compared to experimental results from local tests with steel and timber components, as well as full-scale tests of 15 joints, using conventional transducers alongside digital image correlation techniques. Finally, numerical modeling and parametric analysis of the joints are conducted, focusing on verifying the applicability of the proposed analytical procedure across a broader range of geometries. The findings indicate that the structural performance of these joints is significantly influenced by the rotational stiffness of the link, the thickness of the end-plate, and the diameter of the bonded-in rods. The joints demonstrate considerable versatility, allowing for design as full-strength, equal-strength, or partial-strength connections, depending on the resistance of the key components. The analytical proposition based on the component method shows good predictive capability regarding initial rotational stiffness and joint mechanical capacity for both stiffened and unstiffened end-plates with two and four bonded-in rod rows.

KEYWORDS: Bonded-in rods connections; Component method; Moment-resisting timber joints; Monotonic tests of connections; Parametric analysis

RESUMO

O sector da construção civil é uma das indústrias com maior consumo de energia e contribui significativamente para as emissões globais de CO_2. Dentro deste sector, a madeira destaca-se como um material com grande potencial para ajudar a reduzir estas emissões. As árvores absorvem dióxido de carbono da atmosfera durante o seu crescimento e armazenam-no na sua biomassa, permitindo que este carbono permaneça sequestrado durante toda a vida útil do edifício. Os recentes avanços nos produtos de madeira engenheirada expandiram as possibilidades de construção de edifícios com estruturas de madeira e, na última década, o número de edifícios de madeira maciça cresceu significativamente, especialmente nos que possuem até oito pisos de altura.No entanto, ainda existem algumas limitações. Em estruturas de madeira de média e grande dimensão, continua a ser necessário empregar sistemas de madeira lamelada cruzada (CLT) ou pórticos de madeira lamelada colada (glulam), nos quais os elementos verticais e diagonais são ligados através de juntas de cavilhas com chapas de aço. Embora eficazes, estes sistemas estruturais impõem restrições arquitectónicas, particularmente no que diz respeito a grandes vãos. Sistemas estruturais alternativos, como os pórticos de madeira resistentes ao momento (MRTF), têm sido propostos, mas a sua eficácia depende da obtenção de ligações com resistência ao momento, rigidez rotacional e ductilidade adequadas.

Reconhecendo a importância das juntas de madeira resistentes ao momento no desenvolvimento de edifícios de madeira, bem como a necessidade de juntas com ductilidade suficiente para contribuir para a redistribuição das forças internas, prevenir roturas frágeis repentinas e aumentar a robustez das estruturas, esta tese centra-se no comportamento estrutural das juntas aço-madeira resistentes ao momento, nas quais a madeira é ligada a uma chapa de aço através de varões colados e acoplada a um perfil de aço. O principal objetivo é propor um procedimento de dimensionamento abrangente e direto, utilizando o método dos componentes para estimar a resistência ao momento, a rigidez rotacional inicial e a capacidade rotacional destas juntas. A metodologia de investigação envolve a compreensão e a formulação de propostas para componentes onde existe interação entre a madeira e o aço, a adaptação e o desenvolvimento de modelos analíticos para determinar a rigidez rotacional e a melhoria da precisão do método dos componentes para este tipo de junta.

Distinguindo-se de estudos anteriores, esta investigação analisa juntas com múltiplos arranjos de varões colados, nomeadamente com duas e quatro fiadas, chapas terminais rigidificadas e o comportamento acoplado de vários componentes. As previsões analíticas são comparadas com resultados experimentais obtidos a partir de ensaios locais com componentes de aço e madeira, bem como de ensaios à escala real de 15 juntas, recorrendo a transdutores convencionais e a técnicas de correlação de imagens digitais. Por fim, é realizada a modelação numérica e a análise paramétrica das juntas, com foco na verificação da aplicabilidade do procedimento analítico proposto a uma vasta gama de geometrias. Os resultados indicam que o desempenho estrutural destas juntas é significativamente influenciado pela rigidez rotacional do perfil de aço, pela espessura da chapa terminal e pelo diâmetro dos varões colados. As juntas demonstram uma versatilidade considerável, permitindo o dimensionamento como ligações de resistência total, resistência igual ou resistência parcial, dependendo da resistência dos componentes principais. A formulação analítica baseada no método dos componentes apresenta uma boa capacidade preditiva relativamente à rigidez rotacional inicial e à resistência ao momento das juntas com chapas terminais rigidificadas e não rigidificadas, com duas e quatro fiadas de varões colados.

PALAVRAS-CHAVE: Análise paramétrica; Ensaios monotónicos de ligações; Juntas de madeira resistentes a momentos; Ligações de varões colados; Método das componentes.

TABLE OF CONTENTS

ACKNOWLEDGMENTS iii

ABSTRACT v

RESUMO vi

TABLE OF CONTENTS vii

LIST OF TABLES x

LIST OF FIGURES xii

LIST OF ABBREVIATIONS AND SYMBOLS xix

INTRODUCTION 1

1.1. Background and motivation 1

1.2. Objectives 5

1.3. Overall methodology 6

1.4. Contents 7

2. DUCTILITY IN MOMENT-RESISTING TIMBER JOINTS 9

2.1 Ductility 9

2.2 Moment-resisting joints in timber structures 12

2.2.1 Reinforced bolted slotted-in steel plate connections 14

2.2.2 Bonded-in rods connections 20

2.3 Ductility comparison between main joint types 28

3. COMPONENT METHOD IN MOMENT-RESISTING TIMBER JOINTS 34

3.1. The component method 34

3.2. Application of the component method to steel-timber joints 39

4. EXPERIMENTAL RESEARCH 48

4.1. Introduction 48
4.2. Steel tests 49
4.3. Bonded-in rods tests 52
4.4. T-stub compressing timber parallel to the grain test 54
4.4.1. Experimental methodology 54
4.4.2. Component resistance and failure modes results 57
4.4.3. Initial stiffness results 63
4.5. Experimental tests on full-scale joints 65
4.5.1. Specimens and methodology 65
4.5.2. Test setup and instrumentation 69
4.5.3. Results and discussion 74
5. ANALYTICAL PROCEDURE BASED ON COMPONENT METHOD 88
5.1. Methodology 88
5.2. Joint moment resistance 92
5.2.1. Steel link (Macro-component 1) 92
5.2.2. Timber beam (macro-component 2) 95
5.2.3. End plate to timber beam connection (Macro-component 3) 95
5.3. Joint initial rotational stiffness 116
5.3.1. Stiffness coefficient of link flange in bending ($\boldsymbol{klfb}$) 118
5.3.2. Stiffness coefficient for end-plate in bending under tension ($\boldsymbol{kep,t}$) 119
5.3.3. Stiffness coefficient for bonded-in rods in tension ($\boldsymbol{kbr,t}$) 119
5.3.4. Stiffness coefficient for end-plate and GLT in compression ($\boldsymbol{kep,c}$) 120
5.3.5. Stiffness of rib stiffeners ($\boldsymbol{krb,c}$) 122
5.4. Joint rotation capacity 122
5.5. Discussion of analytical results 126
5.5.1. T-stub compressing timber parallel to the grain 128

5.5.2. Joint results 131
6. NUMERICAL AND PARAMETRIC ANALYSIS 139
6.1. Numerical modelling for model validation 139
6.1.1. Geometry and boundary conditions 139
6.1.2. Mesh definitions 140
6.1.3. Materials 145
6.1.4. Interactions 145
6.1.5. Model validation 147
6.2. Parametric analysis 151
6.2.1. Critical parameters for mechanical behavior 152
6.2.2. Proposed analytical procedure comparison 157
7. CONCLUSIONS AND FUTURE DEVELOPMENTS 160
7.1. Conclusions 160
7.2. Future developments 165
REFERENCES 167

LIST OF TABLES

Table 2.1. Proposed ductility classes for connections or components. (Adapted from Smith *et al.* (2006)). 11

Table 2.2. Ductility classes for structure (Adapted from EN 1998-1:2013). 12

Table 2.3. Summary of response of connections under monotonic and cyclic loading (Lam *et al.*, 2008). 15

Table 2.4. Experimental results comparison of bolted connections with slotted-in steel plates. 30

Table 2.5. Experimental results comparison of bonded-in rods connections 31

Table 3.1. Comparison between theoretical and experimental specimens. Adapted from Tomasi *et al.* (2008) 41

Table 3.2. Summary of theoretical and experimental results by adapted from Andreolli *et al.* (2011) 42

Table 3.3. Names of components used in mechanical model. Adapted from Yang *et al.* (2016). ... 43

Table 3.4. Comparison between theoretical and experimental joint moment resistance. Adapted from Yang *et al.* (2016). 44

Table 3.5. Experimental and analytical results comparison for joint initial rotational stiffness. Adapted from Yang *et al.* (2016). 44

Table 4.1. Results for steel end-plate samples. 49

Table 4.2. Results for steel link samples. 50

Table 4.3. Results of single BiR pull-out tests. 53

Table 4.4. Summary of the steel and timber specimens tested. 56

Table 4.6. Statistical results for experimental resistance. 58

Table 4.7. Summary of experimental failure modes at maximum force instant. 63

Table 4.8. Mean GLT Stiffness coefficient for all tested series. 64

Table 4.9. Summary of the tested joints. 68

Table 4.10. Moment resistance and initial rotational stiffness of the tested joints. 75

Table 4.11. Summary of failure modes of each tested joints. 81

Table 5.1. Deformation factor values according to fy, sl. 93

Table 5.2. Limits of classes related to flange and web buckling. 93

Table 5.3. Relationship between analytical and experimental resistance of BiRs 103

Table 5.4. Equations for effective lengths in unstiffened and stiffened end-plate extension. 107

Table 5.5. Basic components catalogue 127

Table 5.6. Comparison between experiments and analytical approaches for the component resistance 128
Table 5.7. Component stiffness coefficient and deformation capacity comparison between experimental and the variable elastic approach 129
Table 5.8. Comparison of failure modes 132
Table 5.9. Comparison between prediction and experimental development of prying forces. 132
Table 5.10. Comparison between predicted and observed joint moment resistance 134
Table 5.11. Comparison between predicted and observed initial rotational stiffness 135
Table 5.12. Comparison between predicted and observed joint rotation capacity 136
Table 6.1. Mesh dimensions of the components tested in portioned models. 143
Table 6.2. Summary of mesh sizes of each part in mm. 144
Table 6.3. Properties of steel applied in numerical modelling for model validation 145
Table 6.4. Anisotropic properties of timber beam (EN 14080:2013) 145
Table 6.5. Parameters and dimensions for the joints 151

LIST OF FIGURES

Figure 1.1. Moment-resisting stiffened end-plate steel-timber joint with steel link and BiRs rows. 5
Figure 2.1. Different methods to calculate the yielding point. (a) Karacabeyli and Ceccotti (1998); (b) EN 12512:2001; and (c) Yasumura (1998)..... 11
Figure 2.2. Different types of rotational stiffness in a timber joint (a) semi-rigid connection representation; (b) Joint moment-rotation behavior. 13
Figure 2.3. Moment-rotation curves of the reinforced connection. (a) Monotonic load (b) Cyclic load, adapted from Lam *et al.* (2008). 15
Figure 2.4. Typical failure for reinforced slotted-in plate connection under cyclic loads, plug shear, splitting and wood embedment failures, respectively, adapted from Lam *et al.* (2010)..... 16
Figure 2.5. Moment and rotational angle relationships under monotonic loading tests, adapted from Wang *et al.* (2015)..... 16
Figure 2.6. Steel-timber joint layout. (Solarino *et al.*, 2017)..... 17
Figure 2.7. Experimental results. (a) Monotonic test; (b) Specimen at failure, adapted from Solarino *et al.* (2017). 17
Figure 2.8. Comparison of the failure modes Sun *et al.* (2020): (a) finite element model, (b) specimen from Lu *et al.* (2016); (c) specimen from Wang *et al.* (2015); and (d) specimen, adapted from Lam *et al.* (2008). 18
Figure 2.9. Moment–rotation curve: (a) model 1 (d = 20 mm) and (b) model 2 (d = 24 mm), adapted from Sun *et al.* (2020). 18
Figure 2.10. Specimen (Reinforced by STS under cyclic load), adapted from Dong *et al.* (2021).... 19
Figure 2.11. Geometries used in reinforced slotted-in ductile moment resisting connections, including positions and number of dowel and screws. 20
Figure 2.12. Moment resisting glulam connections tested by Buchanan and Fairweather (1993)... 23
Figure 2.13. Moment resisting glulam connections tested by Buchanan and Fairweather (1993)... 23
Figure 2.14. Summary of moment-resisting specimens arrangements Buchanan *et al.* (2001). 24
Figure 2.15. Joint parts configuration tested by Tomasi *et al.* (2008). 24
Figure 2.16. Load-displacement experimental curves for each specimen adapted from Tomasi *et al.* (2008)..... 25
Figure 2.17. Monotonic and cyclic moment–rotation relationship experimental results for (a) specimen P6; (b) specimen P10 adapted from (Andreolli *et al.*, 2011). 26
Figure 2.18. Joint geometry and steel components Yang *et al.* (2016). 27

Figure 2.19. Load-displacement curves for specimens (a) JT2-1 (b) JT3-1 under monotonic tests Yang *et al.* (2016). 27
Figure 2.20. Moment-rotation curves for monotonic tests Yang *et al.* (2016). 27
Figure 2.21. Comparative ductility performances of moment-resisting connections based on different ductility factors. 29
Figure 2.22. Geometric configurations and failure modes of bonded-in rods connections. 32
Figure 3.1. Idealizations of moment-rotation curves. 35
Figure 3.2. Main parameters to define tri-linear moment-rotation curve. 35
Figure 3.3. Approximations of the component behavior (a) Bilinear (b) Post-limit linear. 37
Figure 3.4. Steel extended end-plate bolted joint (a) Identification of the basic components and their positions (b) Mechanical model (spring model). Adapted from Coelho and Bijlaard (2010) 37
Figure 3.5. Mechanical model of the joint with bonded-in rods. Adapted from Vašek and Vyhnálek (2006)..... 39
Figure 3.6. Basic components and mechanical model. Adapted from Tomasi *et al.* (2008). 40
Figure 3.7. Moment versus rotation for the specimen P10: (a) left joint experimental data; (b) right joint experimental data; (c) theoretical model Tomasi *et al.* (2008). 41
Figure 3.8. Setup for monotonic and cyclic tests: 1, steel profile connected to the reaction base; 2, displacement transducer 100 mm; 3, displacement transducer 500 mm; 4, load cell; 5, hydraulic jack. The upper part of the figure shows the cyclic test protocol according to EN 12512:2005. Andreolli *et al.* (2011). 42
Figure 3.9. Joint Geometry and basic components for glulam beam–column connection. (Yang *et al.*, 2016)..... 43
Figure 3.10. Glulam beam–column joint specimens (a) at the beginning of both experiments (b) at the end of cyclic load experiment (Yang *et al.,* 2016)..... 44
Figure 3.11. Joint parts and components presentation (Tao *et al.*, 2020)..... 45
Figure 3.12. Component method definition. (a) identification of components on connection. (b)mechanical model. (c) simplified component method (Tao *et al.*, 2020). 46
Figure 3.14. Component method model for stiffened end-plate moment-resisting steel-timber joint with steel link and two BiR rows (a) Division in macro-components (b) Mechanical spring model 47
Figure 4.1. Dimensions of rods samples, in mm..... 50
Figure 4.2. Tension test on threaded rods attached by nut (a) Test setup; (b) Thread galling failure mode. 51

Figure 4.3. Specimens of BiR connections for tensile tests. Dimensions in mm. 52
Figure 4.4. Load-displacement curves of the test for (a) M12, (b) M14, (c) M16. 53
Figure 4.5. BiR pull-out tests performed. (a) setup; (b) tensile failure of the steel rod; (c) shear failure of the timber adjacent to the bondline. 54
Figure 4.6. Position of component defined by the steel T-stub compressing the timber parallel to the grain. 54
Figure 4.7. Detailed geometry of the specimens, including T-stub and GLT, the DIC painted front face and positions of T-stub Series and Reference specimens. Dimensions in mm. 55
Figure 4.8. Steel T-stub geometry. Dimensions in mm. 56
Figure 4.9. Overview of displacement measurement techniques: (a) DIC Surface (b) LVDTs. The right and left ones were named based on the front face of the specimen (painted surface). 57
Figure 4.10. Force-displacement curves for all different T-stub flange thicknesses of G1, G2, and G3, measured by central LVDT. 58
Figure 4.11. Variability in experimental maximum force due to flange thickness and specimen grouping. 59
Figure 4.12. Correlation between the T-stub flange thickness and the experimental maximum force. 59
Figure 4.13. Variable vertical displacements across the width of the T-stub in the elastic range, as measured using the Digital Image Correlation (DIC) (a)T20 G2 S2 (b) T6 G2 S3. 60
Figure 4.14. Force-displacement curve for T6 G2 S4 with deformed shapes at relevant positions. . 61
Figure 4.15. Failure of specimen T6 G1 S2 due to T-stub flange yielding. 61
Figure 4.16. Local embedment of the timber under the steel plate observed in specimen REF G2 S4. 61
Figure 4.17. Different failure modes for the component: (a) T20 G1 S4 specimen (b) T6 G2 S3 specimen. 62
Figure 4.18. Correlation between the T-stub flange thickness and the experimental resistance. 65
Figure 4.19. Variability in experimental initial stiffness due to flange thickness and specimen grouping. 65
Figure 4.20. Schematic representation of tested stiffened end-plate moment-resisting steel-timber joints with steel link and bonded-in rods rows. 66
Figure 4.21. Joints of group 1 (dimensions in mm). 67
Figure 4.22. Joints of group 2 (dimensions in mm). 67

Figure 4.23. Stages of the manufacturing and assembly process of the joints specimens. 69
Figure 4.24. Overview of loading test. 70
Figure 4.25. Position of load cell and LVDT instrumentations. 71
Figure 4.26. Strain gauge positions: (a) On threaded rods; (b) On timber beam. 72
Figure 4.27. Equipment used in the DIC measurements. 72
Figure 4.28. Main points and lines defined for DIC technique measurements. 73
Figure 4.29. Measurement methodology of displacements. 73
Figure 4.30. Key points defined for experimental curves. 74
Figure 4.31. Experimental moment-rotation curves for G1 joints. 76
Figure 4.32. Experimental moment-rotation curves for G2 joints. 76
Figure 4.33. Representative failure modes for: (a) G1.t20.d20; (b) G1.t15.d20. 79
Figure 4.34. Comparison of the moment-rotation curves of mean results of the G1 joints. 79
Figure 4.35. Representative failure modes for: (a) G2.t20.d12; (b) G2.t15.d14. Failure of threaded rods due to thread galling, no plastic deformations identified in end-plate and link. 80
Figure 4.36. Representative failure modes for G2.t12.d16. Link yielding with no yielding lines in the end-plate and no damage in timber beam. 81
Figure 4.37. Moment-rotation curves for the primary components of the G1 joints considered individually. 82
Figure 4.38. Moment-rotation curves for the primary components of G2 joints considered individually. 82
Figure 4.39. BiR tension forces generated by applied moment for (a) G2.t20.d12, (b) G2.t15.d14, (c) G2.t12.d16. 84
Figure 4.40. Comparisons of the TB and EP vertical displacements for (a) G1.J1.t20.d20, (b) G1.J6t15.d20, (c) G2.J1.t20.d12, (d) G2.J4.t15.d15, (e) G2.J7.t12.d16. 85
Figure 4.41. Rotational behavior of the joint subjected to bending moment (a) Link only (b) End-plate only (c) Timber beam only (BiR) (d) Link + end-plate + timber beam (BiR). 87
Figure 5.1. Joints' configurations and mechanical models. 90
Figure 5.2. Joint design procedure flowchart. 91
Figure 5.3. Cross-section classification and corresponding bending resistances according to EN 1993-1-1:2014 on (a) Moment-curvature for steel sections in bending; (b) Bending resistances based on classifications. 92

Figure 5.4. Experimental moment-rotation curves of G2.t12.d16 joints and theoretical remarks for steel link moment resistance..... 94
Figure 5.5. Geometrical features of BiR connections..... 97
Figure 5.6. Failure modes of axially loaded BiRs (Jockwer *et al.*, 2023)..... 99
Figure 5.7. Main lengths to allow plastic elongation of BiRs. 100
Figure 5.8. Analytical comparison of prediction of BiR failure (Parida, Johnsson and Fragiacomo, 2013)..... 101
Figure 5.9. Design philosophy of ductile BiR failure mode (Bouchard *et al.*, 2021). 102
Figure 5.10. General failure modes of stiffened extended end-plate joint. 105
Figure 5.11. Values of α for stiffened end-plates (EN 1993-1-8:2010). 106
Figure 5.12. Elongation length for bonded-in rods connected to end-plate. 108
Figure 5.13. Analytical load distribution between the timber beam and end-plate and idealized cantilever of end-plate..... 109
Figure 5.14. Different effective areas according to load type: (a) compression only; (b) compression and bending; (c) bending only. Adapted from Wald et al. (Wald *et al.*, 1998). 110
Figure 5.15. Equivalent T-stub in compression. 111
Figure 5.16. The effective area of T-stub in compression: (a) short projection; (b) large projection. Adapted from EN 1993-1-8:2010..... 112
Figure 5.17. Structural idealization of the component corresponding to the steel T-stub applying compression parallel to grain in timber member and the additional bearing width (ct). 113
Figure 5.18. Structural idealization of the component corresponding to the steel T-stub applying compression parallel to grain in timber member and the plastic additional bearing width (ctp). .. 113
Figure 5.19. Structural idealization for T-stub and timber in compression component with a variable stress distribution and variable additional bearing width (ctv). 114
Figure 5.20. Location of compression center for different joint types (a) unstiffened end-plate (b) stiffened end-plate. Adapted from Landolfo *et al.* (2018)..... 115
Figure 5.21. Cantilever end-plate assumptions for stiffness coefficient. 120
Figure 5.22. Schematic component deformation focused on the relative edge displacement for a steel T-stub compressing timber parallel to the grain. 121
Figure 5.23. Main geometrical parameters of rib stiffener. Adapted from Lee (2002). 122
Figure 5.24. Analytical assumptions of joint rotations based on main deformation of the components. 123

Figure 5.25. Stress-strain relationship for timber in compression parallel to the grain. Adapted from Blaß (1987) 124
Figure 5.26. Bilinear stress-strain curve idealization for timber in direction parallel to the grain. Adapted from Buchanan (1990). 125
Figure 5.27. Deformation capacity approach for steel T-stub flange in bending due to timber parallel to the grain compression. 126
Figure 5.28. Analytical and experimental component load-displacement curve comparison for all series. 130
Figure 5.29. Theoretical lever arms for joints with compression side working as (a) T-stub compressing timber parallel to the grain, (b) End-plate in bending under compression. 133
Figure 5.31. Comparison of the moment-rotation curves for G1 joint..... 138
Figure 5.32. Comparison of the moment-rotation curves for G2 joint..... 138
Figure 5.33. Comparison of the moment-rotation curves for joints P6, P8 and P10. 138
Figure 6.1. Detailed geometry of joints modelled. 140
Figure 6.2. Boundary conditions and external constraints of the model. 140
Figure 6.3. Comparison between non-partitioned and partitioned models (a) non-partitioned end-plate, (b) partitioned end-plate, (c) non-partitioned timber beam ,and (d) partitioned timber beam. 142
Figure 6.4. Moment-rotation curve for non-partitioned and partitioned models compared with experimental results. 142
Figure 6.5. Mesh sensitivity analysis for main tested mesh dimensions..... 143
Figure.6.6. Mesh discretization of end-plate and link..... 144
Figure 6.7. Abaqus model with mesh discretization. 144
Figure 6.8. Interactions between main components..... 146
Figure 6.9. Moment-rotation curves comparison for (a) Joint t15 and (b) Joint t20. 147
Figure 6.10. Typical engineering stress-strain curve for hot-rolled carbon steel (Yun and Gardner, 2017)..... 147
Figure 6.11. Typical moment-rotation curves for failure in different components (a) Link, (b) BiR (Andreolli *et al.*, 2011), and (c) End-plate (Andreolli *et al.*, 2011). 148
Figure 6.12. Moment-rotation curves and key identifications for relevant components. 149
Figure 6.13. Stresses when the end-plate started yielding in t15 model, at Moment of 27.60 kNm and load step 0.024. Stress units in MPa..... 149

Figure 6.14. Stresses when the link started yielding in t20 model, at Moment of 43.63 kNm and load step 0.150. Stress units in MPa. 149
Figure 6.15. Comparison between experimental (left) and numerical (right) failure mode of joint t15. 150
Figure 6.16. Comparison between experimental (left) and numerical (right) failure mode of specimen t20. 151
Figure 6.17. Variations on the stiffeners and internal BiR due to the link cross section parameter. 152
Figure 6.18. Statistical variation of initial rotational stiffness for each input parameter. 153
Figure 6.19. Statistical variation of ultimate moment for each input parameter. 153
Figure 6.20. Influence of end-plate thickness and link section parameters on (a) initial rotational stiffness (b) ultimate moment. 154
Figure 6.21. Influence of end-plate thickness and BiR diameter parameters on (a) initial rotational stiffness (b) ultimate moment. 155
Figure 6.22. Comparative analysis between models M9 and M18 for moment-rotation curves and stress-rotation diagrams. 156
Figure 6.23. Correlation of initial rotational stiffness for S2BR, U2BR, S4BR, U4BR between FE and CM 157
Figure 6.24. Correlation of joint yield moment for S2BR, U2BR, S4BR, U4BR between FE and CM. 158
Figure 6.25. Correlation of joint ultimate moment for S2BR, U2BR, S4BR, U4BR between FE and CM. 159

LIST OF ABBREVIATIONS AND SYMBOLS

Δ_{Fu}	Ultimate displacement
Δ_{Fy}	Elastic displacement
Δ_e	Relative edge displacement
Δ_{ec}	Displacements of the edges of the end-plate in the y-direction for compression side
Δ_{et}	Displacements of the edges of the end-plate in the y-direction for tension side
Δ_i	Displacement of the component i
Δ_{tc}	Relative displacement between the timber beam and the end-plate for compression side
Δ_{tt}	Relative displacement between the timber beam and the end-plate for tension side
Δ_u	Plastic deformation capacity of component
h_{eq}	Distance between the equivalent load and the support of the end-plate cantilever
h_r	Distance between bolt-row r and the centre of compression
h_w	Height between flanges
$\ell_{b,ef}$	Effective anchorage length
$\ell_{b,min}$	Minimum anchorage length
ℓ_b	Adopted glued length
$\ell_{eff,1}$	Minimum effective length from circular and non-circular patterns
$\ell_{eff,2}$	Minimum effective length from non-circular patterns
ℓ_{nb}	Unbonded length
γ_{M0}	Partial coefficient of steel
γ_{M2}	Partial coefficient of steel
Δl_p	Plastic elongation of the rod
ε_u	Ultimate strain of the rod
ε_y	Yield strain of the rod
A_{eff}	Effective area
$A_{s,br}$	Nominal area of threaded rod cross-section
E_0	Longitudinal modulus of elasticity of timber in compression parallel to grain
E_h	Strain hardening modulus

$E_{c,0,k}$ Characteristic compressive modulus of elasticity parallel to the grain

E_f Final elongation

$E_{w,0}$ Modulus of elasticity parallel to grain of glulam beam

$F_{R,br,t}$ Resistance of bonded-in rods in tension

$F_{R,ep,c}$ Resistance of end-plate in bending under compression component

$F_{R,ep,t}$ Resistance of steel end-plate in bending under tension

F_{Rd} Plastic resistance of component

F_i Force in component i

$F_{r,Rd}$ Effective resistance of bolt-row r of the joint

$F_{tr,Rd}$ Resistance of weakest component of bolt row r in the tension zone

F_{ud} Theoretical ultimate force

K_z Stiffness of a rectangular rigid plate in an isotropic elastic half-space

L_0 Undeformed length of half of T-stub flange without the web

L_b Elongation length

L_b^* Limit of elongation length

L_{ex} Vertical distance between the end-plate and the link

M_{Et} Bending moment per unit length acting in the timber

$M_{c,Rd}$ Moment capacity of steel link

$M_{c,rb,Rd}$ Design plastic moment resistance of the beam plus the rib cross-section

$M_{j,Ed}$ Elastic moment resistance

$M_{j,Rd}$ Joint moment resistance

M_{pb} Plastic bending moment resistance of the base plate per unit length

$M_{pl,1,Rd}$ Moment for plastic hinge from circular and non-circular patterns

$M_{pl,2,Rd}$ Moment for plastic hinge from non-circular patterns

M_{pl} Plastic moment resistance

$M_{t,Rd}$ Moment resistance of timber beam

M_u Ultimate moment resistance

M_y Yield moment resistance

$P_{u,mean}$ Mean ultimate load

$R_{ax,d}$ Characteristic axial resistance of BiRs

$S_{j,ini}$ Joint initial rotational stiffness

S_n Nut thickness

S_w Washer thickness

$W_{eff,min}$ Minimum effective section modulus

$W_{el,min}$ Minimum required elastic section modulus

W_{pl} Plastic steel section modulus

W_{tim} Elastic section modulus of the timber beam

$Z_{p,eff}$ Effective plastic section modulus

$Z_{p,ep}$ Plastic section modulus of the end-plate

$Z_{p,st}$ Plastic section modulus of the stiffener

a_w Weld throat

b_c Column flange width

b_{eff} Effective width

b_f Steel link flange free width

b_p End-plate width

b_r Length of the rib

c_l Half of the flange width less half of web thickness and the fillet radius

c_{tp} Plastic additional bearing width

c_{tv} Variable additional bearing width

d_h Diameter of the drilled hole

dH_{ep} Horizontal distance between LVDTs 1 and 2

d_l Clear depth between the flanges less twice the fillet radius

d_w Diameter of the washer

e_h Edge-to-end horizontal distance

e_v Edge-to-end vertical distance

$f_{c,0,k}$ Characteristic compressive strength of timber parallel to the grain

$f_{c,0}$ Compression strength parallel to the grain of the GLT

f_{jd} Design bearing strength of the concrete

$f_{m,k}$ Glued laminated timber characteristic bending strength

$f_{u,mean}$ Mean ultimate strength

$f_{u,br}$ Ultimate resistance of bonded-in rod

$f_{u,ep}$ Ultimate strength of end-plate

$f_{u,st}$ Ultimate strength of rib stiffener

f_u Ultimate strength

$f_{v,mean}$ Nominal shear strength of single axially loaded rod parallel to the grain

$f_{vr,k}$ Characteristic bondline strength

$f_{y,mean}$ Mean yield strength

$f_{y,br}$ Characteristic yield strength of the threaded rod

$f_{y,ep}$ Yield resistance of end-plate

$f_{y,sl}$ yield strength of steel link

f_y Yield strength

$k_{br,t}$ Stiffness coefficient for bonded-in rods in tension

k_{ec} Stiffness of the components assembled in the compression/shear zone

$k_{eff,r}$ Effective stiffness coefficient

$k_{ep,c}$ Stiffness coefficient for end-plate and GLT in compression

$k_{ep,t}$ Stiffness coefficient for end-plate in bending under tension

k_{eq} Equivalent stiffness of the connection

k_{et} Stiffness of the components assembled in the tension zone

k_i Stiffness coefficient for each component i

k_{lfb} Stiffness coefficient of link flange in bending

k_{mod} Strength modification factor

k_{pl} Post-limit stiffness coefficient of component

$k_{rb,c}$ Stiffness of rib stiffeners

l_{eff} Effective length

m_2 Geometric parameter for internal distances in end-plate

m_x Geometric parameter for extended end-plate

n_b Number of BiR-rows

r_c	Fillet radius of the rolled section
s_f	Weld leg length
t_{ep}	End-plate thickness
t_f	Flange thickness
t_{rib}	Rib thickness
t_w	Web thickness
t_{wb}	Beam web thickness
t_{wc}	Column web thickness
x_{eq}	Position of the equivalent load
z_{eq}	Equivalent lever arm of the connection
z_{sl}	Equivalent lever arm of the link
$\gamma_{M,tim}$	Partial factor for timber
γ_M	Partial factor for material properties
$\delta_{u,epc,i}$	Deformation capacity of the end-plate
δ_u	Deformation capacity of T-stub compressing GLT component
ε_c	Compressive strain of timber parallel to the grain
ε_s	Strain of outer part of the T-stub flange in bending
ε_{sh}	Strain hardening strain
$\varepsilon_{u,br}$	Ultimate strain of threaded rod
$\varepsilon_{u,ep}$	Ultimate strain of the steel end-plate
$\varepsilon_{u,timber}$	Failure strain of the timber parallel to grain
η_r	Equivalent strut area factor
θ_T	Experimental rotation of the joint
$\theta_{u,l}$	Rotation capacity of the link
θ_u	Ultimate rotation
θ_y	Yield rotation
λ_{FLB}	Flange outstands limiting value
λ_{WLB}	Web in bending limiting value
ρ_{mean}	Mean density of the timber
σ_c	Stress in timber under compression parallel to grain

ϕ_{Cd}	Joint rotation capacity
ϕ_{Xd}	Ultimate rotation
h	Height of the steel link
ℓ	Total length of steel link
m	Geometric parameter for external distances in end-plate
w	Horizontal distance between rods centrelines
ΔL	Variation in the length of the T-stub flange
ε	Deformation factor
A	Total cross-section area of link
E	Young modulus
I	Moment of inertia of link
M	Bending moment
a	Rib height
b	Steel link flange width
c	Additional bearing width
d	Outer diameter of threaded rod
k	Elastic stiffness coefficient of component
n	Geometric parameter
p	Vertical distances between rods rows centerlines
q	Behavior factor
y	Vertical distance between the neutral axis and the outer face of the link flange
z	Lever arm of internal couple
α	Rib strut inclination
β	Coefficient
η	Stiffness modification coefficient
θ	Relative rotation
μ	Ductility factor
ξh_{rib}	Centroid of the Tee section composed by stiffener and flange beam.

CHAPTER 1

INTRODUCTION

This chapter presents the background and motivation of the research, main and specific objectives, research scope, overall methodology and contents of the thesis

1.1. Background and motivation

Global population growth and urbanization are reshaping the environmental impact of the built environment. Between 1975 and 2020, the world's population nearly doubled, increasing from four billion to just under eight billion people. This demographic growth has been accompanied by a steady migration to urban areas: 45% of people live in cities, 35% in towns and semi-dense areas, and only 20% in rural regions (Ehrlich *et al.*, 2024). The spatial distribution of people is significant because cities, despite covering only 3% of the Earth's surface, are responsible for more than 70% of global greenhouse gas (GHG) emissions (Habitat, 2024).

The construction sector plays a decisive role in this scenario. As of 2024, building construction and operations consumed 32% of global energy and accounted for 34% of CO_2 emissions. Much of this impact is linked to the use of energy-intensive materials such as cement and steel. Together, these materials contribute to 18% of global emissions, making them among the largest industrial sources of GHGs (Hamilton *et al.*, 2024). Their production is also associated with high levels of resource extraction and construction waste, raising concerns about both carbon emissions and material efficiency. In contrast, timber provides a lower-carbon alternative for building materials. During their growth, trees absorb carbon dioxide from the atmosphere and store it in their biomass. When harvested sustainably and used in construction, this carbon remains sequestered for the duration of the building's service life (Favero *et al.*, 2023). The substitution of cement and steel with timber therefore offers a double benefit: reducing emissions from conventional materials and increasing the amount of carbon stored in the built environment.

The benefits of timber construction extend beyond carbon storage. It is a renewable resource, which the processing generally requires less energy than that of steel or cement, which reduces emissions along the supply chain. Timber is also compatible with circular economy practices, since it can be reused, recycled, or adapted for new uses at the end of a building's life cycle (Gu *et al.* 2023).

In addition, timber can have high level of prefabrication, it is ease to work, quick to assemble and presents a high strength-to-mass ratio, features that contribute to its use in multi-story buildings. Advances in engineered wood products, such as cross-laminated timber (CLT) and glued-laminated timber (GLT), have further expanded the structural possibilities of wood, enabling its application in mid- and high-rise buildings that were once considered feasible only with concrete or steel.

These advances have significantly contributed to the growth in the global market for mass timber construction that was estimated at US$990.4 Million in 2024 and is projected to reach US$1.3 Billion by 2030 (Global Industry Analysts, 2025) and also in the number of mass timber buildings. Over the past two decades, mid- and high-rise timber structures, such as eight-story buildings, have increasingly been realized worldwide, with nearly half of the 139 buildings recorded by 2021 completed in that year alone (Safarik *et al.*, 2022). With this growth in the number of timber buildings, knowledge about their overall stability and lateral stiffness has become more important, since due to the moderate stiffness and light weight of timber, such buildings may be susceptible to excessive lateral displacements and accelerations, which can lead to damage to the structural and non-structural elements of the building and discomfort for users. To avoid these problems, taller timber buildings have been designed with lateral load-resisting systems such as cross-laminated timber walls (Tulebekova *et al.*, 2023), rigid concrete cores (Fernandez *et al.*, 2020), or glulam truss systems, where diagonal elements are connected through dowelled slotted-in steel plate joints (Abrahamsen, 2017). While effective, these structural systems impose architectural restrictions, particularly regarding large openings.

An alternative is the use of moment-resisting timber frames (MRTFs) with semi-rigid beam-to-column connections. MRTFs offer an architecturally flexible and structurally efficient solution capable of carrying both vertical and horizontal loads (Vilguts *et al.*, 2021). They allow for the construction of timber buildings without shear walls or X-bracing, provided that the connections exhibit adequate rotational stiffness and ductility. Such ductility is essential for redistributing internal forces, ensuring robustness, and preventing sudden brittle failures, as ductile joints provide warning signs through large deformations or cracks. Additionally, the plastic design of ductile connections can reduce material use and improve safety in statically indeterminate systems (Brühl *et al.*, 2011).

Despite these advantages, structural systems such as MRTFs are not yet widespread in practice due to their inherent flexibility. The lateral stability in moment-resisting frames is primarily provided by the flexural stiffness, moment resistance of the joints and horizontal and vertical members. Their

broader adoption depends on the availability of stiffer and ductile moment-resisting connections, which remain scarce in practical applications (Hegeir *et al.*, 2024). In post-and-beam timber structures, many joint types exhibit limited initial rotational stiffness, particularly at beam-to-column joints. These joints often provide only partial moment transfer, leading to flexible behavior and excessive rotations. As a result, the overall frame stiffness is significantly reduced unless additional elements, such as bracing systems or specially designed moment-resisting connections, are introduced to enhance stiffness (Vilguts *et al.*, 2022).

Current design codes, such as Eurocode 8 (EN 1998-1:2013), stipulate that ductility in timber structures should be concentrated in the connections, which must sustain seismic demands in the plastic regime while structural elements remain elastic. In general, timber connections are often prone to brittle failure modes, such as splitting, shear plug formation, or sudden pull-out of fasteners, which occur with little or no warning. These failures limit the energy dissipation capacity of the structure and compromise its overall safety. The lack of ductility in conventional timber joints prevents effective redistribution of stresses and can lead to premature collapse, highlighting the need for connection systems capable of developing controlled, ductile behavior. However, since timber is intrinsically brittle, particularly in tension, ductility in timber joints has been achieved through plastic deformations of steel dowels combined with local compression of timber in dowel-type connections (Jorissen and Fragiacomo, 2011).

To overcome these limitations, recent studies have investigated the mechanical behavior of hybrid steel-timber moment-resisting joints, incorporating steel links, brackets, stiffened end-plates associated with bonded-in rods (BiRs) or screwed-in rods connections. These joints have demonstrated the potential to achieve high moment resistance, improved rotational stiffness, and controlled ductility, effectively enhancing the competitiveness of timber in lateral load-resisting systems.

However, the mechanical interaction among the components is complex. The global joint behavior depends on several interrelated factors, including strength of all components, geometry of the steel parts (link, end-plate and stiffeners), BiRs glued length, bond-slip relationship, and the deformation compatibility between the steel and timber elements. The accurate prediction of these effects is even more challenging, especially when multiple load transfer paths and non-linear behavior are present. To achieve reliable design procedures, a mechanical analytical model capable of representing the contributions of each component is required.

In this perspective, the component method, an analytical method widely utilized for steel joints, emerges as a promising framework for developing an analytical model for these moment-resisting steel-timber joints. Originally developed for steel joints, the component method was formalized in Eurocode 3 (EN 1993-1-8:2005) and has become the basis for joint design in steel structures. Its key principle is to model the joint as an assembly of basic components, each representing a physical deformation mechanism such as bolt tension, plate bending, or column flange compression.

The component method provides simple procedures to evaluate the moment–rotation response of a wide range of joint configurations, and it is based on a simplified mechanical model composed of extensional springs and rigid links. The behavior of a joint is determined based on the equilibrium and compatibility relations between springs arranged in an appropriate layout considering the constitutive relation of each spring. Each spring element, also known as a component, represents a specific region of the joint subjected to a specific type of loading. The components to be considered in a model are only those relevant for the overall joint structural behavior. In general, each component is characterized by a non-linear force–deformation relation, although simpler idealizations are possible (Jaspart and Weynand, 2016).

The method offers a clear physical interpretation of joint behavior, allowing identification of the critical components governing stiffness, strength, and ductility. Moreover, it is highly adaptable, capable of integrating new components or failure mechanisms as new joint typologies emerge.

In recent years, several researchers have adapted the component method to timber and hybrid steel–timber joints, including dowel-type and other configurations (Sobra *et al.*, 2014; Postupka *et al.*, 2016; Guo *et al.*, 2024; Buchholz *et al.*, 2025). However, its application to BiRs connections, particularly those combined with stiffened end-plates and steel links, remains limited. In these joints, new components must be introduced to represent phenomena such as BiRs and end-plate deformations, link bending, and end-plate stiffening effects.

Among hybrid joints, stiffened end-plate steel-timber joints with steel link and BiRs have shown a good performance in terms of moment resistance, rotational stiffness, and ductile behavior. In this joint configuration, presented in Figure 1.1, a steel end-plate, welded to a steel link or short connector element, is attached to steel threaded rods glued into the glued laminated timber beam parallel to the grain. The stiffeners welded to the end-plate improve out-of-plane stiffness and compression resistance, preventing local deformations that could reduce the effective lever arm of the connection. The bonded-in rods, anchored through an epoxy or polyurethane adhesive, provide a distributed tensile

load transfer. This combination of components enables a hybrid yielding mechanism, where plastic deformations are concentrated in the steel elements while the timber remains in the elastic range.

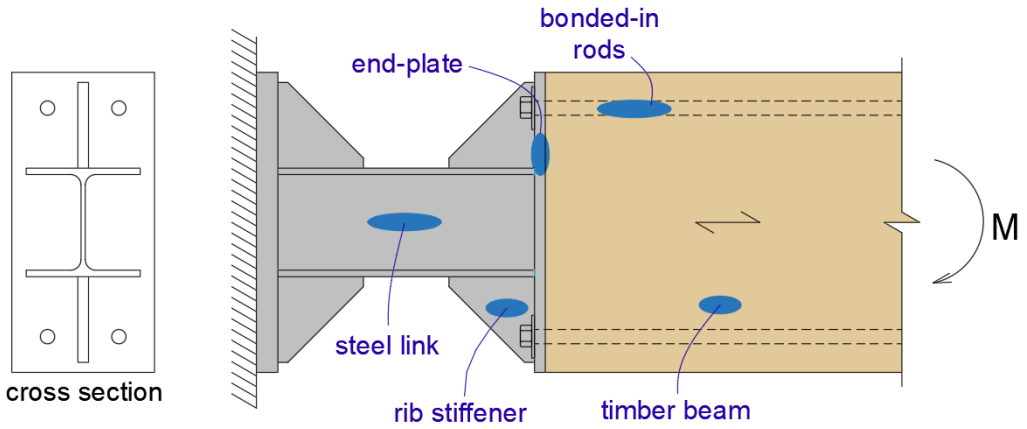


Figure 1.1. Moment-resisting stiffened end-plate steel-timber joint with steel link and BiRs rows.

1.2. Objectives

The main objective of this thesis is to contribute to the development of a comprehensive and straightforward design procedure based on the component method for estimating moment resistance, initial rotational stiffness, and rotational capacity of stiffened end-plate moment-resisting steel-timber joints with steel links and multiple bonded-in rod rows, focusing on interactions between timber and steel components and on coupled behavior of steel link and end-plate. This research aims to enhance the predictive accuracy of the component method in representing the mechanical response of such hybrid joints, particularly their initial rotational stiffness, and to increase confidence in their practical application for multi-storey timber buildings. The selected joint configuration, comprising a stiffened end-plate, steel link, and multiple BiR rows, was identified as having the necessary ductility, moment resistance, and rotational stiffness to enable its effective use in moment-resisting timber frames.

To achieve the main goal, the following specific objectives were outlined within the framework of this thesis:

- To investigate moment-resisting steel-timber joints and identify configurations with high ductility, resistance, and stiffness, avoiding brittle timber failures.
- To assess the use of the component method for predicting the coupled behavior steel link and end-plate.
- To formulate analytical expressions for all active components, focusing on interactions between timber and steel components
- To analyze the mechanical behavior of these joints, including rotational initial stiffness, moment resistance, failure modes, and component interactions.

— To evaluate the applicability of the analytical procedure across a wide range of joint geometries through numerical studies.

1.3. Overall methodology

This section outlines the overall methodology adopted to achieve the objectives of this research. It presents the logical framework used to develop, validate, and apply the proposed analytical model based on the component method for moment-resisting steel–timber joints.

I) Definition of moment resistance, ductility requirements and joint geometry

Study of the main moment resistance and ductility requirements necessary to obtain a joint for prefabricated, semi-rigid, and versatile timber structures, suitable for applications in post-and-beam structural systems. Define a joint type that possesses adequate ductile capacity while maintaining high levels of moment resistance and initial rotational stiffness, without compromising the structural integrity of the timber. This involves avoiding brittle failures in timber and focusing on a ductile failure mode.

II) Application of the component method for predicting the behavior of relevant components

Exploring the application of the component method in predicting the behavior of the various relevant components within the moment-resisting steel-timber joints, focusing on analytical expressions related to components where interactions occur between timber and steel.

III) Experimental characterization of the components

Mechanical characterization of the components identified in the method, based on the evaluation of the strength, stiffness, and deformation capacity characteristics of each component. These components will then be joined together in order to compute the overall parameters of the joint. As the joints are subjected to bending, the characterization will be performed based on the position of each component and its physical behavior (tension, compression, shear), also evaluating their failure modes.

IV) Application of the component method for predicting the joint behavior

Based on knowledge of the models of the components studied, application of the component method to stiffened end-plate moment-resisting joints with steel link and multiple BiR rows. This design approach involves dividing the joint into macro-components, identifying the active components, characterizing each one, and finally assembling them appropriately to determine the joint's mechanical properties.

V) Experimental characterization of the moment-resisting joints

Investigation of the mechanical properties of moment-resisting joints through full-scale experimental testing under monotonic bending loads to determine moment-rotation curves, evaluate post-elastic behavior, ductility, rotation capacity, and failure modes. Use of specimens with different geometries and failure modes to obtain a broader set of results for the joints. Focus on the regions of interaction between the individual parts, mainly between the timber and steel components, to evaluate localized stresses and displacements in the compressed and tensioned regions, as well as to obtain a general mapping of these mechanical properties along the height of the connection.

VI) Numerical and parametric analysis

Finite Element Modelling of the proposed moment-resisting joints geometries using Abaqus software to analyze the distribution of internal stresses among the joint components. Comparison of experimental and numerical results, including rotational stiffness, rotation capacity, and moment resistance capacity, among other relevant factors, in order to adequately discuss the reliability of the proposed joint. Following the experimental validation of the numerical model, a parametric analysis to expand the analysis of the results and facilitate predictions regarding the structural behavior of the joint.

1.4. Contents

The content of this work is organized in seven chapters, as follows:

- **Chapter 1** provides a general introduction to the research topic, presents the framework and motivation of the research, describes the main and specific objectives, overall methodology and, finally, presents the outline of the present work.
- **Chapter 2** provides a comprehensive overview of the principal moment-resisting timber joints that exhibit the capacity to attain elevated levels of ductility. Ultimately, it identifies the moment-resisting joint with the highest potential for ductility, based on the appropriate equations for calculating the ductility factor for this joint type, alongside a comparative analysis of key mechanical parameters, such as moment resistance and initial rotational stiffness.
- **Chapter 3** introduces the component method and its traditional uses in steel connections. It then explores the different applications of the method in ductile moment-resisting timber joints, focusing on BiRs joints with a steel link. Finally, it outlines the key reasons for employing the component method in these types of joints.

- **Chapter 4** presents an experimental study on stiffened end-plate moment-resisting steel–timber joints, focusing on their load-bearing capacity, failure modes, and mechanical behavior. Tests were conducted on individual steel components (end-plates, links, and threaded rods), BiR connections under tension, and compression of steel T-stubs against GLT. Additionally, 15 full-scale joints were tested using both conventional transducers and digital image correlation (DIC). This research explored joints with multiple bonded-in rod arrangements (two and four rows) to trigger failures in different components.
- **Chapter 5** applies the component method on a design procedure to estimate moment resistance, initial rotational stiffness, and rotational capacity of stiffened end-plate moment-resisting steel–timber joints with steel links and multiple bonded-in rods. The study enhances the precision of stiffness predictions by analyzing the coupled behavior of the link with other joint components and introducing new equations for timber–steel interactions. The method divides the joint into macro-components, characterizes each, and assembles them to determine overall mechanical properties. Analytical predictions are then validated using full-scale experimental results.
- **Chapter 6** outlines the key objectives related to the numerical modelling and parametric analysis of moment-resisting steel-timber joints, focusing on verifying the applicability of the proposed analytical procedure across an extended range of geometries. First, detailed numerical models of these joints were developed using Abaqus® software. Next, the structural behavior predicted by the simulations was verified through a comparative analysis with experimental data. Building on this validated modelling approach, the aim was to investigate critical design parameters that influence joint performance, particularly in achieving high moment capacity and initial rotational stiffness. Finally, the chapter includes a parametric analysis to evaluate the applicability range of the component method, examining both stiffened and unstiffened joint configurations with groups featuring either two or four rows of bonded-in rods.
- **Chapter 7** summarises the study developed in the thesis, with the main contributions and the suggestion of future developments based on the gained experiences and result.

CHAPTER 2

DUCTILITY IN MOMENT-RESISTING TIMBER JOINTS

This chapter provides a comprehensive overview of the principal moment-resisting timber joints that exhibit the capacity to attain elevated levels of ductility. Ultimately, it identifies the moment-resisting joint with the highest potential for ductility, based on the appropriate equations for calculating the ductility factor for this joint type, alongside a comparative analysis of key mechanical parameters, such as moment resistance and rotational stiffness

2.1 Ductility

In timber structures, ductility is primarily achieved through the connections between elements. While the structural members themselves generally behave linearly, any nonlinear response must be concentrated in the joints, as prescribed by Eurocode 8 (EN 1998-1:2013). Ductility, defined as the ability of a joint to undergo significant deformation in the plastic range without a substantial loss of resistance, is a fundamental requirement for moment-resisting steel–timber joints intended for use in post-and-beam systems.

In such structures, where global stability depends on the rotational stiffness and moment resistance of the joints, ductile behavior allows for stress redistribution and prevents sudden brittle failures that could compromise safety (Jorissen and Fragiacomo, 2011). Ductile connections need to be designed to provide adequate rotational stiffness in the elastic region, especially in tall timber buildings which are usually governed by the wind serviceability limit state, wherein connections with too little elastic stiffness compromise the overall lateral load system design (Buchanan, 2016). However, achieving this behavior in timber joints is challenging due to the inherently brittle nature of timber, particularly in tension.

The steel parts, if efficiently connected to timber, can contribute significatively to build ductile steel-timber joints. Steel components as end-plate in bending, and beam web in tension are two examples of high ductile components that can be easily connected to timber and improve the joint ductility. They present a load-displacement curve that changes from an initial linear elastic mode into

a second carrying mode which allows increasing displacement with increasing force (Kuhlmann *et al.*, 1998).

This thesis addresses the application of the component method to predict the monotonic behavior of moment-resisting steel–timber joints with sufficient mechanical capacity for effective utilization in post-and-beam or moment-resisting timber structures. While a variety of steel-timber joint configurations have been proposed in the existing literature, it is crucial to identify those that exhibit the highest potential for integrating significant rotational stiffness, moment resistance, and ductility. To achieve optimal performance, these joints must leverage the complementary mechanical properties of both materials: the plastic deformation capacity of steel and the localized compressive behavior of timber.

To identify the potential of these joints, it is initially interesting to define how ductility can be measured. Ductility or ductility factor (μ) is commonly quantified as the ratio between ultimate displacement (Δ_{Fu}) and elastic displacement (Δ_{Fy}), as recommended by standards like EN 12512:2001 and Swiss timber design, Norm SIA 265:2021, and shown in Equation (2.1).

$$\mu = \Delta_{Fu}/\Delta_{Fy} \tag{2.1}$$

The ideal load–displacement curve for potential ductile elements can be described by a linear elastic part, up until the proportional limit with elastic displacement (Δ_{Fy}), a non-linear softening and plasticisation part, up until the maximum load capacity/peak force is reached with respective displacement, and a softening region until the ultimate capacity and ultimate displacement (Δ_{Fu}) are reached. In this case, the total plastic deformation is defined by the difference between ultimate displacement and elastic displacement. Then the ductility factor (μ) can be calculated by Equation (2.2).

$$\mu = (\Delta_{Fu} - \Delta_{Fy})/\Delta_{Fu} \tag{2.2}$$

The process of quantifying ductility depends on the yielding displacement point, defined as the load at which an assembly begins to deform plastically. In theory, this point can be detected under monotonic loading tests. However, most timber connections exhibit a nonlinear load-displacement relationship and an unclear transition between elastic and plastic behavior. Muñoz *et al.* (2008) summarized the commonly used methods (Figure 2.1) and highlighted that using different methods can result in values differing by up to 80%.

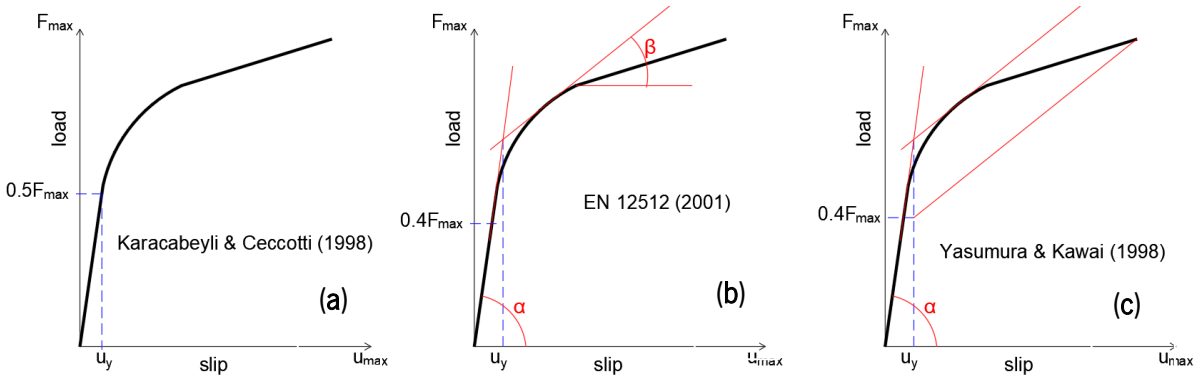


Figure 2.1. Different methods to calculate the yielding point. Adapted from (a) Karacabeyli and Ceccotti (1998); (b) EN 12512:2001; and (c) Yasumura (1998).

A classification system for timber joints was proposed by Smith *et al.* (2006), through which connections and components can be classified in four categories (Table 2.1), associated with a specific failure mode. The ductility factor (μ) used by this classification is the one suggested by EN 12512:2001. The ductility factor can be applied either to an entire timber structure or to specific components, such as subsystems or connections.

Table 2.1. Proposed ductility classes for connections or components. Adapted from Smith *et al.* (2006).

Classification	Average ductility factor
Brittle	$\mu \leq 2$
Low Ductility	$2 < \mu < 4$
Moderate Ductility	$4 < \mu \leq 6$
High Ductility	$\mu > 6$

In Eurocode 8 (EN 1998-1:2013) another classification was suggested. Timber buildings were categorized into three ductility classes—low (L), medium (M), or high (H)—based on their ability to withstand seismic forces through ductile behavior and energy dissipation. These classes, summarized in Table 2.2, correlate with permissible values of the behavior factor (q), which influences seismic design forces.

To qualify for ductility class M, the dissipative zones of the structure (primarily the joints, as previously noted) must sustain plastic deformation for at least three fully reversed cycles at a ductility factor of 4. For the higher class (H), the joints must achieve a ductility factor of 6 while maintaining at least 80% of their resistance, ensuring minimal strength degradation under cyclic loading. This classification system underscores the critical role of connections, the primary source of ductility in timber structures, and aligns with earlier definitions that emphasize deformation capacity without significant strength loss.

Table 2.2. Ductility classes for structure. Adapted from EN 1998-1:2013.

Design concept and ductility class	q	Examples of structures
Low capacity to dissipate energy - DCL	1.5	Cantilevers; Beams; Arches with two or three pinned joints; Trusses joined with connectors
Medium capacity to dissipate energy - DCM	2.0	Glued wall panels with glued diaphragms, connected with nails and bolts; Trusses with doweled and bolted joints; Mixed structures consisting of timber framing and non-load bearing infill
	2.5	Hyperstatic portal frames with doweled and bolted joints
High capacity to dissipate energy - DCH	3.0	Nailed wall panels withe glued diaphragms, connected with nails and bolts, Trusses with nailed joints.
	4.0	Hyperstatic portal frames with doweled and bolted joints
	5.0	Nailed wall panels withe glued diaphragms, connected with nails and bolts.

2.2 Moment-resisting joints in timber structures

Structural joints play an important role in the overall stability, load-bearing capacity, and seismic performance of timber buildings. Among the various joint typologies utilized in timber construction, moment-resisting joints hold particular significance due to their capacity to transfer bending moments between connected members, thereby enhancing structural stiffness and lateral load resistance. The rotational stiffness of timber joints can be classified as either rigid, semi-rigid or pinned, with significant implications for structural performance. In statically indeterminate systems, semi-rigid joints exhibit reduced moment transfer compared to fully rigid ones, leading to a redistribution of internal forces.

The use of semi-rigid joints instead rigid ones results in increased mid-span bending moment in structural members and greater displacements, particularly in systems where deformation is influenced by moment distribution. To better understand this phenomenon, the bending moment (M) within the shear plane of a connection can be expressed as a function of the relative rotation (θ) between adjacent members, as defined by the linear relationship presented in Equation (2.3). A schematic visualization of the rotational stiffness of a rigid, pinned or semi-rigid joint is shown in Figure 2.2.

$$M = k \cdot \theta \tag{2.3}$$

where k is the secant rotational stiffness and will be referred to as the rotational stiffness of the joint.

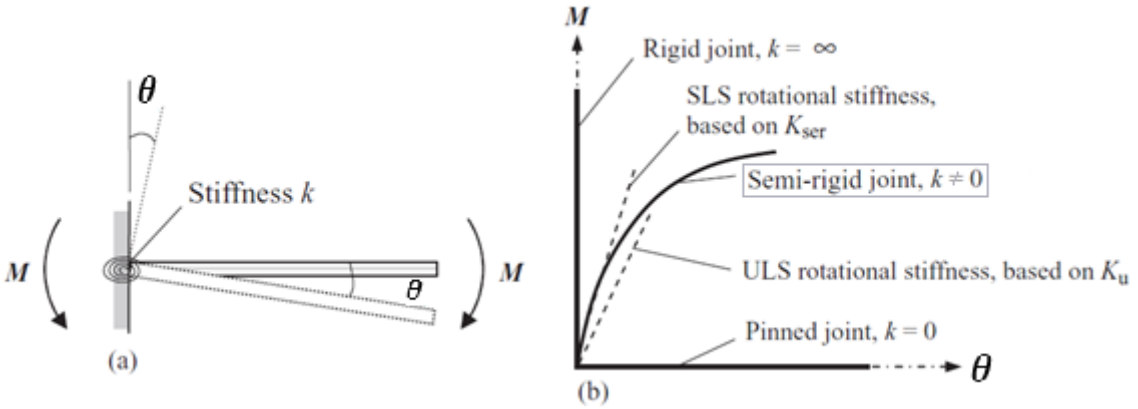


Figure 2.2. Different types of rotational stiffness in a timber joint (a) semi-rigid connection representation; (b) Joint moment-rotation behavior.

Semi-rigid (denominated here as moment-resisting) timber joints can be broadly categorized according to the type of fasteners employed, i.e. mechanical fasteners and/or glued fasteners, which significantly influence their mechanical performance and failure mechanisms.

In joints with mechanical fasteners, such as bolts, dowels, or screws, load transfer between steel and timber occurs primarily through bearing, shear, and friction at the contact points between the fasteners and the timber. The overall stiffness and strength of the connection depend on parameters such as the number, diameter, and spacing of the fasteners, as well as the embedment and bending strength of both materials. These connections typically exhibit semi-rigid behavior, allowing some degree of slip between the steel and timber before full load transfer is achieved. Their ductile response arises mainly from the plastic deformation of steel fasteners and local compression of timber, which also contributes to energy dissipation. In contrast, joints employing glued fasteners, such as glued-in rods or steel plates, transfer load continuously along the bonded surface through the adhesive layer, primarily via shear stresses in the bondline. This mechanism provides a more uniform stress distribution and mitigates the local stress concentrations typical of mechanical fasteners. Properly designed glued joints can achieve high stiffness and strength, behaving closer to a fully rigid connection with minimal slip. However, they tend to exhibit brittle failure modes if the adhesive bond or the surrounding timber fails suddenly, making adequate anchorage and adhesive toughness essential. In summary, while mechanical fasteners generally offer lower initial stiffness and moment capacity, their superior ductility provides desirable warning before failure and allows for controlled deformation under load. Conversely, glued fasteners typically display higher rotational stiffness and moment resistance, making them suitable for high-performance joints in rigid moment-resisting frames, though their limited ductility remains a critical design consideration. The predominant types

of moment-resisting timber joints that have been utilized in timber structures are those with bolted/dowelled slotted-in steel plate connections and those with bonded-in rod connections.

2.2.1 Reinforced bolted slotted-in steel plate connections

A reinforced bolted or dowelled slotted-in steel plate connection consists of one or more steel plates inserted into slots precisely cut into the timber member, typically along its mid-thickness. The steel plate extends beyond the timber face to allow the connection to another structural element, such as a column flange or an end plate. Bolts or steel dowels pass transversely through both the timber and the slotted steel plate, ensuring mechanical interlock between the components. Reinforcement elements, such as self-tapping screws, are often placed around the slotted region or along the grain direction to prevent splitting of the timber.

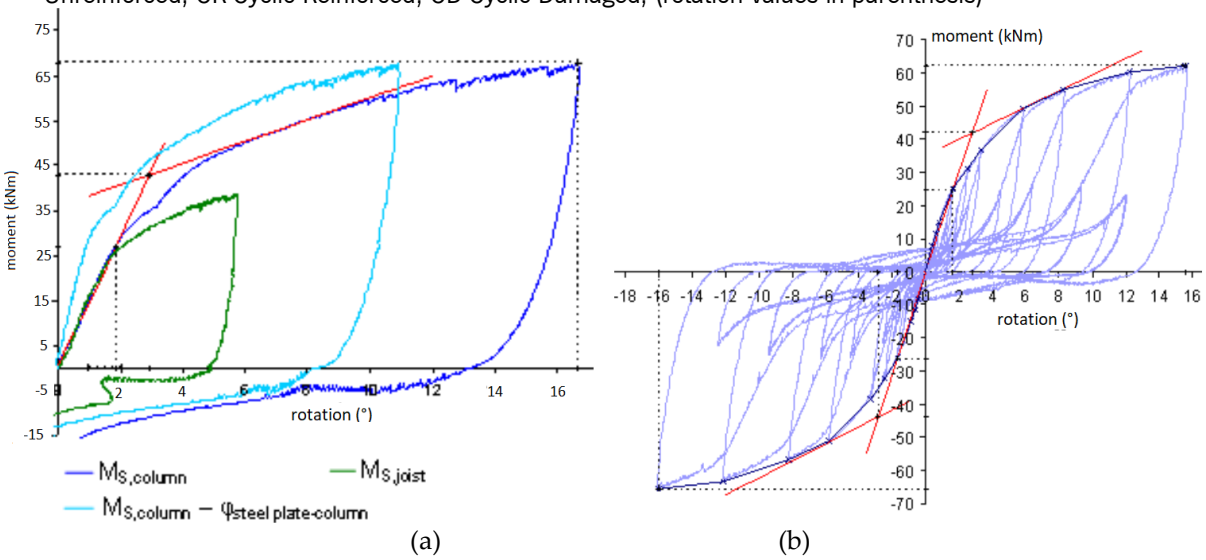
To obtain a ductile failure mode for bolted glulam connections with slotted in steel plates, Lam *et al.* (2008) evaluated the use of self-tapping screws. The screws were installed directly into the wood members without pre-drilling in the direction perpendicular to both the wood grain and the bolts. Connections made by conventional glulam and glulam reinforced by self-tapping screws (STS) were also tested for comparison purposes. The connection specimen geometry was 130 × 305 mm^2 in cross-section and 830 mm long for the beam members and the column members were 272 × 305 mm^2 in cross-section and 1000 mm long. It was demonstrated (Table 2.3) that the experimental results of beam-to-column connection specimens showed that the connections reinforced with self-tapping screws had an increased moment capacity by a factor of 2 and 1.7, under monotonic (M) and reverse cyclic loading (C), respectively, when compared to unreinforced connections, where U is unreinforced connections; R is reinforced connections and D is damaged retrofitted connections.

The moment-rotation curve of the reinforced connection is shown in Figure 2.3. A ductile failure mode was achieved with the reinforcement of the connections. In this specific case, it was observed a plug shear failure on the tension side of the beam member under the bolt towards the bottom end. This indicates that the screws have the capacity to carry the imposed stresses in the perpendicular to grain direction, thereby changing the failure mode to parallel to grain axis failures (Lam *et al.*, 2008). The failed specimens showed Mode I (Johansen Yield Model) type failure in the beam members with heavy wood crushing through the whole length in some of the dowel holes.

Table 2.3. Summary of response of connections under monotonic and cyclic loading (Lam *et al.*, 2008).

	MU	MR	MD	CU	CR	CD
Max Moment([kNm) at Rotation (°)	31.49 (5.06) 2.97 (0.70)	65.88 (2.12) 16.59 (0.06)	58.85 (4.36) 13.29 (2.00)	35.7 (1.63) 4.01 (0.17)	62.54 (1.55) 15.9 (0.17)	54.54 (3.27) 12.65 (1.26)
Failure Moment (kNm) at Rotation (°)	25.19 (4.05) 3.00 (0.65)	- - - -	47.08 (3.49) 14.42 (1.96)	28.83 (1.85) 5.15 (1.24)	- - - -	41.14 (2.33) 11.96 (0.39)
Yield Moment (kNm) at Rotation (°)	- - - -	41.20 (1.58) 2.80 (0.26)	41.16 (7.36) 3.87 (1.55)	34.29 (0.30) 2.22 (0.01)	41.83 (0.83) 3.00 (0.20)	45.49 (1.70) 5.90 (0.40)
Elastic Stiffness (kNm/°) at Rotation (°)	13.73 (1.32)	14.54 (1.16)	12.38 (3.81)	14.96 (0.69)	14.02 (0.77)	9.33 (0.84)
Ductility Ratio (-)	-	>5.97 (0.62)	4.21 (1.50)			

*MU-Monotonic Unreinforced; MR-Monotonic Reinforced; MD-Monotonic Damaged; CU-Cyclic Unreinforced; CR-Cyclic Reinforced; CD-Cyclic Damaged; (rotation values in parenthesis)



(a) (b)

Figure 2.3. Moment-rotation curves of the reinforced connection. (a) Monotonic load (b) Cyclic load. Adapted from Lam *et al.* (2008).

Lam *et al.* (2010) expanded on their previous studies by utilizing self-tapping screws as perpendicular-to-grain reinforcement in three different layouts. They studied the influence of bolt diameter and edge distances of the bolts. The results showed that the moment capacity increased by 22.5% when the bolt diameter in the reinforced connection was increased from 19.0 mm to 25.4 mm. Additionally, a reduction in the edge distances of the bolts in the reinforced connection provided an additional gain in moment capacity of 35.3%, leading to a total capacity increase by a factor of 2.9 when compared to unreinforced connections. However, experimental results under cyclic testing

demonstrated that the larger bolt diameter increased maximum moment and elastic stiffness, but reduced rotation capacity by almost 50%. This also resulted in a brittle failure mode characterized by plug shear, followed by slight crack development and wood embedment failure (Figure 2.4).

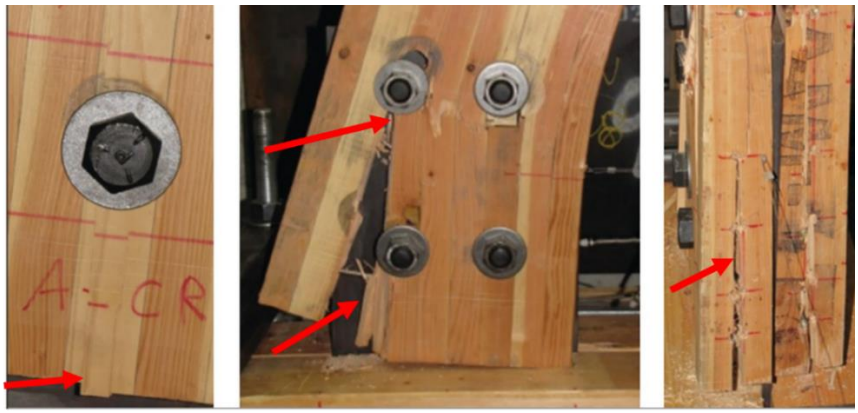


Figure 2.4. Typical failure for reinforced slotted-in plate connection under cyclic loads, plug shear, splitting and wood embedment failures, respectively. Adapted from Lam *et al.* (2010).

Wang *et al.* (2015) studied the rotational behaviour of bolted beam-to-column glulam connections reinforced using locally cross-laminated glulam members. Twenty-two full-scale connections have been tested through monotonic and reversed cyclic loading to establish its moment/rotational angle relationships. These have been divided in six groups: S1 and S4 for glulam unreinforced connections; S2 and S5 for STS-reinforced glulam connections; S3 and S6 for locally cross-laminated glulam connections. Groups S1 to S3 were tested under monotonic loading and Groups S4 to S6 under cyclic loading. The moment-rotational angle relationships of monotonic loading tests are shown in Figure 2.5. They pointed out that the locally cross-laminated technique improved the moment resistance (52% and 46% for monotonic and cyclic loading, respectively), and energy dissipation (25%) of the tested connections. However, STSs were found to be more effective than the locally cross-laminated technique in terms of the moment resistance and energy dissipation.

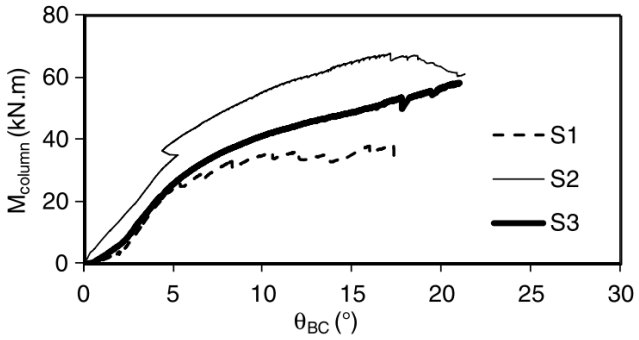


Figure 2.5. Moment and rotational angle relationships under monotonic loading tests. Adapted from Wang *et al.* (2015).

Solarino *et al.* (2017) also analyzed the response of a semi-rigid moment-resisting beam-to-column dowel-type connection. A timber frame connection (Figure 2.6) was subjected to a static monotonic load test. Glulam of strength class GL24h was used, while the fasteners were made of S235 grade steel and had a diameter of 16 mm. A steel plate, 8 mm thick, was slotted into the timber elements. The moment-rotation diagram was generated as a response to the static monotonic load experiment (Figure 2.7a). The test was interrupted due to cracks in the timber column. The brittle failure resulted from the tension perpendicular to the grain observed in the column (Figure 2.7b).

The rotational behavior of typical bolted glulam beam-to-column connections with slotted-in steel plates was also analysed by Sun *et al.* (2020). To validate the finite element model, the failure mode and the moment-rotation curves were compared to experimental results obtained by Lam *et al.* (2008), Lu *et al.* (2016), and Wang *et al.* (2015) (Figure 2.8). It is important to note that the failure modes found in the finite element model were similar to those of the experimental specimens.

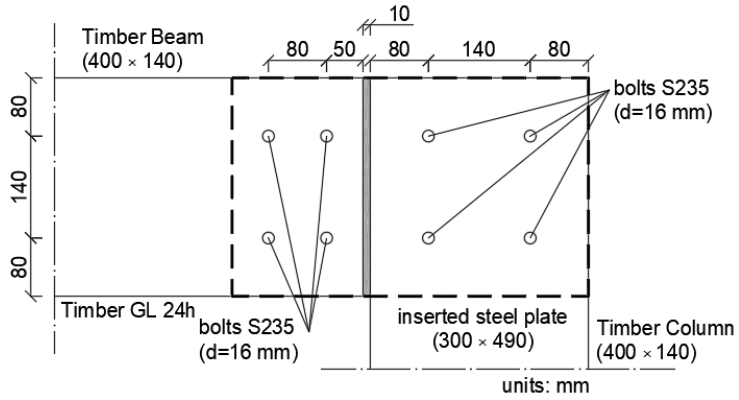
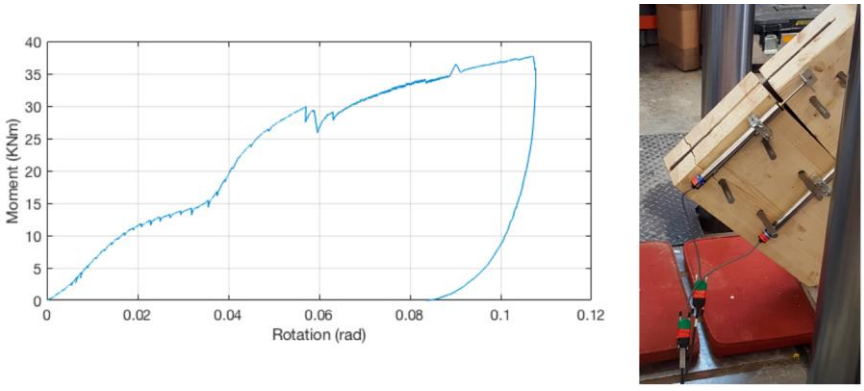


Figure 2.6. Steel-timber joint layout. Adapted from Solarino *et al.* (2017).



(a) (b)

Figure 2.7. Experimental results. (a) Monotonic test; (b) Specimen at failure. Adapted from Solarino *et al.* (2017).

In particular, the experimental initial rotational stiffness and the post-elastic stiffness, were defined according to the secant stiffness method proposed by Yasumura and Kawai (1998). Analyzing the

moment-rotation curves obtained for the two specimens studied, with bolt diameters of 20 mm and 24 mm, it was found that the curve shapes, initial rotational stiffness, and stiffness degradation showed good agreement with the experimental results (Figure 2.9).

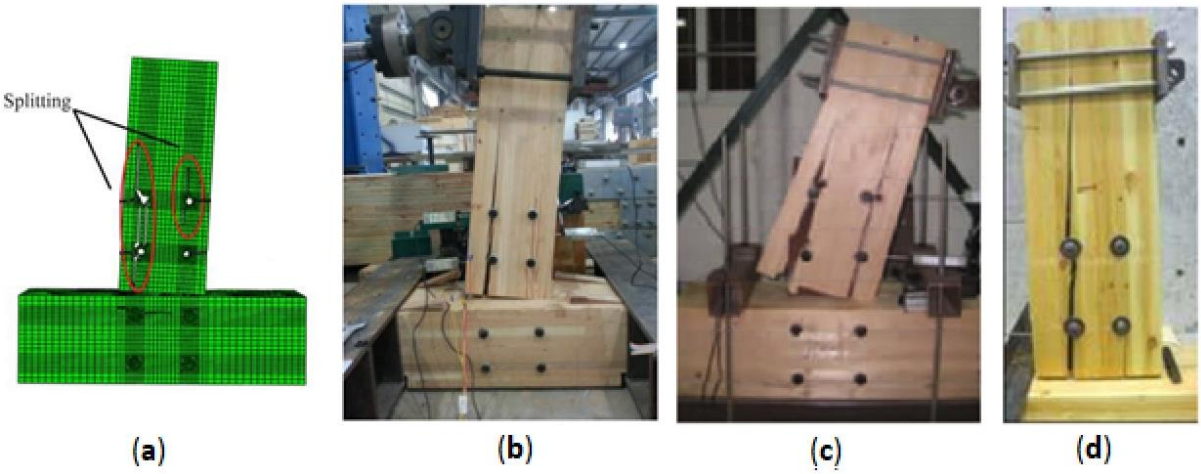


Figure 2.8. Comparison of the failure modes Sun *et al.* (2020): (a) finite element model, (b) specimen from Lu *et al.* (2016); (c) specimen from Wang *et al.* (2015); and (d) specimen. Adapted from Lam *et al.* (2008).

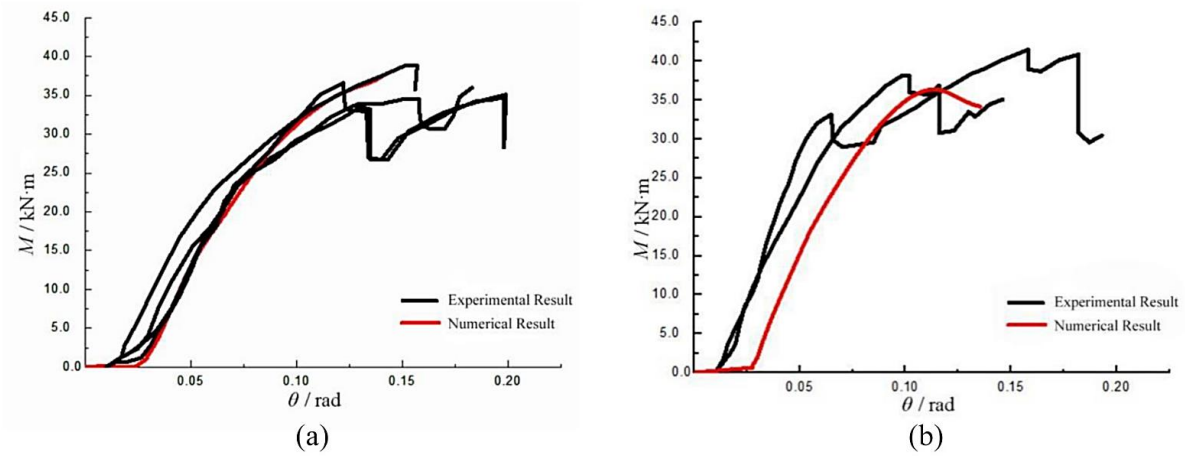


Figure 2.9. Moment–rotation curve: (a) model 1 (d = 20 mm) and (b) model 2 (d = 24 mm). Adapted from Sun *et al.* (2020).

According to Dong *et al.* (2021), connections using bolts or conventional smooth dowels exhibit initial slips and low initial stiffness, mainly due to oversized predrilled holes for fastener installation tolerance. They conducted an experimental and analytical investigation on the rotational behavior of glulam beam-column moment connections with self-drilling dowels (SDD). Seven full-scale connections were tested, both with and without STS reinforcement to address tension perpendicular to grain. All specimens had the same sizes and configurations for the glulam beams and columns, steel plates, and SDDs. The cross sections of the glulam beam and column were 450 × 315 mm² and 315 × 315 mm², respectively, with average densities and moisture contents of 466 kg/m³ and 12%.

Two 8 mm wide slots spaced 88 mm apart were manufactured to accommodate two 6 mm thick inserted steel plates. Additionally, there were 20 mm and 30 mm gaps around the steel plates in the beam and column, respectively, for convenience during installation. The 7.5 × 235 SDDs were used to drill through the glulam members and the two inserted steel plates (Figure 2.10).

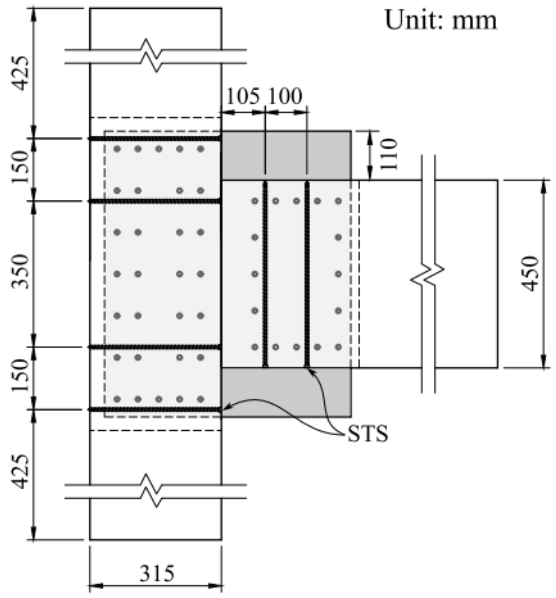


Figure 2.10. Specimen (Reinforced by STS under cyclic load). adapted from Dong *et al.* (2021).

Dong *et al.* (2021) concluded that in the reinforced specimens, timber splitting failure on the gap opening side was prevented by STS. The connections reached a peak load at an average rotation of 1.8°, after which the SDD gradually approached their ultimate bending strength. Connection failure occurred during the fourth cycle, with an average rotation of 3.7°, due to a combination of wood embedment crushing and low cycle fatigue failure of the SDD.

Based on the research discussed, it can be concluded that when the connections were reinforced with STS, a ductile behavior was observed under both monotonic and cyclic loading. To achieve these satisfactory results, the connections were generally constructed with eight dowels, each with a diameter of 19 mm or 20 mm (four on the beam and four on the column), varying the number of screws between four and six for each structural element. These variations in dowel positions, the diameters applied, as well as the number and position of screws are illustrated in Figure 2.11, which includes parameters from Lam *et al.* (2008) and Lam *et al.* (2010) in red, and from Wang *et al.* (2015) and Lu *et al.* (2016) in black. When the dowel diameter and the number of screws were increased, the connections failed in a brittle manner, limiting their ductile behavior. Furthermore, due to the reinforcement, the rotation capacity was reduced, while the maximum moment increased.

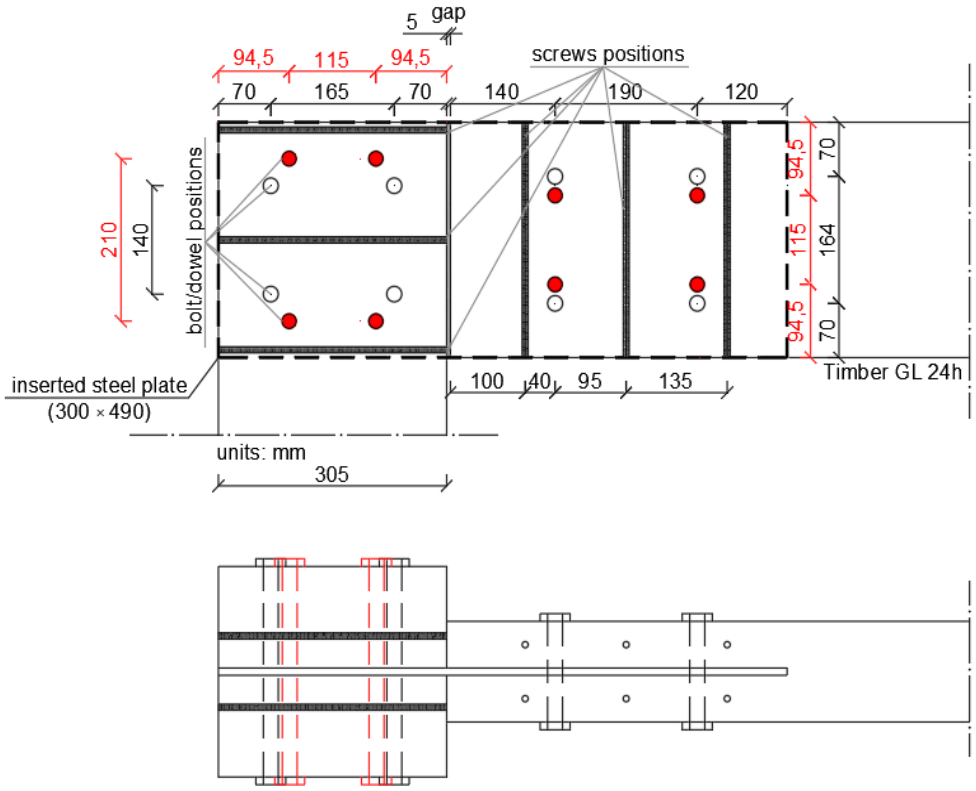


Figure 2.11. Geometries used in reinforced slotted-in ductile moment resisting connections, including positions and number of dowel and screws.

2.2.2 Bonded-in rods connections

Bonded-in rods (BiRs) connections represent a solution in timber engineering, whereby steel rods are adhesively bonded into timber elements. These hybrid connections effectively transfer both axial forces and bending moments, providing numerous advantages such as a high strength-to-weight ratio, stiffness, aesthetic appeal, and cost-effectiveness.

The typical installation process entails embedding rods parallel to the timber grain direction, thereby maximizing load transfer capacity by utilizing the timber's optimal mechanical properties. The prefabricated nature and off-site preparation of these connections facilitate rapid on-site assembly, with the additional benefit of complete concealment of steel components within the timber, offering inherent protection against fire exposure and environmental degradation (Jockwer *et al.,* 2023).

Extensive research efforts over the past decades have significantly enhanced the understanding of BiR connections. Initial investigations primarily concentrating on characterizing pull-out resistance and quantifying the bond behavior between the embedded rod and the surrounding timber. Early studies established fundamental relationships between load and slip, while systematically documenting various failure modes in single-rod configurations (Steiger *et al.*, 2007; Tlustochowicz, *et al.*, 2011; Steiger, 2012; Steiger *et al.*, 2015). This foundational work has enabled the development

of design provisions in several national timber design standards and guidelines as EN 1995-1-1:2014 and SIA 265:2021. Another significant development was the publication of EN 17334:2021, representing the first European test standard specifically addressing bonded-in rods and providing methodology for experimental determination of bond shear strength. In addition, the forthcoming generation of Eurocode 5 will incorporate a dedicated chapter on bonded-in rods (Jockwer *et al.,* 2023), establishing general design rules based in part on bond strength values determined according to EN 17334:2021. However, these improvements are limited to single-rod applications and does not specifically consider multiple-rod arrangements that are commonly encountered in practice. This gap in design guidance is particularly pertinent, as real-world structural applications almost invariably employ groups of rods working in combination, thereby creating a critical need for a comprehensive understanding of their behavior (Stepinac *et al.*, 2013).

Based on a review on literature about the BiRs connections, it was found a significant disparity between the extensive data on single-rod connections and the limited information regarding multiple-rod systems, which exhibit more complex interaction effects and failure mechanisms.Investigations into multiple rod pullout behavior have been conducted by several research teams (Broughton and Hutchinson, 2001; Gehri, 2001; Gattesco *et al.*, 2010; Parida *et al.*, 2013; Gonzalez *et al.*, 2016), with primary objectives including observation of failure modes, assessment of ductility potential, and evaluation of key geometric and mechanical parameter influences. Critical parameters examined include rod diameter, inter-rod spacing, edge distance requirements, anchorage length, and steel rod mechanical properties (particularly yield and ultimate strengths). The experimental methodologies employed generally follow established protocols from ISO 6891:1983 or EN 29816:2021, with measurement of failure loads, ultimate displacements, and detailed documentation of failure modes.

Analytical formulations are typically developed to predict joint capacity by comparing measured pullout resistance with the theoretical yield and tensile capacities of the steel rods. A recurring observation across multiple studies has been the occurrence of timber splitting failures near specimen edges prior to attainment of steel rod yield capacity. Two primary hypotheses have emerged to explain this phenomenon:

I. Practical challenges in achieving perfect alignment and uniform bond quality across all rods in multiple-rod configurations may lead to uneven stress distribution. This issue can potentially be mitigated through reinforcement strategies such as perpendicular screw installation.

II. The influence of adhesive layer thickness has been identified as a significant factor, with most studies employing a 2 mm glue line thickness resulting from drilling holes 4 mm larger than rod diameter. Parida *et al.* (2013) demonstrated that reducing glue line thickness to 1mm improved bond strength but simultaneously increased susceptibility to premature splitting failures. Additional research by Gonzalez *et al.* (2016) has provided important insights regarding minimum edge distance requirements, recommending values of at least 3d (where d represents rod diameter) compared to the $2.5d$ minimum specified in most current standards. Their findings also established $5d$ as the minimum recommended spacing between rods to ensure ductile behavior, with smaller spacings consistently resulting in brittle failure modes. Once an anchorage length exceeding $10d$ is achieved, connection capacity can reasonably be estimated as the summation of individual rod yield forces, provided ductility requirements are satisfied. Achieving uniform stress distribution across all rods in pullout tests requires careful experimental design, typically involving the use of rigid end-plates and sufficient free length for unrestrained rod deformation. The selection of steel grade represents another critical consideration, with high-strength steels generally discouraged for multiple-rod applications due to their limited capacity for load redistribution and heightened sensitivity to construction imperfections, which can lead to actual capacities significantly below predicted values (Bouchard *et al.*, 2021). Following the recommended spacing and edge distance guidelines, as outlined in both standards and research literature, substantially improves the likelihood of successful experimental outcomes.

Regarding moment-resisting joints with BiRs connections, Buchanan and Fairweather (1993) tested seven types of moment-resisting connections between glulam members using steel bars embedded in the timber parallel to the grain. Three portal frame knee joints and four multi-story beam–column connections were tested. In Figure 2.12 (a), a knee joint with epoxied bars passing through the rafter is shown; in Figure 2.12 (b), a mitred connection with steel bars welded to a steel plate in the mitre; and in Figure 2.12 (c), a joint with a steel bracket connected to reinforcing bars. The multi-story connections tested are shown in Figure 2.13, where Figure 2.13 (a) presents a threaded rod connection without steel brackets, Figure 2.13 (b) shows a connection with box steel brackets, Figure 2.13 (c) depicts a connection with a central steel joint, and Figure 2.13 (d) illustrates a connection with lateral steel brackets and nylon plates.

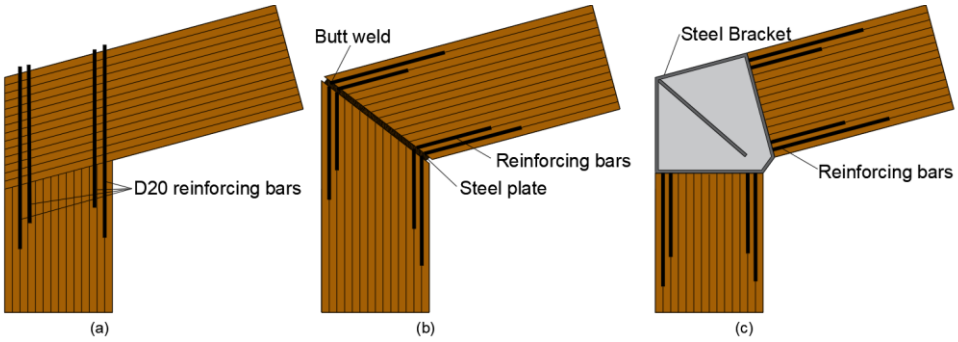


Figure 2.12. Moment resisting glulam connections tested by Buchanan and Fairweather (1993).

A capacity design was adopted in all beam-to-column connections, and the ductility response of each connection was analysed under cyclic loading. Due to the proximity of the BiRs to the edge of the timber elements, most of the connections studied exhibited a brittle behavior. This was primarily due to premature timber failures associated with drilled holes in the rafters or to the split occurred near the inner bars at low load levels. Based on the experimental hysteresis loops obtained, it is possible to conclude that only the steel bracket portal frame knee joint (Figure 2.12 (c)) was suitable for a ductile seismic design, due to inherent ductile achieved by the steel bracket. Related to the multi-story beam-column connections (Figure 2.13), better performance was achieved by the steel bracket joint (Figure 2.13 (b)). In this case, good behavior with a ductility factor (μ) of ± 6.0 was achieved. Local splitting of the steel flange near the weld to the web reduced the load slightly in the last cycle.

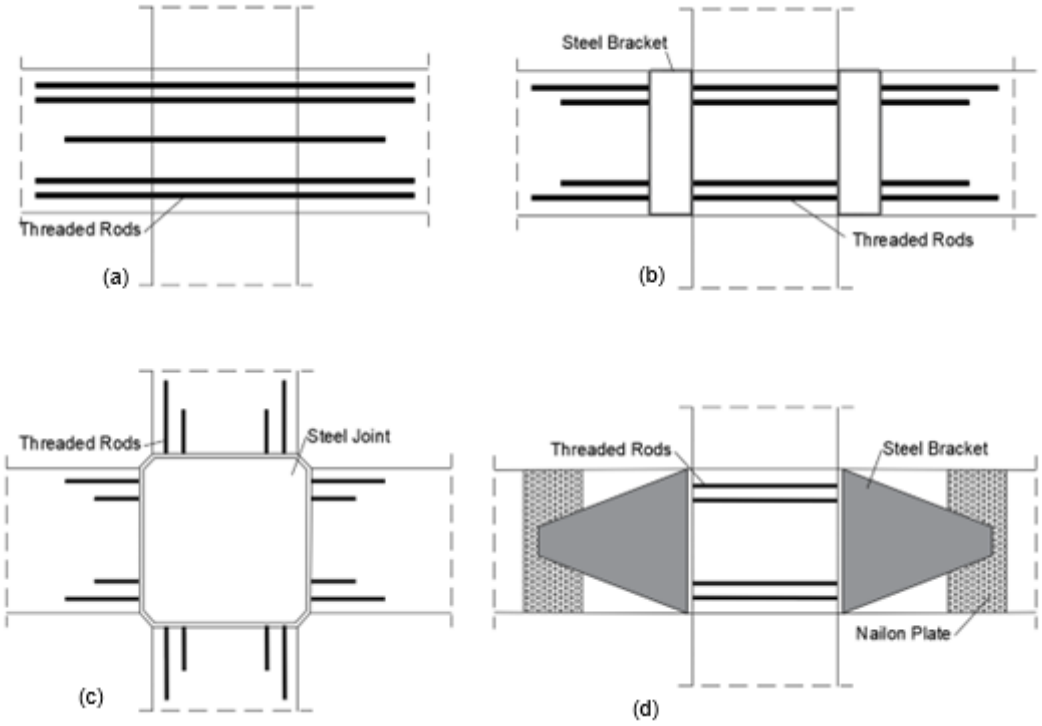


Figure 2.13. Moment resisting glulam connections tested by Buchanan and Fairweather (1993).

After that, Buchanan *et al.* (2001) investigated the ductility through the yielding of steel rods within glulam. Three different arrangements of bars were considered: center bar, angle bar, and tie bar (TB) specimens, as presented in Figure 2.14. Under monotonic tests, the center bar specimens (Figure 2.14 (a)) failed in shear and tension, while the two angle bar specimens (Figure 2.14 (b)) failed in shear with a longitudinal crack down the center of the beam. The tie bar arrangement (Figure 2.14 (c)) demonstrated the best performance, achieving a moment of 155 kNm, but failed due to shear cracks observed from the end of the beam.

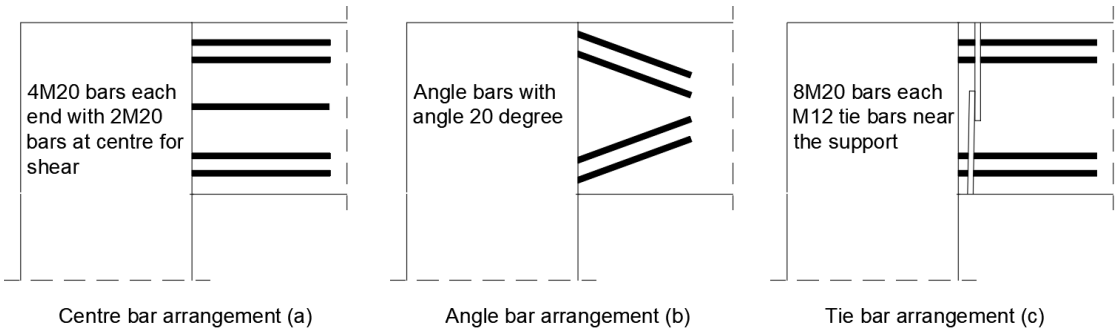


Figure 2.14. Summary of moment-resisting specimens arrangements Buchanan *et al.* (2001).

Based on the findings of prior research, which indicate the challenges associated with achieving high levels of ductility in joints constructed solely with BiR connections, Tomasi *et al.* (2008) and Andreolli *et al.* (2010) proposed an alternative joint configuration in which a timber element is connected to a steel link by means of an end-plate and bonded-in steel rods (Figure 2.15). The transmission of bending moments is facilitated by the end-plate and steel bars, whereas shear forces are transmitted through the bonded-in steel plate located between the timber element and the steel section. To investigate the failure modes, moment resistance, and rotation capacity of this joint, both monotonic and cyclic tests were conducted. In this research, a steel profile (4) was connected to a reinforced timber element (5) via end-plate. The transfer of bending moments is ensured by the presence of steel bars bonded within the timber elements (3), while shear forces are transmitted through a glued steel plate (1) inserted into a centrally grooved slot at the end of the timber element (2).

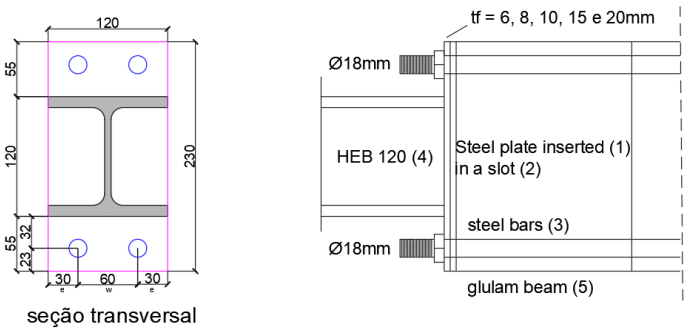


Figure 2.15. Joint parts configuration tested by Tomasi *et al.* (2008).

First, six specimens, varying the thickness of end-plate, were tested under monotonic load to obtain the failure mode of T-stub, tension resistance and load-displacement curves. The capacity design was applied to ensure the failure of the T-stub. All specimens presented a ductile failure mode, except P10w and P20w specimens, where the shear load is directly supported by the steel bars. However, the adhesive is not able to follow such large strains, a progressive reduction of the glued length takes place, and therefore the joint exhibits brittle failure. The joint P20w (reduced section of the bar) also presented brittle failure, through the mode 3. The load-displacement curves of each specimen at monotonic loads are presented in Figure 2.16. For the specimens manufactured without a bonded-in steel plate, and where the shear load is transferred through the bonded-in steel bars, it can be observed that no specimen showed a failure mode associated with stresses orthogonal to the fibres at the interface with steel bars. Timber can produce prying forces in the end-plate. The specimen without steel plate presented better accuracy than others (Andreolli *et al.*, 2011). It is important to note that adopting an appropriate steel end-plate thickness can ensure an overstrength factor. In all the tests performed, the failure modes involved the steel parts of joint rather than the timber ones. In the cases considered, the overstrength of the timber beam was guaranteed by using steel-reinforced glulam beams.

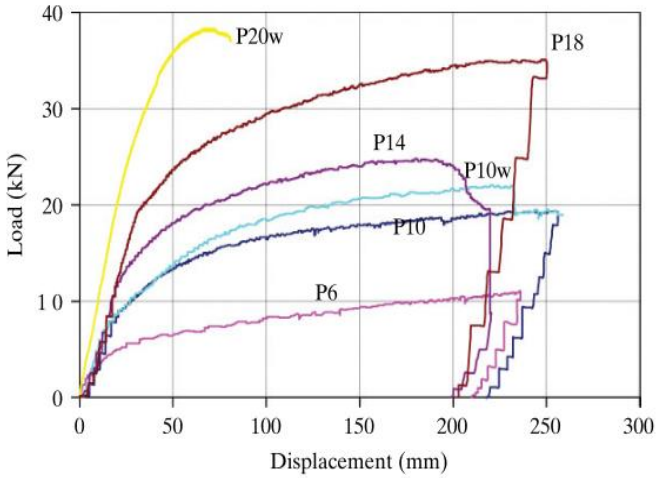


Figure 2.16. Load-displacement experimental curves for each specimen. Adapted from Tomasi *et al.* (2008).

After evaluating the moment-rotation relationship of the joint and assessing its ductility under cyclic tests, it was found that all specimens failed due to bending of the end-plate near the weld, attributed to low cyclic fatigue, except for P20-sp, which exhibited a local bar failure mechanism. Figure 2.17 compares the hysteretic moment–rotation relationships with the monotonic experimental curves for two specimens (P6 and P10). The fracture of the end-plate occurred after several cycles at large plastic displacements, with only a limited reduction in resistance observed in subsequent cycles.

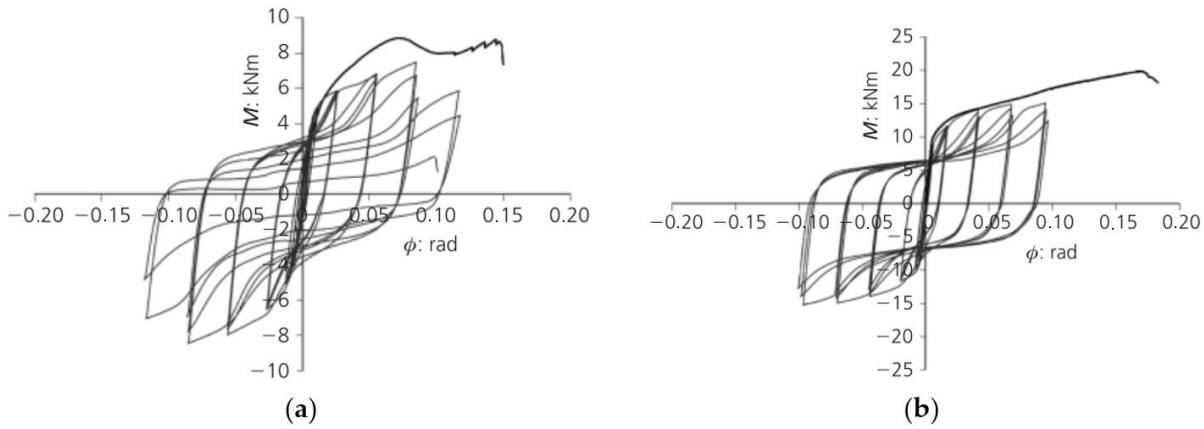


Figure 2.17. Monotonic and cyclic moment–rotation relationship experimental results for (a) specimen P6; (b) specimen P10. Adapted from Andreolli *et al.* (2011).

In a similar study, Yang *et al.,* (2016) proposed a connection involving three separate steel box sections connected with bonded-in rods or bonded-in steel tubes to a glulam beam end and with connecting bolts to a glulam column (Figure 2.18). The steel box section in the middle of the connection was combined with a bonded-in steel tube primarily to transfer shear force and prevent shear failure of the connection, while the other two steel box sections, combined with bonded-in rods, were used to transmit the bending moment. The tube wall and stiffener had a thickness of 6 mm, while the cross-sectional dimensions were 120 mm x 80 mm with a length of 135 mm. The rectangular washers (backing plates) under the nuts measured 67.5 mm x 40 mm x 6 mm. The steel plates were characterized as grade S235, with a modulus of elasticity of 200 GPa, a nominal yield stress of 310 MPa, and an ultimate strength of 420 MPa.

The glulam had an average moisture content of 15.0% with a standard deviation of 0.70, while the average density was 530 kg/m^3 with a standard deviation of 20.0. The bolts and bonded-in rods were grade 8.8, with a yielding strength of 640 MPa and an ultimate strength of 800 MPa, while the grade of the bonded-in steel tube for resisting shear was S235. Moreover, the backing plates and bearing plates were all S235. A two-component epoxy resin with a density of approximately 1500 kg/m^3 and a glue-line thickness of 2.0 mm was used to bond the rods to the glulam beams.

Three series of specimens were tested: one under monotonic load and the other two under cyclic loading. All of the specimens exhibited reasonable ductility. The load–displacement curves and moment-rotation curves are shown in Figures 2.19 and 2.20.

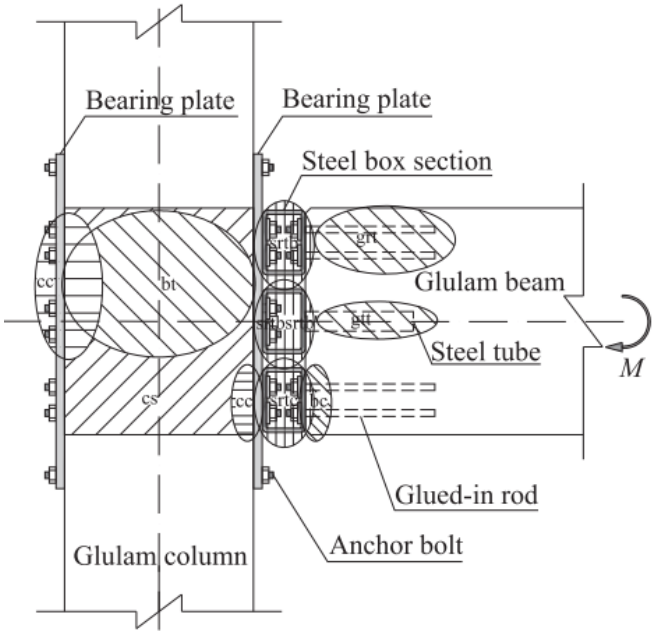


Figure 2.18. Joint geometry and steel components Yang *et al.* (2016).

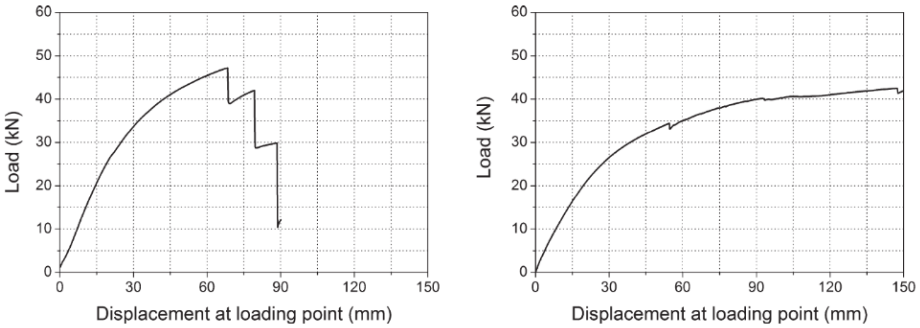


Figure 2.19. Load-displacement curves for specimens (a) JT2-1 (b) JT3-1 under monotonic tests Yang *et al.* (2016).

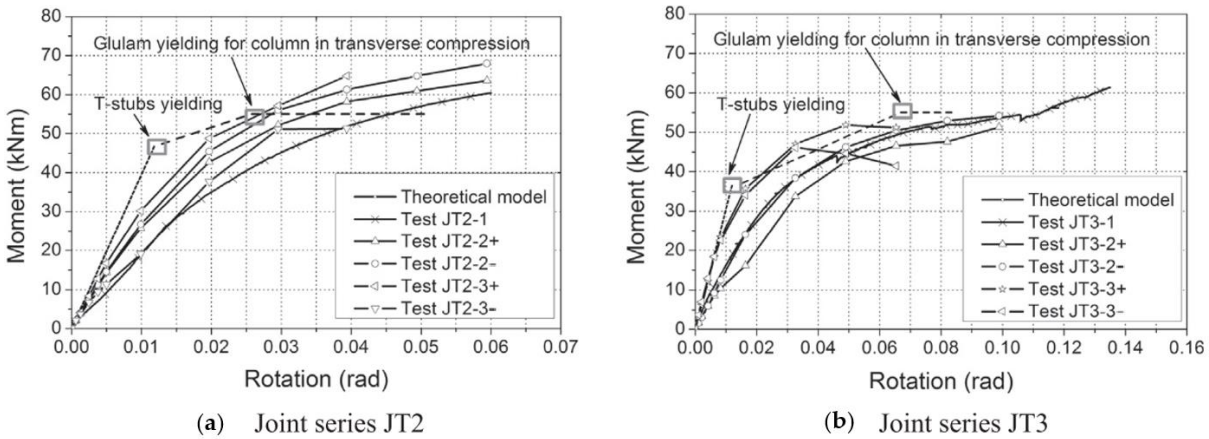


Figure 2.20. Moment-rotation curves for monotonic tests Yang *et al.* (2016).

Recent advancements in moment-resisting joints, including end-plate and BiR connections, exhibit significant improvements in ductility and load-bearing capacity. A comprehensive comparison of the

potential of these joints can be conducted to elucidate which design possesses the most favourable characteristics for achieving high ductility, along with adequate levels of rotational stiffness and moment resistance, suitable for application in timber frame structural systems.

2.3 Ductility comparison between main joint types

Early applications of moment-resisting connections in timber portal frames encountered performance limitations, including premature timber splitting and excessive lateral displacements. These issues were addressed through the development of ductile connection systems, which substantially improved frame behavior by increasing ultimate load capacity while reducing displacements. Most research efforts have concentrated on reinforced dowel-type slotted-in plate connections, with relatively limited experimental data available for moment-resisting timber frames incorporating bonded-in rod connections.

Dowel-type connections with slotted-in steel plates are the most common solution in global practice. In their basic unreinforced form, these connections exhibit low moment capacity and brittle failure under cyclic loading. However, reinforcement strategies can substantially improve their structural performance. Comparing this joint type, as detailed in Table 2.4, reveals that the application of perpendicular self-tapping screws (STS) enhances initial stiffness, moment capacity, and rotation capacity. Nonetheless, even with STS reinforcement, the failure mode remains brittle, although it occurs at significantly higher deformation levels compared to unreinforced configurations.

Bonded-in rod connections present an alternative approach with distinct characteristics. Existing studies indicate that configurations without metallic profiles tend to experience premature timber failures at low load levels. The use of inclined steel rods introduces additional considerations, as these elements can induce internal damage leading to shear failures within the timber. However, significant performance improvements are achieved when combining bonded-in rods with steel profiles or box sections, resulting in enhanced rotation capacity and ultimate moment values. In these hybrid configurations, the steel components typically yield before failure of the bonded-in rods, producing more desirable ductile failure modes. Although there is limited research that has applied this connection to moment-rotation heavy timber structures, as presented in Table 2.5, it has demonstrated a good level of rotation capacity. However, the moment capacity is low compared to bolted connections reinforced with STS, possibly due to the small height of the beams applied in these research tests.

Based on the presented research, the graph that compares the performances of the most representative moment-rotation timber joints in terms of ductility is presented in Figure 2.21. It uses the ductility factors suggested by EN 12512:2001 for the graph's ordinate and those from Equation (2.2) for the abscissa.

The joints that exhibit the highest levels of ductility are the bonded-in rods, classified as high ductility. Bolted slotted-in plate connections reinforced with STS and self-drilled dowels (SDD) also show a good level of ductility but are generally classified as moderate ductility. It is important to note that the definition of the joint to be used must also include fundamental parameters such as moment and rotation capacities, as well as the ability to dissipate energy. Therefore, it is crucial to emphasize that the bonded-in rod connections studied do not have a similar moment capacity to the reinforced bolted slotted-in plate connections.

In general, the bonded-in steel rods presented better results, likely due to the significant influence of steel profiles on connection yielding. Despite their excellent mechanical behavior, the reinforced bolted slotted-in steel plate connections exhibited medium ductility values because they have higher rotation at yield values, which generate small plastic regions where energy dissipation is more critical. Although considerable work has been done on the ductility assessment of timber joints, several questions remain unanswered. Moment-resistant timber connections are governed by very complex mechanisms and depend on a large number of geometrical, material, and configuration parameters and their combinations. The implications of their performance on moment-resistant timber frames are even broader and need to be evaluated from the perspective of the overall behavior of the structure.

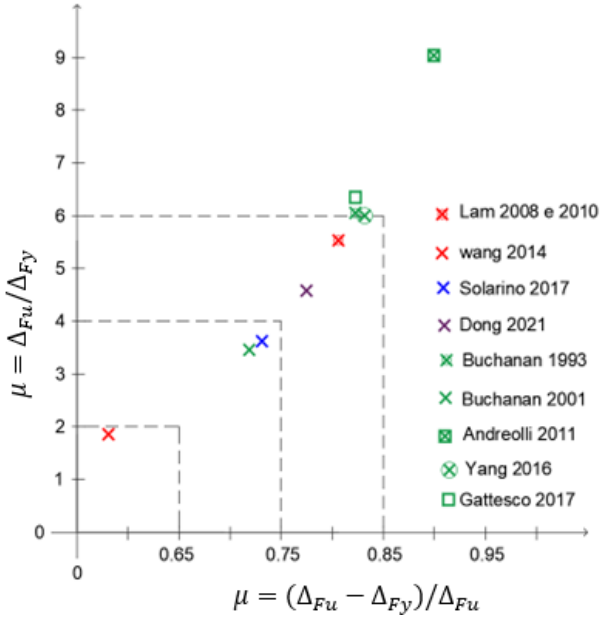


Figure 2.21. Comparative ductility performances of moment-resisting connections based on different ductility factors.

Table 2.4. Experimental results comparison of bolted connections with slotted-in steel plates.

.Reference	Column h×b (mm)	Beam h×b (mm)	Fasteners (n°×d in mm)	Steel plate (mm)	Screws (mm)	Loading	My (kNm)	Θy (°)	Mpeak (kNm)	Θpeak (°)	Failure mode
Lam et al. (2008)	304×272	304×130	4×ϕ19.1	675×300, t = 9.5	l = 300, d = 8	Cyclic and monotonic	41.83	3.00	62.54	15.90	**
Lam et al. (2010)	304×272	304×130	4×ϕ25.4	675×300, t = 9.5	l = 300, d = 8	Cyclic and monotonic	84.79	2.37	105.90	6.84	Splitting (brittle)
Wang et al (2014)	305×272	305×130	4×ϕ20.0	745×305, t = 9.5	l = 300, d = 8	Cyclic and monotonic	50.5	6.9	57.90	12.4	Plug Shear (brittle)
He et al. (2020)	-	260×130	6×ϕ16.0	260×130, t = 10.0	None	Monotonic only	19.8***	1.2***	23.01***	2.34***	Splitting (brittle)
Wang et al. (2019)	390×350	305×130	4×ϕ20.0	Varies, t = 9.5	None	Monotonic only	10.0***	4.3***	20.0***	9.5***	Plug Shear (brittle)
Shu et al. (2019)	325×250	325×250	4×ϕ24.0	931x350, t = 10.0	None	Cyclic and monotonic	-	-	29.0*	4.0*	Embedment (d) and splitting (b)

Results for specimens that presented better performance in each research

*Approximated values obtained from moment-rotation curve.

**Brittle failure did not occur even when the maximum actuator stroke to either side was reached, at rotations around 16°.

***Results from monotonic loading

Table 2.5. Experimental results comparison of bonded-in rods connections

					Monotonic Response		Cyclic Response		
.Reference	Column h×b (mm)	Beam h×b (mm)	Fasteners (n°×d in mm)	Steel profile (mm)	Mpeak (kNm)	Θpeak (°)	Mpeak (kNm)	Θpeak (°)	Failure mode
Vasek and Vyhnálek (2006)	180×180	280×180	4×ϕ14.0	None	16.0*	0.6			Cracks perpendicular to grain (brittle)***
Tomasi et al. (2008)	230×120	230×120	4×ϕ16.0	HEB 120 (S275)	35.66	5.73 (0.1 rad)**			Bar failure and yielding of the T- stub flange (ductile)***
Andreolli et al (2011)	230×120	230×120	4×ϕ18.0	HEB 120 (S275)	24.54	8.02 (0.14 rad)	15.0*	5.73 (0.1 rad)*	yielding of the T- stub flange (ductile)
Yang et al. (2016)	350×151	420×135	8×ϕ20.0 and 1×ϕ20.0 (tube)	Tube (S235), t=6	60.0	7.44 (0.13 rad)			Flange yielding (ductile)

Results for specimens that presented better performance in each research

*Approximated values obtained from moment-rotation curve.

**Brittle failure did not occur even when the maximum actuator stroke to either side was reached, at rotations around 0.10 rad.

***Failure mode in monotonic loading

Based on this analysis, in order to define which of the BiR joints would have the greatest potential to achieve elevated levels of ductility and provide coherent results of moment resistance and rotational stiffness to be viable for application in a moment-resisting timber frame structural system,, the BiR joints were divided into three groups: I) bonded-in rods glued directly in timber; II) bonded-in rods with steel boxes; and III) bonded-in rods with steel link, as shown in Figure 2.22.

The joints of type I (a) have reported brittle failures, with diagonal shear cracks in the middle of the joint. On the other hand, the geometric configuration I (b) presented better ductile performance, as it reached multiple loading cycles and a ductility factor of 6. The bonded-in rods associated with steel boxes and tubes (type II on Figure 2.22), a ductile behavior was observed in the monotonic and cyclic tests, the failure is a steel failure and not a timber member failure. The application of three boxes and STSs for reinforcement is beneficial, as it improved the moment of connection capacity and reduced the probability of cracks and splitting near the supports. Otherwise, when the web thickness of the steel box is very thin, the joint presents buckle diagonally between the stiffeners and not experienced high ductility.

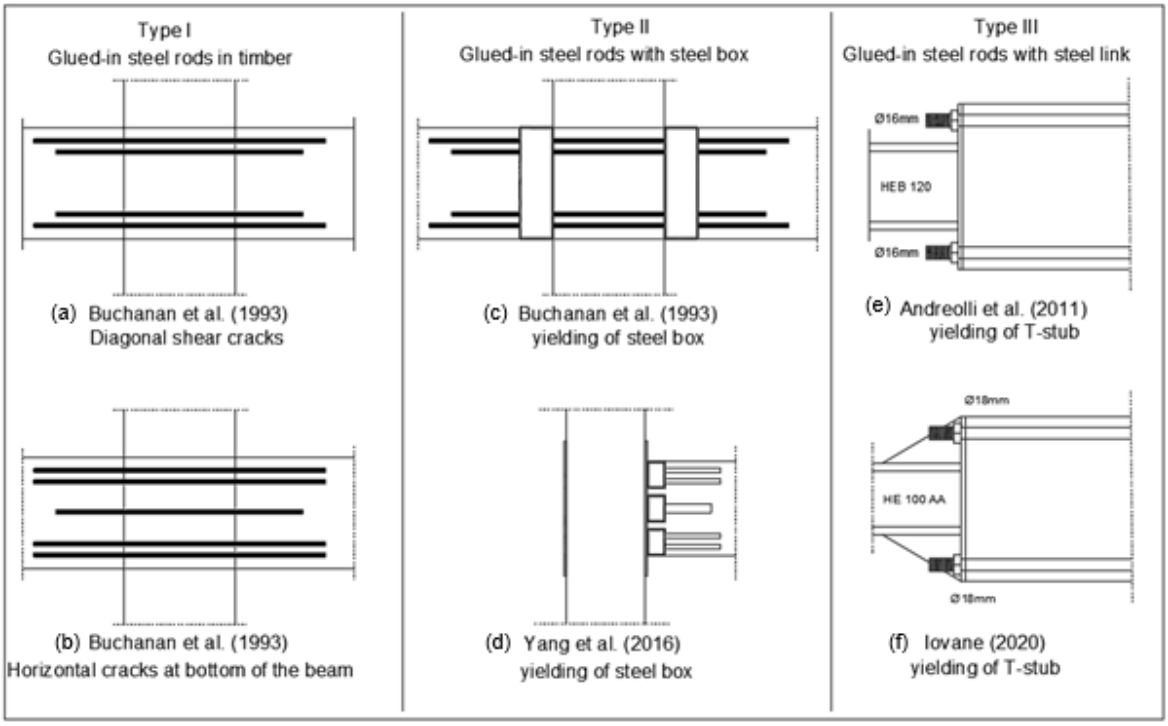


Figure 2.22. Geometric configurations and failure modes of bonded-in rods connections.

Finally in type III (Figure 2.22), the preponderant failure mode in this steel link connection geometry was the ductile T-stub yielding which is always designed to govern the structural behaviour of the connection. In general, this model had the highest degree of ductility due to its high rotational capacity. From the research studied (Tomasi *et al.*, 2008; Andreolli *et al.*, 2011; Iovane, 2020), it was

possible to infer that when end-plate thickness increase, greater are the joint moment resistance and lower are rotation capacity. In most of research in this topic as for specimen P20w in Tomasi *et al.*, (2008) the specimen with high end-plate thickness presents a fragile BiR failure. In general, when the connection is built with inserted steel plates (specimens Px-sp in Andreolli *et al.*, (2011)) showed a reduction in maximum rotation and at the ultimate moment, which also shows a reduction in ductility. Based on the analysis presented herein, it was determined to further investigate the BiR joint with a steel link (Type III in Figure 2.22), as it exhibited the highest ductility and the required versatility to achieve acceptable levels of moment resistance and initial rotational stiffness. This versatility is attributed to the designer's capacity to modify various components of the joint, which can significantly influence its mechanical behavior, including the end-plate, steel link, and bonded-in rods. Furthermore, the proposal to incorporate stiffeners into the end-plate is noteworthy, as it could enhance the joint's initial stiffness. However, implementing this modification necessitates the development of a clear calculation procedure to ensure the joint is designed with precise control over its constituent elements.

CHAPTER 3

COMPONENT METHOD IN MOMENT-RESISTING TIMBER JOINTS

This chapter introduces the component method and its traditional uses in steel connections. It then explores the different applications of the method in ductile moment-resisting steel-timber joints, focusing on BiR joints with a steel link, as discussed in Chapter 2. Finally, it outlines the key reasons for employing the component method in these types of joints.

3.1. The component method

The component method, initially introduced for designing steel connections, has undergone several years of refinement. Zoetemeijer (1974) developed a design approach specifically for the tension side of bolted beam-to-column connections under monotonic loading. Following that, Zoetemeijer (1983) introduced design rules for beam-to-column connections, identifying the component responsible for connection failure and incorporating the calculation of stiffness by summing the flexibilities of the various connection components. Over the years, some researchers have refined this method for semi-rigid steel connections.

According to Faella *et al.* (1999), the first mechanical model that used springs for steel joints were proposed in the 1980s by Wales e Rossow, where the behavior of a beam-column steel connection with web angles were described. Subsequent research done by Tschemmernegg and Humer (1988) identified that the behavior of semi-rigid connections depended on two distinct zones of the connection: the column core panel and the load transmission zone, by carrying out monotonic tests on different connections. Jaspart (1991) studied the semi-rigidity of beam-column joints and its influence on the resistance and stability of steel frames, through the proposition of mechanical models to predict the non-linear behavior of main connections, comparing the results obtained with experiments in isolated connections. An application of these connections was also carried out in linear models of frames calculated analytically and numerically using FEM. The action of COST C1 (COST, 1999) contributed for dissemination of the component method and its application in Eurocode 3. The method was first introduced in the European Prestandard Eurocode 3-Annex J in 1992 for design of steel beam-to-column connection. After gradual improvements, it was finally accepted to the EN 1993-1-8:2005.

Nowadays, the design practice for prediction of the rotational behavior of steel beam-to-column and base plate joints in current Eurocode 3 (EN 1993-1-8:2010) adopts the component method. It considers the whole joint as a set of individual basic components, dividing them into zones of tension, compression and shear. It allows to obtain the design moment resistance, rotation capacity, initial rotational stiffness and build a moment-rotation curve using these data. The non-linear idealization of moment-rotation curve can be represented by bi-linear or tri-linear form (Figure 3.1).

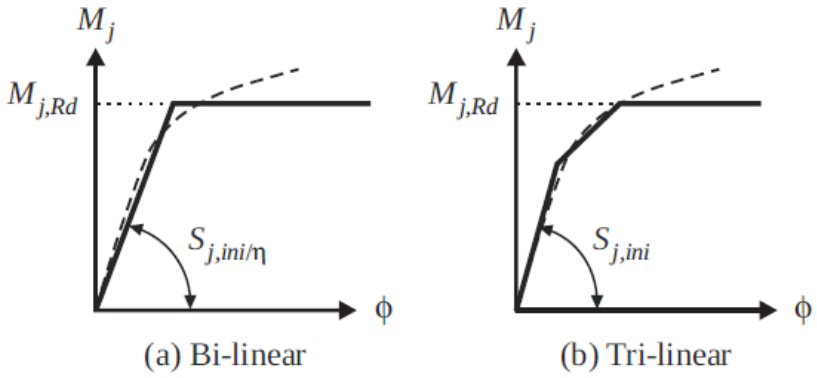


Figure 3.1. Idealizations of moment-rotation curves.

The tri-linear moment-rotation curve (Figure 3.2) is defined by Joint Moment Resistance ($M_{j,Rd}$), Joint initial rotational stiffness ($S_{j,ini}$) and Joint Rotation Capacity (ϕ_{Cd}). In the first part of curve, delimited by $2/3M_{j,Rd}$, also defined as $M_{j,Ed}$, and $S_{j,ini}$, it is considered an elastic-linear behavior. In the part between $M_{j,Ed}$ and $M_{j,Rd}$ there is an elasto-plastic behavior region characterized by stiffness $S_{j,ini}/\eta$ and in the final part, to ϕ_{Xd} until ϕ_{Cd}, it assumes a perfectly plastic behavior, thus neglecting hardening of the material. The η is the stiffness modification coefficient (EN 1993-1-8:2010).

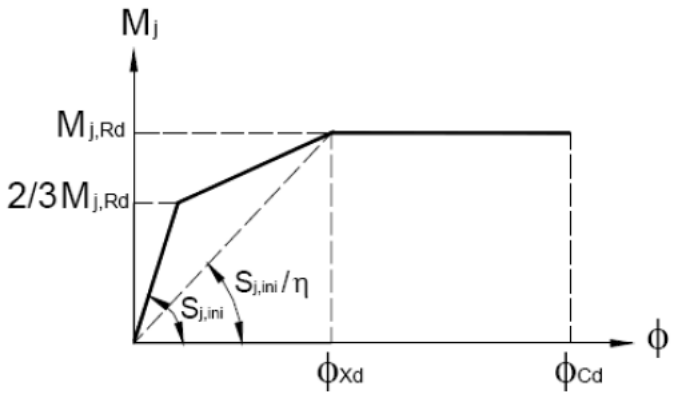


Figure 3.2. Main parameters to define tri-linear moment-rotation curve.

The application of the component method requires the following steps:

I. Identification of the active components in the joint being considered.
II. Evaluation of the stiffness and/or resistance characteristics for each individual basic component
III. Assembly of all the constituent components and evaluation of the stiffness and/or resistance characteristics of the whole joint.

The active components are those responsible for transmitting significant internal forces based on the joint behavior. Each of these fundamental components possesses distinct strength and stiffness characteristics. The coexistence of multiple components within the same joint element can result in stress interactions that may reduce the resistance of the individual basic components. To facilitate the direct application of the method, EN 1993-1-8:2010 provides a chart identifying the primary active basic components commonly employed in steel connections, characterized in terms of stiffness and strength, whether in tension, compression, or shear.

In the framework of the component method, each basic component can be modelled as a nonlinear extension spring subjected to a tension, compression, or shear force, and idealized by a bilinear elasto-plastic response. According to the EN 1993-1-8:2010, this response can be characterized by the initial elastic stiffness (Ek), where k is called "elastic stiffness coefficient", the plastic resistance (F_{Rd}), and the plastic deformation capacity (Δ_u) as shown in Figure 3.3 (a), which can be obtained by means of experimental tests or analytical models. Another way is considering the post-limit response of each component in a bilinear approximation. Jaspart and Maquoi (1991) proposed a general methodology to characterize this response using the post-limit stiffness coefficient (k_{pl}) and the deformation capacity (Δ_u) in a bilinear approximation as shown in Figure 3.3 (b). Basically, the post-limit stiffness coefficient is defined computing the strain hardening stiffness, since the effects of material strain hardening after yielding of the component are dominant, as shown in Equation (3.1), that can be used for column web in compression, column web in tension, column flange in bending, and end-plate in bending components. E_h is the strain hardening modulus.

$$k_{pl} = \frac{E_h}{E} \cdot k \tag{3.1}$$

f_y was replaced by f_u to determine the ultimate resistance (F_u), the ultimate stress of the structural steel in expressions to calculate F_{Rd}. The deformation capacity (Δ_u) from the intersection of the post-limit behavior with F_u, as presented in Equation (3.2).

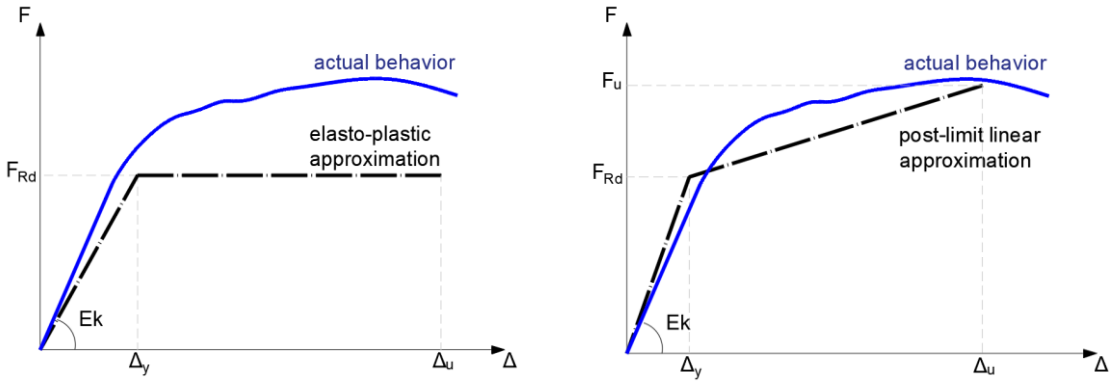


Figure 3.3. Approximations of the component behavior (a) Bilinear (b) Post-limit linear.

$$\Delta_u = \frac{F_{Rd}}{k} + \frac{F_u - F_{Rd}}{k_{pl}} \tag{3.2}$$

The third step, assembly, involves deriving the mechanical properties of the entire joint (moment resistance and initial rotational stiffness) from those of the individual constituent components. Before this step, it is essential to define how external forces act on the joint and how internal forces are distributed among the components in a manner that satisfies equilibrium and respects the behavior of the components. The spring assembly is used to determine the initial rotational stiffness of the connection, which is one of the main parameters for generating the moment-rotation curve of the full joint. To illustrate this, an example of an extended end-plate bolted steel connection is presented in Figure 3.4 (Coelho and Bijlaard, 2010).

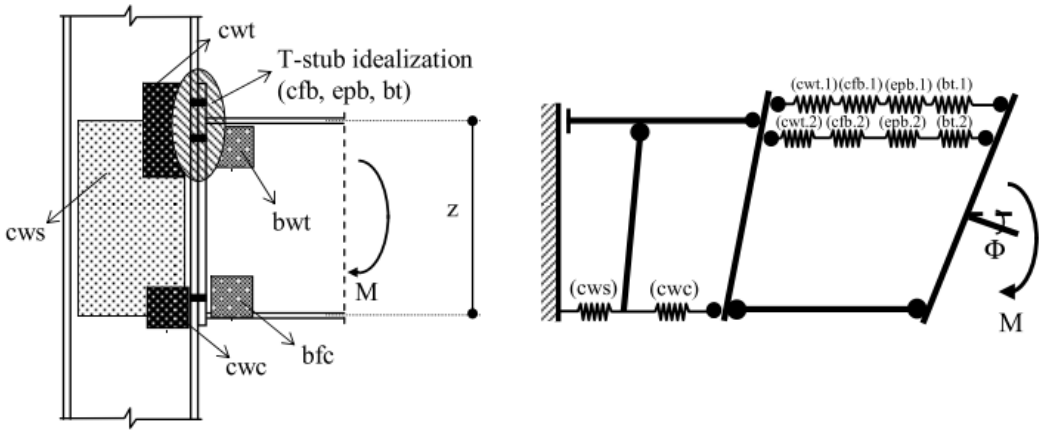


Figure 3.4. Steel extended end-plate bolted joint (a) Identification of the basic components and their positions (b) Mechanical model (spring model). Adapted from Coelho and Bijlaard (2010)

For end-plate joints with two bolt rows in tension zone, the joint moment resistance ($M_{j,Rd}$) in the absence of an axial force can be determined by Equation (3.3). The procedure can be summarized as follows:

I. Calculate the plastic resistance for each individual row (starting at that one farthest of center of compression), at this stage, the presence of all the other rows is ignored.

II. For each bolt row, an effective length of equivalent T-stub is determined for each possible yield line pattern. The effective design resistance of the row is the lowest resistance considering the end-plate in bending, the bolt failure and the beam web in tension.

III. The plastic resistance of groups of bolt rows is evaluated using the same procedures. The effective lengths of equivalent T-stubs for groups of rows are given by the specific yield line patterns. If rows are separated by a flange or stiffener, they cannot act as a combined group, and the resistance of the group can be neglected.

Ultimately, it is feasible to ascertain the effective resistance of each bolt row in detail. For instance, in the first bolt row, the weakest component was identified as the end-plate in bending, characterized by the formation of a non-circular yield pattern due to double curvature and failure mode 2. From this analysis, the moment resistance of the joint can be determined. It is crucial to emphasize that if the failure mode for any row is not ductile, the effective design resistances of the lower rows must be constrained to a linear distribution, indicating that there is no redistribution of forces between rows.

$$M_{j,Rd} = \sum_{r=1}^{n} F_{tr,Rd} \cdot h_r \tag{3.3}$$

Where h_r is the distance between bolt-row r and the centre of compression, $F_{tr,Rd}$ is the resistance of weakest component of bolt row r in the tension zone.

Initial rotational stiffness is calculated from the mechanical model. Springs may be combined in series or in parallel, depending on their interaction. In constructing the model, note that series springs are subjected to the same force, while parallel springs undergo the same deformation. Initial rotational stiffness of any joint can be determined using Equation (3.4). If the components are in the bolt row, it is necessary to calculate the effective stiffness coefficient for the bolt row, which must account for all individual components arranged in parallel within the row.

$$S_{j,ini} = \frac{z^2}{\frac{1}{k_{ec}} + \frac{1}{k_{et}}} \tag{3.4}$$

Where k_{ec} is stiffness of the components assembled in the compression/shear zone, k_{et} is stiffness of the components assembled in the tension zone.

3.2. Application of the component method to steel-timber joints

The component method has been previously examined in two categories of timber joints: carpentry timber joints, characterized by load transfer primarily through wood-to-wood contact, and timber joints that incorporate mechanical fasteners, wherein load transfer between elements is facilitated by various types of fasteners, including the moment-resisting joints discussed in Chapter 2 of this thesis. The first application of the component method to timber joints was proposed by Wald *et al.* (2000) for carpentry joints. Their approach defined the component assembly procedure based on the geometry of the connection and the properties of its components, taking into account that the pin resists shear forces and determines the position of the connection's center of rotation. Following this early development, major subsequent studies extended the method to timber joints with mechanical fasteners, where the interaction between steel and timber components introduces additional sources of stiffness and nonlinearity. The present section focuses specifically on reviewing the application of the component method to moment-resisting steel–timber joints with BiRs.

In a study on moment-resisting timber joints, Vašek and Vyhnálek (2006) conducted experimental tests on BiRs beam-to-column joints to obtain moment-rotation curves for each configuration. They applied the component method to express the relationship between bending moment and rotation. For the first joint geometry (BiRs on both sides), the mechanical model shown in Figure 3.5 has been suggested.

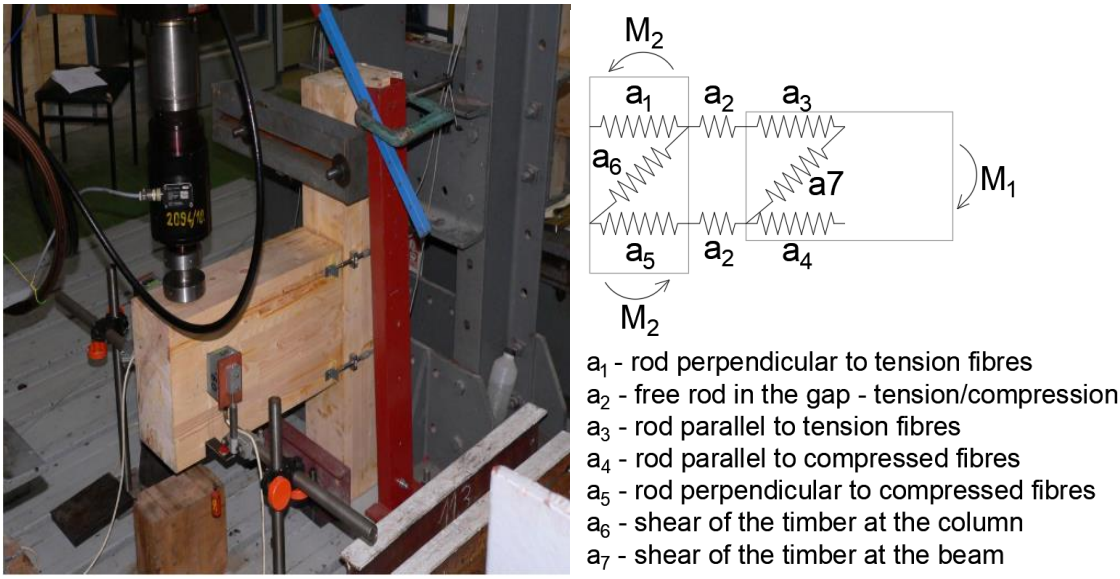


Figure 3.5. Mechanical model of the joint with bonded-in rods. Adapted from Vašek and Vyhnálek (2006).

Tomasi *et al.* (2008) explored the ductile behavior of a steel-timber joint, which consists of an end-plate, steel profile, and BiRs, specifically for heavy timber structures. They proposed that much of the previous work on semi-rigid joints in steel frameworks, utilizing the component method, could be adapted to develop a viable general model for timber structures. Consequently, the component method was employed to determine the joint moment resistance, based on a simplified trilinear moment-rotation curve of the joint as suggested by EN 1993-1-8:2010, for monotonic loading.

A mechanical model was proposed to describe the distribution of internal forces and the associated stiffness. Figure 3.6 illustrates the basic joint components, which are divided into three parts: the steel end-plate under bending tension (k_p), the BiRs under tension (k_b), and the timber under compression (k_t). As depicted in Figure 3.6, both k_p and k_b are located on the tension side of the mechanical model.

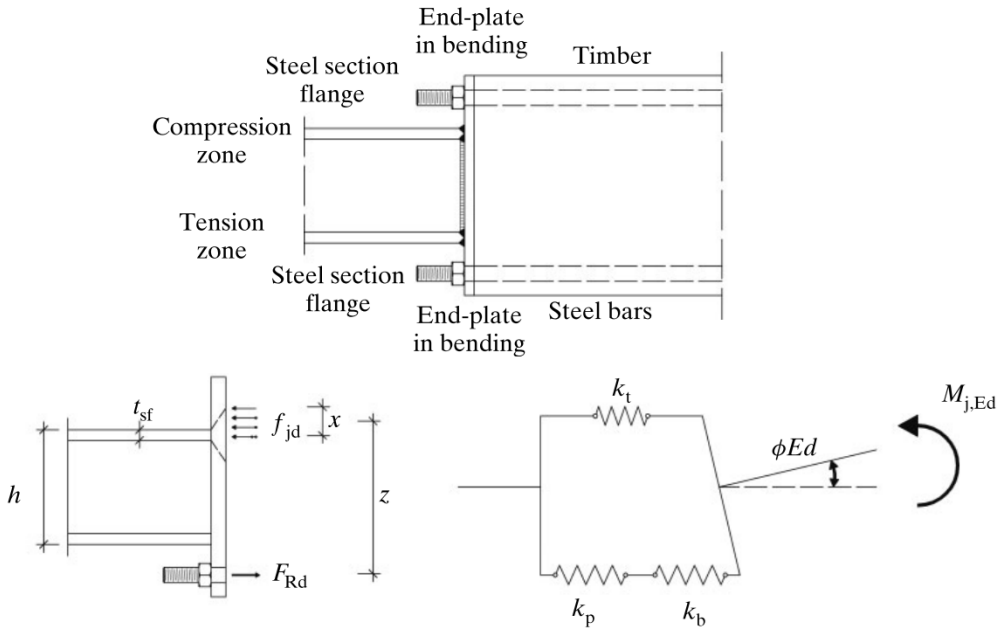


Figure 3.6. Basic components and mechanical model. Adapted from Tomasi *et al.* (2008).

To determine the joint moment resistance, the researchers identified the weakest component of the joint based on the failure mode, which was theoretically determined in accordance with EN 1993- 1-8:2010 and experimentally verified through a three-point loading test. A total of six specimens were tested, as detailed in Table 3.1. The numeral following "P" in the specimen's designation denotes the thickness of the end-plate, which was the sole variable parameter in this study. In specimens P10w and P20w, the HEB120 was substituted with a built-up welded profile.

Table 3.1. Comparison between theoretical and experimental specimens. Adapted from Tomasi *et al.* (2008)

Specimen	Profile	End-plate steel			Failure mode of T-stub in tension	Theoretical resistance (kNm)	Experimental resistance (kNm)
		ε_u (%)	f_y (MPa)	f_u (MPa)			
P6	HEB120	35,50	316,53	442,38	Mode 1	5,92	11,29
P10	HEB120				Mode 2a	13,72	19,79
P10w	Welded				Mode 2a*	14,19	22,46
P14	HEB120	36,50	302,51	444,97	Mode 2a**	19,90	25,21
P18	HEB120				Mode 2a	27,86	35,66
P20w	Welded				Mode 3	32,82	38,91

*Tension failure of the bar
**Fracture of the end-plate

By comparing theoretical and experimental results depicted in the Table 3.1, Tomasi *et al.* (2008) pointed out that the experimental results confirm the capability of the model to satisfactorily approximate the mechanical behaviour of the joint in terms of moment resistance and failure modes. However, it was found a large discrepancy in the moment values, that varies from 18% to P20w specimen until approximately 90% for the P6 specimen. The moment-rotation curve for the specimens P10 is presented in Figure 3.7. A comparison for initial rotation stiffness was not evaluated by the authors.

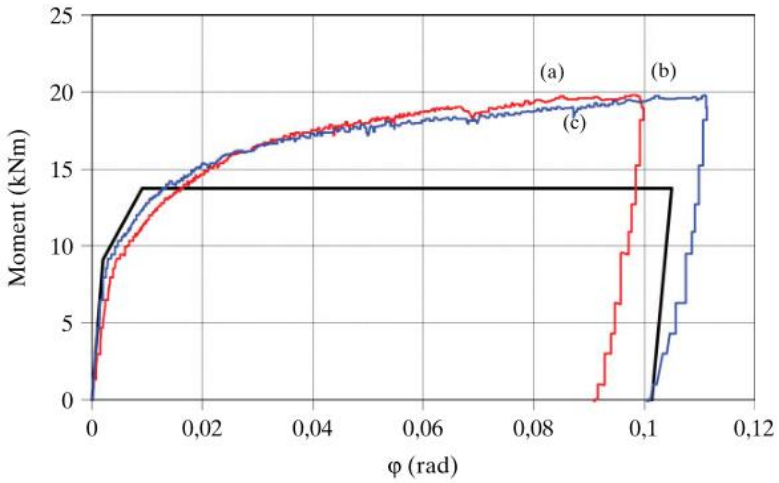


Figure 3.7. Moment versus rotation for the specimen P10: (a) left joint experimental data; (b) right joint experimental data; (c) theoretical model. Adapted from Tomasi *et al.* (2008).

Andreolli *et al.* (2011) extended the work presented by Tomasi *et al.* (2008) using a similar joint configuration and mechanical model, to validate a component method analytical model to predict the joint response in terms of the following parameters: failure mode, ultimate resistance and rotation capacity. An extensive experimental program was done focused on the cyclic behaviour of the joint, due to its importance in seismic design (strength loss and energy dissipation under alternate loading

of the joint are determined). Eight specimens were tested, as reported in Table 3.2, where "Th" means theoretical results and "Exp" experimental results. The "Px" stands for the thickness of the end-plate in mm. Specimens manufactured with the glued-in steel plate for the shear load were labelled "Px-sp". The test setup was designed so that bending and shear were both acting on the joint (Figure 3.8) and the same set-up was used for both monotonic and cyclic tests.

Table 3.2. Summary of theoretical and experimental results by Andreolli *et al.* (2011)

Specimen	End-plate steel measured properties			Failure mode		Moment resistance (kNm)		Rotation Capacity (rad)	
	ε_u(%)	f_y(MPa)	f_u(MPa)	Th	Exp	Th	Exp	Th	Exp
P6-sp	38.5	299.6	377.2	1	1	7.08	15.07	0.15	0.20
P6				1	1	6.56	8.85	0.15	0.15
P8-sp	38.6	275.5	367.5	1	2	10.66	16.59	0.16	0.19
P8				1	2	10.51	14.99	0.16	0.21
P10-sp	45.9	256.6	374.0	2	2	15.37	17.14	0.14	0.12
P10				2	2	15.8	19.85	0.13	0.18
P15-sp	35.7	295.5	383.1	2	2	21.82	24.54	0.13	0.14
P20-sp	36.4	278.2	400.6	3	3	28.51	32.29	0.06	0.07

Monotonic tests were performed to investigate the behavior of the connection with special regard to the joint ductility and the influence of the different failure modes on the capacity in terms of ultimate rotation. According to the authors, no specimen tested under monotonic loading showed brittle failure, even when large displacements were achieved. Only collapse of the T-stub in tension occurred, mostly in the more ductile modes 1 and 2. However, specimen P20-sp collapsed according to mode 3. Table 3.2 shows that the analytical model predicted the experimental failure mode for almost all the specimens, the exceptions were P8-sp and P8, which failed in mode 2 while mode 1 was predicted.

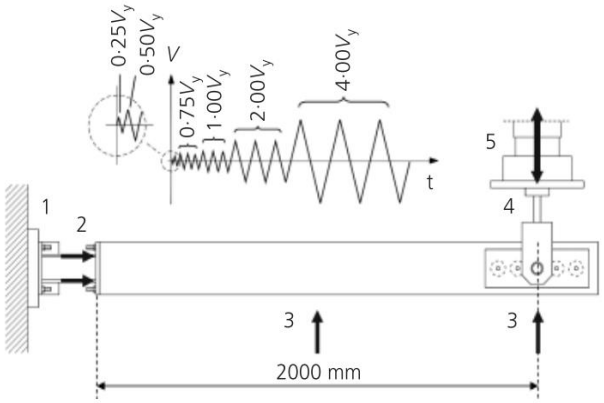


Figure 3.8. Setup for monotonic and cyclic tests: 1, steel profile connected to the reaction base; 2, displacement transducer 100 mm; 3, displacement transducer 500 mm; 4, load cell; 5, hydraulic jack. The upper part of the figure shows the cyclic test protocol according to EN 12512:2005 (Andreolli *et al.*, 2011).

By comparing the analytical predictions with the experimental results for the joint moment resistance, it was found a difference that varies from 11.7% for specimen P20sp to approximately 53% for specimen P6sp. The rotation capacity presented better accuracy. The results for initial rotational stiffness were not discussed.

Yang *et al.* (2016) applied the component method to develop an analytical method of the determination of the moment resistance, initial stiffness and the rotation capacity of glulam beam–column connections with bonded-in rods. They studied a connection three separate steel box sections connected with bonded-in rods or bonded-in steel tube to glulam beam end and with connecting bolts to glulam column. The basic components and mechanical model are presented in Figure 3.9, the names of components are presented in Table 3.3. The steel box section was analysed as equivalent T-stub components, considering three main failure modes for it: complete flange yielding, bolt failure with flange yielding, and bolt failure. The tension resistance of the component was defined as the smallest value for these three possible failure modes.

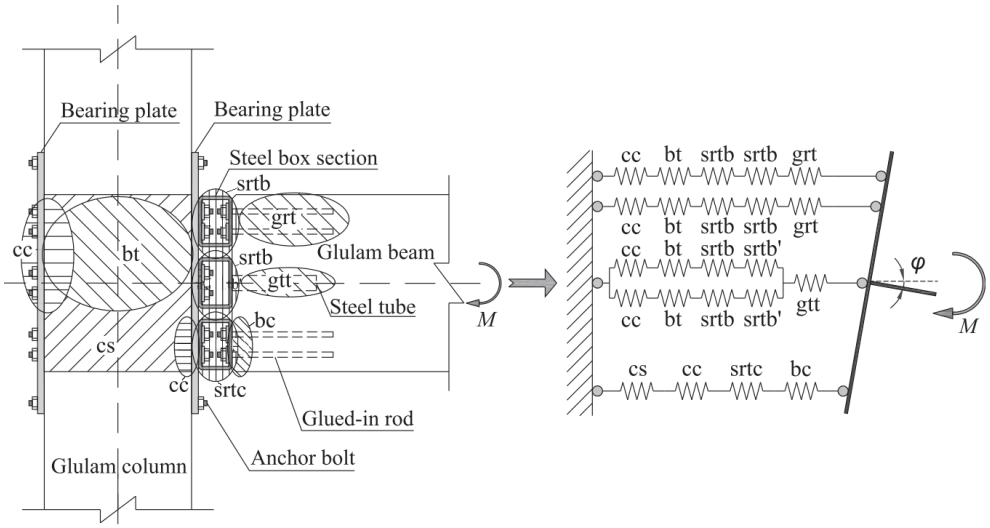


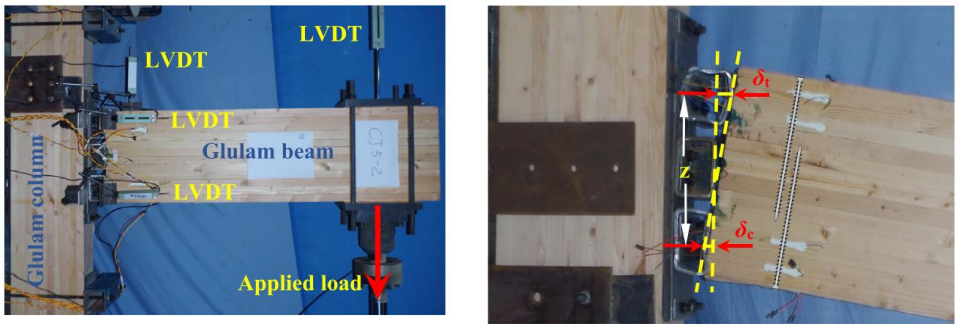
Figure 3.9. Joint Geometry and basic components for glulam beam–column connection (Yang *et al.*, 2016).

Table 3.3. Names of components used in mechanical model. Adapted from Yang *et al.* (2016).

Abbreviation	Component
bc	Beam in compression
bt	Bolts in tension
cc	Column in compression
cs	Column in shear
grt	Bonded-in rods in tension
gtt	Bonded-in tube in tension
srtb	Steel box section in bending
srtb'	Steel box section in bending under tension force of glued steel tube
srtc	Steel box section in compression

To validate the analytical model, Yang *et al.* (2016) tested two series of joint specimens, each one included three specimens, one tested under monotonic load and the other two tested under cyclic load (Figure 3.10). The group of specimens that have stiffeners (JT2) had an average ductility factor of 2.7, while the other group, without stiffeners and thicker (8mm against 6mm), had an average ductility factor of 4.4. This indicates a satisfactory ductility for this kind of joints.

The comparison of joint moment resistant between experimental mean values and the theoretical values were provided in Table 3.4. According to the authors, the theoretical values of the joint moment resistant agreed well with that of experimental ones and the theoretical results proved to be a little conservative.



(a) (b)

Figure 3.10. Glulam beam–column joint specimens (a) at the beginning of both experiments (b) at the end of cyclic load experiment (Yang *et al.,* 2016).

Table 3.4. Comparison between theoretical and experimental joint moment resistance. Adapted from Yang *et al.* (2016).

Series reference	N° of replicates	t_f (mm)	Stiffening	Joint moment resistance $M_{j,Rd}$ (kNm)		
				Experimental	Analytical	Diff. (%)
JT2	3	6	Yes	64.1	54.1	-15.6
JT3	3	8	No	54.6	51.8	-5.1

Yang *et al.* (2016) also evaluated the joint initial stiffness using the mechanical spring model presented in Figure 3.9. For those spring components with two values, the former one and latter one represents JT2 series and JT3 series, respectively. Joint initial rotational stiffness was compared to the experimental mean values as indicated in Table 3.5, according Yang *et al.* (2016) the results showed a high agreement between the theoretical and experimental results.

Table 3.5. Experimental and analytical results comparison for joint initial rotational stiffness. Adapted from Yang *et al.* (2016).

Series reference	N° of replicates	t_f (mm)	Stiffening	Joint initial stiffness $S_{j,ini}$ (kNm)		
				Experimental	Analytical	Diff. (%)
JT2	3	6	Yes	2187	2264	+3.5
JT3	3	8	No	1760	1722	-2.1

More recently, Tao *et al.* (2020) proposed a beam-to-column joint where the connection was built with steel angles, bolts, channels and plates glued into the glulam beam (Figure 3.11). The authors concluded that this type of connection has high pull-out and shearing capacities, making it suitable for glulam beam-column connections. Top and seat angles are used to behave as both bearing elements and energy dissipation devices, functioning as deformation-controlling elements at the upper and lower ends of the timber beam. The theoretical model used by the authors to predict the mechanical response of the joint is based on the component method for steel connections (Silva and Coelho, 2001; Borges, 2003; Coelho, 2004). The mechanical model and the corresponding simplified model are presented in Figure 3.12.

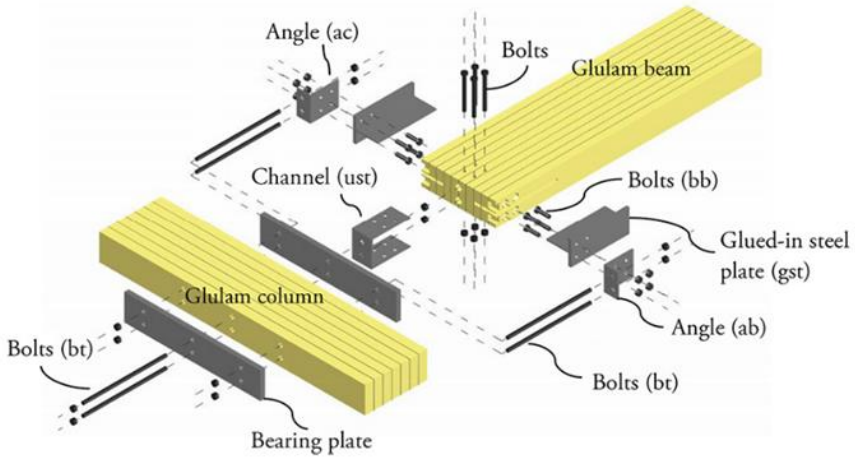


Figure 3.11. Joint parts and components presentation (Tao *et al.*, 2020).

The study determined that the angle component fails before other components, aligning with theoretical calculations that indicate the angle's ultimate bending resistance is the lowest among these components. This failure mode demonstrates that the angle is the most critical component in such hybrid connections.

When comparing the experimental results from monotonic loading tests on full-scale joints with those obtained through analytical methods, the authors found that the theoretical moment resistance for the angle was nearly 11% higher than the experimental results. This discrepancy arises from an overestimation of the tensile resistance of the angle, which is subjected to both tension and bending loads during testing. Tao *et al.* (2020) also examined the initial rotational stiffness of the hybrid connection and observed an 8.6% difference between experimental and theoretical results, indicating good agreement in the theoretical method used to determine the initial stiffness of the joint. However, when comparing rotation capacity, the theoretical results showed significant differences from the test results, with a maximum deviation of 32.4%.

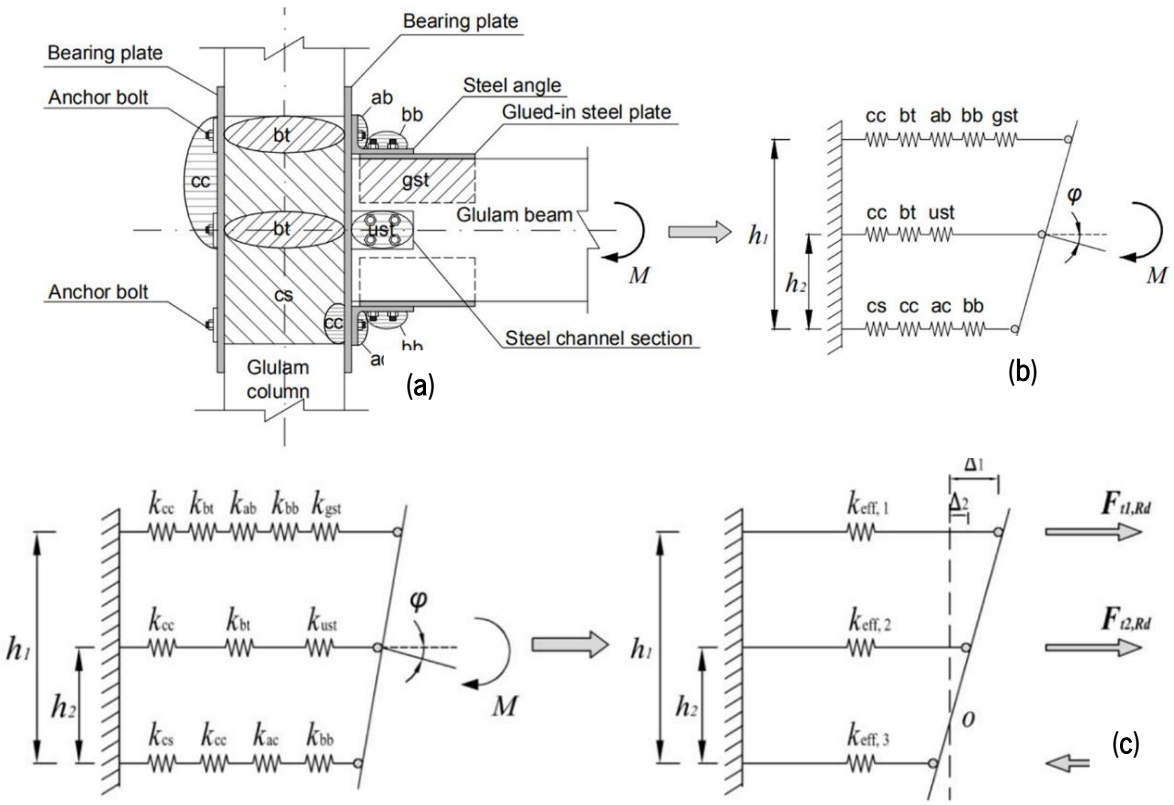


Figure 3.12. Component method definition. (a) identification of components on connection. (b)mechanical model. (c) simplified component method (Tao *et al.*, 2020).

Other authors have applied the component method to moment-resistant timber joints to calculate the stiffness and force distribution of inclined threaded rods inserted into timber (Stamatopoulos *et al.*, 2022) and to calculate the moment resistance of the self-centering hybrid joint (Li *et al.*, 2023).

Considering the potential of moment-resistant joints constructed with steel links, timber beams, steel end-plates, and BiRs, as discussed in Chapter 2, and based on the state-of-the-art review about component method application, there are few studies addressing analytical calculation procedures for these joint types. Furthermore, there is a knowledge gap concerning the interaction between timber and steel, whether under tension or compression. A more profound understanding of these regions is crucial, particularly in connections involving various active components. Given the considerable versatility of this type of joint, the development of a comprehensive calculation process that yields results for moment resistance, initial rotational stiffness, and rotation capacity, essentially, the complete mechanical response of the joint, can enhance reliability and improve comprehension of all components (the link, timber beam, and plate–BiR connection). This would optimize the utilization of their integrated behavior as a cohesive unit.

Moreover, for the design procedure to be widely adopted, it should be simple, directly applicable, and not rely solely on empirical equations derived from experimental tests performed on a specific and limited range of samples.

To propose a complete design procedure based on the component method and to enhance the prediction of the mechanical performance of moment-resisting joints applicable to post-and-beam structural systems, this thesis focuses on stiffened end-plate moment-resisting steel-timber joints with steel links and four bonded-in rod rows. It also addresses unstiffened joints and those with two bonded-in rod rows. An example of this joint type is illustrated in Figure 3.13. Due to the substantial number of components and the complexity of the mechanical behavior of this joint, the calculation process has been simplified by dividing it into three macro-components: the steel link, the connection (the contact region between the steel end-plate and the timber), and the timber beam, as depicted in Figure 3.13 (a). The proposed mechanical spring model (highlighted in red) is presented in Figure 3.13 (b) and is composed of the following components: link flange in tension (lft), link flange in compression (lfc), end-plate in tension (ept), bonded-in rods in tension (brt), rib stiffener in compression (rsc), and end-plate in compression (epc). This model demonstrates some advancements compared to those proposed by other authors, including: the incorporation of steel link components to predict their behavior in conjunction with the connection; the positioning of the rib-stiffeners on the compression side; and the end-plate component under compression that can be analyzed as a timber beam in compression, considering that these two structural elements are in contact within this component.

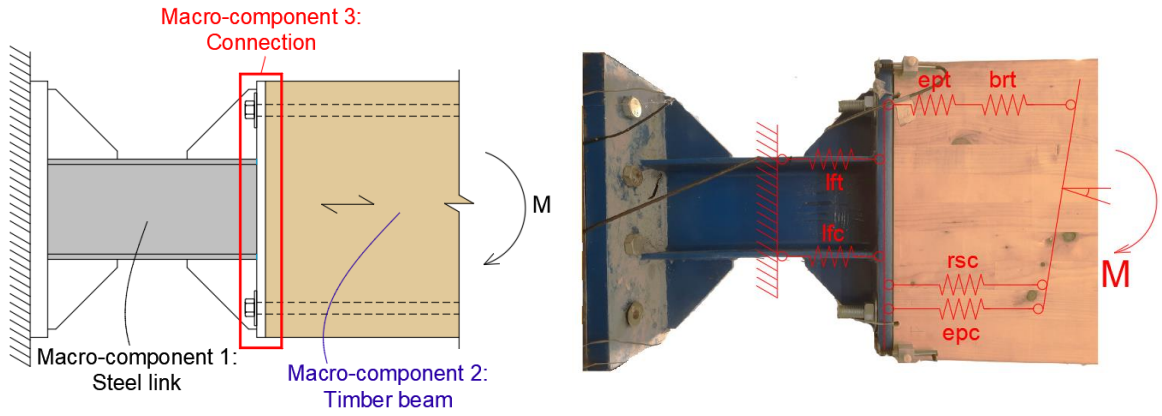


Figure 3.13. Component method model for stiffened end-plate moment-resisting steel-timber joint with steel link and two BiR rows (a) Division in macro-components (b) Mechanical spring model

CHAPTER 4

EXPERIMENTAL RESEARCH

This chapter details an experimental investigation into stiffened end-plate moment-resisting steel–timber joints, with a focus on their load-bearing capacity, failure modes, and mechanical behavior. The study involved testing individual steel components, as well as BiR connections under tension and the compression of steel T-stubs against GLT. Furthermore, 15 full-scale joints were tested using both measurements techniques: conventional transducers and digital image correlation (DIC). Distinct from prior research, this study investigated joints with multiple bonded-in rod arrangements (two and four rows) to induce failures in various components. The methodology underscores practical engineering objectives by addressing low component overstrength ratios.

4.1. Introduction

From the previous chapter, it is clear that to contribute to the development of a calculation procedure based on the component method, it is essential to understand the experimental mechanical behavior of the joint. This understanding serves as a reference for evaluating the accuracy of the analytical method. Specifically, for the component method, it is crucial to determine the moment resistance, initial rotational stiffness, rotation capacity of the joint, and its moment-rotation curve. Additionally, the mechanical properties of the active components that significantly influence the mechanical response of the joint are also important. This chapter details the experimental tests conducted for this purpose, focusing on stiffened end-plate moment-resisting steel-timber joints. Initially, tests were performed on the primary steel elements involved in the study, including the steel from the end-plate, link, and threaded rods. Furthermore, pull-out tests were carried out on BiR connections, and specific compression tests were conducted to evaluate the behavior of a steel T-stub compressing the GLT parallel to the grain.

Regarding the complete joint, this study involves testing 15 full-scale joints using conventional transducers and digital image correlation (DIC) measurement techniques. Distinguishing this research from previous experiments, it investigates joints with multiple bonded-in rod arrangements, specifically two and four rows, to achieve failure in different structural components, such as the end-plate, steel

link, and bonded-in rods. This methodological approach reflects practical engineering considerations, particularly through the reduction of component overstrength ratios.

4.2. Steel tests

The steel components that significantly influence the mechanical behavior of the joint are the end-plate, the link, and the threaded rods. The nominal strength class of the steel employed in the joint tests for the end-plate, the link, and the other elements was uniformly S235, as specified by the suppliers. The threaded rods were classes 4.8 and 8.8. Since experimental resistances typically exceed the nominal resistances declared by suppliers, it was essential to determine these values to accurately model the joint's behavior, both for the component method and for numerical modelling. Therefore, tensile tests were conducted on steel samples from the end-plate and link, in accordance with ISO 6892-1:2019.

For the end-plate and steel link, three samples of steel were extracted from the same batch used in the full-scale joint tests and adhered to the dimensions recommended by ISO 6892-1:2019, with original gauge lengths of 70, 80, and 90 mm. The specimen's name "Tx" indicates the thickness of the end-plate used in the joint tests. For instance, T20 signifies that the steel sample was extracted from the end-plates with a thickness of 20 mm. And the specimen's name HEA160 or IPE160 indicates the steel profile applied in the joint tests.

The results obtained from the tensile tests are presented in Table 4.1 for the end-plate and Table 4.2 for the link, where, f_y is the yield strength, $f_{y,mean}$ is the mean yield strength, f_u is the ultimate strength, $f_{u,mean}$ is the mean ultimate strength and E_f is the final elongation.

Table 4.1. Results for steel end-plate samples.

N	Specimen	f_y (N/mm²)	$f_{y,mean}$ (N/mm²)	Coef. of variance (%)	f_u (N/mm²)	$f_{u,mean}$ (N/mm²)	Coef. of variance (%)	E_f (%)
1	T20	356			446			22.7
2	T20	348	357.0	2.67	448	461.7	5.51	27.7
3	T20	367			491			31.1
4	T15	387			464			23.3
5	T15	388	377.0	2.41	472	379.7	1.59	27.6
6	T15	356			484			30.3
7	T12	314			379			29.7
8	T12	303	312.7	5.82	374	473.3	2.13	26.9
9	T12	321			386			35.1

Table 4.2. Results for steel link samples.

N	Specimen	f_y (N/mm²)	$f_{y,mean}$ (N/mm²)	Coef. of variance (%)	f_u (N/mm²)	$f_{u,mean}$ (N/mm²)	Coef. of variance (%)	E_f (%)
1	HEA160 (T20)	267			395			30.0
2	HEA160 (T20)	248	258.0	3.70	358	381.0	5.27%	28.8
3	HEA160 (T20)	259			390			23.8
4	HEA160 (T15)	293			402			26.3
5	HEA160 (T15)	259	276.0	6.16	413	402.0	2.74%	28.8
6	HEA160 (T15)	276			391			31.3
7	IPE160	287			431			25.0
8	IPE160	299	294.0	2.12	418	417.0	3.48%	27.5
9	IPE160	296			402			28.8

The mechanical characterization tests of the steel used in the end-plate revealed mean yield strengths ($f_{y,mean}$) of 357.0, 377.0, and 312.7 MPa, as well as mean ultimate strengths ($f_{u,mean}$) of 461.7, 379.7 and 473.3 MPa for the specimens of the type T20, T15 and T12, respectively. For the steel link, the results of mean yield strengths ($f_{y,mean}$) were 258.0, 276.0, and 294.0 MPa for the specimens HEA160 (T20), HEA160 (T15) and IPE160, respectively. Regarding the mean ultimate strengths ($f_{u,mean}$), the results were 381.0, 402.0, and 417.0 MPa, respectively. The results indicated higher yield and ultimate strengths than the nominal values, particularly for the end-plate.

For the threaded rods, metric MGS 1000 from Rothoblaas were used, with a declared strength class of 8.8 and 4.8. Tensile tests according to ISO 6892-1:2019 were performed on six rods specimens extracted from each batch corresponding to the respective strength class. In this case, circular samples were extracted with an initial length of 60 mm, total length of piece of 170.58 mm, original internal radius of 8 mm and external radius of 12 mm, as shown in Figure 4.1. As results for rods class 8.8, it was found a mean yield strength ($f_{y,mean}$) of 896.1 MPa (CoV 4.51%) and a mean ultimate strength ($f_{u,mean}$) of 1024.5 MPa (CoV 3.05%). And for 4.8, a mean yield strength ($f_{y,mean}$) of 440.5 MPa (CoV 5.00%) and a mean ultimate strength ($f_{u,mean}$) of 501.8 MPa (CoV 3.85%).

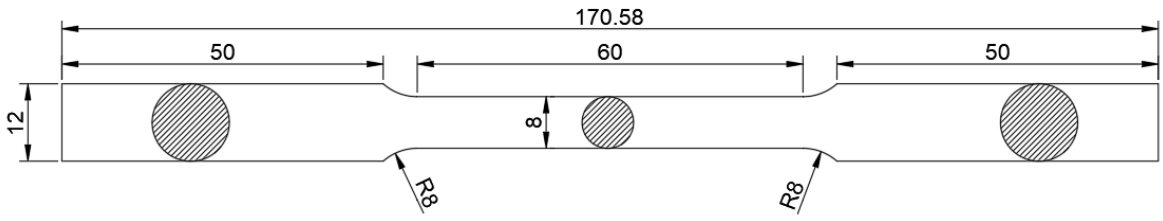
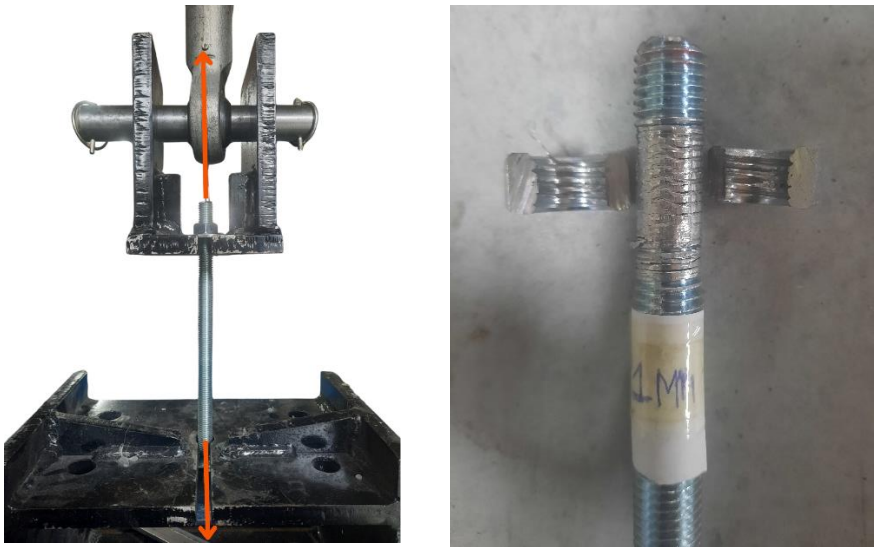


Figure 4.1. Dimensions of rods samples, in mm.

The standards cited in technical sheets specify the nominal yield and ultimate tensile strength of the threaded rod samples subjected to tensile coupon testing. However, they do not specify the maximum strength for the connection composed by rods affixed to the nuts. Consequently, it is important to understand the range of strengths related to the connection between the rod and nuts. Overestimating the ultimate strength of this connection can lead to undesirable results when threaded rods are utilized in BiRs connections, as brittle failure of the timber or in the bondline. To evaluate the behavior of the rod-nut connection, threaded rods classified under strength class 4.8 were tested, with nuts that adhered to the same specifications as those utilized in the joint tests.

The test setup is illustrated in Figure 4.2 (a). Tensile tests were conducted on six specimens for each diameter (M12, M14, and M16). These tests were performed under monotonic loading conditions, with tension incrementally increased until the specimens failed. Steel rigid supports were employed at both ends to secure the threaded rods, and a laser level was utilized to ensure vertical alignment of the rods. In all tested diameters, a failure mode was observed between the nut and the rod, characterized by thread galling. This phenomenon involved the nut scraping against the threads of the rods and being subsequently dragged until it was entirely detached from the rod (Figure 4.2 (b)).



(a) (b)

Figure 4.2. Tension test on threaded rods attached by nut (a) Test setup; (b) Thread galling failure mode.

As a result, the experimental tensile resistance of the rod-nut connection is observed to be lower than tensile strength obtained from the coupon tensile test in steel. Upon comparison of the mean ultimate load capacities derived from these two tests (tensile test of steel and tensile test of the rod-nut connection) under different boundaries conditions, and taking into account the effective area of

the threaded rods as specified by the manufacturer, it can be inferred that the ultimate load capacity associated with thread galling is approximately 76% of that obtained from the mean ultimate strength of coupon tensile test (specifically, 76.08% for M12, 76.28% for M14, and 77.39% for M16). This phenomenon occurred because the rod-nut connection did not comply with all the manufacturing requirements specified by the screw manufacturing standards, particularly EN 15048:2022.

4.3. Bonded-in rods tests

To evaluate the tensile performance of the bonded-in rods (BiRs), timber specimens measuring 80 mm×80 mm×900 mm (B×H×L) were prepared and threaded rods were bonded at both ends. A glued length of 270 mm, adopting a glue thickness of 2 mm, and an unbonded length equal to 30 mm from the timber top were used (the same as those adopted for the full-scale joint tests with four BiRs rows) as shown in Figure 4.3. Regarding the materials used, the timber was GLT made from Norwegian spruce (*Picea abies*) with strength class GL24h (EN 14080:2013).

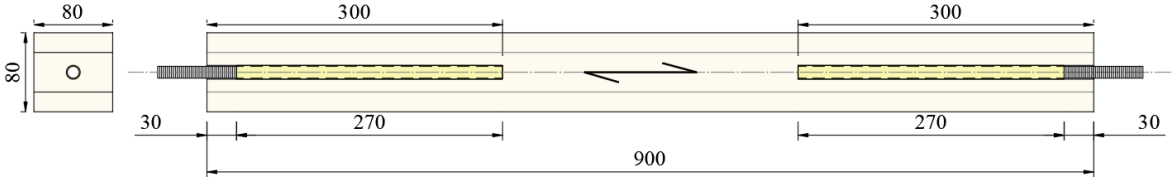


Figure 4.3. Specimens of BiR connections for tensile tests. Dimensions in mm.

After production, all specimens were kept inside the laboratory for at least 7 days before the test. The laboratory temperature and relative humidity were measured during these 7 days. A mean temperature of 22°C and mean relative humidity of 65% were found. The moisture content of the timber was measured a few minutes before the tests, using EN 13183-2:2005 recommendations. MGS 1000 metric threaded rods with strength class of 4.8 were used, and the bonding was performed with XEPOX F from Rothoblaas. This is a fluid two-component epoxy adhesive that is applied by injection into holes, provided the slots are properly sealed.

For the gluing process, the surface of the threaded rods and the holes in the timber were cleaned using the air compressor. The gluing was carried out with the beam in a vertical position, with the holes facing upwards. Firstly, the amount of glue was precisely measured to ensure the designed unbonded length would be achieved. Then the glue was poured into the holes, and the threaded bars were inserted one by one applying circular movements to expel any air bubbles. Finally, the steel piece was positioned to ensure the correct fit of the bars. A minimum curing time of 7 days was respected before the tests.

Monotonic pull-out tests were performed on six bonded-in rod (BiR) specimens for each of the designated diameter (M12, M14, and M16). The specimens were subjected to progressively increasing tensile loading until failure occurred. To ensure proper alignment and stability, steel rigid supports were utilized to secure the threaded rods at both ends, while a laser level was employed to maintain precise vertical positioning throughout testing. The experimental setup is illustrated in Figure 4.5 (a).

The summary of results of the tested BiR specimens are shown in Table 4.3, including ultimate mean load ($P_{u,mean}$) and the main failure modes. In Figure 4.4 are presented the load-displacement curves for each specimen tested. The results show an increase in ultimate load as the diameter of the threaded rods increases, with an average value of 39.56 kN for M12, 53.50 kN for M14, and 68.51 kN for M16. As this BiR configuration would be applied identically to the tested joints, all were designed so that the failure mode would be tensile failure of the rod (failure on the steel only), in order to obtain ductile failure and prevent failure from occurring in the timber. Sixteen of the 18 tests performed resulted in the predicted failure, and only two (one of M16 and the other of M12) presented shear failure of the wood adjacent to the bondline. These failure modes are shown in Figure 4.5 (b) and (c), respectively.

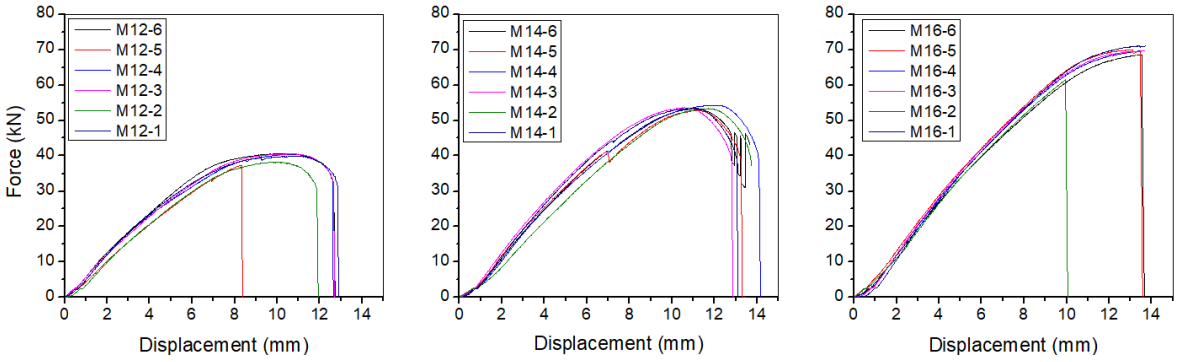


Figure 4.4. Load-displacement curves of the test for (a) M12, (b) M14, (c) M16.

Table 4.3. Results of single BiR pull-out tests.

Specimen	$P_{u,mean}$ (kN)	CoV (%)	Failure mode
M12	39.56	3.55	Tensile failure of the rod
M14	53.50	1.05	Tensile failure of the rod
M16	68.51	5.19	Tensile failure of the rod



(a) (b) (c)

Figure 4.5. BiR pull-out tests performed. (a) setup; (b) tensile failure of the steel rod; (c) shear failure of the timber adjacent to the bondline.

4.4. T-stub compressing timber parallel to the grain test

4.4.1. Experimental methodology

The application of the component method to moment-resisting timber joints typically assumes that the tensile region, supported by steel, is represented as an equivalent T-stub in the tension component. The structural behavior of this element has been extensively researched over the years and is well defined by the EN 1993–1-8:2010. However, in the moment-resisting timber joint in study and in another joints already mentioned in this thesis (Vašek and Vyhnálek (2006); Tomasi *et al.* (2008); Andreolli *et al.* (2011); Yang *et al.* (2016)), the contact between the steel and the timber element results in compression parallel to the grain in the timber, and, in some cases, the reaction of this compression can lead to significant stresses in steel part.

Depending on the joint geometry, the compression region can be divided in different components. The compressed region of the joint in study (see Figure 3.13) can be modelled as a component called "steel T-stub compressing the timber parallel to the grain" highlighted in blue in Figure 4.6. When the joint in subject to a bending moment, this part composed by the flange of the steel link and a portion of end-plate compress the timber locally.

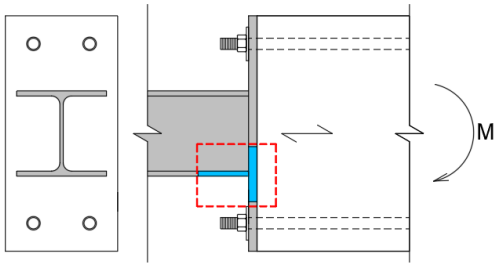


Figure 4.6. Position of component defined by the steel T-stub compressing the timber parallel to the grain.

Based on the component method methodology presented in Chapter 3, the resistance of the weakest components under compression and tension determines the joint moment resistance. Without a comprehensive understanding of the behavior of each component, including this steel T-stub component, designers are at risk of inadvertently compromising the tensile resistance of components by constraining them to maintain force equilibrium, as well as affecting the joint moment resistance. Furthermore, it is crucial to calculate the initial stiffness of the joint using the spring mechanical model, and this component typically demonstrates significant stiffness within the compression zone. As consequence, a more precise characterization of the steel T-stub compressing the timber parallel to the grain component is needed to accurately predict the structural behavior and ensure the safe design of the joints. In this section, an experimental campaign of this component was performed to improve the understanding of its behavior and to contribute to its characterization, which was addressed in further chapters. An experimental campaign composed by compression tests on 90 specimens of steel T-stubs, with five different flange thicknesses (6, 8, 10, 15 and 20 mm), in contact to glued laminated timber (GLT) specimens of three different cross sections ("SERIES" in Figure 4.7) was conducted.

This experimental study compared the behavior of rigid plates compressing GLT (reference tests) with steel T-stubs compressing GLT. Due to the smaller thickness of the T-stub flange compared to rigid plates, they have lower stiffness and, therefore, their structural behavior differs from that subjected to conventional compression using a rigid plate. For the reference compression tests a rigid plate with a thickness equal to 40 mm was used, these specimens are regular plates, not T-stubs ("REF" in Figure 4.7). Five tests were made for each specimen type.

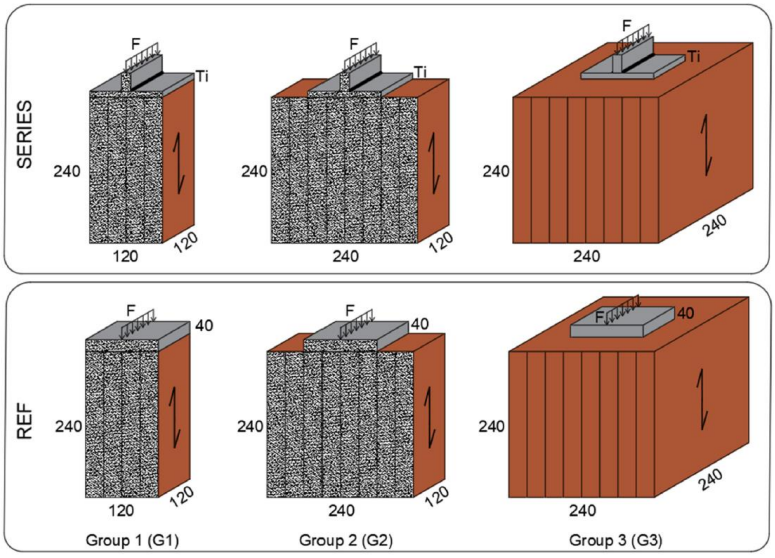


Figure 4.7. Detailed geometry of the specimens, including T-stub and GLT, the DIC painted front face and positions of T-stub Series and Reference specimens. Dimensions in mm.

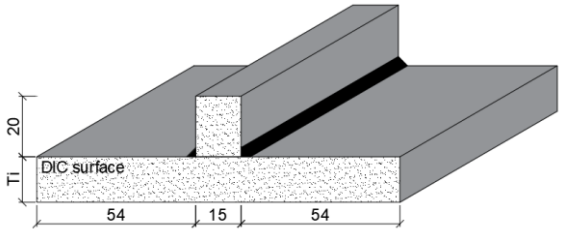


Figure 4.8. Steel T-stub geometry. Dimensions in mm.

The compression tests of the specimens were carried out on a hydraulic jack with a load cell of 1500 kN under displacement control at a rate of 3 mm/min. The load was applied along the center part of steel T-stub. The tests were stopped when the force reached 80 % of the maximum force, or the central displacement reached 2,5 % of the total height of the specimen. The vertical displacements were monitored by three LVDTs positioned according to Figure 4.9 (b): the central one measured the total displacement of the GLT; the left and right ones measured the displacement from each T-stub edge to the GLT. The 3D displacements on the surface between the two materials were determined by the Digital Image Correlation (DIC) technique (Figure 4.9 (a)). In the scope of these tests, INSTRA 4D V4.4.7 × 64 software was used along with two cameras (Master and Slave) of 2.0 megapixels positioned 100 cm between each other. The acquisition frequency to obtain the frames was 1 Hz.

Table 4.4. Summary of the steel and timber specimens tested.

Series	number of tests	Steel		GLT		
		T-stub name	Thickness [mm]	GLT group	Cross section	Height
REF G1	5	REF	40	G1	120×120	240
REF G2				G2	120×240	
REF G3				G3	240×240	
T20 G1		T20	20	G1	120×120	
T20 G2				G2	120×240	
T20 G3				G3	240×240	
T15 G1		T15	15	G1	120×120	
T15 G2				G2	120×240	
T15 G3				G3	240×240	
T10 G1		T10	10	G1	120×120	
T10 G2				G2	120×240	
T10 G3				G3	240×240	
T8 G1		T8	8	G1	120×120	
T8 G2				G2	120×240	
T8 G3				G3	240×240	
T6 G1		T6	6	G1	120×120	
T6 G2				G2	120×240	
T6 G3				G3	240×240	



(a) (b)

Figure 4.9. Overview of displacement measurement techniques: (a) DIC Surface (b) LVDTs. The right and left ones were named based on the front face of the specimen (painted surface).

4.4.2. Component resistance and failure modes results

The measurement of the experimental stress produced by the T-stub flange on the GLT in compression parallel to the grain is complex, as there is a gradual reduction in the contact area between the two materials, due to the bending of the T-stub flange edges. Therefore, due to the difficulty of measuring the distribution of stresses acting on GLT, the component resistance can be better characterized in terms of force. In Table 4.5, the mean maximum force values (defined as the experimental resistance of the component) and the corresponding coefficient of variation for each of the tested groups were displayed.

The results for REF specimens represent the experimental maximum force of GLT under compression parallel to the grain and were utilized as a reference for the results obtained for the steel T-stubs. In the results for REF, the force decreased gradually after maximum point, whereas for all T-stub series, the force stayed on a plateau with a large increase in displacement, as can be visualized in the force-displacement curves measured by the central LVDT for tests with mean response in each thickness for Groups 1, 2 and 3 (Figure 4.10). The T20 specimens exhibited behavior similar to the REF in the G1 tests, as their thickness is closer to that of the REF and the cross-section of the GLT is reduced. In this instance, the GLT specimen experiences total compression rather than the partial compression observed in G2 and G3.

Table 4.5. Statistical results for experimental resistance.

Series	Mean Exp. Max Load (kN)	CoV (%)
REF G1	444.6	6.76
REF G2	480.3	5.21
REF G3	471.3	10.09
T20 G1	440.5	4.06
T20 G2	456.4	6.00
T20 G3	441.3	5.05
T15 G1	342.7	4.59
T15 G2	359.7	4.95
T15 G3	380.1	5.61
T10 G1	296.4	9.38
T10 G2	307.3	5.58
T10 G3	289.2	3.87
T8 G1	269.8	9.44
T8 G2	217.9	8.54
T8 G3	245.7	3.39
T6 G1	231.9	4.91
T6 G2	235.0	8.27
T6 G3	203.1	7.53

Furthermore, it can be observed that the thinner the T-stub flange, the lower the maximum force of the component. Specifically, the maximum force of the T20 specimens was nearly equivalent to that of the reference (REF) results, whereas the resistance of the T6 specimens was approximately half that of the REF group.

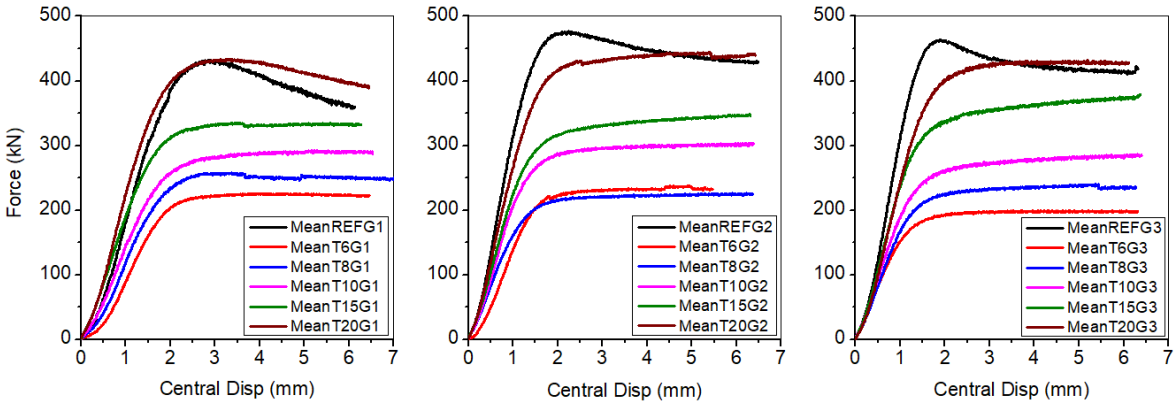


Figure 4.10. Force-displacement curves for all different T-stub flange thicknesses of G1, G2, and G3, measured by central LVDT.

Figure 4.11 illustrates the variability of the experimental results obtained for the resistance (maximum force) of both the REF and steel T-stub specimens in relation to the flange thickness. The

figure indicates that in the steel T-stub specimens, the maximum force was not influenced by the dimensions of the GLT, since they presented very similar results with the variation of the GLT groups. Moreover, Figure 4.12 demonstrates a reduction in the experimental resistance of the T-stub as the thickness of its flange decreases. This demonstrates that the maximum force of this component is closer to the flexural strength of the steel plate than to the compressive strength of the GLT, for plate thickness lower than 20 mm.

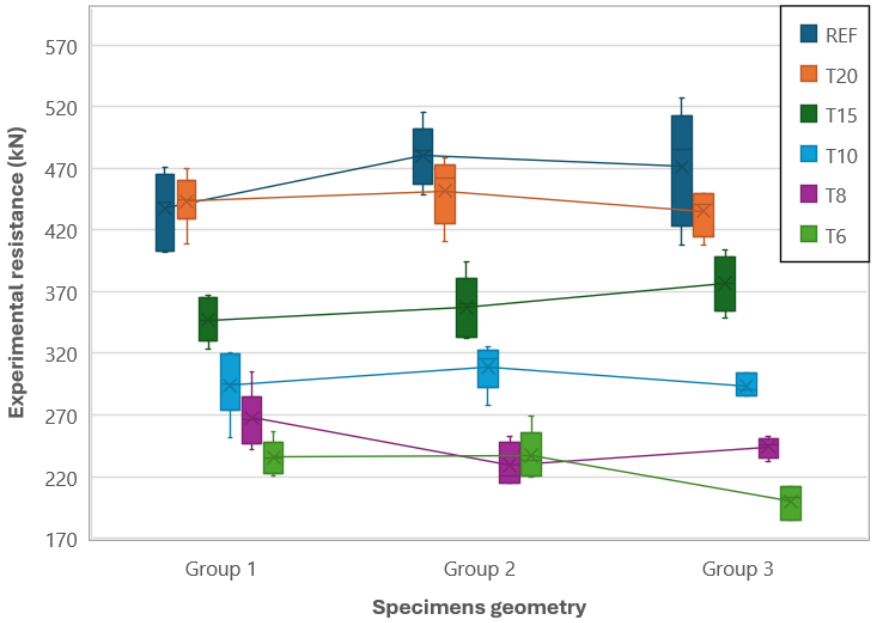


Figure 4.11. Variability in experimental maximum force due to flange thickness and specimen grouping.

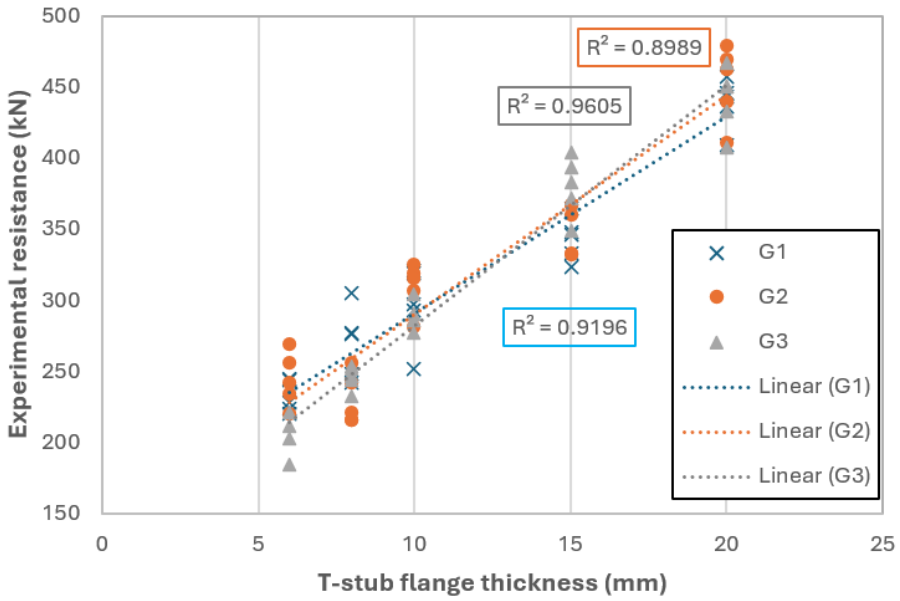
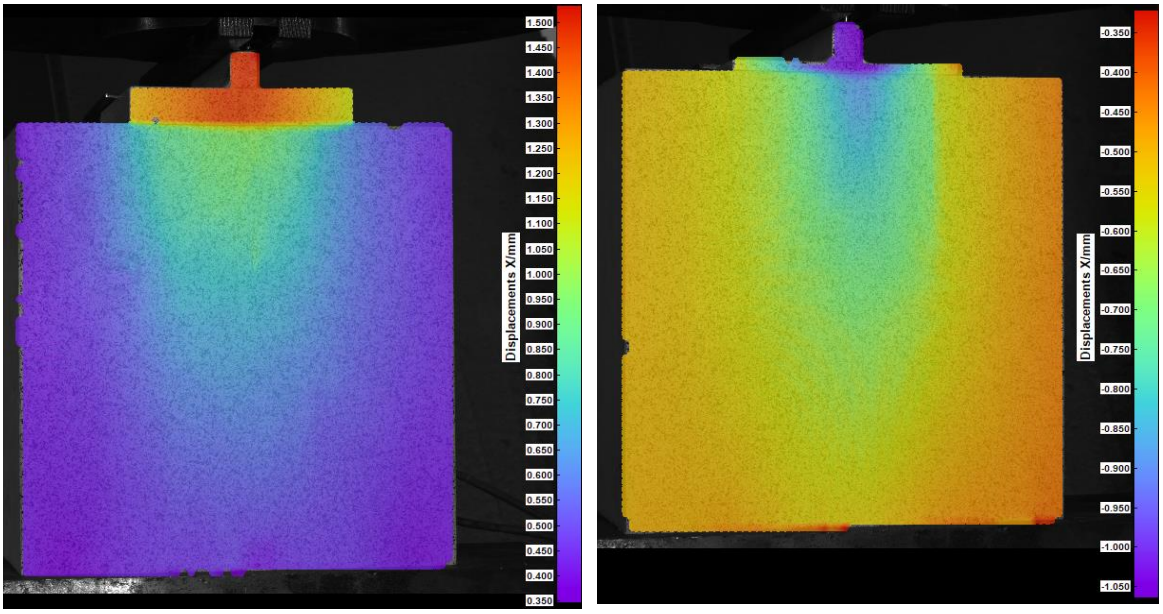


Figure 4.12. Correlation between the T-stub flange thickness and the experimental maximum force.

In all T-stub series (except REF), it was identified a higher displacement of the center of the T-stub flange in relation to the ends (relative edge displacement) from the beginning of the test (Figure 4.13). It is evident that the use of a deformable T-stub changes the nature of the resistance evaluation, shifting the focus from the GLT alone (REF) to the component as a whole. As a result, there is a decrease in the effective compression area between the T-stub and the GLT. So, in REF specimens the effective compression area was equal to the total area of the plate, while in T-stubs ones, it can be approximated by the effective area using the equivalent width.



(a) (b)

Figure 4.13. Variable vertical displacements across the width of the T-stub in the elastic range, as measured using the Digital Image Correlation (DIC) (a)T20 G2 S2 (b) T6 G2 S3.

For example, Figure 4.14 shows the deformed shape of one T6 G2 specimen when the maximum force was achieved. Negative displacements for left and right LVDTs occurs when the T-stub flange edges deforms in opposite direction in relation to the positive vertical displacements. As expected, the smaller the flange thickness, the greater was the relative edge displacement (bending of the flange), as consequence of the lower bending stiffness of the flange plate. Based on the observed behavior, it is evident that in most tests, component failure was attributed to the steel T-stub, which exhibited excessive displacement of its edges (deformation of the T-stub flange). In contrast, the wood demonstrated localized embedment around the central region (Figure 4.15). To be noted that it is considered that the T-stub flange yielding was achieved when the strain reached the yield strain for hot rolled structural steel S235 (ε_y equal to 0,1119 %). On the other hand, in "REF" series the GLT presented only the local plastic deformation (embedment failure) due to compression parallel to the grain under the loading plate (Figure 4.16).

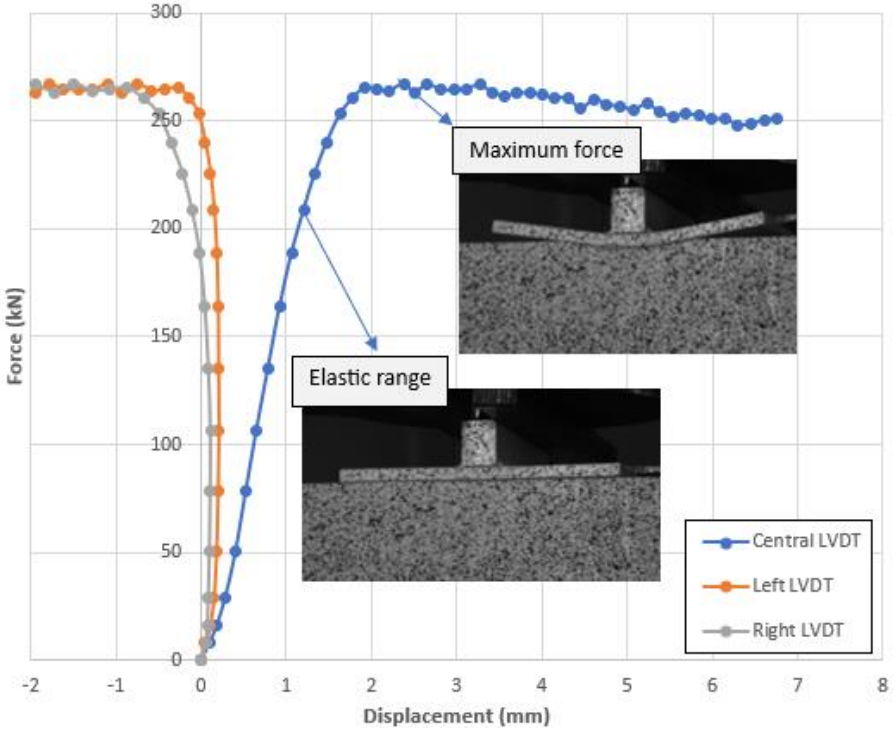


Figure 4.14. Force-displacement curve for T6 G2 S4 with deformed shapes at relevant positions.

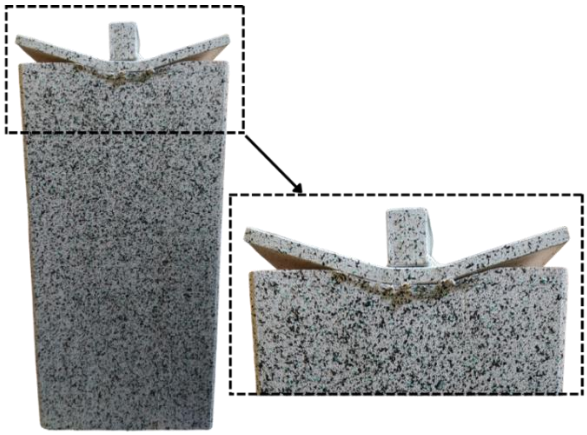


Figure 4.15. Failure of specimen T6 G1 S2 due to T-stub flange yielding.

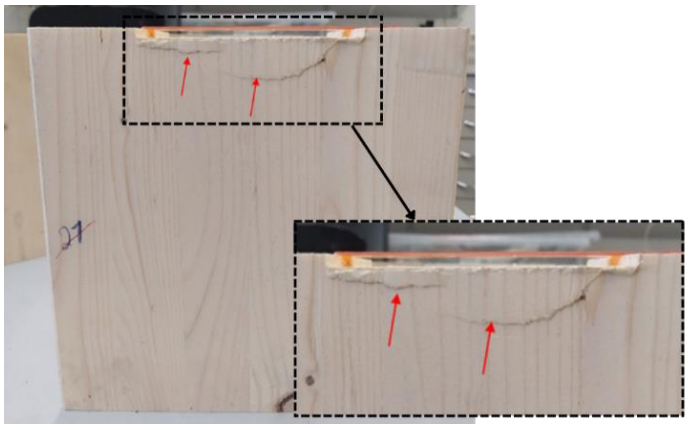
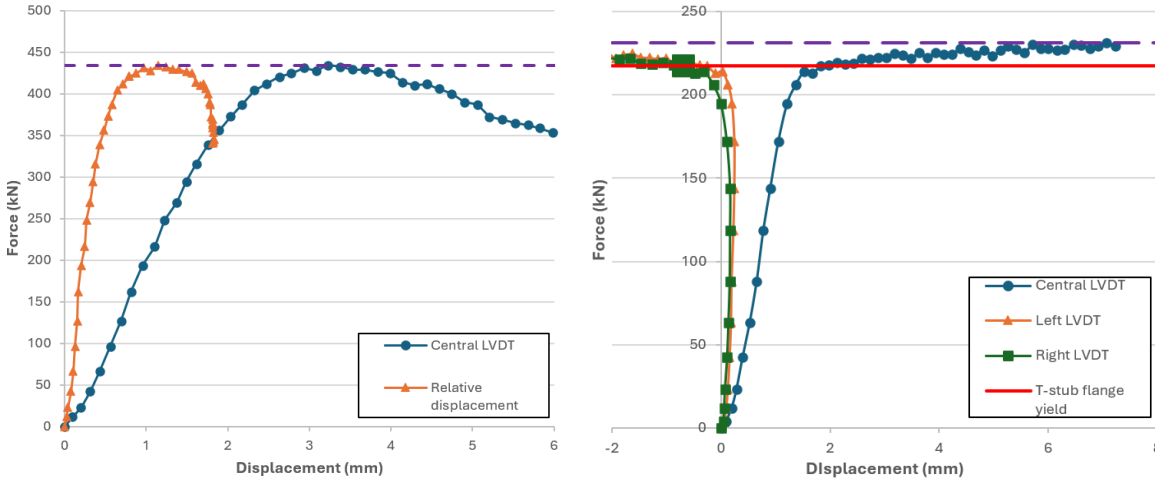


Figure 4.16. Local embedment of the timber under the steel plate observed in specimen REF G2 S4.

In Figure 4.17, it is possible to identify the two examples of failure, in T20 G1 S4 specimen (Figure 4.17 (a)) there is a local compressive failure, with a clear maximum force and without T-stub flange yielding. While in T6 G2 S3 specimen, the yielding occurs soon, due to the smaller thickness of the plate, and there is a long plateau without clear timber failure.



(a) (b)

Figure 4.17. Different failure modes for the component: (a) T20 G1 S4 specimen (b) T6 G2 S3 specimen.

In Table 4.6, the failure modes, the mean values of maximum force, T-stub flange strain and GLT displacement are presented for each series. All these data were measured at the maximum force instant. The T-stub flange strain was measured using DIC method, from the ratio of change in length to the original length. Furthermore, in series in which the component failed due to timber compression, there was a clear maximum force, with the respective displacement smaller than the series in which the failure was due to T-stub flange yielding. Therefore, the use of a thick plate (almost rigid) making a total compression on the GLT (not partial compression) lead to timber compression failure. Thus, the component experimental behavior is based on identifying whether the stress applied by the T-stub to the GLT is sufficient to reach the compressive strength parallel to the grain before yielding its flange. Except for T20 G1 series, in all T-stub thickness studied, the elastic limit of timber has been clearly reached, but it happened after the T-stub yielding and due to reduction in the contact area between the T-stub and GLT, leading to an increase in compression stresses in GLT.

Table 4.6. Summary of experimental failure modes at maximum force instant.

Series	Max Force (kN)	T-stub strain at max force	GLT displacement at max force (mm)	Failure mode
REF G1	444.6	0.031%	2.878	GLT embedment
REF G2	480.3	0.042%	2.142	
REF G3	471.3	-	2.098	
T20 G1	440.5	0,320%	2.797	GLT embedment
T20 G2	456.4	0,314%	5.710	
T20 G3	441.3	-	4.897	
T15 G1	342.7	0,358%	4.278	T-stub flange yielding
T15 G2	359.7	0,349%	6.686	
T15 G3	380.1	-	6.310	
T10 G1	296.4	0,371%	5.399	
T10 G2	307.3	0,350%	3.261	
T10 G3	289.2	-	4.922	
T8 G1	269.8	0,390%	4.278	
T8 G2	217.9	0,408%	4.827	
T8 G3	245.7	-	6.463	
T6 G1	231.9	0,426%	5.180	
T6 G2	235.0	0,412%	4.379	
T6 G3	203.1	-	4.919	

4.4.3. Initial stiffness results

For the component characterization, it is important to highlight that there is a slight difference between the modulus of elasticity and stiffness coefficient for GLT under compression parallel to the grain. The modulus of elasticity can just be defined using the rigid (undeformable) plate to compress GLT and considering just the middle region of the specimen, without the damage zone near to the edges. In addition, according to EN 408:2012, the strain should be measured along to a central height equal to four times the lower cross section size. The longitudinal modulus of elasticity in compression parallel to grain (E_0) is obtained by Equation (4.1), computing the displacement from 20% to 40% of the maximum force applied, along the longitudinal direction.

$$E_0 = \frac{\sigma_c}{\varepsilon_c} \tag{4.1}$$

As explained in the Chapter 3, the elastic behavior of each component is idealized by a spring, which the force-displacement relationship is given by Equation (4.2) (Weynand *et al.*, 1995). The initial stiffness of the joint ($S_{j,ini}$) is derived from the elastic stiffnesses of the components, that are called "stiffness coefficients", defined here as k_i, for each component i. Graphically, the stiffness coefficient is defined by the relation between force and displacement, directly obtained from load-displacement

curve from 20% to 40% maximum force applied. The displacements were collected along the specimen's full height.

$$k_i = \frac{F_i}{\Delta_i} \tag{4.2}$$

where F_i is the force in the component "i"; k_i is the stiffness coefficient of the component "i" and; Δ_i is the displacement of the component "i".

In the analysis of the experimental results, Table 4.7 presents the average stiffness coefficient values along with the corresponding coefficients of variation (CoV) for each of the tested groups composed by 5 specimens each. It is important to emphasize that the results obtained from the REF specimens denote the initial stiffness of GLT under compression parallel to the grain, serving as a reference for the results obtained for the T-stubs.

Table 4.7. Mean GLT Stiffness coefficient for all tested series.

Series	Number of specimens	Mean GLT Stiffness coefficient (N/mm)	CoV (%)
REF G1	5	247746	12.8%
REF G2		371792	4.8%
REF G3		382586	6.1%
T20 G1		278088	11.7%
T20 G2		317487	9.4%
T20 G3		295090	18.4%
T15 G1		203687	12.1%
T15 G2		259487	14.4%
T15 G3		280078	17.4%
T10 G1		179105	19.4%
T10 G2		240225	15.2%
T10 G3		189423	27.9%
T8 G1		184499	13.8%
T8 G2		184467	16.0%
T8 G3		206227	7.7%
T6 G1		149310	8.7%
T6 G2		191334	20.6%
T6 G3		177868	8.9%

A variation in the initial stiffness of the specimens was observed based on the thickness of the T-stub flange. Specimens with greater thickness exhibited higher initial stiffness, as shown in Figure 4.18. Although the load-displacement curves display initial slip due to the flattening of the contact surface between the GLT and the plate, a clear initial elastic behavior of both the GLT and T-stub flange can be identified in all tested specimens (see Figure 4.10).

Regarding the size effect, the specimens in group G1 demonstrated less stiffness than the others across all tested thicknesses (Figures 4.18 and 4.19). This suggests that GLT subjected to partial compression exhibits higher stiffness than those experiencing compression across the entire cross-section. This phenomenon was also noted by Totsuka et al. (2022), that used rigid plates in both full and partial compression of GLT.

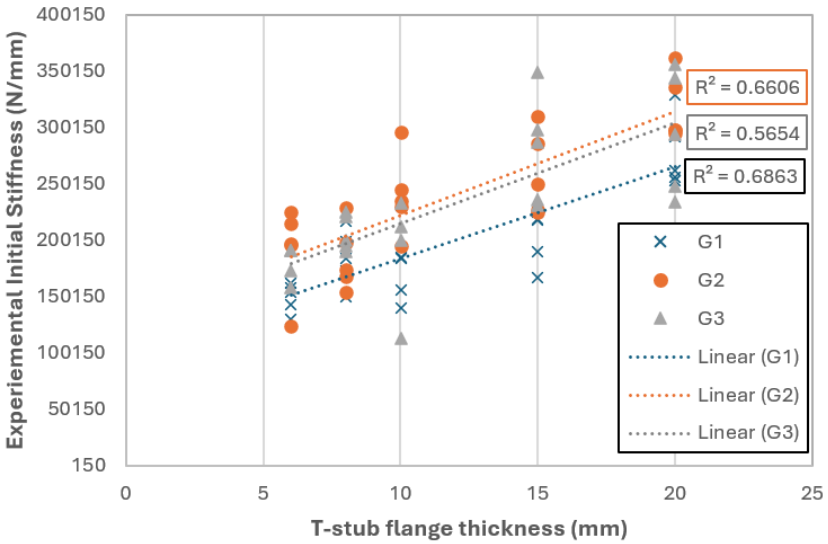


Figure 4.18. Correlation between the T-stub flange thickness and the experimental resistance.

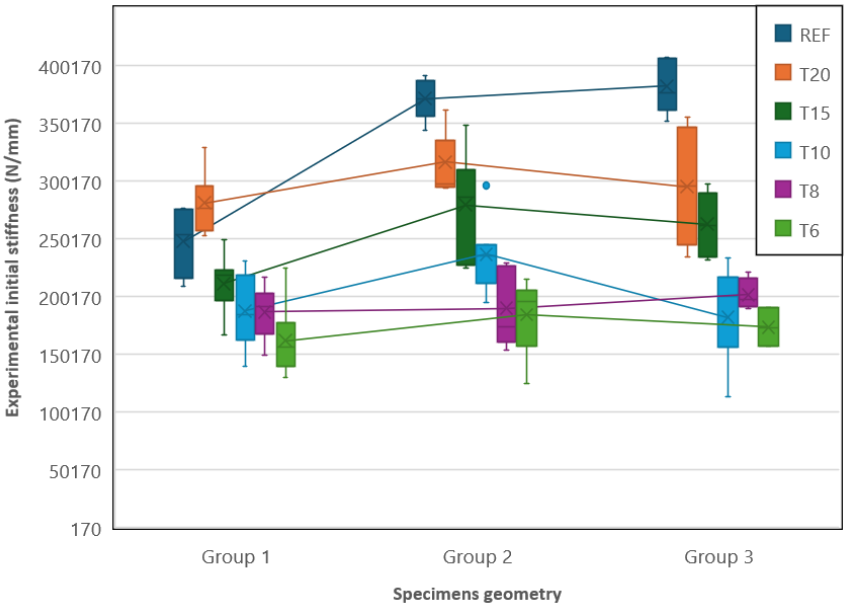


Figure 4.19. Variability in experimental initial stiffness due to flange thickness and specimen grouping.

4.5. Experimental tests on full-scale joints

4.5.1. Specimens and methodology

In this work, all tests were performed in stiffened end-plate moment-resisting steel-timber joints with steel link, and two or four bonded-in rods rows. All were composed of six elements: a rectangular

rigid plate, a steel link (H-section beam), four stiffeners connected to the plates and link, a rectangular steel end-plate with holes, bonded-in rods, and a GLT beam. The last one is connected to the end-plate through nuts attached to the BiR. The end-plate and rigid plate were connected to the link and stiffeners using fillet welds. A schematic overview of the joints tested is shown in Figure 4.20.

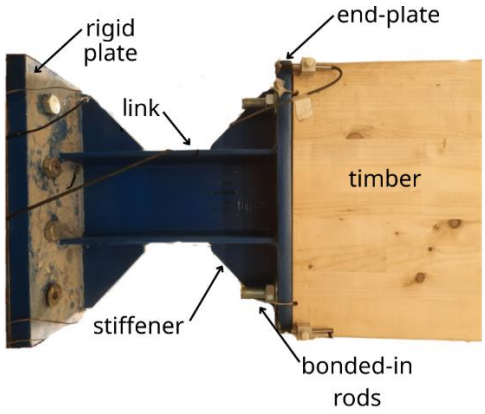


Figure 4.20. Schematic representation of tested stiffened end-plate moment-resisting steel-timber joints with steel link and bonded-in rods rows.

The main variables considered in definition of the tests included the thickness of the end-plate, the cross section and length of the link, and the diameter of the BiRs. The joints were intentionally designed to exhibit failure in different components (i.e. end-plate, steel link, BiRs) to explore all potential ductile failure modes that can occur in this type of joint and avoiding brittle failures. Additionally, some specimens were engineered to be equal-strength, partial-strength, or full-strength joints. All joints were defined so that the difference in resistance between its main components was small, aiming to replicate scenarios where the designer seeks to optimize material use and obtain cost savings. The main characteristics of the joint and initial sizing of end-plate thickness were defined based on Andreolli (2011) and Iovane (2020).

The specimens were divided into two groups: group 1 (G1) and group 2 (G2). This classification was based on the differences in geometry between the specimens. In the first experimental campaign, tests on G1 were conducted with the objective to analyze the behavior of a joint that exhibited significant deformations in the link and end-plate, resulting in a coupled behavior of these components with low levels of deformation in the BiR and timber beam. In the second experimental campaign, tests were performed on G2 to examine the behavior of the joint with four rows of BiR, focusing on the failure of these components. In this case, a slight overstrength was also implemented between the link and the end-plate to maintain the coupled behavior.

The G1 specimens were constructed with two rows of BiR, using metric threaded M20 rods, with a glued length of 800 mm and an unbonded length of 100 mm (5 times the outer diameter of the rod). The timber beam and the end-plate had cross-sectional dimensions of b × h = 200 mm × 420

mm. The steel link used was a HEA 160 profile, with a total length of 360 mm and a spacing of 120 mm between the stiffeners. The holes for the threaded rods were drilled with a diameter of 24 mm. The bond line thickness was equal to 2 mm. In this group, a total of 6 specimens were tested, with three specimens having an end-plate thickness of 20 mm and the remaining three specimens having a thickness of 15 mm.

The specimens in G2 were arranged in four rows of BiR. They had varying diameters, with M12, M14, and M16 metric threaded rods being used, and their glued lengths were equal to 270 mm for all of them, with an unbonded length of 30 mm from the timber end to the bondline. The bondline thickness was equal to 2 mm. Regarding the steel parts, the thickness of the end-plate also varied among the specimens, with values of 20 mm, 15 mm, and 12 mm. The steel link was an IPE 160 with a total length of 200 mm and a spacing of 40 mm between the stiffeners. The width and height of the timber beams and end-plates were consistent across all specimens in this group, with cross-sectional dimensions of b × h = 160 mm × 320 mm. Table 4.8 summarizes the nomenclature and main characteristics of the individual specimens, while Figure 4.21 and Figure 4.22 illustrate their dimensions and details.

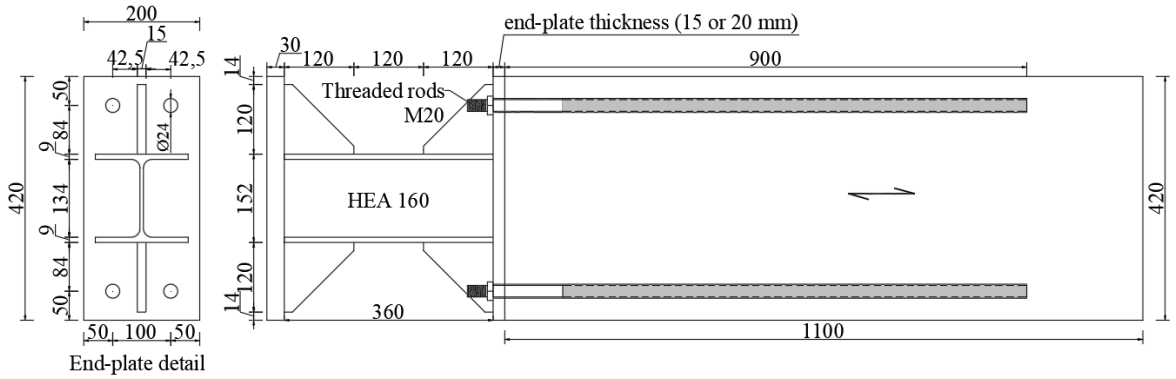


Figure 4.21. Joints of group 1 (dimensions in mm).

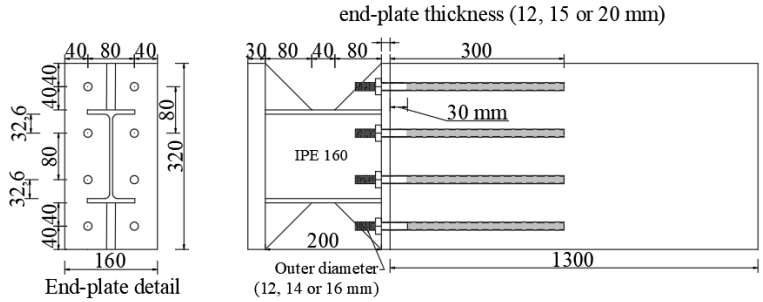


Figure 4.22. Joints of group 2 (dimensions in mm).

Regarding to the materials, the GLT elements used in the joint tests were made from Norwegian spruce (*Picea abies*) and of GL24h strength class (EN 14080:2013). To minimize discrepancies, the timber parts were manufactured and drilled using CNC control. The samples were stored in the

laboratory for at least 7 days before testing. During this period, the laboratory's temperature and relative humidity were monitored, yielding an average temperature of 21 °C and an average relative humidity of 64%. The moisture content was measured a few minutes before the test according to EN 13183–2 (2005). All steels used in the tests are of strength class S235 and belong to the same batch as those tested separately, which were described in Section 4.2. Similarly, the threaded rods used for the BiRs are from the same batch as those tested and described in Section 4.2. Class 8.8 threaded rods were used in G1, while class 4.8 threaded rods were used in G2.

Table 4.8. Summary of the tested joints.

Joint	Bonded-in rods			End-plate			Steel link	Timber beam	
	Rows	Outer diameter (mm)	Glued length (mm)	Thickness (mm)	Width (mm)	Height (mm)		Width (mm)	Height (mm)
G1.J1.t20.d20	2	20	800	20	200	420	HEA 160	200	420
G1.J2.t20.d20									
G1.J3.t20.d20									
G1.J4.t15.d20				15					
G1.J5.t15.d20									
G1.J6.t15.d20									
G2.J1.t20.d12	4	12	270	20	160	320	IPE 160	160	320
G2.J2.t20.d12									
G2.J3.t20.d12									
G2.J4.t15.d14		14	270	15					
G2.J5.t15.d14									
G2.J6.t15.d14									
G2.J7.t12.d16		16	270	12					
G2.J8.t12.d16									
G2.J9.t12.d16									

The bonding and assembly process was conducted with a level to ensure the BiR was positioned as accurately as possible. Before the gluing process, both the threaded rods and the holes in the timber were thoroughly cleaned using compressed air to remove dust and debris, ensuring optimal adhesion. The gluing procedure was carried out with the beam positioned vertically, with the holes facing upward to facilitate adhesive application. To ensure the designed unbonded length of the bars, pieces of plastic tubing were temporarily inserted into the holes. These spacers acted as physical barriers, preventing adhesive from bonding to the specified portions of the rods. The required amount of adhesive was then carefully measured and poured into the holes. Each threaded rod was inserted individually using slow, circular movements. This technique helped distribute the adhesive evenly

along the bonded area and expel any trapped air bubbles, promoting full contact between the rod, adhesive, and timber surface.

Once all rods were in place, a steel fixture was positioned to align and maintain them in their correct orientation. The joints were left to cure for a minimum of 7 days under controlled conditions, allowing the adhesive to achieve its full mechanical strength before testing. Figure 4.23 illustrates the stages of the manufacturing and assembly process of the specimens.

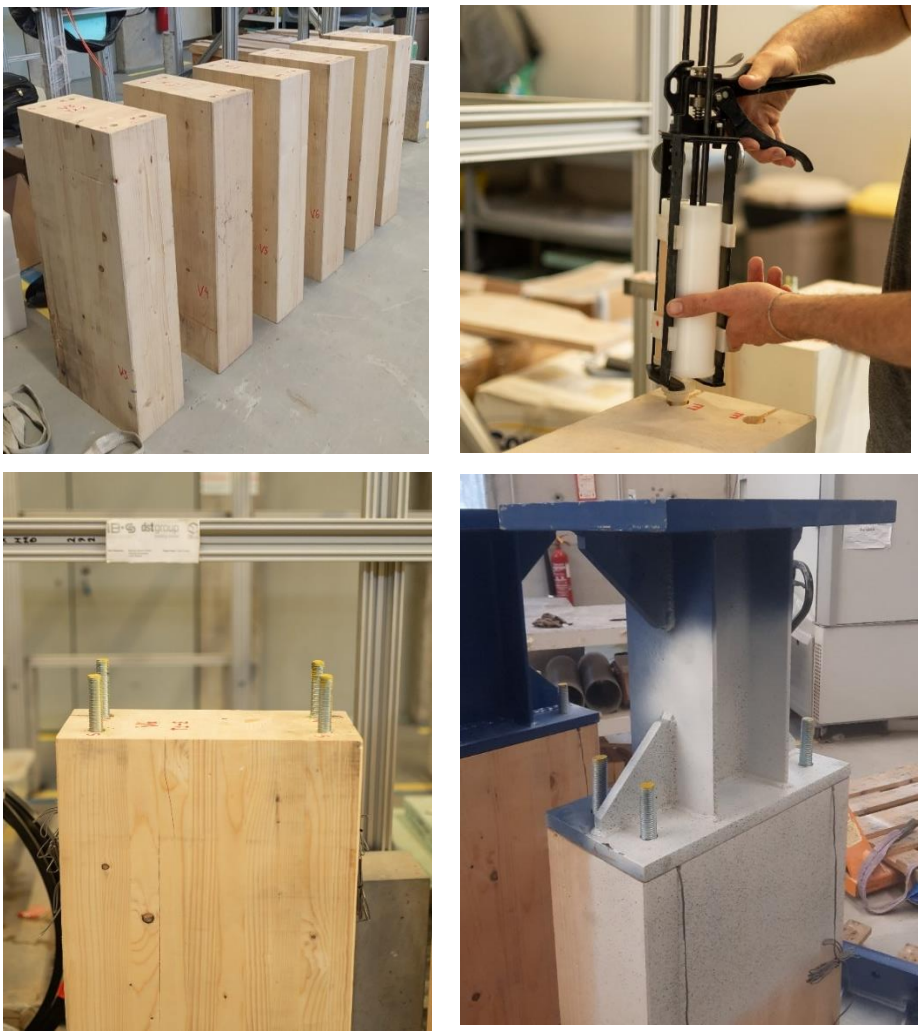


Figure 4.23. Stages of the manufacturing and assembly process of the joints specimens.

4.5.2. Test setup and instrumentation

The tests were conducted with the joints in a vertical position. The lower part of the steel link was attached to the reaction frame with anchor bolts, restrained against horizontal and vertical displacements, as well as in-plane rotations. The load was applied to the beam end through a hydraulic jack, placed 1300 mm from the reaction frame. The hydraulic jack was attached to the timber beam using a loading rig. Since significant beam rotation was expected for these tests, the loading system

was designed as a dual-pin mechanism, which could release horizontal forces and moments caused by the linked rotation of the loading jack. In addition, a lateral restraint was installed to avoid potential out-of-plane deformation of the specimens due to accidental eccentricity of the load or global buckling. An overview of the experimental setup employed is shown in Figure 4.24.

The test was conducted by applying a lateral load using a 300 kN load cell at a speed of 3.0 mm/min, following the recommendations of EN 26891:1991. The maximum load applied in the loading procedure was estimated based on preliminary test. The load was applied up to 0.4 of the maximum load and maintained for 30 seconds. Subsequently, the load was reduced to 0.1 of the maximum load and held for an additional 30 seconds. Following this, the load was incrementally increased until the ultimate load was reached. The testing was concluded either upon the failure of the specimen.

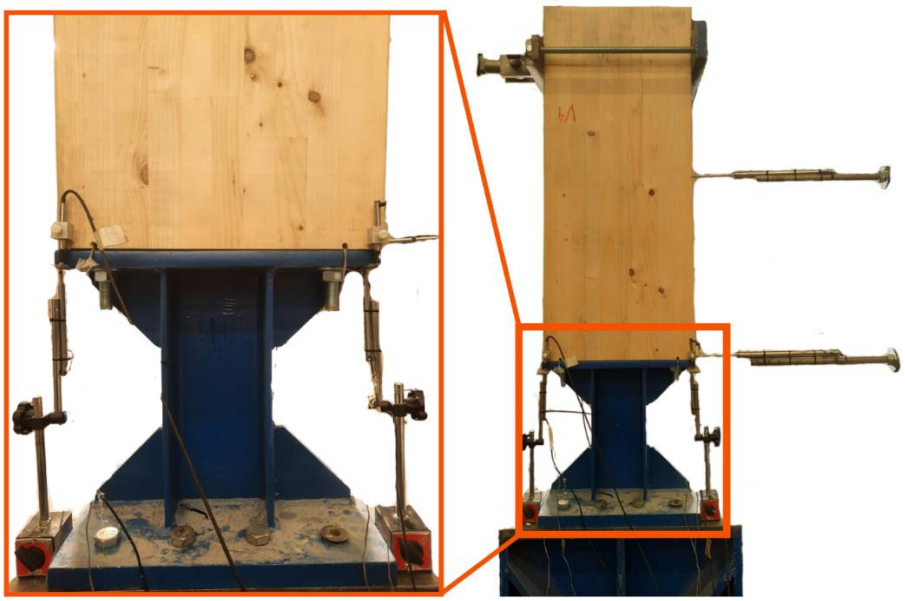


Figure 4.24. Overview of loading test.

Linear variable displacement transducers (LVDTs) and strain gauges were used to measure displacements in the joint and deformations in the BiRs. All distances and positions of the load cell (indicated as force Fext) and LVDTs are indicated in Figure 4.25. LVDTs 1 and 2 measured the displacements of the edges of the end-plate in the y-direction (Δ_{et} and Δ_{ec}), while LVDTs 3 and 4 measured the relative displacement between the timber beam and the end-plate (Δ_{tt} and Δ_{tc}). The sum of these two displacements provides the total displacement at each connection edge. The rotation of the joint (θ_T) is the rotation of the timber beam, which was calculated from the displacements in the y-direction and the horizontal distance between LVDTs 1 and 2 (dH_{ep}), which corresponds approximately to the height of the end-plate, as shown in Equation (4.3). The measured distances

dLep1, dLep2, dLb2, dLb2, and dLb3 are 17, 18, 20, 550, and 895 mm, respectively. LVDTs 5, 6, and 7 were positioned to measure displacements in the x-direction along the length of the timber beam to monitor the horizontal displacement along the timber beam.

$$\theta_T = \frac{(\Delta_{tt} + \Delta_{et}) + (\Delta_{tc} + \Delta_{ec})}{dH_{ep}} \tag{4.3}$$

One line of threaded rods under tension on each G2 joint was instrumented with strain gauges (SG) featuring a gauge length of 3 mm, a gauge factor of 2.09%, and a gauge resistance of 118.5 Ω. To attach the SG, the threads of the rods were removed before gluing, and afterward, the SGs were covered with resin for protection. The alignment of the SG was ensured to be perpendicular to the end-plate during the gluing of the rods, allowing for accurate measurement of strains in the connection moment plane (Figure 4.26 (a)). To achieve satisfactory data acquisition, the SG was positioned in the unbonded length, 30 mm from the end of the timber beam (Figure 4.26 (b)), as recommended by Sarti et al., (2016).

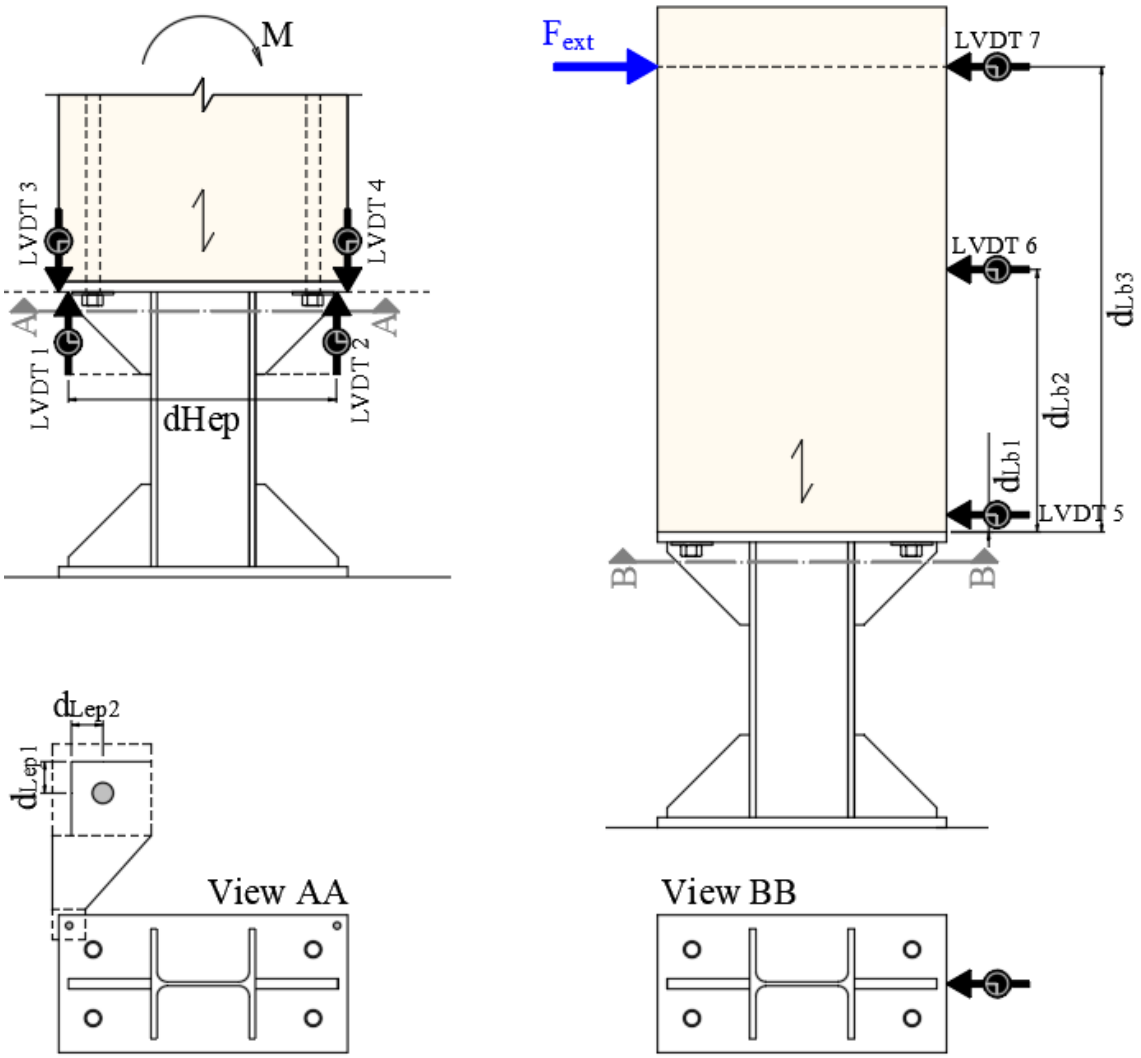
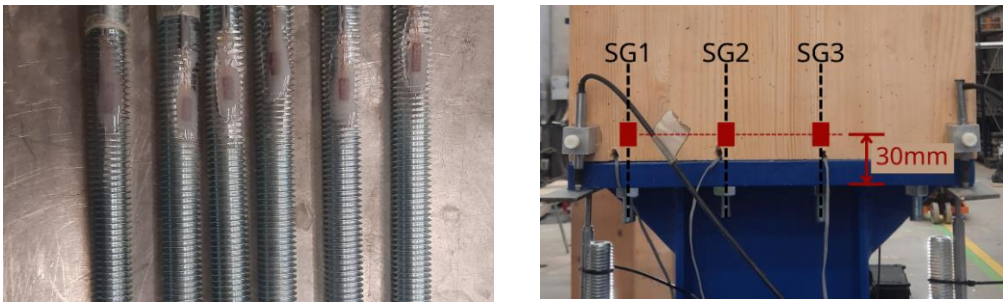


Figure 4.25. Position of load cell and LVDT instrumentations.



(a) (b)

Figure 4.26. Strain gauge positions: (a) On threaded rods; (b) On timber beam.

In addition to the two measurement methods mentioned, the Digital Image Correlation (DIC) technique was used in the experimental campaign to obtain a full-field displacement measurement, i.e., a displacement map on the face of each specimen, specifically focusing on the connection region between the end-plate and the timber beam. This technique falls under the category of optical, non-interferometric methods, which determine deformation by comparing changes in the surface image of an object before and after deformation (Pan *et al.*, 2009).

The measurement of displacement and deformation using the DIC system involves several stages that must be conducted consecutively. These stages include preparing the surface of the specimen through patterning, calibrating the device using the DIC system calibration, recording images of the object's surface both before and during movement or deformation, analyzing the images using specialized software, and finally, visualizing the results (Górszczyk *et al.*, 2019). The DIC system employed in this study was developed by Dantec Dynamics and consists of two cameras (designated as Master and Slave) with a resolution of 2.0 megapixels. These cameras were positioned at a distance of 120 cm from the specimens, with a separation of 240 mm between them (Figure 4.27). The acquisition frequency for frame capture was set at 1 Hz. Data processing was performed using the associated software for the system, specifically INSTRA 4D V4.4.7 x64.

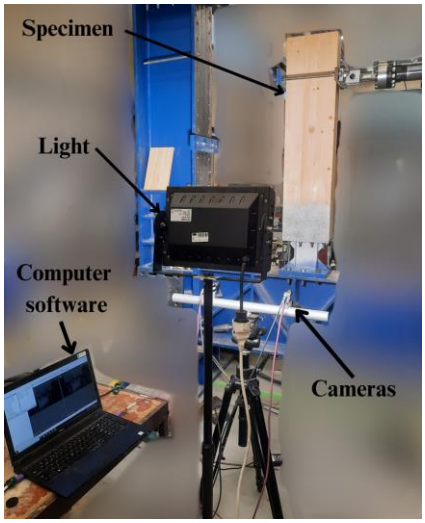


Figure 4.27. Equipment used in the DIC measurements.

Measurements were made from specific points positioned at the ends of the end-plate (EP_C and EP_T), on the timber beam (TB_C and TB_T), and along the axis of the link flanges (L_C and L_T). In addition, to obtain displacement maps, measurements were made from straight lines positioned along the axis of the end-plate and the end of the timber beam, as shown in Figure 4.28.

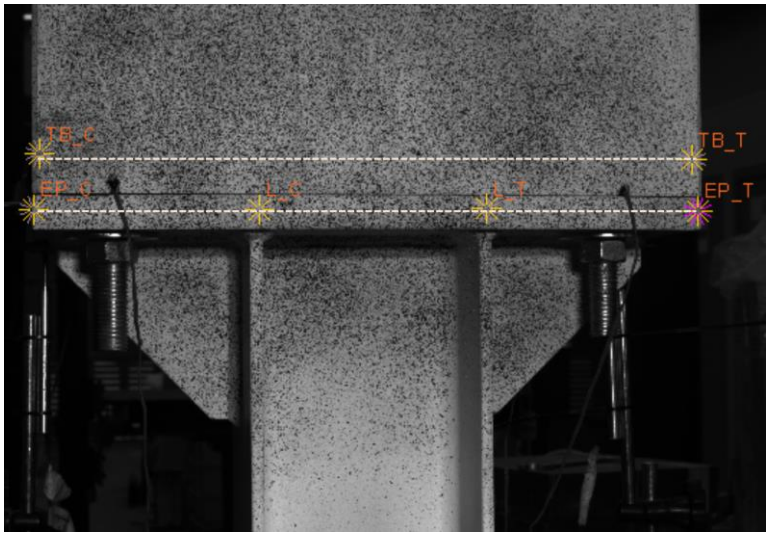


Figure 4.28. Main points and lines defined for DIC technique measurements.

To better interpret the results, it was assumed that the displacements occurring in the central region of the end-plate, between the steel profile flanges, are caused by the rotation of the link (shown in blue in Figure 4.29). Based on this assumption, the rotation of the end-plate is derived solely from the cantilevers, specifically from the centerline of the link flange to the edge of the end-plate, as indicated in red in Figure 4.29. With this information, it was possible to calculate the rotation that each part of the joint contributes to the entire structure. The link's rotation was measured by summing the displacements along the axis of each flange and dividing by the horizontal distance between them. The end-plate's rotation was determined by subtracting the total displacements at the end of the end-plate from the displacements resulting from the projection of the link's rotation.

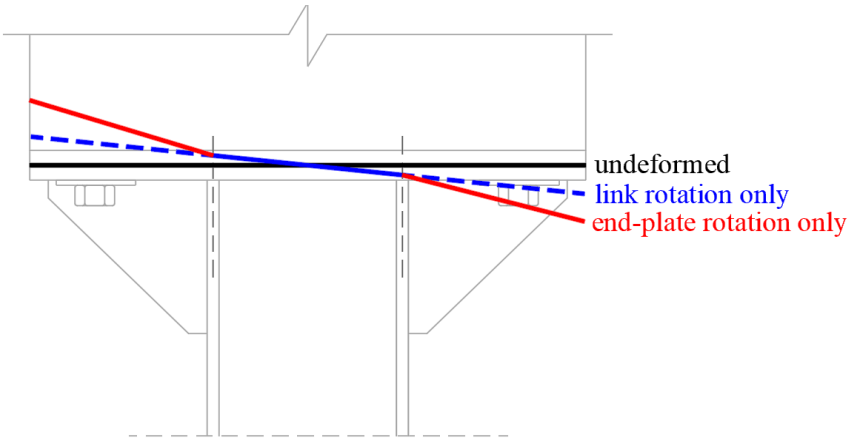


Figure 4.29. Measurement methodology of displacements.

4.5.3. Results and discussion

4.5.3.1. Moment-rotation characteristics and failure modes

The definitions of critical characteristics extracted from a tested moment-rotation curve are crucial to understanding joint mechanical behavior. The yield point corresponds to the moment and rotation of the entry into the plastic range (My, θy). Theoretically, from this point, the joint starts to present plastic deformations. As already mentioned in the chapter 2, it was calculated according to the EN 12512:2001 by the intersection between two lines, the first between 10% and 40% of the maximum moment (corresponding to the initial rotational stiffness, Sj,ini), and the second one by a tangent line to the moment-rotation curve with a slope of 1/6 of initial stiffness (Figure 4.30 (a)). When the moment-rotation curve of the tested joint does not have a clear maximum force, the second line is defined as the force when the curve reaches a plateau. Some joints presented a plateau that characterizes the formation of a plastic hinge, as the connection no longer offers rigidity to the applied load (Figure 4.30 (b)). As the failure mode of the joint is ductile, it is necessary to identify where the plastic hinge was formed in each joint. For this purpose, the relative displacements and rotations of the end-plate and the link were studied in two regions: (I) in the elastic range and (II) during the plastic range, as shown in Figure 4.30 (b). Other points describing the failure of the specimen at large deformations are also highlighted in Figure 4.30. These include the post-limit stiffness (Sj,p) that corresponds to the tangent slope of the post-limit range, the ultimate moment Mu and its corresponding rotation θu. The joint moment resistance is calculated considering the lever arm from the load cell to the connection between the end-plate and timber beam, as schematically illustrated before, see Figure 4.25.

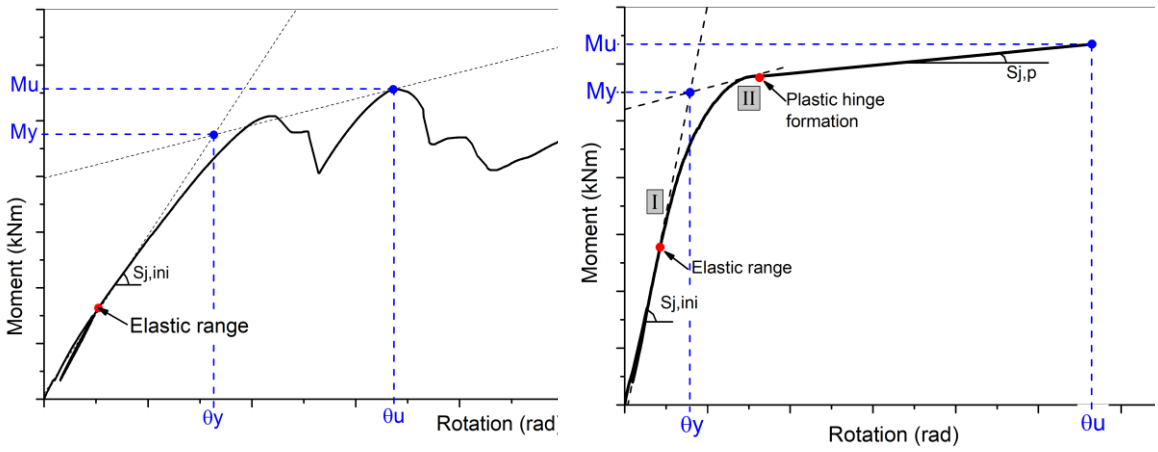


Figure 4.30. Key points defined for experimental curves.

The derived moment-rotation curves obtained from LVDTs are shown in Figure 4.31 and 4.32. The joint moment resistance can be determined based on the ultimate moment (Mu) or the yield moment (My), depending on the joint's failure mode and the component in which the failure occurs. For instance, when the link undergoes the plasticization, that is the state where the entire cross-section of the link has yielded, meaning all its material has reached its yield stress. This occurs when the link is subjected to a high enough bending moment, forming a plastic hinge, which allows the section to undergo further rotation and deformation without resisting additional load. This study identifies this region as where the moment-rotation curve exhibits a horizontal plateau. In this instance, it is considered that the link has reached its resistance limit. The results for all tested joints are shown in Table 4.9.

Table 4.9. Moment resistance and initial rotational stiffness of the tested joints.

Joint	My (kNm)	θy (rad)	Mean My (kNm)	Mu (kNm)	θu (rad)	Mean Mu (kNm)	Sj,ini (kNm/rad)	Mean Sj,ini (kNm/rad)
G1.J1.t20.d20	52.74	0.0135		59.17	0.119		4008.74	
G1.J2.t20.d20	55.03	0.0158	54.30	63.47	0.113	61.49	3656.34	4148.47
G1.J3.t20.d20	55.12	0.0121		61.82	0.120		4780.31	
G1.J4.t15.d20	53.96	0.0163		56.16	0.102		3521.87	
G1.J5.t15.d20	52.69	0.0151	53.01	56.79	0.108	55.71	3746.46	3586.65
G1.J6.t15.d20	52.38	0.0156		54.19	0.111		3491.61	
G2.J1.t20.d12	21.67	0.0143		24.92	0.019		2586.77	
G2.J2.t20.d12	18.91	0.0041	18.59	25.69	0.008	24.97	4528.52	3879.73
G2.J3.t20.d12	15.19	0.0035		24.30	0.016		4523.91	
G2.J4.t15.d14	25.63	0.0073		27.87	0.011		3664.06	
G2.J5.t15.d14	21.00	0.0062	23.45	26.30	0.031	27.24	3669.31	3476.89
G2.J6.t15.d14	23.74	0.0082		27.54	0.016		3097.31	
G2.J7.t12.d16	33.13	0.0102		36.51	0.027		3171.11	
G2.J8.t12.d16	32.92	0.0101	32.88	35.61	0.022	36.48	3232.52	3280.76
G2.J9.t12.d16	32.60	0.0098		37.33	0.028		3438.64	

The experimental results reveal clear distinctions in the structural response of the different joint groups. For group 1, the specimens in G1.t20 exhibited a relatively high Mean My of 54.30 kNm, with individual values ranging from 52.74 to 55.12 kNm, indicating consistent yielding behavior. The mean

ultimate moment (Mu) reached 61.49 kNm, corresponding to an approximate 13% increase compared to the yield capacity.

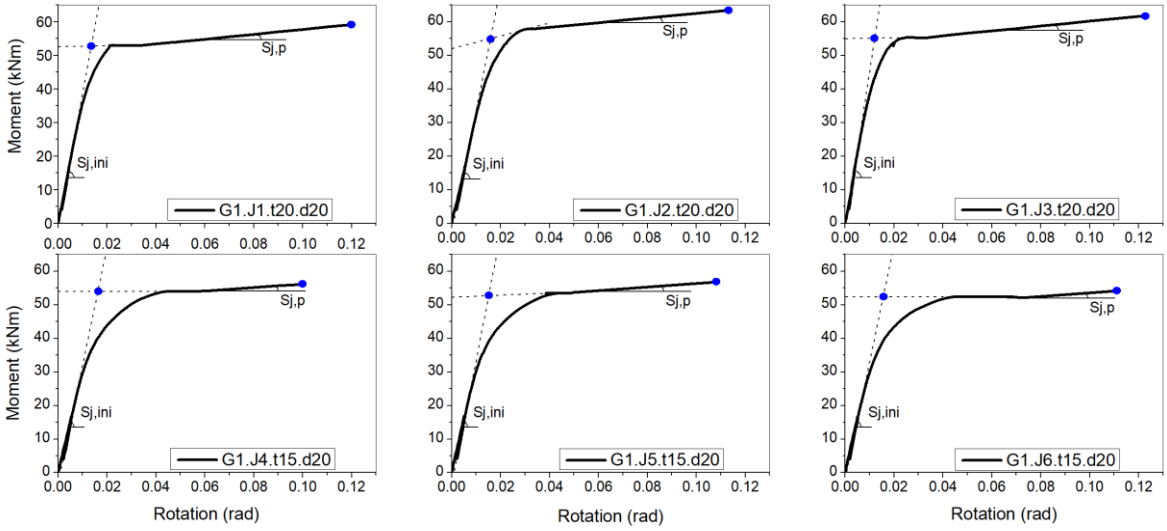


Figure 4.31. Experimental moment-rotation curves for G1 joints.

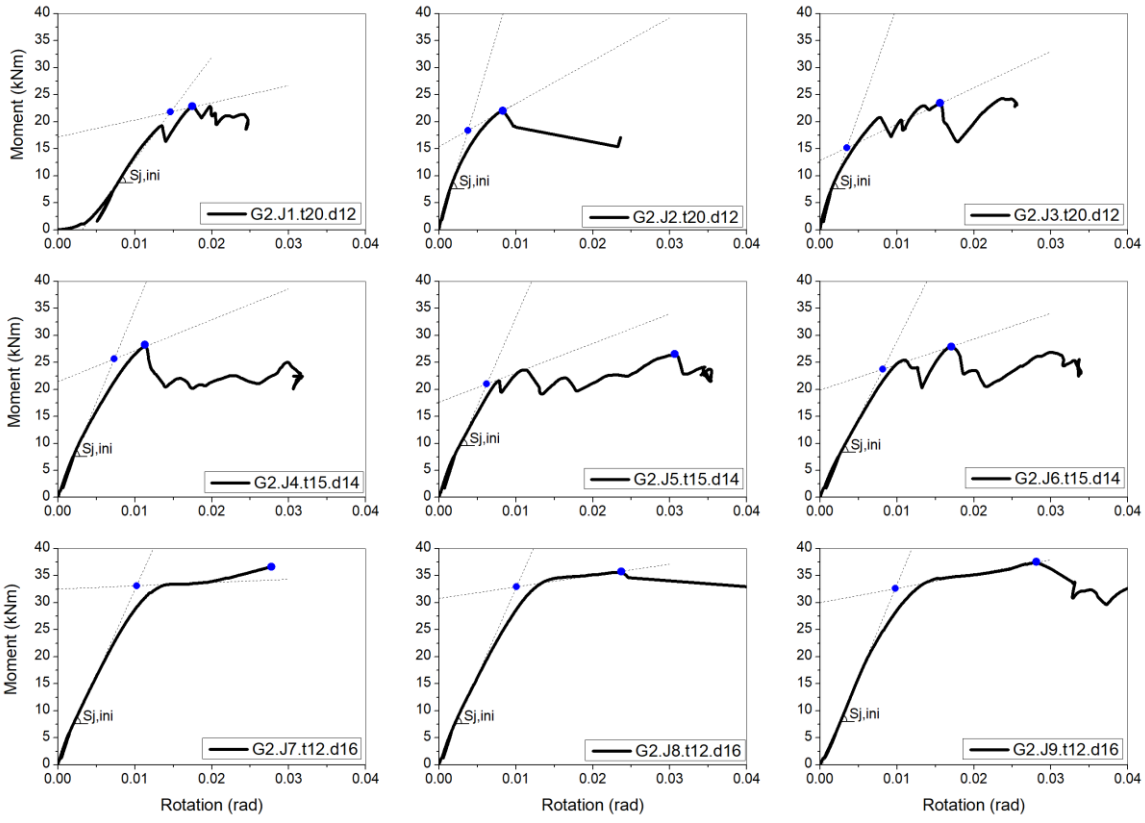


Figure 4.32. Experimental moment-rotation curves for G2 joints.

The ultimate rotations (θu) were considerably larger than the yield rotations (θy), with averages of 0.117 rad and 0.014 rad, respectively, confirming a pronounced ductile response. The initial rotational stiffness (Sj,ini) averaged 4148.47 kNm/rad, with a variation between specimens (3656– 4780 kNm/rad). This dispersion suggests sensitivity of stiffness to local variations in material

properties or execution. Overall, G1.t20 demonstrated both high moment capacity and favorable ductility. The joints in G1.t15 displayed a slightly lower mean yield moment of 53.01 kNm, compared to G1.t20. The mean ultimate moment was 55.71 kNm, showing only a 5% increase after yielding, considerably smaller than the post-yield enhancement observed in G1.t20. Ultimate rotations averaged 0.107 rad, reflecting a more limited ductile capacity. The mean initial stiffness was 3586.65 kNm/rad, consistently lower than that of G1.t20. The reduction can be attributed to the smaller end-plate thickness, which influenced both stiffness and post-yield rotation. Thus, G1.t15 specimens exhibited adequate strength but a less favorable ductility profile compared to the thicker end-plate configuration.

For group 2, the mean yield moment of G2.t20.d12 was 18.59 kNm, approximately one-third of G1 values, while the mean ultimate moment was 24.97 kNm. Yield rotations varied substantially (0.0035–0.0143 rad), and ultimate rotations were very limited, averaging 0.014 rad, which indicates a brittle response. Interestingly, the mean stiffness was relatively high, 3879.73 kNm/rad, with some specimens exceeding 4500 kNm/rad. This reflects a structural configuration that restricts initial deformation, concentrating stiffness but limiting ductile capacity. The joints in G2.t15.d14 exhibited improved performance compared to G2.t20.d12. The mean yield moment was 23.45 kNm, with the mean ultimate moment reaching 27.24 kNm, an approximate 16% post-yield increase. Yield rotations remained limited (0.0062–0.0082 rad), and ultimate rotations averaged only 0.019 rad. The mean stiffness was 3476.89 kNm/rad, slightly lower than G2.t20.d12 but with reduced dispersion. This suggests that increasing BiR diameter from 12 mm to 14 mm allowed a moderate gain in moment resistance, while maintaining comparable rotational stiffness. However, the ductility remained restricted compared to G1. The most favorable response within G2 was observed in G2.t12.d16. The mean yield moment was 32.88 kNm, while the mean ultimate moment reached 36.48 kNm, corresponding to a 10% strength increase after yielding. Ultimate rotations averaged 0.026 rad, which is a significant improvement in ductility relative to the other G2 subgroups. The mean stiffness was 3280.76 kNm/rad, slightly lower than G2.t15.d14, but with consistent results (3171–3439 kNm/rad). This balance between stiffness and ductility suggests that larger BiR diameter (d16) promotes a more favorable global joint performance.

A global comparison between G1 and G2 reveals that beam height played a decisive role in the joint behavior. The G1 specimens, with a timber beam height of 420 mm, achieved markedly higher moment capacities than the G2 specimens, which were limited by a smaller beam height of 320 mm. This difference can be explained by fundamental mechanics: the bending resistance of a joint is strongly governed by the lever arm between compression and tension forces, which scales with beam

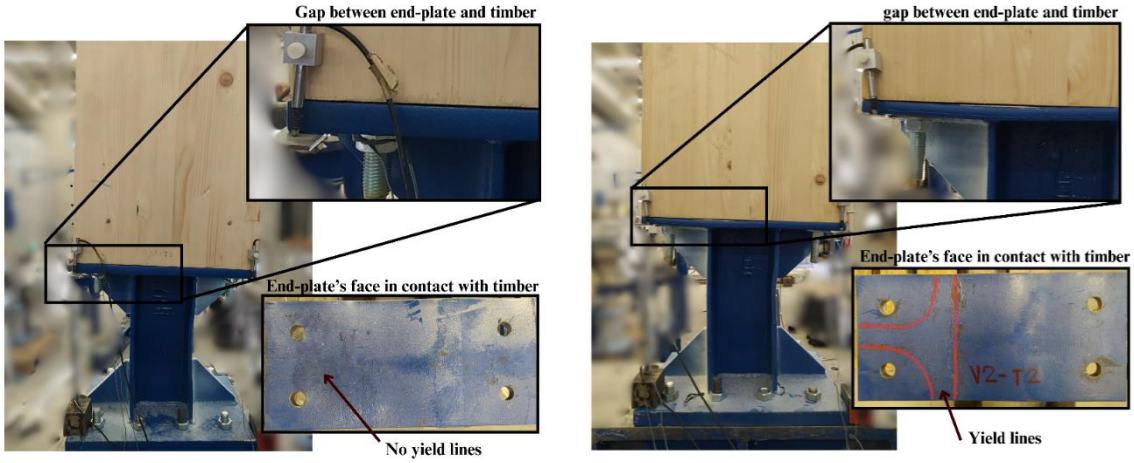
depth. When normalizing the ultimate moment capacity (Mu) by beam height, the influence becomes clearer. For G1, the mean normalized capacity was approximately 0.146 kNm/mm (61.49/420), whereas for G2 it ranged from 0.078 to 0.114 kNm/mm, depending on the configuration. This indicates that while G1 achieved higher absolute moments, the efficiency per unit depth of G2.t12.d16 can approach that of G1 due to the design that was oriented to BiR connection. In terms of stiffness, the effect of beam height was less pronounced. In terms of stiffness, for Group G1, this ratio averaged approximately 9.6–9.9 kNm/rad per mm (4148/420), whereas for Group G2 it ranged from 10.3 to 12.1 kNm/rad per mm (e.g., 3879/320 and 3281/320). This normalization shows that, despite their lower absolute stiffness, the G2 specimens were in fact stiffer relative to their depth than the G1 specimens. This finding reinforces that local joint geometry (end-plate thickness, BiR rows spacing and diameter) exerts greater influence on stiffness than beam height.

From a design perspective, these results highlight that increasing beam height is the most effective strategy for enhancing moment resistance, as demonstrated by the performance of G1. However, in cases where beam depth is limited, adjustments to joint detailing, specifically the thickness of the end-plate and the spacing of BiR rows, exert a more substantial influence on initial stiffness. In contrast, the BiR diameter, as seen in G2.t12.d16, is related to moment resistance. To better understand this behavior, it is essential to identify the hierarchy of joint resistance, considering both macro-components and sub-components. The calculation of component resistance and the prediction of this hierarchy are addressed in Chapter 5.

In addition, it was identified that in this type of joint, the failure hierarchy is a very important factor, since the strength of the weakest component of the connection determines the joint yield moment and also influences the ultimate moment. In all tests conducted, failure was observed in the steel elements, and it occurred in a ductile manner, which was attributed to their yielding. No damage to the timber was identified in any of the tests, leading to the conclusion that the timber remained within the elastic range.

Regarding G1 joints, there were notable variations in failure occurrence despite the small difference in the thickness of the end-plates. In the case of G1.t20.d20, no discernible plastic displacements were observed in the end-plate. The predominant failure mechanism for this joint was the plastic deformation of the steel link by bending, as shown in Figure 4.33 (a) (full strength connection), Iovane and Faggiano (2021) observed comparable failure modes. In G1.t15.d20, the yield moment resistance of the link and the potential for end-plate yielding were closely aligned, indicating that it can be classified as an equal-strength connection. The specific location within the

joint where yielding began is complex to be determined. The link displayed plastic deformations, and the tension side of the end-plate exhibited greater deformation, resulting in a visible gap between the end-plate and the timber beam. Yield lines were also observed in the end-plate, as illustrated in Figure 4.33 (b). Although the end-plate is connected to a timber beam, this shape of end-plate failure is similar to the steel stiffened extended end-plate beam-to-column joints as studied by Shi *et al.* (2007) and Tartaglia *et al.* (2018).



(a) (b)

Figure 4.33. Representative failure modes for: (a) G1.t20.d20; (b) G1.t15.d20.

Observing the moment-rotation curve with the mean results for the two types of G1 joints (Figure 4.34), it is evident that the t20 joints exhibit a longer linear section, reaching the plastic phase at a higher moment value and a lower rotation compared to the t15 group. This difference in the curve's shape indicates that in t20, yielding and plasticization occurred only in the link, while in t15, the yielding initiated in the end-plate, the weakest component, later the plasticization occurring in the link, as characterized by the horizontal plateau.

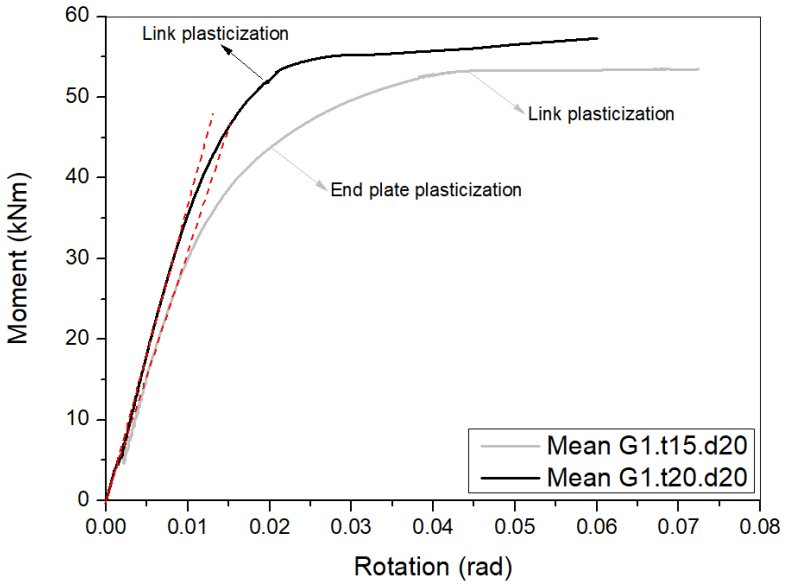
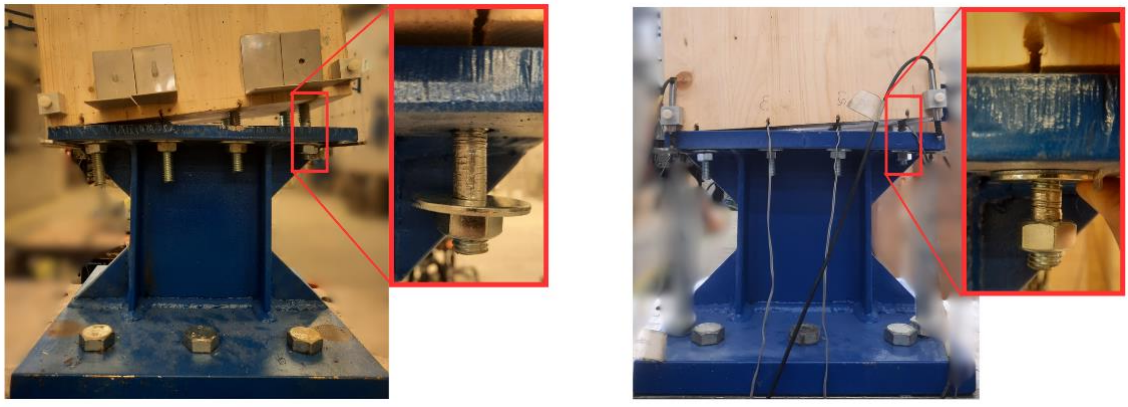


Figure 4.34. Comparison of the moment-rotation curves of mean results of the G1 joints.

In the case of G2 joints, the variability in the thickness of the end-plate and in the diameter of the BiRs resulted in different failure modes compared to G1 joints. In both G2.t20.d12 and G2.t15.d14, no prying forces were observed in the connection between the timber and end-plate, the failure mode occurred on BiR (Figure 4.35). The specimens demonstrated significant rotations in the timber, primarily due to tensile deformations in the steel of the bonded-in rods, which governed the failure modes. Notably, following the identification of the failure in the first row of bonded-in rods, there was an increase in the moment resistance of the joint, indicating the ability to redistribute internal forces to the other rows.

It is worth emphasizing that, as depicted in Figure 4.35, the failure did not involve the adhesive joint between the rod and the timber, as it solely occurred in the threaded rod (steel) due to thread galling. As discussed in Section 4.2, galling of threads occurs when the nut and threaded rod slide against each other due to tension, leading to the tearing or seizing of both materials. As a result, the tensile resistance of the connection between the threaded rod and the nut is observed to be lower than the corresponding to the tensile strength of the threaded rod obtained from coupon tensile tests. In these cases, regarding design, it is permissible to use a reduction coefficient of the tensile strength of threaded rods equal to 0.85, as proposed in EN 1993-1-8:2010.



(a) (b)

Figure 4.35. Representative failure modes for: (a) G2.t20.d12; (b) G2.t15.d14. Failure of threaded rods due to thread galling, no plastic deformations identified in end-plate and link.

The G2.t12.d16 specimens exhibited failure in the link due to the increase in the nominal diameter of the rods to 16 mm and the reduction in the end-plate thickness to 12 mm. This failure was observed without yielding lines in the end-plate, as shown in Figure 4.36. A summary of the failure modes for each of the tested joints are shown in Table 4.10.

Table 4.10. Summary of failure modes of each tested joints.

Joint	Component with greater rotations	Failure mode
G1.J1.t20.d20	Link	Link yielding and plasticization
G1.J2.t20.d20		
G1.J3.t20.d20		
G1.J4.t15.d20	End-plate/Link	End-plate yielding link plasticization
G1.J5.t15.d20		
G1.J6.t15.d20		
G2.J1.t20.d12	Bonded-in rods	Failure of threads of bonded-in rods
G2.J2.t20.d12		
G2.J3.t20.d12		
G2.J4.t15.d14		
G2.J5.t15.d14		
G2.J6.t15.d14		
G2.J7.t12.d16	Link	Link yielding and plasticization
G2.J8.t12.d16		
G2.J9.t12.d16		

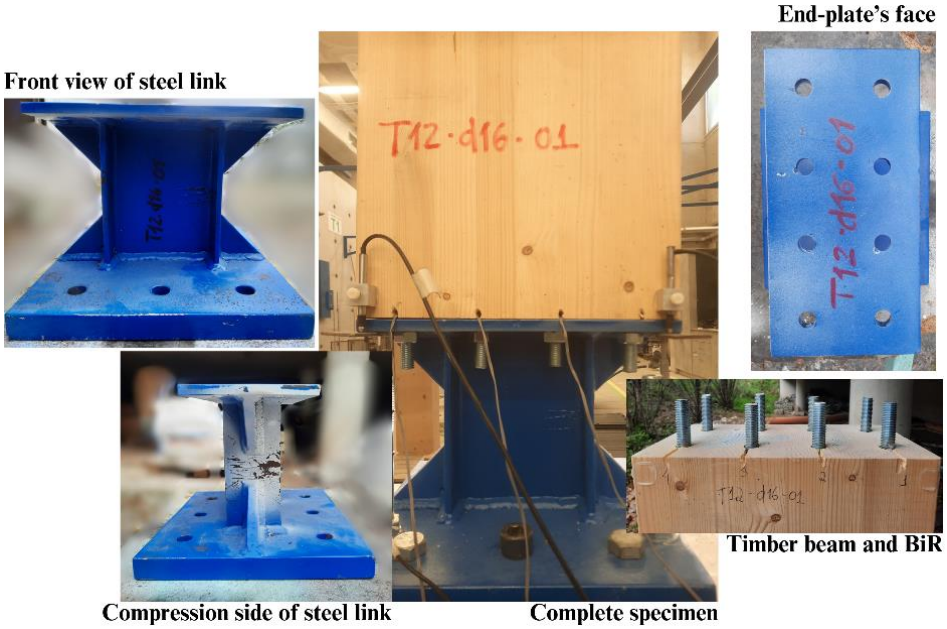


Figure 4.36. Representative failure modes for G2.t12.d16. Link yielding with no yielding lines in the end-plate and no damage in timber beam.

4.5.3.2. Individual components behavior

As discussed in Section 4.5.3.1, the failure was identified to occur either at the link or within the tension zone of the joint, indicating that this zone is pivotal in determining the joint's overall behavior. Additionally, when the failure mode of the joint is ductile and the whole joint deforms, it is necessary to identify which component reaches the yielding first or if it is occurring almost simultaneously. For

this purpose, the DIC technique was employed to accurately quantify the displacements of individual components. Specifically, the displacements of the BiR were determined by measuring the relative displacements between the timber beam and the end-plate within the tension zone. The relationship between the rotations of the joint components is shown in Figure 4.37 and 4.38 for groups 1 and 2, respectively.

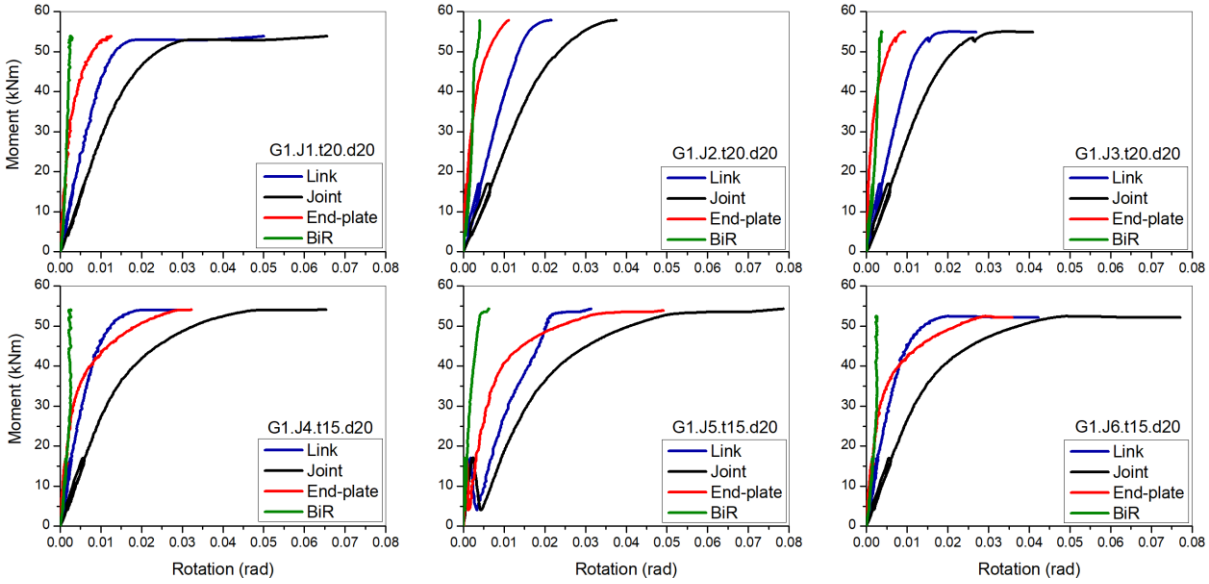


Figure 4.37. Moment-rotation curves for the primary components of the G1 joints considered individually.

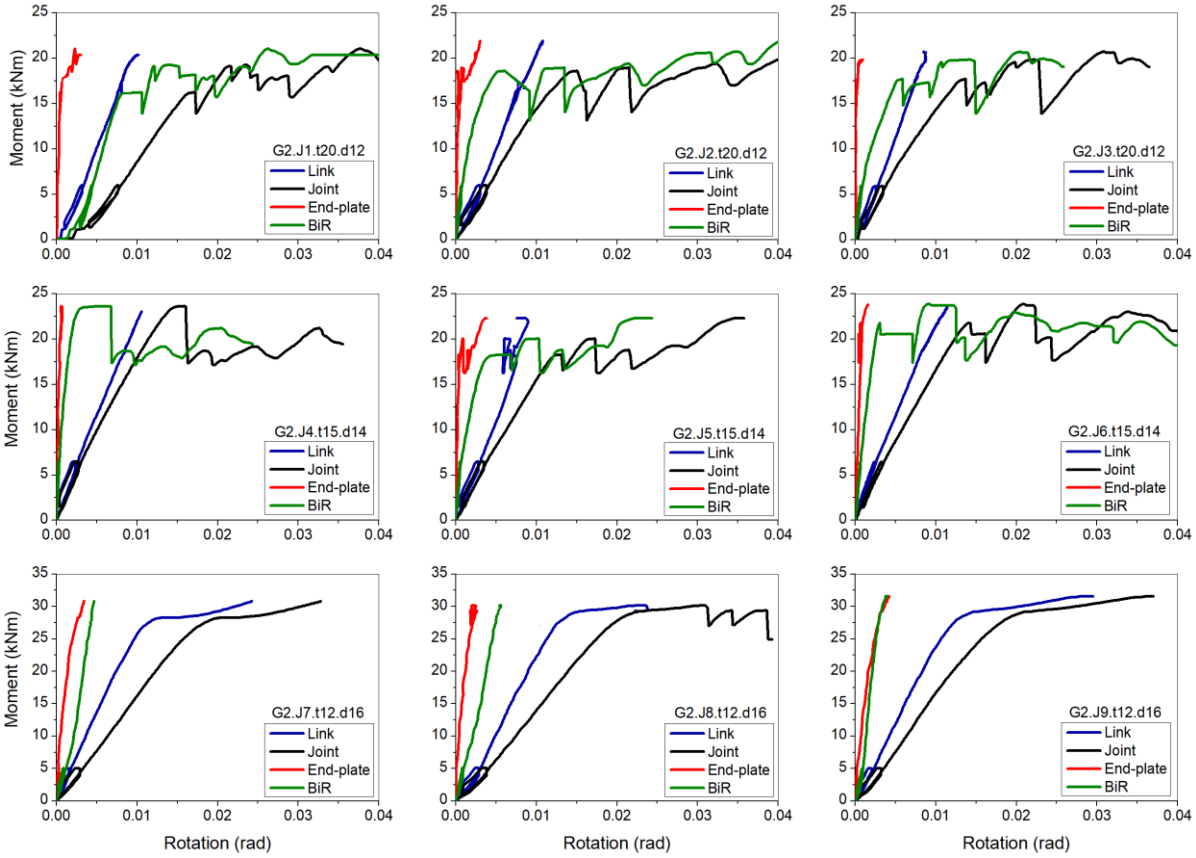


Figure 4.38. Moment-rotation curves for the primary components of G2 joints considered individually.

In the presented curves, the component that exhibits the greatest rotation prior to failure (indicated by a decrease in the curve) or enters the plastic range (characterized by pronounced nonlinearity) is the component that dictates the failure of the joint. It is possible for a specific component to not experience the greatest rotation yet still reach failure before others, as observed in joints G2.t15.d14, where failure was identified due to a clear decrease in the moment-rotation curve. Based on this information, it can be inferred that in the G1.t20.d20, the joint rotation is primarily governed by the link component, which also undergoes yielding. Conversely, the end-plate and BiR experienced significantly lower levels of rotation, remaining within the elastic range, indicating that this connection has full-strength characteristics. In contrast, in the G1.t15.d20 joints, both the end-plate and the link exhibited similar levels of rotation, making it difficult to determine which component yields first. However, despite this proximity, DIC measurements reveal that the end-plate yields first, indicating the onset of non-linearity at lower moment levels. This is followed by the yield of the link, which dictates the failure of the joint due to the plastic hinge development (horizontal plateau). Consequently, G1.t15.d20 joints can be classified as equal-strength connections.

Despite variations in end-plate thickness and BiR diameter, the G2.t20.d12 and G2.t15.d14 joints exhibited similar rotational behavior of their components. In both cases, the dominant rotations stemmed from the BiR, while the link and end-plate remained within the elastic range. Therefore, it is possible to deduce that the BiR diameter is a crucial parameter in designing these joints. It affects moment resistance and influences the joint failure mode, potentially resulting in brittle failures. Thus, this connection can be classified as partial-strength. In contrast, in the G2.t12.d16 joints, greater rotations were identified in the link, which reached yielding while the end-plate and BiR remained in the elastic range, classifying it as full-strength connection.

To gain a deeper understanding of the distribution of forces between the rods and to ascertain the location of the neutral axis of the connection, the tension forces in BiR generated by the applied moment were determined from strain gauges measurements and experimental stress-strain behavior of threaded rods in tension. The loading stages corresponding to the three curves in Figure 4.39 were defined as follows: the lowest moment is in the elastic stage; the second one is around the yield point, where the nonlinearity and partial plasticity occur; and the higher moment corresponds to a point close to the ultimate moment. The negative values mean the BiR is under compression, the positive values indicate BiR in tension and the gray dashed lines mark the position of link flange.

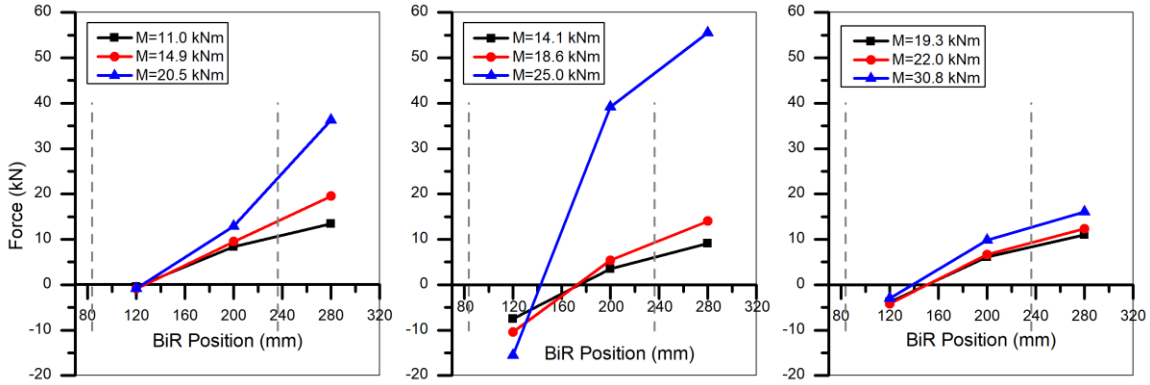


Figure 4.39. BiR tension forces generated by applied moment for (a) G2.t20.d12, (b) G2.t15.d14, (c) G2.t12.d16.

From Figure 4.39, it can be observed that, for the G2.t15.d14 and G2.t12.d16 joints, the neutral axis of the connection within the elastic range is approximately aligned with the centreline of the BiR group (between 150 and 160 mm). This alignment corresponds with the centreline of the joint when the BiR are symmetrically arranged about the centreline of the link section. Conversely, in the case of the G2.t20.d12 joints, the thicker end-plate results in lower rotations, thereby positioning the neutral axis closer to the compression side of the link flange (approximately at the 120 mm mark). In all joints, the maximum tensile force is observed in the first BiR row, while the tensile force in the second bolt row develops progressively. In the G2.t12.d16 joint, the relatively low levels of BiR forces are attributed to the reduced thickness of the end-plate, which influences the failure mode of this type of joint.

Regarding timber behavior, a comparison was made between the displacements of the timber beam (TB) and the end-plate (EP) in both the elastic and plastic ranges. The measurements were conducted utilizing the Digital Image Correlation (DIC) technique, as explained in Section 4.5.2. Based on the outcomes depicted in Figure 4.40, it is evident that the timber beam exhibited rigid body behavior in all tested specimens, indicating the absence of localized deformations in both the compressed and tensioned zones. This behavior substantiates the timber remaining within the elastic range, without undergoing significant damage.

Conversely, the end-plate exhibited different characteristics. In G1 joints, it mirrored the rotations of the timber beam in the compressed region. However, due to the displacement difference between the central part of the end-plate and its compressed end, it can be concluded that the compression from the timber led to the bending of this region of the end-plate. Additionally, the end-plate displayed significant deformations in the tensioned zone (Figure 4.40 (a) and (b)), ultimately reaching the point of yielding in the G1.t15.d20 specimens, as previously discussed. These figures clearly illustrate the behavior of the T-stub under tension and the development of prying forces.

In the G2.t20.d12 and G2.t15.d14 specimens, the end-plate visibly showcased smaller displacements compared to the timber beam, attributable to the lower stiffness of the BiR (Figure 4.40 (c) and (d)). In G2.t12.d16, the timber beam and the end-plate exhibited minimal and closely aligned vertical displacements. In this instance, the reduction in end-plate thickness and the increase in the diameter of the BiRs resulted in larger displacements within the compressed region. As the link emerged as the weakest component of the joint, this condition led to a reduction in rotation at the connection and consequently a decrease in the magnitude of the force in the BiRs (Figure 4.40 (e)).

Based on this data, it is observed that as the connection moves further into the tension zone, the neutral axis tends to shift towards the compressed region. Generally, the neutral axis of the timber beam does not align with that of the end-plate, and this discrepancy is more pronounced in joints where the rotation caused by the deformation of the BiR was more significant. Additionally, despite the use of stiffeners, the approximate neutral axis in the G1 and G2.t20.d12 tested connections was closer to the compression zone of the link flange. In G2.t15.d14 and G2.t12.d16, the neutral axis in the elastic range was situated near the centerline of the cross-section.

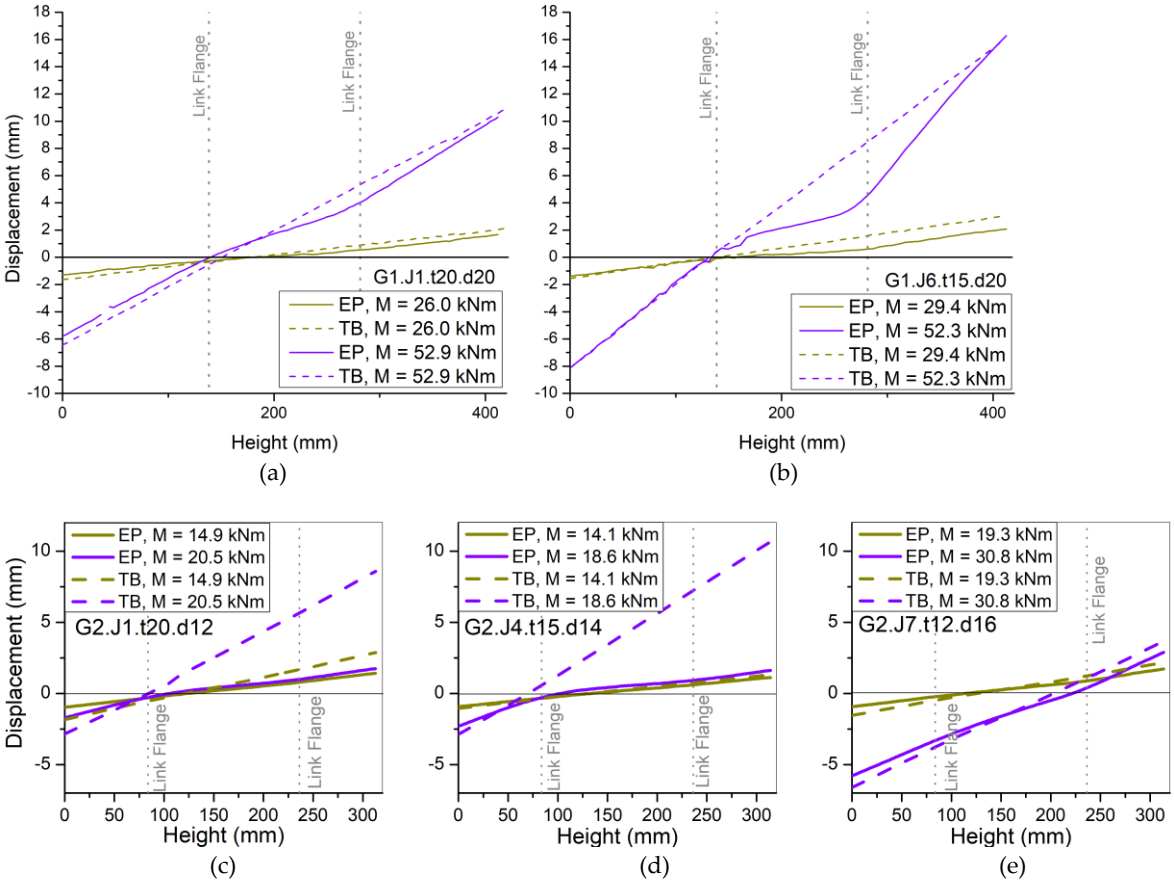


Figure 4.40. Comparisons of the TB and EP vertical displacements for (a) G1.J1.t20.d20, (b) G1.J6t15.d20, (c) G2.J1.t20.d12, (d) G2.J4.t15.d15, (e) G2.J7.t12.d16.

4.5.3.3. Joint structural behavior

While the structural behavior of the joint under investigation exhibits certain similarities to steel extended end-plate connections, it presents greater complexity due to the deformations experienced by the link, which also contribute to the overall rotation of the connection. Furthermore, the presence of timber in contact with the end-plate introduces two additional interactions: tension occurs with the bonded-in rods rather than bolts, and compression is confined to the flanges of the end-plate, lacking a supporting column behind it.

Based on the experimental results, it was found that the rotation of the link influences the position of the neutral axis of the connection. When the link rotates slightly (as in partial-strength connections), the neutral axis tends to be close to the centerline of the cross-section. In contrast, with greater link rotation, it aligns more with the compressed side. Additionally, the development of prying forces in the tension side resulted in behavior similar to that of a T-stub in tension, while the absence of these forces caused significant displacements at the tension end of timber beam. In the compressed region, the presence of a connection geometry with a free end-plate flange created a substantial compressed area between the timber beam and the end-plate, which, in some cases, led to noticeable bending of the end-plate that could result in failure of this component.

Based on the discussion, the structural behavior of this type of joint can be described by examining the relationship between the stiffness and resistance of its main components. The final rotation of the joint is determined by the deformations of all its main components (link, end-plate, timber beam and bonded-in rods). Figure 4.41 illustrates the possible rotational behaviors of the joint. When the rotational stiffness of the link is significantly lower than that of the other components, the joint can function as a "fuse." In this scenario, most of the rotation occurs in the link, with only minimal deformations observed in the others (Figure 4.41 (a)), as observed in G2.t12.16 and also pointed out by Iovane (2020). Conversely, if the end-plate exhibits the lower stiffness, only the sections of the end-plate beyond the link flanges rotate, while the central region connecting the link and end-plate experiences negligible deformations; this phenomenon was also identified by Tomasi *et al.* (2008) and Andreolli *et al.* (2011) (Figure 4.41 (b)).

It is also plausible that the bonded-in rods have a low tensile strength, resulting in the connection between the timber beam and the end-plate possessing the lowest rotational stiffness among all the components. Significant rotations occur in the timber beam in such cases, while the other parts remain unaffected (refer to failure modes for G2.t20.d12 and G20.t15.d14) (Figure 4.41 (c)). Lastly, if all the

primary components exhibit comparable stiffness, the joint displays a global behavior with significant rotations in all elements (Figure 4.41 (d)) until yielding occurs, as observed in tested joint types G1.t20.d20 and G1.t15.d20. It is worth emphasizing that failure occurs in the component with the lowest resistance, by capacity design, commonly employed in steel connections. Consequently, this criterion can classify the connection as partial, equal, or full-strength.

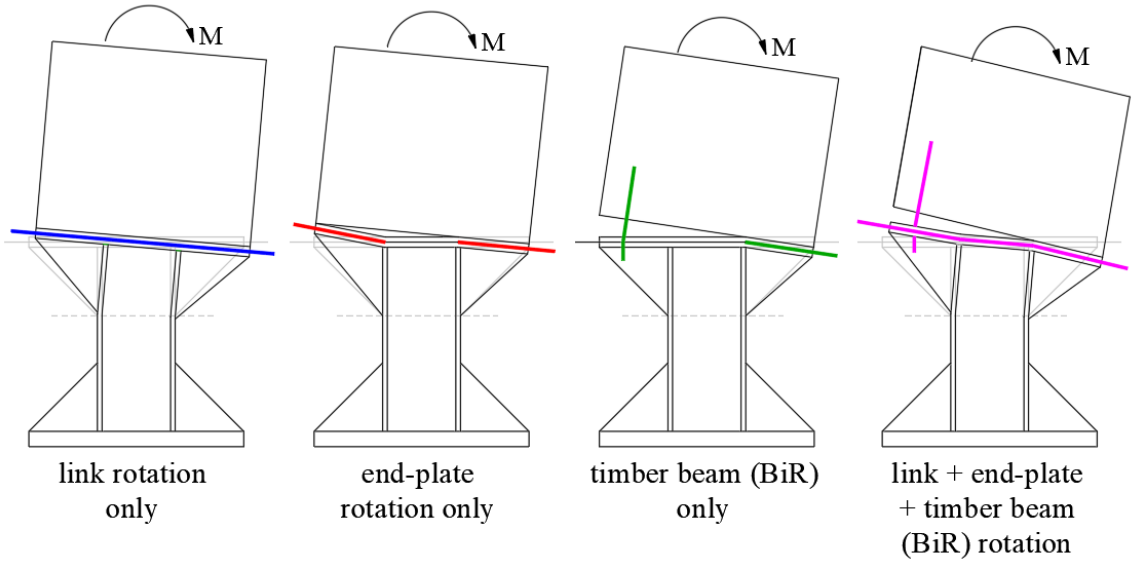


Figure 4.41. Rotational behavior of the joint subjected to bending moment (a) Link only (b) End-plate only (c) Timber beam only (BiR) (d) Link + end-plate + timber beam (BiR).

The diverse mechanical behaviors exhibited by the joint illustrate significant versatility, which can be effectively harnessed through a well-defined and reliable calculation procedure. Such a procedure would enable the designer to pre-determine the desired type of connection, ascertain the intended failure mode, and identify the essential mechanical characteristics to prioritize, such as moment resistance, initial rotational stiffness, or rotation capacity.

CHAPTER 5

ANALYTICAL PROCEDURE BASED ON COMPONENT METHOD

This chapter present a design procedure based on the component method to estimate moment resistance, initial rotational stiffness, and rotational capacity of stiffened end-plate moment-resisting steel–timber joints with steel links and multiple bonded-in rods. The study enhances the precision of initial rotational stiffness predictions by analyzing the coupled behavior of the link with other joint components and introducing new equations for timber–steel interactions. The method divides the joint into macro-components, characterizes each, and assembles them to determine overall mechanical properties. Analytical predictions are then validated against full-scale experimental results

5.1. Methodology

The joint behavior influences the distributions of internal forces and moments within a structural frame, as well as its global deformation. Landolfo *et al.* (2018) worked on design criteria to develop a clear hierarchy of strengths considering macro-components and sub-components for selected configurations of steel joints. It was proposed that a joint can be divided into macro-components that can be individually designed using the component method formulations and then simple capacity design criteria are applied to define which component will govern the joint behavior. Moreover, three design objectives were proposed to the connection with emphasis in yielding: full-strength (the connection is designed to be stronger than other macro-components, such that yielding occurs in other parts of the joint (beam or column web panel)), equal-strength (the connection is designed to have a strength close to the one of the beam or column web panel, or both), and partial-strength (the connection is designed to develop plastic deformations with its components). Based on these definitions, in this thesis, as already mentioned at the end of Chapter 3, the joints are divided into three macro-components (see Figure 3.13 (a)):

- The link, stiffened or unstiffened steel profile welded to end-plates
- The connection, composed of stiffened or unstiffened rectangular steel end-plate attached by BiRs
- The timber beam.

In this case, the connection between the link and the column was considered to be rigid. As already discussed in Chapter 4, several factors contribute to increase complexity of the structural behavior of joint in study. In this context, the deformations experienced by the link also contribute to the overall rotation of the joint. Moreover, timber in contact with the end-plate introduces two new interactions: tension occurs with the bonded-in rods rather than bolts, and compression occurs only in the flanges of the end-plate, without a column behind to provide support. Specifically regarding BiR connections, the following conditions were considered: the behavior of BiRs is not solely dependent on the failure of the steel component, it is also influenced by factors such as bondline resistance, the presence or absence of unbonded lengths, shear resistance at the interface between the adhesive and the timber, and the transverse stresses that may develop on the surface of the timber beam in the absence of unbonded lengths. Furthermore, the resistance and stiffness of bonded-in rods are generally lower than those of bolted connections, and the development of prying forces in BiRs connections exhibits distinct characteristics due to the increased bonded length compared to conventional bolts. Considering these assumptions, in this chapter, an analytical procedure based on the component method is proposed for three joint types: the unstiffened extended end-plate with two rows of BiRs (Figure 5.1 (a)), the stiffened extended end-plate with two rows of BiRs (Figure 5.1 (c)), and the stiffened extended end-plate with four rows of BiRs (Figure 5.1 (e)). Additionally, the basic components and mechanical models corresponding to these joints are depicted in Figure 5.1 (b), (d) and (f) respectively. The joint was divided into two sections: the upper section, which contained components subjected to tensile forces, and the lower section, which comprised components subjected to compressive forces. For clarification, each active component was designated as follows:

- Link in tension (lft)
- Link in compression (lfc)
- End-plate in bending under tension (ept)
- End-plate in bending under compression (epc)
- Bonded-in rods in tension (brt)
- Rib stiffener in compression (rsc).

This study outlines a calculation procedure for assessing the moment resistance, initial rotational stiffness, and rotation capacity of a specific type of joint composed of multiple macro-components that work together. A summary of the design procedure is presented in Figure 5.2. A key advancement of this research is the integration of the steel link behavior into the mechanical spring model, allowing

the coupled interaction between the link and the connection components to be explicitly considered. Furthermore, on the compression side, the contribution of the rib stiffener under compression and the end-plate in bending under compression were newly incorporated, supported by the development of new analytical equations for the latter component. This study also introduced a joint configuration with two rows of BiRs in tension, whose unbonded lengths were designed to promote ductile failure of the joint.

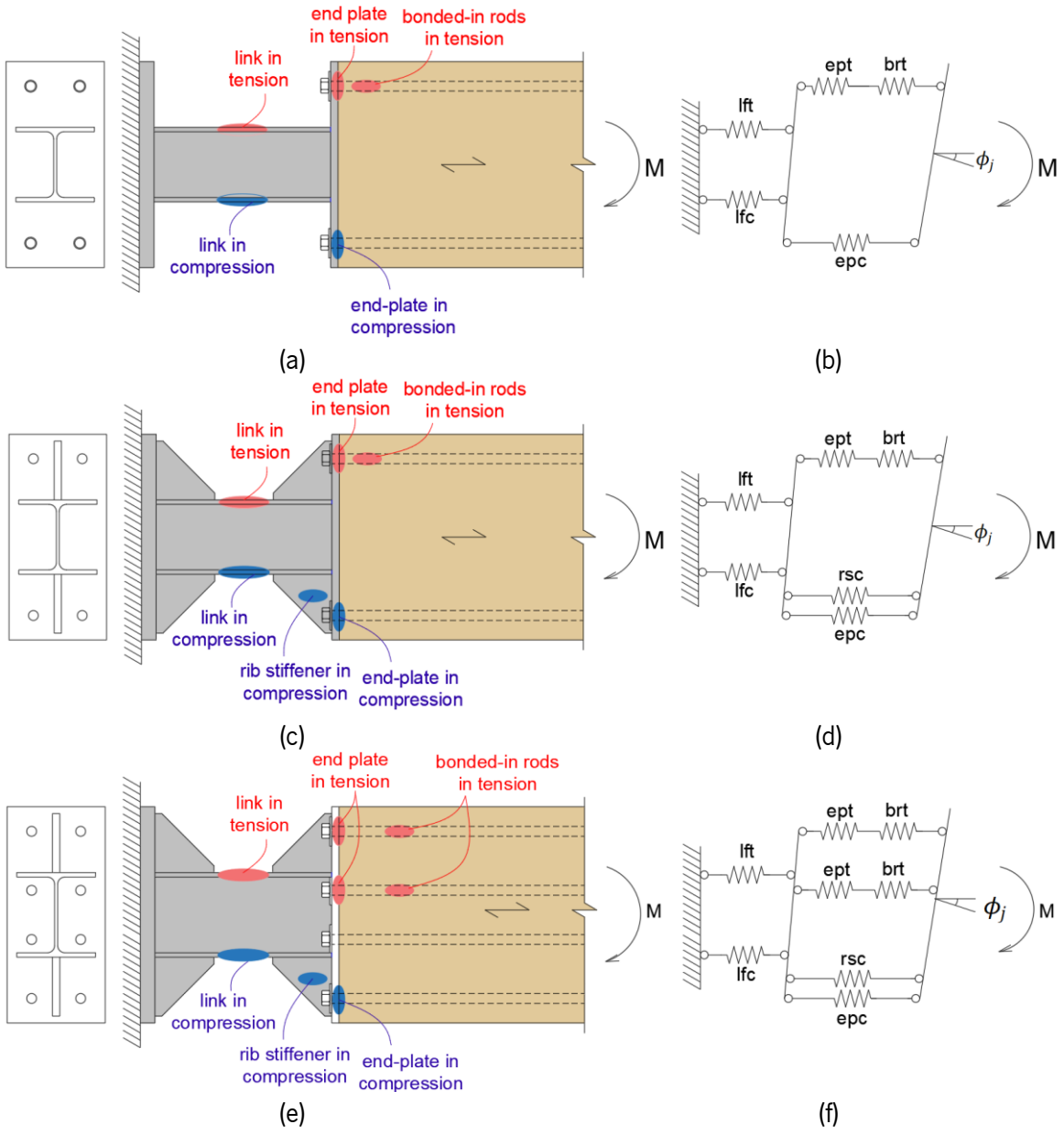


Figure 5.1. Joints' configurations and mechanical models.

To evaluate the joint moment resistance, the strengths of each active component were determined first, followed by the individual and group resistances of the BiRs, and finally the moment resistance of each macro-component. The joint moment resistance corresponds to the resistance of the weakest macro-component. It was based on the concept of capacity design (Paulay and Priestley, 1992), where

joints should be properly detailed to ensure the required global ductility of the structure and potentially brittle mechanisms, such as shear or bending failure outside the connection zone, must be prevented by checking that the timber elements have sufficient strength. Then, in this study it was considered that weakest macro-component (the one which has the lower moment resistance) yield first and then governs the failure mode of the joint. The brittle failure modes on timber beam or BiRs bondline were avoided.

For the initial rotational stiffness, the stiffness coefficients of each component (spring) were established first. These coefficients were then incorporated into a mechanical spring model to calculate the initial rotational stiffness of the macro-components. The joint's initial rotational stiffness was derived from the contributions of all macro-components. The mechanical model incorporated the behavior of steel acting with the connection components, the end-plate in bending under compression and the rib-stiffener working together in compression side, as well as two BiR rows under tension.

Regarding rotation capacity, only the deformation capacity of the weakest macro-component was determined. The capacities of the other components were calculated as partial deformation capacities based on the weakest one. The joint's rotation capacity is the sum of all these deformations, taking into account their positions within the joint geometry.

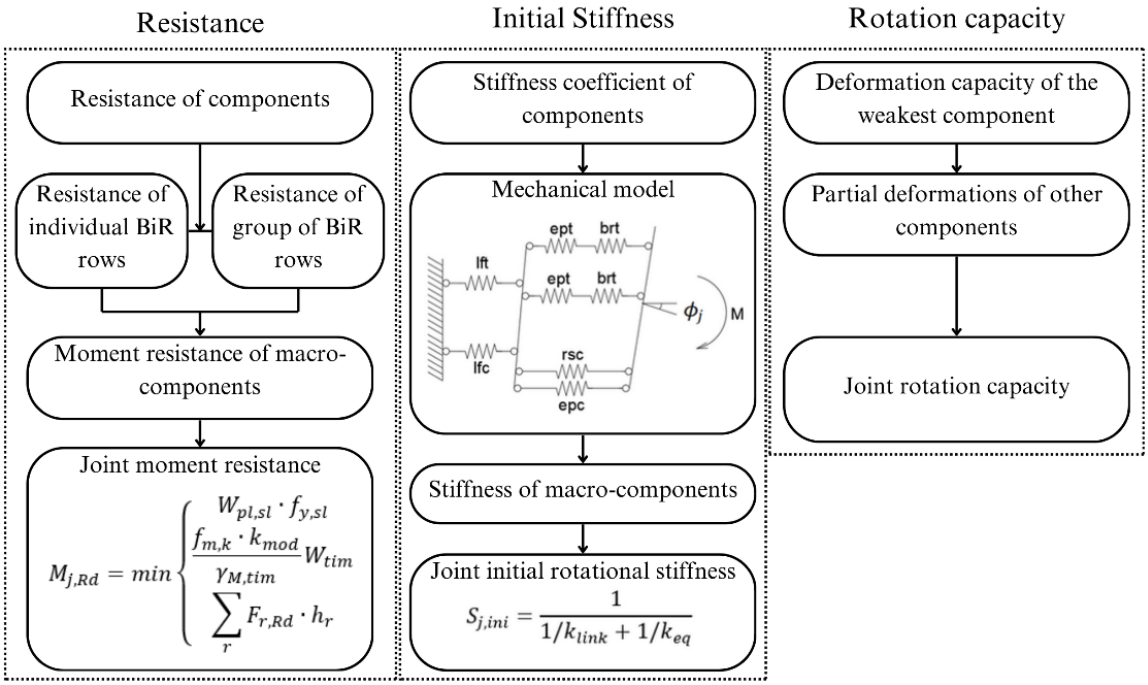


Figure 5.2. Joint design procedure flowchart.

5.2. Joint moment resistance

5.2.1. Steel link (Macro-component 1)

The moment resistance of steel link was defined based on the behavior of a steel beam under bending. In current design specifications, even if an element has a high rotation capacity, the plastic deformation capacity of a member is usually limited by instability that, in most cases, occurs before the element reaches maximum rotation capacity. Instability in flexural members includes flange local buckling (FLB) and web local buckling (WLB). EN 1993-1-1:2014 classify the cross sections in categories related to buckling: Class 1: those which can form a plastic hinge with the rotation capacity required from plastic analysis without reduction of the resistance; Class 2: those which can develop their plastic moment resistance, but have limited rotation capacity because of local buckling; Class 3: those in which the stress in the extreme compression fiber of the steel member assuming an elastic distribution of stresses can reach the yield strength, but local buckling is liable to prevent development of the plastic moment resistance; Class 4: those in which local buckling will occur before the attainment of yield stress in one or more parts of the cross-section. Typical moment–curvature relationships and bending resistances for each class are shown in Figure 5.3. Where M_u is the ultimate moment resistance, M_{pl} is the plastic moment resistance, M_{el} is the yield moment resistance, b_f is the flange free width, b is the flange width, t_f is the flange thickness, t_w is the web thickness, h_w is the height between the flanges, h is the height of the steel link.

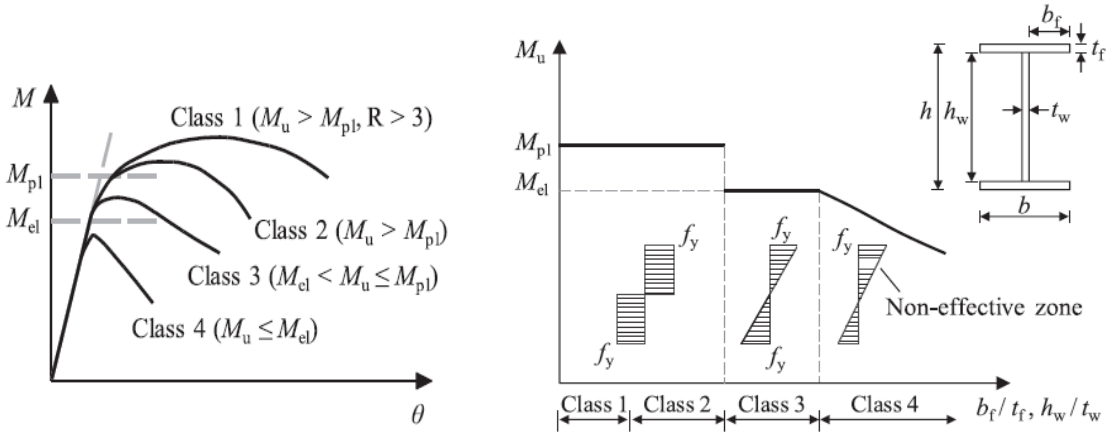


Figure 5.3. Cross-section classification and corresponding bending resistances according to EN 1993-1-1:2014 on (a) Moment-curvature for steel sections in bending; (b) Bending resistances based on classifications.

In order to achieve the maximum plastic deformation, the steel cross-section must be classified as one that can develop their maximum plastic moment resistance. In all cases, the possibility of

buckling must be checked based on cross-section classification that depends on the deformation factor (ε) (Table 5.1). For H-section subjected to bending with compression parts, the slenderness limits per class should be considered. Then, the flange outstands limiting value (λ_{FLB}) and the web in bending limiting value (λ_{WLB}) should be calculated according to Equations (5.1) and (5.2), respectively. After that, the moment capacity of the connection can be directly related to the link class, as shown in Table 5.2.

Table 5.1. Deformation factor values according to $f_{y,sl}$.

$\varepsilon = \sqrt{235/f_{y,sl}}$	$f_{y,sl}$	235	275	355	420	460
	ε	1.00	0.92	0.81	0.75	0.71

Table 5.2. Limits of classes related to flange and web buckling

	Flange outstand limiting value (c_l/t_f)	Web in bending limiting value (d_l/t_w)	Moment capacity $(M_{c,Rd})$
Class 1	9ε	72ε	$\frac{W_{pl} \cdot f_{y,sl}}{\gamma_{M0}}$
Class 2	10ε	83ε	$\frac{W_{pl} \cdot f_{y,sl}}{\gamma_{M0}}$
Class 3	14ε	124ε	$\frac{W_{el,min} \cdot f_{y,sl}}{\gamma_{M0}}$
Class 4			$\frac{W_{eff,min} \cdot f_{y,sl}}{\gamma_{M0}}$

$$\lambda_{FLB} = \frac{c_l}{t_f} \tag{5.1}$$

$$\lambda_{WLB} = \frac{d_l}{t_w} \tag{5.2}$$

where c_l is the half of the flange width less half of web thickness and the fillet radius; d_l is the clear depth between the flanges less twice the fillet radius.

Subsequently, the moment resistance of this macro-component is also grounded in the concept of the nonlinear replaceable link (NRL) as articulated by Shen *et al.* (2011) and further examined for steel-timber joints by Gohlich *et al.* (2018). The regular NRL employs an unaltered section designed

to endure a moment at its midpoint, achieving full moment plastic capacity (i.e., plastic hinge formation) at a specified distance from the column face, thereby safeguarding the brittle components of the connection. Capacity design principles are implemented to constrain the transfer of forces to the connections, columns, and foundation. The moment resistance about one principal axis ($M_{c,Rd}$) is computed as delineated in Equation (5.3).

$$M_{c,Rd} = W_{pl,sl} \cdot f_{y,sl} \tag{5.3}$$

where $W_{pl,sl}$ is the plastic steel section modulus of the steel link; and $f_{y,sl}$ is the yield strength of the steel link.

The use of this equation is aligned with the experimental results obtained in Chapter 4 for joints that behaved as full-strength connections. For typical hot-rolled steel, these joints exhibited a moment-rotation curve with a distinct horizontal plateau following yielding. As discussed in Chapter 4 and illustrated in Figure 5.4, this region corresponds to the plasticization of the link's cross-section, characterized by the formation of a plastic hinge, which occurs when all fibers of the cross-section have reached the yield strength. The figure outlines the stages of this process from the yield moment to the formation of the plastic hinge. The yield point (M_{el}) marks the end of the elastic range and the beginning of the plastic range, at which point the outer fibers of the link start to plasticize. The moment of plasticization (M_{pl}) is when the fibers on the flange have already reached plasticization, but the entire section has not yet completely plasticized. The ultimate moment (M_u) is reached when the plastic hinge is completely formed. Furthermore, considering the experimental mean yield strength of the steel of the links, the analytical results from Equation (5.3) match closely, with a difference of 2.82% for G1.t20.d20 and 0.32% for G2.t12.d16.

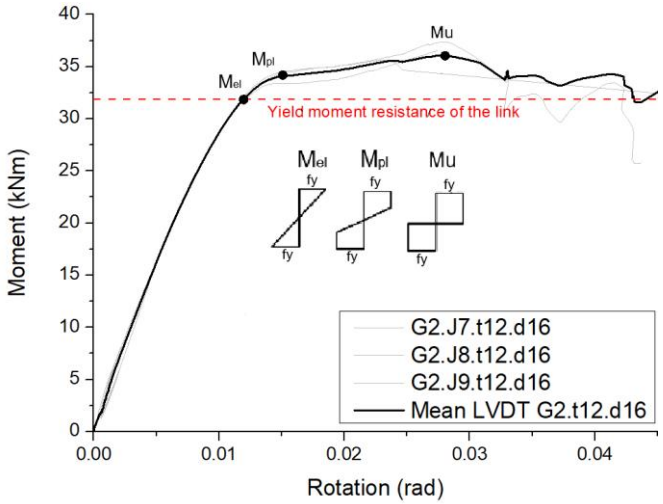


Figure 5.4. Experimental moment-rotation curves of G2.t12.d16 joints and theoretical remarks for steel link moment resistance.

5.2.2. Timber beam (macro-component 2)

The moment resistance of timber beam was defined considering the bending resistance of the cross-section under bending. The recommendations of the most recent Eurocode 5 (EN 1995-1-1:2014) were applied and the moment resistance is calculated as in Equation (5.4).

$$M_{t,Rd} = \frac{f_{m,k} \cdot k_{mod}}{\gamma_{M,tim}} W_{tim} \tag{5.4}$$

where $f_{m,k}$ is the glued laminated timber (GLT) characteristic bending strength; k_{mod} is the strength modification factor for the effect of load duration and moisture content; $\gamma_{M,tim}$ is the partial factor for timber; and W_{tim} is the elastic section modulus of the timber beam.

However, due to the inherent brittle failure of this macro-component, it is not an ideal choice for the joint failure. Therefore, to mitigate the risk of timber failure occurring prematurely in relation to the other two macro-components, an overstrength factor of 1.5 was implemented.

5.2.3. End plate to timber beam connection (Macro-component 3)

The moment resistance of end-plate to timber beam connection, hereinafter referred to as "connection", is based on the resistance of the weakest component of this macro-component. For the joint types described in Section 5.1, the moment resistance of the connection ($M_{j,Rd}$) can be determined by Equation (5.5).

$$M_{j,Rd} = F_{Rd} \cdot z \tag{5.5}$$

where F_{Rd} is the resistance of the weakest component of the connection; z is the lever arm of the internal couple.

The weakest component of the connection is calculated considering the strengths of each active component. In scenarios where multiple rows of bolts/BiRs are subjected to tension, or where the placement of active components substantially influences the moment resistance of the joint, it is essential to calculate the moment resistance based on the definition of the weakest component in each row (Equation (5.6)). This methodology is endorsed by EN 1993-1-8:2010 and has been utilized in the analysis of steel-timber joints by some researchers as Yang *et al.* (2016) and Tao *et al.* (2020).

$$M_{j,Rd} = \sum_{r} F_{r,Rd} \cdot h_r \tag{5.6}$$

where $F_{r,Rd}$ is the effective resistance of bolt-row r of the joint, which should be taken as the smallest value of the design tension resistance from the weakest component relative to bolt-row r; and h_r is the distance between each row r and the center of compression of the connection.

5.2.3.1. Resistance of bonded-in rods in tension ($F_{R,br,t}$)

Among alternatives to traditional fastenings of timber structures, joints with BiRs can provide high stiffness, load-bearing capacity, and offer aesthetic solutions by hiding the steel rods inside the timber. The complexity of the interaction of different materials in the joint (adhesive, rod, and wood) and non-linear stress distribution along the bondline present special challenges for the precise characterization of the resistance and stiffness properties relevant to the design.

From the joint's perspective, it is preferable for the end-plate and/or link to fail before the BiRs, as they commonly present greater ductility than the BiRs. However, due to the design versatility of this joint type, a designer aiming for greater initial rotational stiffness may find that BiRs failure is more suitable. Therefore, it is essential to know the resistance of the BiRs in order to identify which component has the lowest resistance in the connection.

According to Steiger *et al.* (2015), the resistance of the BiRs connections can be impacted by the many parameters: the geometry, material stiffness and strength, the loading conditions, the variability of all properties, fracture mechanical properties of timber and adhesive, even the wood species or quality control during manufacturing.

Regarding geometry, it is essential to follow the design recommendations established by several researchers (Blass and Laskewitz, 1999; Gehri, 2009; Muciaccia, 2019) and recently incorporated in prEN 1995-1-1:2022. The main geometrical features of BiRs connections are illustrated in Figure 5.5. Minimum spacing between rods (r_s) and edge-to-end distances (e_h, e_v) should be equal to the specified values, $5d$ and $2.5d$, respectively, with exceptions for BiR with an unbonded length (ℓ_{nb}) of at least 80 mm, which can reduce these spacings by 30%. The anchorage length must exceed the minimum defined by Equation (5.7), considering a maximum slenderness ratio (ℓ_b/d) of 110. Additionally, the capacity of the timber member should be assessed while maintaining a balanced stiffness between the rods and the timber, accounting for the diameters of the pre-drilled holes in the timber cross-section.

$$\ell_{b,min} = max\begin{cases}0.5 \cdot d^2 \\ 10 \cdot d\end{cases} \tag{5.7}$$

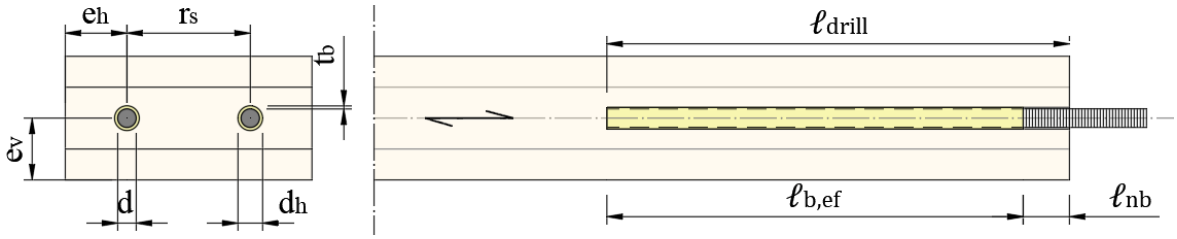


Figure 5.5. Geometrical features of BiR connections.

Several studies examined the pull-out behavior and the prediction of the BiRs connection resistance. Feligioni *et al.* (2003) found a strong correlation between the pull-out strength of BiRs and the volume of adhesive, which depends on anchorage length and bondline thickness. They concluded that bondline thickness is a crucial parameter, as it optimizes stress transfer from timber to threaded rod. Steiger *et al.* (2004) investigated the relationship between timber density and pull-out strength, demonstrating that pull-out strength is significantly influenced by the timber density around the anchorage zone, particularly for BiRs parallel to the grain. Their studies also examined the geometry of the tested samples, including anchorage length, rod diameter, and the slenderness ratio (the ratio of anchorage length to drill-hole diameter). They found a negative correlation between anchorage length and shear strength in the anchorage zone, while shear strength increased with larger drill-hole and rod diameters. In another study, Steiger *et al.* (2007) noted that glued-in rods transfer force solely at the interface between the rod and the adhesive, with load transfer between the adhesive and timber primarily governed by shear rather than compression due to indentation.

Due to a large number of relevant parameters that impact in the load-bearing capacity of BiRs connections, many different design approaches were presented in literature, but there is not a universal agreement around one specific calculation formulae. From a questionnaire with professionals, Stepinac *et al.* (2013) defined the following equations as the most used calculation methods. The most commonly applied were DIN:1052:2008, EC5:Annex C (discontinued), and CNR-DT-206 Italian Code (Ricerche, 2018). The equations proposed are following detailed:

I) DIN 1052 (2010) and CNR DT 206 (2007): $R_{ax,d} = \pi \cdot d \cdot \ell_{ad} \cdot f_{k1,d}$

II) Eurocode 5, Annex C (2001): $R_{ax,d} = \pi \cdot d_{equ} \cdot \ell_a \cdot f_{v,\alpha,k}$

III) GIROD (2003) (Bengtsson and Johansson, 2002): $P_f = \tau_f \cdot \pi \cdot d \cdot \ell \cdot \frac{\tan \omega}{\omega}$

IV) Steiger et al. (2007) (Steiger, Gehri and Widmann, 2007): $F_{ax,mean} = \pi \cdot d_h \cdot \ell \cdot f_{v,0,mean}$

Where $R_{ax,d}$, P_f is the characteristic axial resistance. $F_{ax,mean}$ is the mean axial resistance. ℓ, ℓ_{ad}, ℓ_a is the glued-in length/effective anchorage length. d is the nominal diameter of rod. d_h is the

diameter of drilled hole. d_{equ} is the equivalent diameter. ω is the stiffness ratio of the joint. τ_f is the local bondline shear strength. $f_{v,\alpha,k}$, $f_{k1,d}$ is the shear strength of the wood at the angle between the rod and grain direction/ value of bond line strength. $f_{v,0,mean}$ is the nominal shear strength of single axially loaded rod parallel to the grain. Meanwhile, the model presented by Aicher *et al.* (1999) for the resistance of the bondline has been applied to recent studies and provided accurate results. According to this method, the mean pull-out capacity can be calculated using Equation (5.8).

$$F_{R,br,t} = \pi \cdot d_h \cdot \ell_{b,ef} \cdot f_{v,mean} \tag{5.8}$$

with d_h (mm) as the diameter of the drilled hole and $f_{v,mean}$ calculated as in Equation (5.9)

$$f_{v,mean} = min\begin{Bmatrix} 8 \\ 129 \cdot d^{-0.52} \cdot \lambda^{-0.62} \cdot \left(\frac{\rho}{480}\right)^{0.45} \end{Bmatrix} \tag{5.9}$$

λ as the slenderness ratio of the rod.

Recently, prEN 1995-1-1:2022 introduced equations that incorporate some of that key studies. According to this standard, the axial resistance of the BiRS in tension ($F_{R,br,t}$) can be calculated as shown in Equation (5.10). The first two equations are associated with the resistance of the steel threaded rods, while the remaining ones are related to the resistance of the bondline of BiR connections.

$$F_{R,br,t} = min\begin{Bmatrix} A_{s,br} \cdot f_{yk,br} \\ 0.9 \cdot A_{s,br} \cdot f_{uk,br} \\ \pi \cdot d \cdot \ell_{b,ef} \cdot f_{vr,k} \\ E_s \cdot A_{s,br} \cdot \varepsilon_{u,timber} \end{Bmatrix} \tag{5.10}$$

where $f_{y,br}$ is the characteristic yield strength of the threaded rod, $f_{u,br}$ is the characteristic ultimate strength of the threaded rod, $A_{s,br}$ is the nominal area of threaded rod cross-section and $\ell_{b,ef}$ is the effective anchorage length can be found by Equation (5.11).

$$\ell_{b,ef} = min\begin{Bmatrix} \ell_b \\ 40 \cdot d \\ 1000\ mm \end{Bmatrix} \tag{5.11}$$

where ℓ_b is the adopted glued length based on $\ell_{b,min}$; $f_{vr,k}$ is the characteristic bondline strength; and $\varepsilon_{u,timber}$ is the failure strain of the timber parallel to grain. For softwood timber, it can be equal to 2,4 ‰.

Simply applying these equations does not always lead to accurate predictions of the failure mode of BiRs, especially when a ductile failure mode is desired due to tensile failure of the threaded rod. Single BiRs axially loaded parallel to the grain can exhibit several failure modes, which may occur in the wood substrate, the rod, the adhesive, or at the wood-adhesive or rod-adhesive interfaces (Tlustochowicz *et al.*, 2011). The following failure modes (Figure 5.6) are the main ones commonly considered:

a) Tensile failure of the rod

b) Compression (buckling) failure of the rod

c) Failure of the adhesive within the glue line or in the bondline with the rod and/or timber

d) Shear failure of the wood adjacent to the bondline

e) Splitting of the wood starting from the bonded-in rods

f) Plug shear failure of the wood in a joint with several bonded-in rods

g) Net tension failure of the wood et the end of the rod.

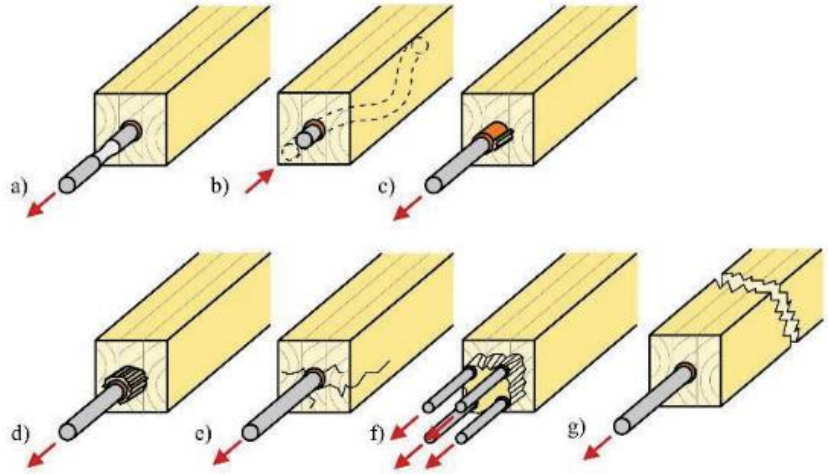


Figure 5.6. Failure modes of axially loaded BiRs (Jockwer *et al.*, 2023).

Several authors have explored this topic, and some recommendations can be found in the literature. Steiger *et al.* (2007) indicated that plastic deformation of the steel threaded rods can occur only if there is sufficient free length to allow for elongation. To achieve this, a portion of the rod, referred to as the length for plastic elongation (L_{pl}), should remain unbonded and may also be necked down to a slightly smaller diameter, as shown in Figure 5.7. Steiger *et al.* (2007) recommended an unbonded length equal to or greater than 5 times the outer diameter of threaded rod, to reduce the risk of splitting on the wood surface in contact with the BiRs and allow plastic deformation.

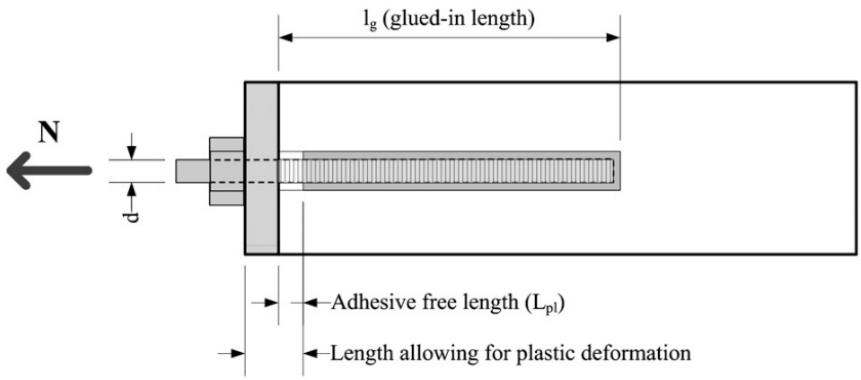


Figure 5.7. Main lengths to allow plastic elongation of BiRs.

In this context, a patented connection system called GSA was developed by ASTORit AG in Switzerland. This system ensures steel plasticization by necking down the rods in high-stress areas. Consequently, plasticization will occur only in the necked section, avoiding the nut and the bonded length. By adjusting the length of the unbonded section, it is possible to control the ductility of the connection using the Equation (5.12).

$$\Delta l_p = \left(\varepsilon_u - \varepsilon_y\right) \cdot L_{pl} \tag{5.12}$$

where Δl_p is the plastic elongation of the rod, ε_u is the ultimate strain of the rod, ε_y is the yield strain of the rod

Parida *et al.* (2013) suggested that to achieve plasticization, the yield strength of steel threaded rods should be lower than the pull-out strength of bondline. They also indicated that lower steel grades of threaded rod can help to achieve ductile behavior easily. These conclusions were obtained from a study made with BiRs with different steel grades, diameters and slenderness ratio λ (glued length/diameter). The main results are presented in Figure 5.8. In summary, if the predicted pull-out strength of the BiR connection is in Zone I, the connection should fail by shear failure of the wood adjacent to the bondline, which means that the pull-out capacity was reached before any plasticization of rods occurs and the failure was brittle. To achieve plasticization, the yield strength of rods should be lower than the pull-out strength. In this case, the predicted pull-out strength will be in Zone II, which indicates that the steel threaded rod would plasticize, but the ultimate failure would be brittle by shear in wood. Last, the location of a diamond representing the pull-out strength in Zone III indicates that the steel threaded rod would fail in a ductile manner in tension with plasticization and without a final pull-out of the rod.

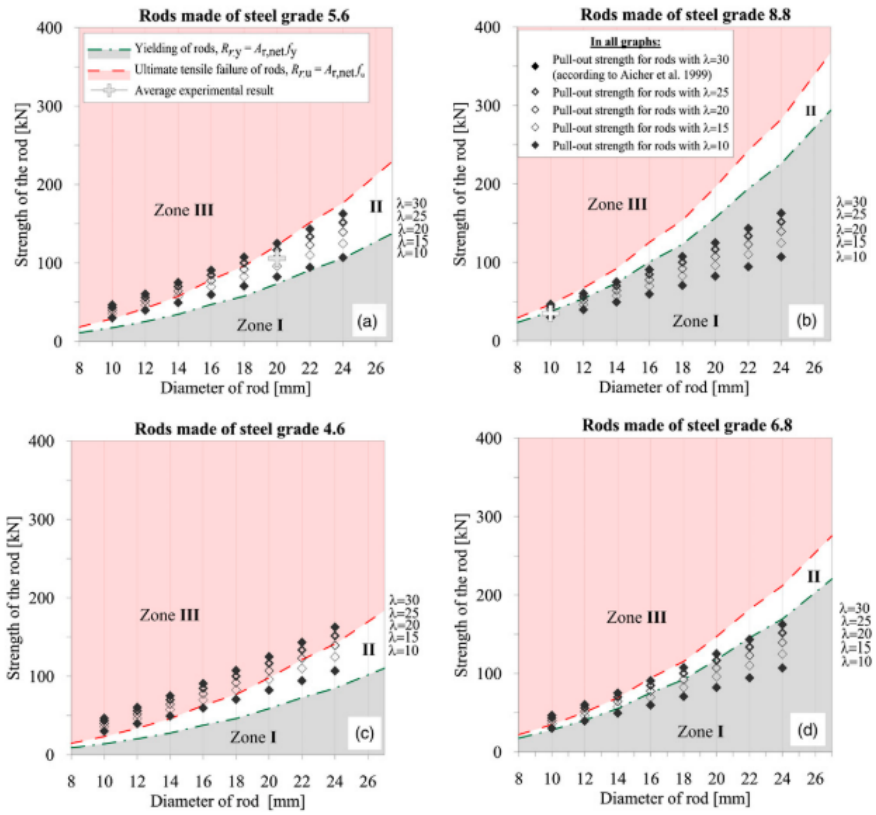


Figure 5.8. Analytical comparison of prediction of BiR failure (Parida, Johnsson and Fragiacomo, 2013).

Bouchard *et al.* (2021) emphasized the importance of considering the variability of strengths of BiRs elements for accurately assessing load-carrying capacity and identifying governing failure modes. For instance, wood, adhesive, and bondline exhibit significant variability in load-carrying capacity and susceptibility to brittle failure modes. In contrast, mild-steel rods demonstrate predictable ductile failure through yielding, especially when the quality of the steel is controlled. Consequently, different partial safety factors are applied to various failure modes in the design process. Figure 5.9 illustrates this design philosophy and qualitatively highlights the differences between the strengths of these materials.

The strength distribution of the mild steel rods is represented in grey, while the pull-out resistance is shown in orange. When the yield failure mode governs the design, the bondline strength is underutilized but remains capacity protected. Ductile failure is achievable when the design resistance of a mild steel rod is significantly lower than the pull-out resistance it can provide. While joints with high-strength rods of the same size may exhibit greater strength, they are more susceptible to brittle failures.

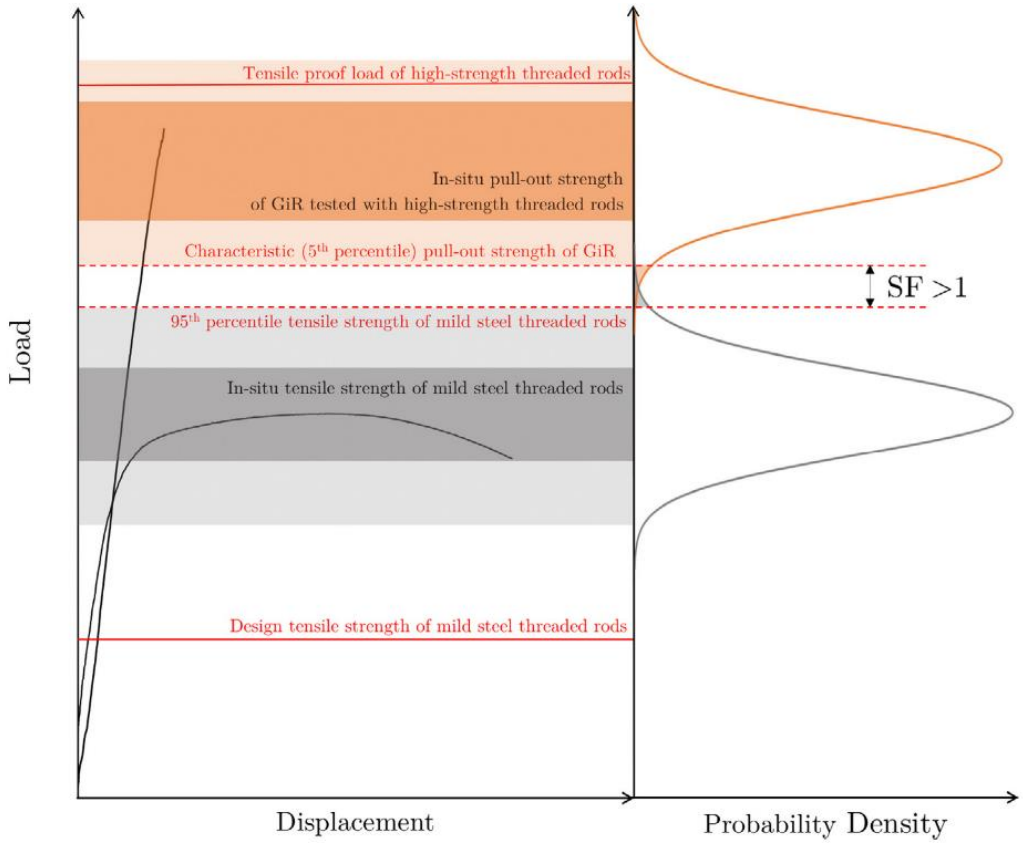


Figure 5.9. Design philosophy of ductile BiR failure mode (Bouchard *et al.*, 2021).

More recently, the prEN 1995-1-1:2022 indicated that ductility can be achieved by ensuring that the ductile failure of the bonded-in rod occurs prior to the brittle failure of the bondline and any other brittle failure modes in the timber. For this, the design value of the bondline resistance should be equal or greater than 1.5 times the design value of the tensile resistance of the steel rod.

In the design procedure proposed in this thesis, the focus was on determining the component's resistance to prevent brittle failure in the connection. To achieve ductile failure in the BiRs, Equation (5.10) was used, prioritizing tensile failure in the threaded rods as the lowest resistance value. Due to the variability in the mechanical properties of the materials, experimental tests conducted on the BiRs and threaded rods (Chapter 4) served as a reference for determining the strength of this component. The results of the tensile tests on the steel threaded rods (Section 4.2) revealed that the ratio between the experimental ultimate force ($P_{u,mean}$) and the theoretical ultimate force (F_{ud}) reached a maximum of 1.30, indicating that the ultimate forces obtained experimentally were 30% greater than those predicted analytically. From this, a Limit Fu value equal to 1.3 times Fu was established, as shown in Table 5.3. Given that the most significant failure modes are the tensile failure of the rod and the shear failure of the bondline, to ensure the ductile tensile failure of steel threaded rod, a safety factor of at

least 1.2 was applied between the theoretical resistance of the bondline ($F_{R,br,t}$), calculated using Equation (5.8), and Limit Fu.

It is important to note that the determination of connection resistance (macro-component 3) does not depend solely on the resistance of this component, i.e., even if ductile failure is ensured in the BiRs, the distribution of forces to them is carried out by other components of the connection. Thus, in practice, in a joint under moment, the greatest tensile forces in the BiRs will occur in those furthest from the neutral axis, but other components may fail first, leading to an uneven distribution of forces to the BiRs.

Table 5.3. Relationship between analytical and experimental resistance of BiRs

Specimen	$P_{u,mean}$ (kN)	CoV (%)	F_{ud} (kN)	$\frac{P_{u,mean}}{F_{ud}}$	Limit Fu	$F_{R,br,t}$ (kN)
M12	39.56	3.55	30.348	1.30	39.452	75.566
M14	53.5	1.05	41.544	1.29	54.007	83.145
M16	68.51	5.19	56.412	1.21	73.335	90.321

5.2.3.2. Resistance of steel end-plate in bending under tension ($F_{R,ep,t}$)

The resistance and failure modes of the end-plate in bending under tension can be derived from EN 1993-1-8: 2010, using the equivalent T-stub flange approach. It is important to note that EC3 emphasizes that application of equivalent T-stub in tension is for bolted connections, but there are some applications for BiRs connections that have obtained consistent results for prediction of the joint moment resistance using this approach (Tomasi *et al.*, 2008; Andreolli *et al.*, 2011; Yang *et al.*, 2016; He *et al.*, 2020). Furthermore, this analysis focuses solely on one possible failure modes of BiRs, specifically tensile failure of steel threaded rod. Other failure modes of BiRs were also considered in the calculation procedure, using the methodology described in section 5.2.3.1.

The resistance of equivalent T-stub in bending under tension ($F_{R,ep,t}$) is the minimum resistance of four possible failure modes. In Mode 1 (Yielding of the flange, $F_{T,1}$) the resistance is associated with the formation of a plastic yield mechanism in the flange. The failure occurs with the formation of four plastic hinges. In such a case, the BiRs are sufficiently strong to resist the applied axial tension forces, including the prying forces. Mode 2a (Tensile failure of steel threaded rods further to a partial yielding of the flange, $F_{T,2}$) mixed failure is achieved through the formation of yield lines in the flange (the full plastic mechanism being not reached) and the failure of the steel BiRs in tension (again

including prying effects). Mode 2b (Failure of the flange without prying forces, $F_{T,1-2}$) in this case the deformability of the BiRs is so high that prying forces cannot develop, and the failure of the end-plate occurs with the formation of two plastic hinges only. Finally in Mode 3 (Failure of the bolts, $F_{T,3}$) the resistance is linked to the failure of the BiRs in tension. The deformation of the flange in bending is small, resulting in an absence of prying effects.

A schematic representation of all the previously mentioned failure modes is presented in Figure 5.10. Equations (5.13), (5.14), (5.15), and (5.16) can be used to calculate the resistance of the component for each possible failure mode respectively. For unstiffened end-plate extension, m_x must be used instead of m, while for the second rod row m_2 must be used.

$$F_{T,1,Rd} = \frac{(8 \cdot n - 2 \cdot 0.25 \cdot d_w) \cdot M_{pl,1,Rd}}{2 \cdot m \cdot n - 0.25 \cdot d_w \cdot (m + n)} \tag{5.13}$$

$$F_{T,2,Rd} = \frac{2 \cdot M_{pl,2,Rd} + n \cdot \sum F_{t,Rd}}{m + n} \tag{5.14}$$

$$F_{T,1-2,Rd} = \frac{2 \cdot M_{pl,1,Rd}}{m} \tag{5.15}$$

$$F_{T,3,Rd} = \sum \frac{0{,}9 \cdot f_{u,br} \cdot A_{s,br}}{\gamma_{M2}} \tag{5.16}$$

where γ_{M0} is the partial coefficient; γ_{M2} is the partial coefficient; L_{ex} is the vertical distance between the end-plate and the link; w is the horizontal distance between rods centrelines; p is the distances between rods rows centerlines, subscripts in numbers refer to each row; b_p is the end-plate width; b_c is the column flange width; d_w is the diameter of the washer; t_{ep} is the end-plate thickness; $f_{y,ep}$ is the yield resistance of end-plate; $f_{u,br}$ is the ultimate resistance of bonded-in rod (see Section 5.2.3.2); $A_{s,br}$ is the nominal stress area according to EN ISO 898-1 for threaded rods; t_{wb} is the beam web thickness; t_{wc} (mm) is the column web thickness; s_f is the weld leg length ($s = a_w \cdot \sqrt{2}$, where a_w is the weld throat); r_c is the fillet radius of the rolled section; m is the geometric parameter (see Table 5.4); m_x is the geometric parameter, $m_x = L_{ex} - e_x - s_f$; m_2 is the geometric parameter, $m_2 = p - t_f - L_{ex} - e_x - s_f$; and n is the geometric parameter, $n = e$, if $n \leq 1.25 \cdot m$.

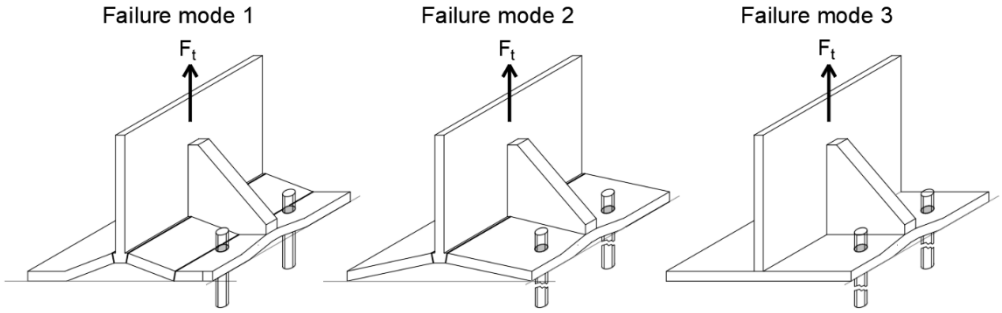


Figure 5.10. General failure modes of stiffened extended end-plate joint.

The moment for plastic hinge formation is defined as shown in Equations (5.17) and (5.18). To calculate the ultimate resistance of this component, $f_{u,ep}$ was used instead of $f_{y,ep}$, in Equations (5.17) and (5.18).

$$M_{pl,1,Rd} = \frac{0{,}25 \cdot \ell_{eff,1} \cdot {t_{ep}}^2 \cdot f_{y,ep}}{\gamma_{M0}} \tag{5.17}$$

$$M_{pl,2,Rd} = \frac{0{,}25 \cdot \ell_{eff,2} \cdot {t_{ep}}^2 \cdot f_{y,ep}}{\gamma_{M0}} \tag{5.18}$$

where $\ell_{eff,1}$ is the minimum effective length from circular and non-circular patterns; $\ell_{eff,2}$ (mm) is the minimum effective length from non-circular patterns.

The effective length (ℓ_{eff}) was calculated based on Brown *et al.* (2013). There is a clear differentiation between the possible yield patterns formations for the unstiffened and stiffened end-plate, and these effective length equations are shown in Table 5.4 for bolt-row acting alone in equivalent T-stubs. To determine the effective length of specific yield patterns of stiffened end-plates it also necessary to calculate the parameter α, Figure 5.11 can be utilized, alongside the calculation of the geometrical parameters λ_1 and λ_2, as shown in Equations (5.19) and (5.20).

$$\lambda_1 = \frac{m}{m + e} \tag{5.19}$$

$$\lambda_2 = \frac{m_x}{m + e} \tag{5.20}$$

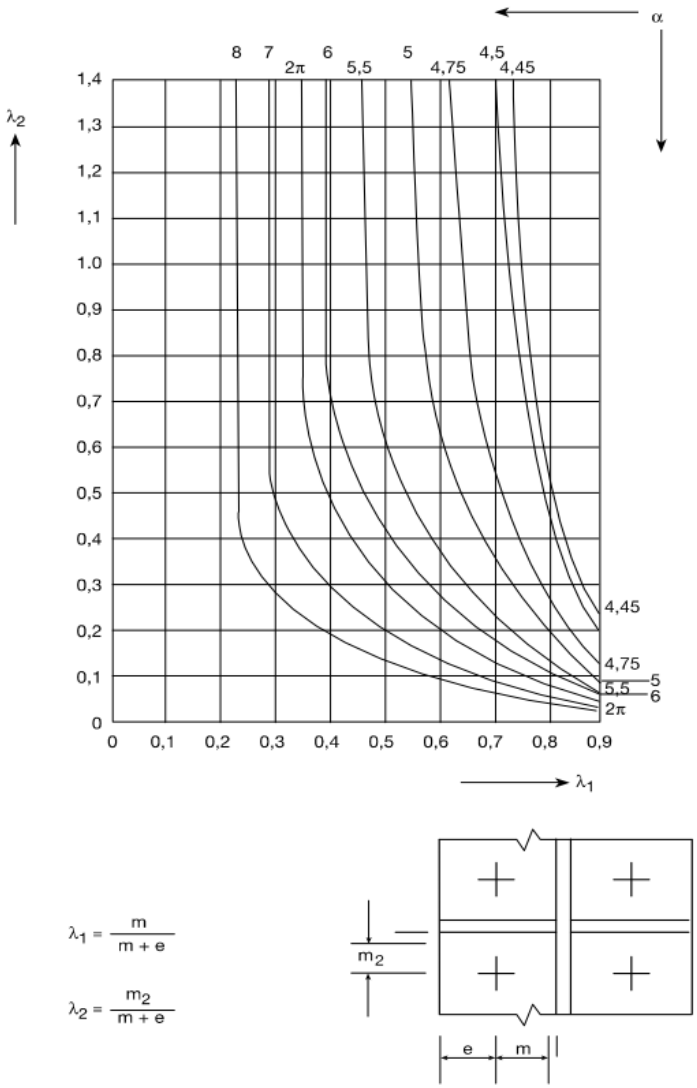


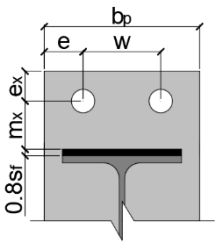
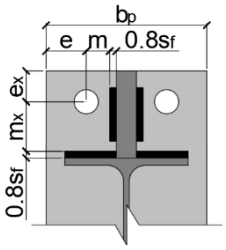
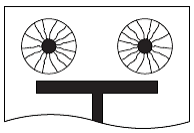
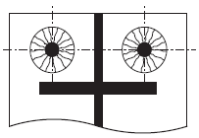
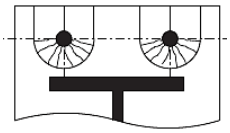
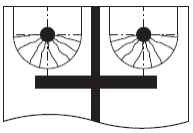
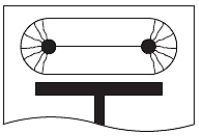
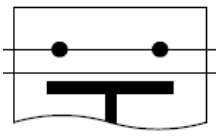
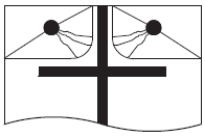
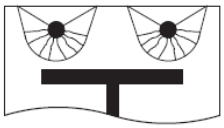
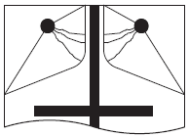
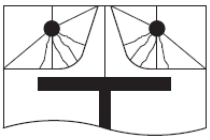
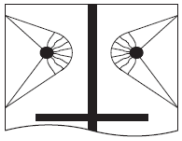
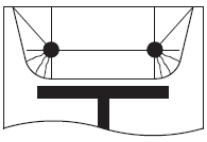
Figure 5.11. Values of α for stiffened end-plates (EN 1993-1-8:2010).

In addition, to determine the failure mode of connection, it is necessary to check the presence of prying forces. The value of elongation length is important as it influences the rods stiffness and the development of prying forces between the end-plate and the surface that it is in direct contact. According to Wald et al. (2008), the presence of prying forces can change the failure mode of T-stub in a steel base plate with anchor bolts connected to a concrete base, and the bolt elongation length must be limited to define the boundary of prying action equal to zero (failure mode 2). According to EN 1993-1-8:2010, if $L_b < L_b^*$, there is development of prying force. L_b^* is the limit of elongation length defined in Equation (5.21).

$$L_b^* = \frac{8{,}8 \cdot {m_x}^3 \cdot A_{s,br} \cdot n_b}{\Sigma \ell_{eff,1} \cdot {t_{ep}}^3} \tag{5.21}$$

where n_b is the number of BiR-rows.

Table 5.4. Equations for effective lengths in unstiffened and stiffened end-plate extension.

Pair of bolts in an unstiffened end-plate extension		Pair of bolts in a stiffened end plate extension	
			
Circular patterns ($\ell_{eff,cp}$)			
	Circular yielding $2\pi m_x$		Circular yielding $\ell_{eff,cp} = 2\pi m$
	Individual end yielding $\pi m_x + 2e_x$		Individual end yielding $\ell_{eff,cp} = \pi m + 2e_x$
	Circular group yielding $\pi m_x + w$		
Non-circular patterns ($\ell_{eff,nc}$)			
	Double curvature $0.5b_p$		'Corner yielding $\alpha m - (2m + 0.625e) + e_x$
	Individual end yielding $4m_x + 1.25e_x$		Corner yielding away from the stiffener/flange (m_x large) $2m + 0.625e + e_x$
	Corner yielding $2m_x + 0.625e_x + e$		Side yielding (m_x and e_x large) $4m + 1.25e$
	Group end yielding $2m_x + 0.625e_x + \frac{w}{2}$		

Regarding the determination of the elongation length (L_b), it was observed that the connection between the steel end-plate and the timber beam utilizing BiRs exhibits behavior closer to that of the steel base plate with anchor bolt connections. However, the current propositions based on the study

conducted by Wald *et al.* (2008) yield inadequate values, as the BiRs connection possesses unique characteristics, notably the presence of a free length that allows plastic deformation. Consequently, this study introduces a novel equation that defines the elongation length as the sum of the free length L_{bf} and the effective embedded length L_{be}, as illustrated in Equation (5.22) and Figure 5.12.

$$L_b = \ell_{b,min} + \ell_{nb} + t_{ep} + S_w + \frac{S_n}{2} \tag{5.22}$$

where ℓ_{nb} is the unbonded length; S_w is washer thickness; and S_n is the nut thickness.

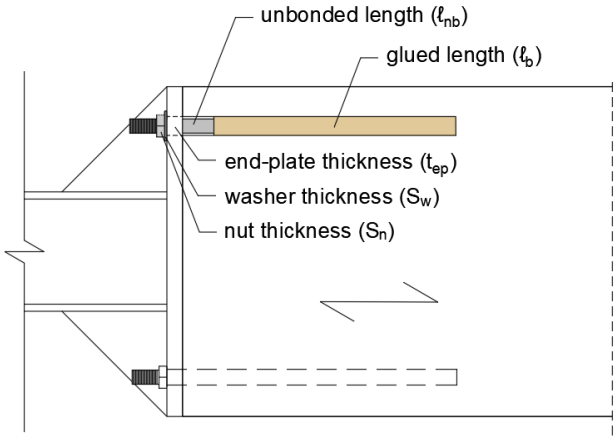


Figure 5.12. Elongation length for bonded-in rods connected to end-plate.

The effective embedded length can be equal to the glued length (ℓ_b), but considering the minimum anchorage length $\ell_{b,min}$ that should be taken as shown in Equation (5.7). Then, for component method application to BiRs, it is coherent to use L_{be} equal to ℓ_b, but respecting the value of $\ell_{b,min}$.

5.2.3.3. Timber beam and end-plate in compression ($F_{R,ep,c}$)

Other researchers have identified T-stub behavior in compression in studies of joints with similar geometry (Tomasi *et al.*, 2008; Andreolli *et al.*, 2011). However, the experimental campaign conducted revealed that, depending on the free length of the end-plate's flange, the flexural behavior of the end-plate ends due to compression was significant. This behavior occurs because, unlike steel connections where a column supports the compression and prevents end-plate bending, the joints under study allow the flanges to rotate freely. It is hypothesized that this effect becomes more pronounced with longer flanges and thinner end-plates.

Considering that the joint in question has a symmetrical geometry, and that experimental results indicate the neutral axis of the connection is near the centerline between the link flanges in the elastic range, it is reasonable to conclude that the neutral axis is located along this centerline.

To model the behavior of the contact between the timber beam and the end-plate under compression, a triangular load resulting from the moment in the contact area between these elements was considered, as illustrated in Figure 5.13. The position of the equivalent load of this triangular area influences the behavior of the compression zone. If the equivalent load was positioned within the link flange thickness, the behavior of the component is associated with the steel T-stub compressing timber parallel to the grain and its resistance can be calculated as described in Section 5.2.3.3a. On the other hand, if the position falls outside of this region, the end-plate behaves as a flat beam experiencing bending due to the presence of the free length between the outer face of the link flange and the edge of the end-plate. In this case, its resistance can be determined as explained in Section 5.2.3.3b.

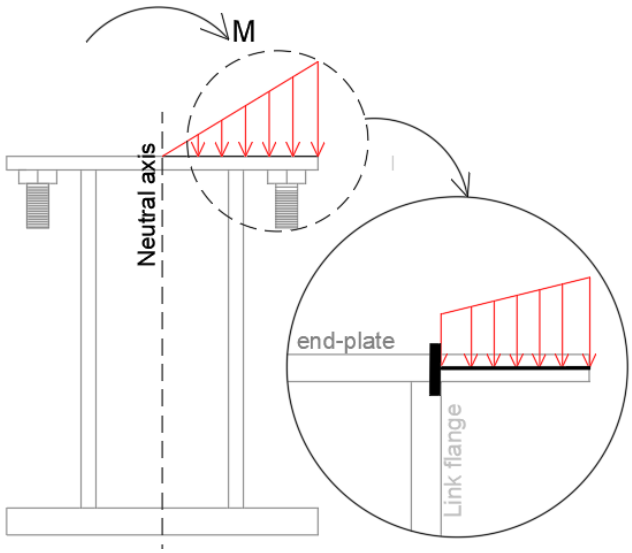


Figure 5.13. Analytical load distribution between the timber beam and end-plate and idealized cantilever of end-plate.

a) Equivalent T-stub in compression approach

The interaction between steel and timber in connections can be found in several projects of the area, but the behavior of the steel T-stub compressing timber parallel to the grain component is quite specific. The “T-stub” is a geometric idealization of a region of the steel beam composed of the flange in tension or compression and the end-plate in bending. The use of the T-stub has the advantage that the different steel plated components in bending may be studied with the same model. But the well characterized behavior of the T-stub is not enough, as the timber also has an important role in this

component. Currently, considering both materials working together, there is no specific approach in the literature to characterize this component. Some research has been based on the equations of the base plate in bending and concrete in compression component addressed in the EN 1993-1-8:2010 to design steel to timber joints (Vašek and Vyhnálek, 2006; Tomasi *et al.*, 2008; Andreolli *et al.*, 2011). The equations recommended by EN 1993-1-8:2010 are based on the equivalent T-stub in compression approach, where the flexible base plate is modelled as a rigid plate of equivalent area compressing a concrete block. The stresses between the plate and the concrete are assumed to be uniformly distributed on a fictitious rigid equivalent plate (Stockwell, 1975; Murray, 1983; Steenhuis *et al.*, 2008). The equivalent area, also known as the effective area, varies depending on the loading pattern. The size of the effective area changes based on the amount of compression and bending moment that the joint experiences. Figure 5.14 illustrates a qualitative representation of the effective area for a flexible plate, demonstrating how the T-stubs can be determined for three different loading patterns. When the joint is only subjected to pure compression force (Figure 5.14 (a)), one T-stub is built up under the web and two T-stubs are built up under the flanges to form the equivalent area. When there is a bending moment, the effective area is limited to the compressed part of the steel profile (Figure 5.14 (b) and (c)).

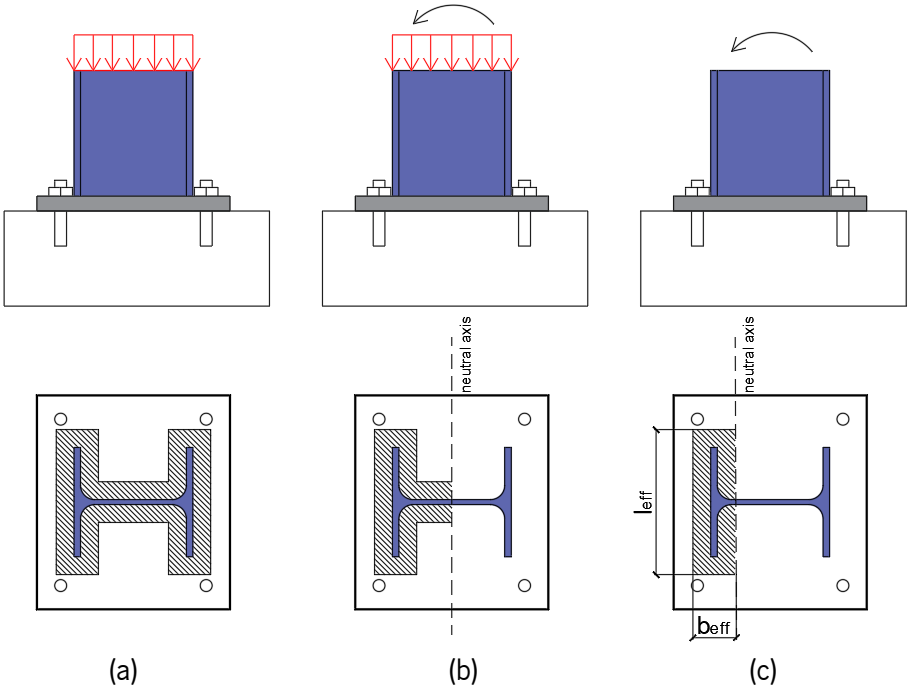


Figure 5.14. Different effective areas according to load type: (a) compression only; (b) compression and bending; (c) bending only. Adapted from Wald *et al.* (1998).

For the compression side, in all load cases presented in Figure 5.14, the effective area is determined based on the additional bearing width "c" of the equivalent T-stub in compression, as

shown in Figure 5.15, where F is the load applied and t_w is the thickness of the T-stub web. This theory considers that plastic deformations would not occur in the flange of the T-stub (Steenhuis *et al.*, 2008) and it is assumed a uniform stress distribution. Therefore, the resistance per unit length of the T-stub flange is taken as the elastic moment resistance of a plate (Equation (5.23)). In addition, the bending moment per unit length in the base plate, acting as a cantilever with span "c", is calculated by Equation (5.24).

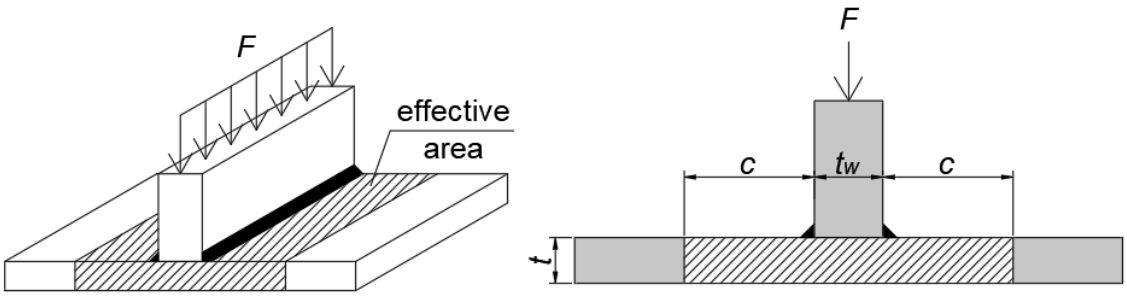


Figure 5.15. Equivalent T-stub in compression.

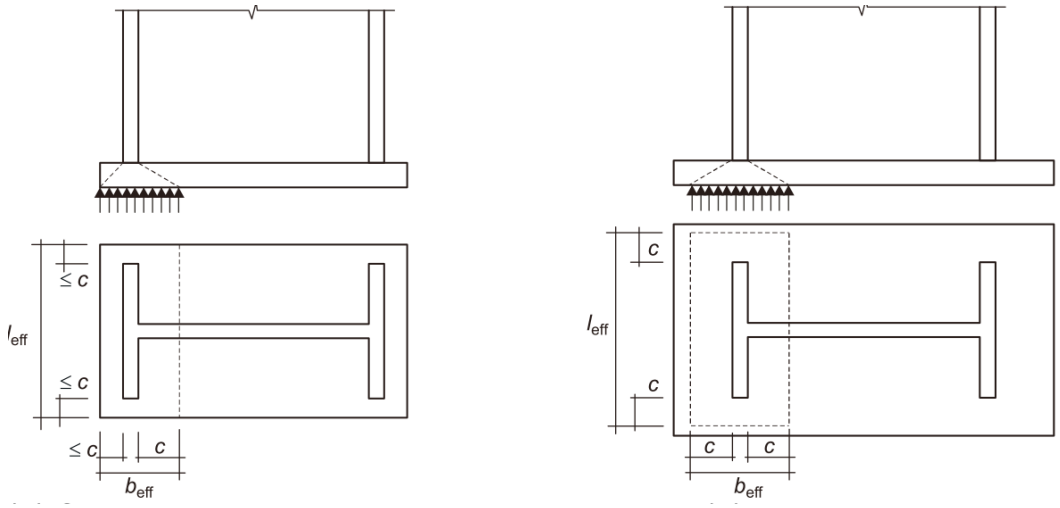
$$M_{Rd} = \frac{t^2 \cdot f_{yd}}{6 \cdot \gamma_{M0}} \tag{5.23}$$

$$M_E = \frac{c^2 \cdot f_{j,d}}{2} \tag{5.24}$$

Then, "c" can be determined considering $M_{Rd} = M_E$, which means that the equivalent width ($t_w + 2c$) is the equivalent timber region necessary to resist to compression caused by T-stub in the elastic range. The additional bearing width c is calculated by Equation (5.25). When the connection is subjected to a bending moment only, the effective length (l_{eff}) and widthb_{eff} () is obtained as shown in Figure 5.16 (b), by adding the additional bearing width from the steel beam connected the end-plate (Equations (5.26) and (5.27)). In specific cases, where the end-plate is thick and the distances between the beam flange and end-plate edge is short, it can be determined as shown in Figure 5.16 (a). The effective area (A_{eff}) is obtained by Equation (5.28).

$$c = t\sqrt{\frac{f_y}{3 \cdot f_{jd} \cdot \gamma_{M0}}} \tag{5.25}$$

Where: t is the thickness of the T-stub flange; f_y is the yield strength of the T-stub flange; γ_{M0} is partial factor for resistance of cross-sections; f_{jd} is the design bearing strength of the concrete.



(a) (b)

Figure 5.16. The effective area of T-stub in compression: (a) short projection; (b) large projection. Adapted from EN 1993-1-8:2010.

$$l_{eff} = b + 2 \cdot c \tag{5.26}$$

Where: b (mm): the width of the steel beam flange

$$b_{eff} = t_f + 2 \cdot c \tag{5.27}$$

Where: t_f (mm): the flange thickness of the steel beam flange

$$A_{eff} = l_{eff} \cdot b_{eff} \tag{5.28}$$

Based on these research, three approaches for calculating the additional bearing width of the component are presented called uniform elastic, uniform plastic and variable elastic. From which it will be possible to obtain the effective length, the effective width and consequently the effective area for the component under study, applying Equations (5.26), (5.27) and (5.28), respectively.

In the uniform elastic approach, the equation for elastic additional bearing width for timber (c_t) (Equation (5.29)) was proposed by Tomasi *et al.* (2008) based on the Equation (5.25), basically changing the design bearing strength of the concrete by the compression strength parallel to the grain of the GLT, as illustrated in Figure 5.17. It considered that the compression stress is uniformly distributed over a rectangular fictitious area defined by an effective length (l_{eff}) and width (b_{eff}), and steel and timber remain in the elastic range.

$$c_t = t_{ep}\sqrt{\frac{f_y}{3 \cdot f_{c,0} \cdot \gamma_M}} \tag{5.29}$$

Where, t_{ep} is the thickness of the T-stub flange, $f_{c,0}$ is the compression strength parallel to the grain of the GLT, and γ_M is the partial factor for material properties, in this case equal to 1.

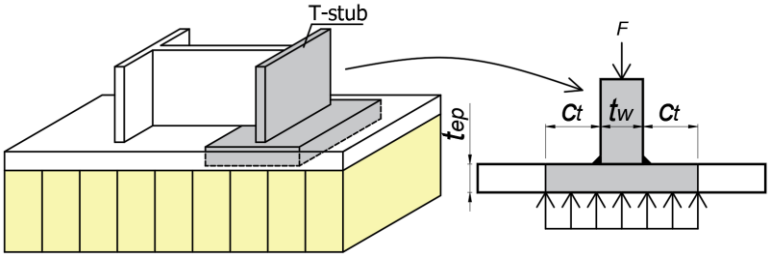


Figure 5.17. Structural idealization of the component corresponding to the steel T-stub applying compression parallel to grain in timber member and the additional bearing width (c_t).

In the proposed uniform plastic approach, each side of T-stub was modelled as a cantilever beam and considered a uniform stress distribution in the contact between the plate and the timber, as shown in Figure 5.18. The plastic additional bearing width (c_{tp}) (Equation(5.32)) was determined equating the plastic bending moment resistance of the base plate per unit length (M_{pb}) and the base plate bending moment per unit length acting in the timber (M_{Et}). In this approach, the M_{pb} can be calculated as presented in Equation (5.30) and the M_{Et} in Equation (5.31).

$$M_{pb} = \frac{1}{4} t_{ep} \cdot f_y \tag{5.30}$$

$$M_{Et} = \frac{{c_{tp}}^2 \cdot f_{c,0}}{2} \tag{5.31}$$

$$c_{tp} = t_{ep} \sqrt{\frac{f_y}{2 \cdot f_{c,0} \cdot \gamma_M}} \tag{5.32}$$

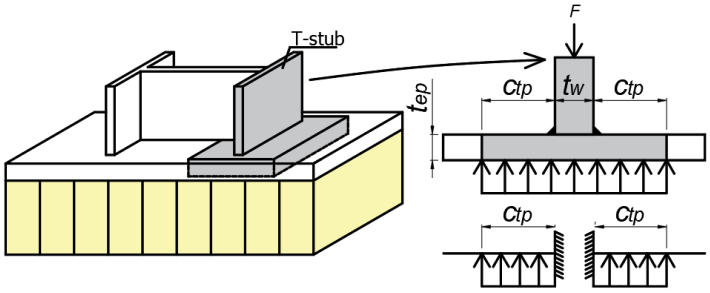


Figure 5.18. Structural idealization of the component corresponding to the steel T-stub applying compression parallel to grain in timber member and the plastic additional bearing width (c_{tp}).

As identified in the experimental research presented in Section 4.4, there is a non-uniform distribution of vertical displacements in the contact between steel plate and timber. The displacements are more significant around the central part of the T-stub, reducing towards the edges. Based on those

observations, the variable additional bearing width (c_{tv}) is proposed. It considers an equivalent area defined by a variable distribution of stresses in contact between both materials, which remains constant up to 40% of the T-stub flange span length (L). Afterward, it varies linearly until reaching the end of the effective width, as illustrated in Figure 5.19.

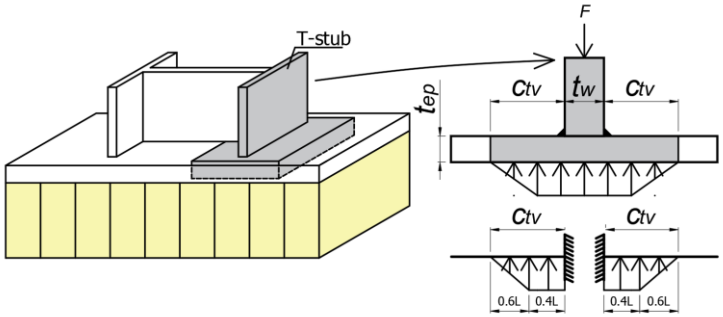


Figure 5.19. Structural idealization for T-stub and timber in compression component with a variable stress distribution and variable additional bearing width (c_{tv}).

Considering this new stress distribution and assuming that the plate is in the elastic range, the c_{tv} can be calculated by the Equation (5.34). It was developed equating the elastic bending moment resistance of the base plate per unit length (M_{Rd}) and the base plate bending moment per unit length acting in the GLT (M_{Etv}). Due to the variable distribution of stresses showed in Figure 5.19, the M_{Etv} is determined as in Equation (5.33).

$$M_{Etv} = 0.26 \cdot {c_{tv}}^2 \cdot f_{c,0} \tag{5.33}$$

$$c_{tv} = \mathrm{t}_{ep} \sqrt{\frac{f_y}{1.56 \cdot f_{c,0} \cdot \gamma_{M0}}} \tag{5.34}$$

In joints that have a direct contact between the end-plate and the timber, the GLT beam and the steel end-plate/steel link flange in compression were modelled as equivalent T-stub in compression. In this case, the effective area of compression plays an important role, as it is directly related to the compressive resistance and stiffness of the component. As the effective area considers the T-stub flange's behavior, the resistance of T-stub compressing timber parallel to the grain component ($F_{R,tb,c}$) can be determined by Equation (5.35). It is important to notice that the values of b_{eff} and l_{eff} are calculated based on the additional bearing width proposition presented in Equation (5.34), as this one showed better accuracy with experimental results, and the effective area is defined as shown in Figure 5.16.

$$F_{R,tb,c} = f_{c,0} \cdot b_{eff} \cdot l_{eff} \tag{5.35}$$

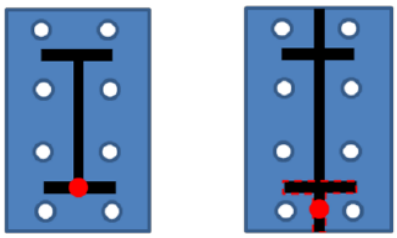
b) End-plate in bending under compression

For steel connections where the end-plate is supported by a column, the plastic resistance of the steel section flange under compression has been determined based on the findings of the EqualJoints Project (Landolfo *et al.*, 2018), which specifically examined steel stiffened end-plate connections. In the design procedure of extended end-plate beam-to-column joints, it is assumed that connection is designed for the bending moment and shear force at the column face corresponding to the formation of the plastic hinges in the beam (near to the stiffener), accounting for material overstrength and strain hardening. The resistance of this component can be determined by Equation (5.36).

$$F_{R,rb,c} = \frac{M_{c,rb,Rd}}{h_{sl} + \xi h_{rib} - 0.5 \cdot t_f} \tag{5.36}$$

where $M_{c,rb,Rd}$ is the design plastic moment resistance of the beam plus the rib cross-section; ξh_{rib} is the centroid of the Tee section composed by stiffener and the parts of the end-plate and the flange beam welded to the stiffener.

The results found by Abidelah *et al.* (2012) and numerical simulations performed by EqualJoints Project (Landolfo *et al.*, 2018) showed that for steel hogging bending moment, the joint compression center is located above the steel beam flange. In the stiffened end-plate connections, the center of compression is located at the centroid of the Tee section composed by stiffener and the flange beam welded to the stiffener (Figure 5.20). On the other hand, bolt rows located close to the compression center develop negligible tension forces, due to flexibility of the end-plate and limited ductility of the bolt rows at the tension flange.



(a) (b)

Figure 5.20. Location of compression center for different joint types (a) unstiffened end-plate (b) stiffened end-plate. Adapted from Landolfo *et al.* (2018).

However, the compression center position of a stiffened end-plate attached to a timber beam behaves differently as this contact occurs without the support of a column. This situation allows the

end-plate greater freedom of rotation and, consequently, less stiffness. Then, the resistance of the component was modelling based on the Figure 5.13, by equating the moment acting on the end-plate considering the cantilever with a span equal to $e_x + m_x$ (Equation (5.37)), and the plastic moment capacity of the end-plate (Equation (5.38)).

$$M_{E,ep} = F_{ep,c} \cdot h_{eq} \tag{5.37}$$

$$M_{p,ep} = f_{u,ep} \cdot Z_{p,ep} = \frac{{t_{ep}}^2 \cdot f_{u,ep} \cdot b_p}{4} \tag{5.38}$$

where h_{eq} is the distance between the equivalent load and the support of the end-plate cantilever; and $Z_{p,ep}$ is the plastic section modulus of the end-plate.

When the end-plate is stiffened, the stiffeners work in conjunction with the end-plate to resist the bending moment. Since the effective cross-sectional area includes both elements, the plastic section modulus of a stiffened plate depends on the geometry of the stiffeners and the end-plate. For simplicity, it is assumed that both the plate and the stiffeners reach their yield strength simultaneously, which is a reasonable approximation in many practical situations. For a rectangular plate with longitudinal stiffeners, the effective plastic section modulus ($Z_{p,eff}$) can be calculated as the sum of the contributions from the end-plate and the stiffeners (Equation (5.39)). The plastic moment capacity of the stiffened end-plate can then be determined using this effective plastic section modulus.

$$Z_{p,eff} = Z_{p,ep} + Z_{p,st} \tag{5.39}$$

where $Z_{p,st}$ (mm) is the plastic section modulus of the stiffener (Equation (5.40).

$$Z_{p,st} = \xi h_{rib} \cdot t_{rib} \cdot a \tag{5.40}$$

where t_{rib} is rib thickness and a is the rib height.

Then, the resistance of end-plate in bending under compression component for stiffened end-plate ($F_{R,ep,c}$) can be determined by Equation (5.41).

$$F_{R,ep,c} = \frac{Z_{p,ep} \cdot f_{u,ep} + Z_{p,st} \cdot f_{u,st}}{h_{eq}} \tag{5.41}$$

5.3. Joint initial rotational stiffness

The initial rotational stiffness of the joint is derived from the elastic stiffness of its components. Each component's elastic behavior can be modeled as a spring, and the mechanical relationship between force and deformation of this spring is represented by Equation (5.42).

$$F_i = E \cdot k_i \cdot \Delta_i \tag{5.42}$$

where F_i is the force in the spring I, E is the young modulus of the material, $k_i$is the stiffness coefficient of the component I, Δ_i is the displacement of the spring i.

Using the component method, these springs can be combined to create a spring model that reflects the components within the joint. The moment (M_E) acting on the spring model is equal to the force (F) in each spring multiplied by the lever arm (z), which is the distance between the center of tension and the center of compression of the joint. The rotation in the joint (ϕ) is equal to the sum of the component displacements divided by the lever arm. Thus, the initial rotational stiffness ($S_{j,ini}$) of the joint is calculated as shown in Equation (5.43).

$$S_{j,ini} = \frac{M_E}{\phi} = \frac{F \cdot z}{\frac{\sum_i \Delta_i}{z}} = \frac{F \cdot z^2}{\frac{F}{E} \cdot \sum_i \frac{1}{k_i}} = \frac{E \cdot z^2}{\sum_i \frac{1}{k_i}} \tag{5.43}$$

In joints with multiple BiR rows, it is assumed that the deformations of all rows are proportional to their distance from the center of compression, while the elastic forces in each row depend on the stiffness of the components. This results in an effective spring model for each BiR row, characterized by an effective stiffness coefficient $k_{eff,r}$ (r is the index of the row number), as presented in Equation (5.44). Additionally, all springs in the tension and compression zones can be replaced by an equivalent stiffness coefficient (Equation (5.45)), which can then be directly integrated into Equation (5.44). When k_{eq} is used, it is necessary to consider this in z, which turns into z_{eq} (Equation (5.46)).

$$k_{eff,r} = \frac{1}{\sum_r \frac{1}{k_{i,r}}} \tag{5.44}$$

$$k_{eq} = \frac{\sum k_{eff,r} \cdot h_r}{z_{eq}} \tag{5.45}$$

$$z_{eq} = \frac{\sum_r k_{eff,r} \cdot {h_r}^2}{\sum_r k_{eff,r} \cdot h_r} \tag{5.46}$$

For the timber joints examined in this study, a similar methodology was utilized. Based on the geometry of the joints and the specific mechanical models of the springs developed, the most general case, incorporating multiple rows of bonded-in rods, was illustrated in Figure 5.1 (see Section 5.1). The contribution of the third row's components to the joint rotation is significantly smaller than that of the others, and in some cases, this row may be subjected to compression, therefore, it can be

neglected. For other joint geometries, the same components were used but limited to those included in the joint design.

Since these joints are divided into macro-components, it is preferable for joint failure to occur at the link or connection. The initial stiffness of the joint depends on the stiffness of these macro-components. When a moment is applied, the two macro-components can rotate freely, and the rotation of each significantly impacts the overall joint rotation. However, because they are not part of the same "connection" (being geometrically distinct macro-components), the total stiffness of the joint is determined by the rotational stiffness of each individual part, namely the link (k_{link}) and connection (k_{eq}), which includes components ept, brt, rsc, and epc. The joint can be linked to a system of springs arranged in series. The total initial rotational stiffness of the joint can be estimated using Equation (5.47).

$$S_{j,ini} = \frac{1}{1/k_{link} + 1/k_{eq}} \tag{5.47}$$

The initial rotational stiffness of the steel link and of the connection can be calculated by Equation (5.48), considering the specific lever arm of each one, i.e. lever arm of the steel link equal to the distance between central axis of each flange (Equation (5.49)).

$$k_{link} = \frac{E_s \cdot {z_{sl}}^2}{\frac{1}{k_{lfb,c}} + \frac{1}{k_{lfb,t}}} \tag{5.48}$$

$$z_{sl} = h - t_f \tag{5.49}$$

5.3.1. Stiffness coefficient of link flange in bending (k_{lfb})

The stiffness coefficient of the link flange in bending can be determined according to classic mechanics theory for a beam under bending. It was divided into two springs: one for the tension side and the other for the compression side. The lever arm is equal to the distance between the mid-thickness of each flange. Each spring was defined as the relation between the force and the displacement in each side, as shown in Equation (5.50). Considering the elastic behavior of the steel link, the displacement of tension side is equal to that of compression side and can be determined as in Equation (5.51). The force on each side can be calculated as shown in Equation (5.52). Thus, the stiffness coefficient of each side of the steel link is calculated as in Equation (5.53).

$$k_{lfb} = \frac{F_s}{\Delta_s} \tag{5.50}$$

$$\Delta_s = \frac{M \cdot y \cdot \ell}{E_s \cdot I} \tag{5.51}$$

$$F_s = \frac{M \cdot y \cdot A}{4 \cdot I} \tag{5.52}$$

$$k_{lfb} = \frac{E_s \cdot A}{4 \cdot \ell} \tag{5.53}$$

where A is the total cross-section area of link; I is the moment of inertia of link; y is the vertical distance between the neutral axis and the outer face of the link flange; and ℓ is the total length of steel link.

5.3.2. Stiffness coefficient for end-plate in bending under tension ($k_{ep,t}$)

The stiffness coefficient is defined according to EN 1993-1-8:2010 for an end-plate in bending under tension, considering scenarios ranging from a single bonded-in row to four bonded-in rows in tension, with prying forces in Equations (5.54) and without prying forces in Equation (5.55). For the second row use m instead m_x.

$$k_{ep,t} = \frac{0.85 \cdot \ell_{eff} \cdot {t_{ep}}^3}{{m_x}^3} \tag{5.54}$$

$$k_{ep,t} = \frac{0.425 \cdot \ell_{eff} \cdot {t_{ep}}^3}{{m_x}^3} \tag{5.55}$$

5.3.3. Stiffness coefficient for bonded-in rods in tension ($k_{br,t}$)

The stiffness coefficient of the BiRs in tension was defined based on the withdrawal stiffness correlation for BiRs parallel to the grain, as proposed by Binck and Frangi (2024). This correlation is derived from experimental results obtained through tensile tests conducted on connections utilizing metric threaded rods of classes 4.8 and 8.8, with nominal diameters of 16 mm, 20 mm, and 24 mm. These rods were glued into timber members composed of GL28h, machine-graded glued-laminated Norway spruce, in accordance with EN 14080:2013. To derive a stiffness coefficient that accurately reflects the behavior of the T-stub under tension, the withdrawal equation of BiRs was multiplied by factors of 1.6 or 2.0, depending on the action of the prying forces. This equation was then divided by the modulus of elasticity of steel, as presented in Equations (5.56) (with prying forces) and (5.57) (without prying forces).

$$k_{br,t} = \frac{1.6 \cdot 25 \cdot d^{1.7} \cdot {\rho_{mean}}^{0.65}}{E_s} \tag{5.56}$$

$$k_{br,t} = \frac{2.0 \cdot 25 \cdot d^{1.7} \cdot {\rho_{mean}}^{0.65}}{E_s} \tag{5.57}$$

where ρ_{mean} is the mean density of the timber.

5.3.4. Stiffness coefficient for end-plate and GLT in compression ($k_{ep,c}$)

According to position of the equivalent load of the methodology proposed in Section 5.2.3.3, the stiffness coefficient of the end-plate follows a similar procedure. If the equivalent load position falls outside of the link flange thickness, the deformed shape of the end-plate under compression without stiffener exhibits similarities to that of a cantilever beam. In this scenario, the specific section of the end-plate experiences a trapezoidal load, considering the estimated position of the neutral axis of the connection, as depicted in Figure 5.21.

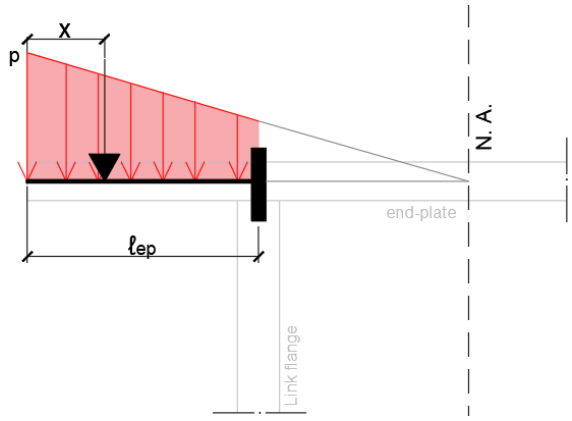


Figure 5.21. Cantilever end-plate assumptions for stiffness coefficient.

Consequently, by considering the Bernoulli beam theory, the vertical deflection can be determined, at any given section in terms of x, using Equation (5.58).

$$w_{ep,c}(x) = \frac{p{\ell_{ep}}^4}{12E_s I_{ep}} \cdot \left(-\frac{x^5}{10{\ell_{ep}}^5} + \frac{x^4}{{\ell_{ep}}^4} - \frac{x}{2\ell_{ep}} + \frac{13}{5} \right) \tag{5.58}$$

As stiffness coefficient of this component ($k_{ep,c}$) is defined by the relationship between the applied force and the displacement of the end-plate at the point of application of the equivalent force, the $k_{ep,c}$ can be calculated using Equation (5.59), where x_{eq} represents the position of the equivalent load.

$$k_{ep,c} = \frac{1.5 \cdot p \cdot \ell_{ep}}{E_s \cdot w_{ep,c}\,(x_{eq})} \tag{5.59}$$

If the equivalent load position falls within the link flange thickness, the behavior of the component is associated with the steel T-stub compressing timber parallel to the grain. In terms of the component behavior for flange thickness commonly applied in steel joints design (from 6 to 20 mm), when the T-stub compresses timber in the grain direction, the timber deforms in compression, and the T-stub flange bends, presenting a relative edge displacement called Δ_e, as shown in Figure 5.22. The elastic stiffness coefficient of this component is influenced by the flexibility of the plate (modulus of elasticity, strength, span/thickness ratio) and the modulus of elasticity of the timber in compression parallel to the grain. The stiffness coefficient (k_{tb}) is calculated by Equation (5.60) proposed by Tomasi *et al.* (2008) to predict the stiffness coefficient of GLT beam in compression. This equation was validated by experimental campaign presented in Section 4.4 with different configurations of loading interaction between T-stub and GLT. The results are presented in Section 5.5.

$$k_{tb,c} = \frac{E_{w,0}\sqrt{b_{eff,c} \cdot \ell_{eff,c}}}{\beta \cdot E_s} \tag{5.60}$$

where $E_{w,0}$ is the modulus of elasticity parallel to grain of glulam beam; $b_{eff,c}$ is the effective width; $\ell_{eff,c}$ is the effective length of the T-stub compressing timber parallel to the grain component; and β is the coefficient, which can be approximated to 4.

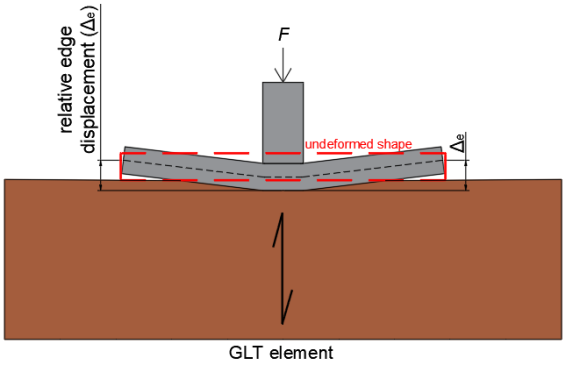


Figure 5.22. Schematic component deformation focused on the relative edge displacement for a steel T-stub compressing timber parallel to the grain.

In this case, the modulus of elasticity of timber ($E_{w,0}$) was considered and the factor β was calculated using Equation (5.62). This factor is associated with the stiffness of a rectangular rigid plate in an isotropic elastic half-space (K_z) (Richart *et al.*, 1970), shown in Equation (5.62).

$$K_z = \frac{P}{\delta_r} = \frac{G}{1-\nu} \cdot \beta_z \cdot \sqrt{B \cdot L} \tag{5.61}$$

where P is the applied force, δ_r is the vertical displacement under the rigid foundation, G is the shear modulus of the elastic half-space material, ν is the Poisson's ratio of the elastic half-space material, B and L are the dimensions of the rectangular plate and β_z is a coefficient that can be determined by the graph for plate dimensions (Tomasi *et al.*, 2008).

Considering $\nu \approx 0.4$ and $E_w/G = 16$ for timber, the factor β can be defined as in Equation (5.62).

$$\beta = \frac{16 \cdot (1-\nu)}{\beta_z} \cong 4.0 \tag{5.62}$$

5.3.5. Stiffness of rib stiffeners ($k_{rb,c}$)

The stiffness coefficient for rib stiffness can be calculated by Equation (5.63), as suggested Lee (2002). An equivalent strut-and-tie model was proposed to predict the resistance and stiffness of the rib stiffness. The equivalent strut area and length of the rib are defined by Equations (5.64) and (5.65). The main geometrical parameters are shown in Figure 5.23.

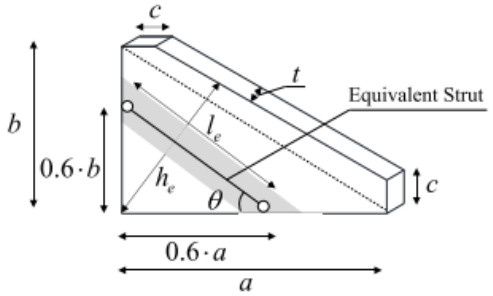


Figure 5.23. Main geometrical parameters of rib stiffener. Adapted from Lee (2002).

$$k_{rb,c} = \frac{A_{eq}}{L_{strut}} \cdot \cos(\alpha) \tag{5.63}$$

$$A_{eq} = \frac{\eta_r (a \cdot b_r - c^2)}{\sqrt{(a-c)^2 + (b_r - c)^2}} \tag{5.64}$$

$$L_{strut} = 0.6 \cdot \sqrt{(a^2 + {b_r}^2)} \tag{5.65}$$

where α is the rib strut inclination; η_r is the equivalent strut area factor and it is equal to 1.5; b_r is the length of the rib; a is the height of the rib; and c is the fillet of the rib.

5.4. Joint rotation capacity

The joint rotation capacity is dictated by the deformation capacity of the component exhibiting the lowest strength. This component contributes with its full deformation capacity, whereas the other components contribute with displacements at stress level corresponding to that strength (Beg et al.,

2004). Nevertheless, when the link rotates, the region between the link flanges, located along the central axis of the end-plate, also experiences the same rotation. Consequently, it has been established that the rotation of this section is equivalent to the rotation of the link (see Section 4.5.3.3). Given that within the elastic range, the surface of the end-plate between the profile flanges remains flat and the rotation of the end-plate is considered as the rotation of its flanges. It is also possible to derive a rotation from the elongation of BiRs (ductile behavior of steel threaded rods), which leads to a rotation in the timber on the tension side without significant deformations of the end-plate on the tension side. In this scenario, on the compression side, the timber and the end-plate would rotate together, as they remain in contact. The global rotation of the joint can be ascertained from the sum of the rotation of the link, the end-plate, and the timber as illustrated in Figure 5.24.

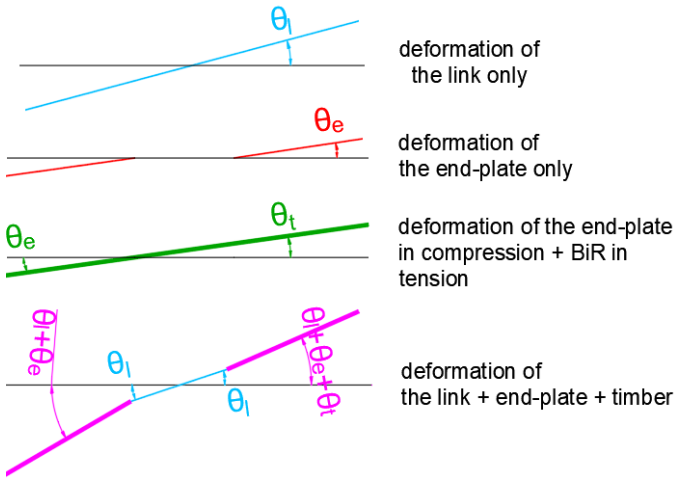


Figure 5.24. Analytical assumptions of joint rotations based on main deformation of the components.

As the link and connection are distinct macro-components, it has been identified that their contributions to the joint displacements are significant until the weakest macro-component reaches plastic deformations, and beyond this threshold, only the latter undergoes rotation. Furthermore, it has been observed that the contribution of the timber beam to the overall deformation is relatively negligible, as experimental tests demonstrated that this macro-component exhibited only rigid body rotation (see Section 4.5.3). To accurately delineate the displacement attributable to each component, simplified force–displacement curves for the components were established based on its strength ($F_{R,i}$), initial elastic stiffness (k_i), and deformation capacity ($\delta_{u,i}$).

The deformation capacity of the end-plate ($\delta_{u,epc,i}$) was calculated based on equations proposed by Beg *et al.* (2004) for modes 1, 2 and 3, assuming the equivalent T-stub in bending under tension for the outmost two BiR-rows in tension zone, as presented in Equations (5.66), (5.67) and (5.68).

$$\delta_{u,epc,1} = 2 \cdot \varepsilon_{u,ep} \cdot m \tag{5.66}$$

$$\delta_{u,epc,2} = 0.1 \cdot L_{bf} \cdot \left(1 + k \cdot \frac{m}{n}\right) \tag{5.67}$$

$$\delta_{u,epc,3} = \varepsilon_{u,br} \cdot L_{bf} \tag{5.68}$$

where $\varepsilon_{u,ep}$ is the ultimate strain of the steel end-plate; and $\varepsilon_{u,br}$ is the ultimate strain of threaded rod.

For the link, the rotation capacity ($\theta_{u,l}$) is defined based on a nonlinear regression model developed by Araújo and Castro (2014) from experimental data published by D'Aniello *et al.* (2012). The expressions for predicting the monotonic rotation capacity (in rad) for IPE, HEA and HEB profiles are presented in Equations (5.69), (5.70) and (5.71), respectively.

$$\theta_{u,l\,(IPE)} = 925.42 \cdot \left(\frac{b_f}{2 \cdot t_f}\right)^{-0.336} \cdot \left(\frac{h}{t_w}\right)^{-2.264} \tag{5.69}$$

$$\theta_{u,l\,(HEA)} = 5318.8 \cdot \left(\frac{b_f}{2 \cdot t_f}\right)^{-2.139} \cdot \left(\frac{h}{t_w}\right)^{-1.893} \tag{5.70}$$

$$\theta_{u,l\,(HEB)} = 73.18 \cdot \left(\frac{b_f}{2 \cdot t_f}\right)^{-1.052} \cdot \left(\frac{h}{t_w}\right)^{-1.258} \tag{5.71}$$

And finally for the T-stub compressing timber parallel to the grain, first it is necessary to introduce some concepts. In general, when the timber is under compression parallel to the grain, it exhibits a linear stress-strain relationship up to a certain proportional limit, often producing a long decreasing yield plateau. Some stress-strain relationship curves were defined by different authors to characterize the behavior of timber in compression quantitatively. Blaß (1987) proposed a correlation between the ultimate compressive strain (ε_c) and ultimate compressive strength, deduced from stress-strain curves similar to that depicted in Figure 5.25. Buchanan (1990) assumed a bilinear relationship, where the first part is linear until $f_{c,0,k}$ and after that, the slope falls in a certain ratio of the modulus of elasticity. The schematic curve can be found in Figure 5.26.

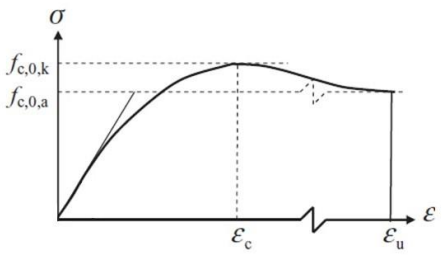


Figure 5.25. Stress-strain relationship for timber in compression parallel to the grain. Adapted from Blaß (1987)

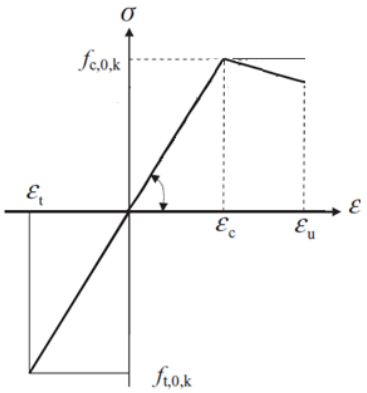


Figure 5.26. Bilinear stress-strain curve idealization for timber in direction parallel to the grain. Adapted from Buchanan (1990).

To apply this concept in assessing the deformation capacity of timber under compression parallel to the grain and provide safer results from a design point of view, the equation proposed by Blaß (1987) was used employing the 5-percentile characteristic compressive resistance ($f_{c,0,k}$), and accordingly the characteristic compressive modulus of elasticity parallel to the grain ($E_{c,0,k}$), as shown in Equation (5.72). Thus, for timber of strength class C24 (EN 338:2016) the ε_c would be equal to 0.00375.

$$\varepsilon_c = \frac{1250 \cdot f_{c,0,k}}{E_{c,0,k}} \tag{5.72}$$

Result of strain in parts per thousand (‰)

In terms of GLT, Frese *et al.* (2012) carried out fifty compression parallel to the grain tests with GLT made of Spruce, strength class GL24h (EN 14080:2013), specimens with cross section width of 80 mm, height of 200 mm (5 lamellae) and length of 480 mm. The maximum compressive stress was associated with a maximum strain ε_c between 0.0025 and 0.0055. The mean of ε_c, normally distributed, was 0.0040. The $E_{0,mean}$ amounts to 13000 MPa. In compression, the curve is linear, up to about 80 percent of the maximum load. However, those reference values for ε_c was determined by compressing the timber with a rigid plate with a cross-section larger than the GLT specimen, which diverge the objective of this study: a partial compression made by flexible T-stubs on GLT. In addition, this deformation value does not consider the damage zones in contact between the steel plate and the GLT. In this region, the displacements are much larger. According to Totsuka et al. (2022), these strains can be almost 10 times greater than the limit mentioned above.

As in the component under study, the GLT is compressed by a steel T-stub that is not rigid, it is expected that the T-stub governs the failure mode of the component, therefore deformation capacity

proposed here is focused on the behavior of T-stub flange in bending. The plastic mechanism of T-stub flange in bending due to the GLT compression is illustrated in Figure 5.27. The strain at the outer surface of the flange in bending is limited to the steel hardening strain ε_{sh}, then the strain cannot be larger than 10 times ε_y, as a reference value for hardening strain (Vogel, 1985).

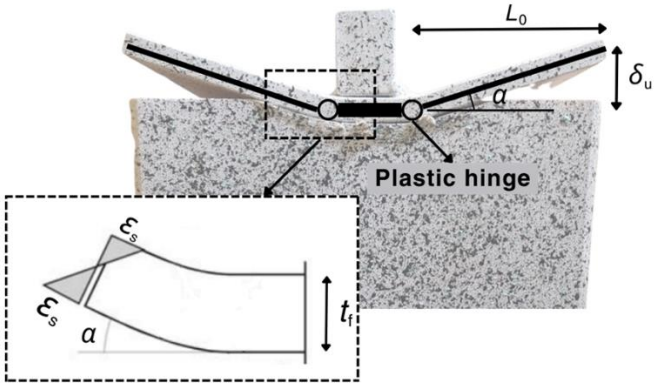


Figure 5.27. Deformation capacity approach for steel T-stub flange in bending due to timber parallel to the grain compression.

The deformation capacity δ_u of this component can be calculated using Equation (5.75), which was derived from Figure 5.27. Equation (5.73) provides the precise definition of vertical deformation. Taking into account the deformed shape of the T-stub flange and the definition of strain, Equation (5.74) defines the angle α. The parameter ΔL represents the variation in the length of the T-stub flange on the tension side caused by its deformation.

$$\delta_u = \alpha \cdot L_0 \tag{5.73}$$

$$\alpha = \frac{\Delta L}{t_f/2} = \frac{2 \cdot \varepsilon_s \cdot L_0}{t_f} \tag{5.74}$$

To obtain the final equation for defining the deformation capacity of the component under study, the value of α is replaced in Equation (5.73) with the steel hardening strain ε_{sh} as the maximum strain.

$$\delta_u = \frac{2 \cdot \varepsilon_{sh} \cdot {L_0}^2}{t_f} \tag{5.75}$$

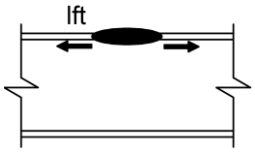
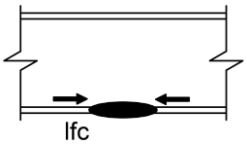
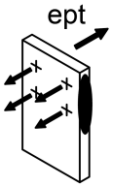
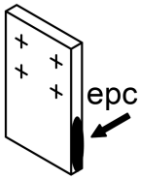
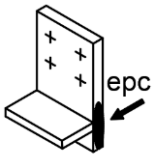
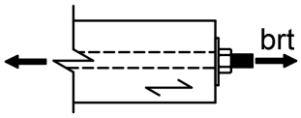
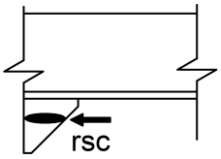
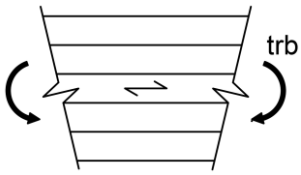
where L_0 is the undeformed length of half of T-stub flange without the web, t_f is the T-stub flange thickness, ε_s is the strain of outer part of the T-stub flange in bending.

5.5. Discussion of analytical results

To facilitate the discussion of the results and summarize the information on the calculation of the components detailed in this chapter, a basic component catalog is presented in Table 5.5. This catalog

includes a summary of the calculation references for each active component of the studied joint. It is important to note that specific guidelines for applying these equations are outlined in Chapter 5 of this thesis and are essential for the correct application of the calculation procedure for moment-resisting steel-timber joints with multiple BiR, end-plate, and steel link.

Table 5.5. Basic components catalogue

	Component			Reference to calculation		
				Resistance	Stiffness coefficient	Rotation capacity
1	lft	Link in tension		EN 1993-1-1:2014	Section 5.3.1	Araújo & Castro (2014)
2	lfc	Link in compression		EN 1993-1-1:2014	Section 5.3.1	Araújo & Castro (2014)
3	ept	End-plate in bending under tension		6.2.6.5, EN 1993-1-8:2010*	6.3.2, EN 1993-1-8:2010*	6.4.2, EN 1993-1-8:2010*
4	epc	End-plate in bending under compression		Section 5.2.3	Section 5.3.2	-
5	epc	T-stub compressing timber parallel to the grain		Section 5.3.2	Tomasi *et al* (2008).	Section 5.4
6	brt	Bonded-in rods in tension		Aicher *et al.* (1999)	Binck & Frangi (2024)	6.4.2, EN 1993-1-8:2010*
7	rsc	Rib stiffener in compression		Landolfo *et al.* (2018)	Landolfo *et al.* (2018)	-
8	tb	Timber in bending		EN 1995-1-1: 2014	EN 1995-1-1:2014	-

*Consider the adjustments proposed in sections 5.2, 5.3, and 5.4 of this thesis.

5.5.1. T-stub compressing timber parallel to the grain

A component-level validation was carried out based on the characterization of the component in terms of resistance, stiffness coefficient and deformation capacity proposed in Sections 5.2.3, 5.3.4 and 5.4. All analytical values were calculated computing the nominal strengths of materials $f_{c,0,k}$ = 24 MPa and $E_{c,0,mean}$ = 11600 MPa according to EN 338:2016 and f_y = 235 MPa, γ_{M0} = 1.0 (EN 1993-1-1:2014).

Table 5.6 compares the mean experimental value of component resistance with the value obtained from the analytical component methodology, using the effective area approaches presented in section 5.2.3.3. The variable elastic approach, which provided the variable additional bearing width, showed the best approximation to the mean experimental results. Although the percentage differences may appear large, it is essential to define a safe-sided value for analytical equations applicable in daily design due to timber variability. In real-world conditions, material parameters such as moisture content can vary considerably, reducing the resistance of the GLT. Furthermore, the variable elastic approach enhances the accuracy of the analytical results, calculated from the differences between experimental and analytical results, by approximately 74% for the T20 series and 23% for the T6 series compared to the formulations proposed by Andreolli *et al* (2011)

Table 5.6. Comparison between experiments and analytical approaches for the component resistance

Series	Mean Exp resistance (kN)	Uniform elastic (kN)	Diff (%)	Variable elastic (kN)	Diff (%)	Increase in accuracy
T20 G1	440.5	251.32	-42.9%	331.81	-24.7%	74.1%
T20 G2	456.4	251.32	-44.9%	331.81	-27.3%	64.6%
T20 G3	441.3	251.32	-43.0%	331.81	-24.8%	73.5%
T15 G1	342.7	199.29	-41.8%	259.66	-24.2%	72.7%
T15 G2	359.7	199.29	-44.6%	259.66	-27.8%	60.3%
T15 G3	380.1	199.29	-47.6%	259.66	-31.7%	50.1%
T10 G1	296.4	147.26	-50.3%	187.51	-36.7%	37.0%
T10 G2	307.3	147.26	-52.1%	187.51	-39.0%	33.6%
T10 G3	289.2	147.26	-49.1%	187.51	-35.2%	39.6%
T8 G1	269.8	126.45	-53.1%	158.65	-41.2%	29.0%
T8 G2	217.9	126.45	-42.0%	158.65	-27.2%	54.3%
T8 G3	245.7	126.45	-48.5%	158.65	-35.4%	37.0%
T6 G1	231.9	105.64	-54.4%	129.78	-44.0%	23.6%
T6 G2	235.0	105.64	-55.0%	129.78	-44.8%	23.0%
T6 G3	203.1	105.64	-48.0%	129.78	-36.1%	32.9%

Table 5.7 presents a comparison between the stiffness coefficient and deformation capacity obtained using the variable elastic approach and the experimental results. Overall, the analytical stiffness coefficient falls within the range of the experimental initial stiffness values of the T-stub and the GLT for all series, considering the three different groups of specimens.

Table 5.7. Component stiffness coefficient and deformation capacity comparison between experimental and the variable elastic approach

Series	Mean GLT Exp. Stiffness coefficient (N/mm)	Analytical stiffness coefficient (N/mm)	Diff (%)	Mean Experimental T-stub flange relative displacement at max force (mm)	Analytical deformation capacity (mm)	Diff (%)
T20 G1	278088		22.6	2.01		53.2
T20 G2	317487	340988	7.4	3.42	3.08	9,9
T20 G3	295090		15.6	-		-
T15 G1	203687		48.1	4.56		9.8
T15 G2	259487	301644	16.2	4.30	4.11	4.4
T15 G3	280078		7.7	-		-
T10 G1	179105		43.1	6.86		10.2
T10 G2	240225	256331	6.7	6.47	6.16	4.8
T10 G3	189423		35.3	-		-
T8 G1	184499		27.8	8.05		4.2
T8 G2	184467	235779	27.8	8.51	7.71	9.4
T8 G3	206227		14.3	-		-
T6 G1	149310		42.8	10.33		0.1
T6 G2	191334	213257	11.5	10.94	10.28	6.0
T6 G3	177868		19.9	-		-

In terms of the stiffness coefficient, group G1 exhibited greater percentage differences relative to the experimental values. This phenomenon can be attributed to the total compression experienced by the timber specimens in this group, which results in a diminished experimental stiffness value. Given that the equation for calculating the stiffness coefficient is associated with localized compression of the timber in the region of contact with the steel T-stub, the percentage differences for group G1 were notably higher. Conversely, the specimens from groups G2 and G3 demonstrated lower discrepancies in relation to the experimental results, ranging from 6.7% to 27.8%. These groups more accurately reflect practical scenarios in connections, characterized by partial localized compression of the timber. Consequently, it is reasonable to conclude that the analytical approach reached a satisfactory approximation of the results.

The analytical values of deformation capacity are compared with the experimental the T-stub flange relative displacement at maximum force. The deformation capacity results are consistent with the

experimental data, in the cases where force–displacement diagrams exhibited a plastic plateau being the deformation capacity close to the displacement values related to the steel hardening strain ε_{sh}. As depicted in Table 5.7, except for specimen T20 G1, the disparities between the analytical and experimental values are small (from 0.1 to 10.2%), highlighting good precision.

In order to evaluate the characterization considering resistance, stiffness coefficient and deformation capacity, the analytical bilinear curves using the variable elastic approach are compared with the mean experimental load-displacement curves for all studied thickness (Figure 5.28). The analytical values of stiffness coefficient presented a good fit, as they are positioned between the GLT and T-stub flange initial stiffness. The deformation capacity is coherent with the relative displacement of T-stub flange.

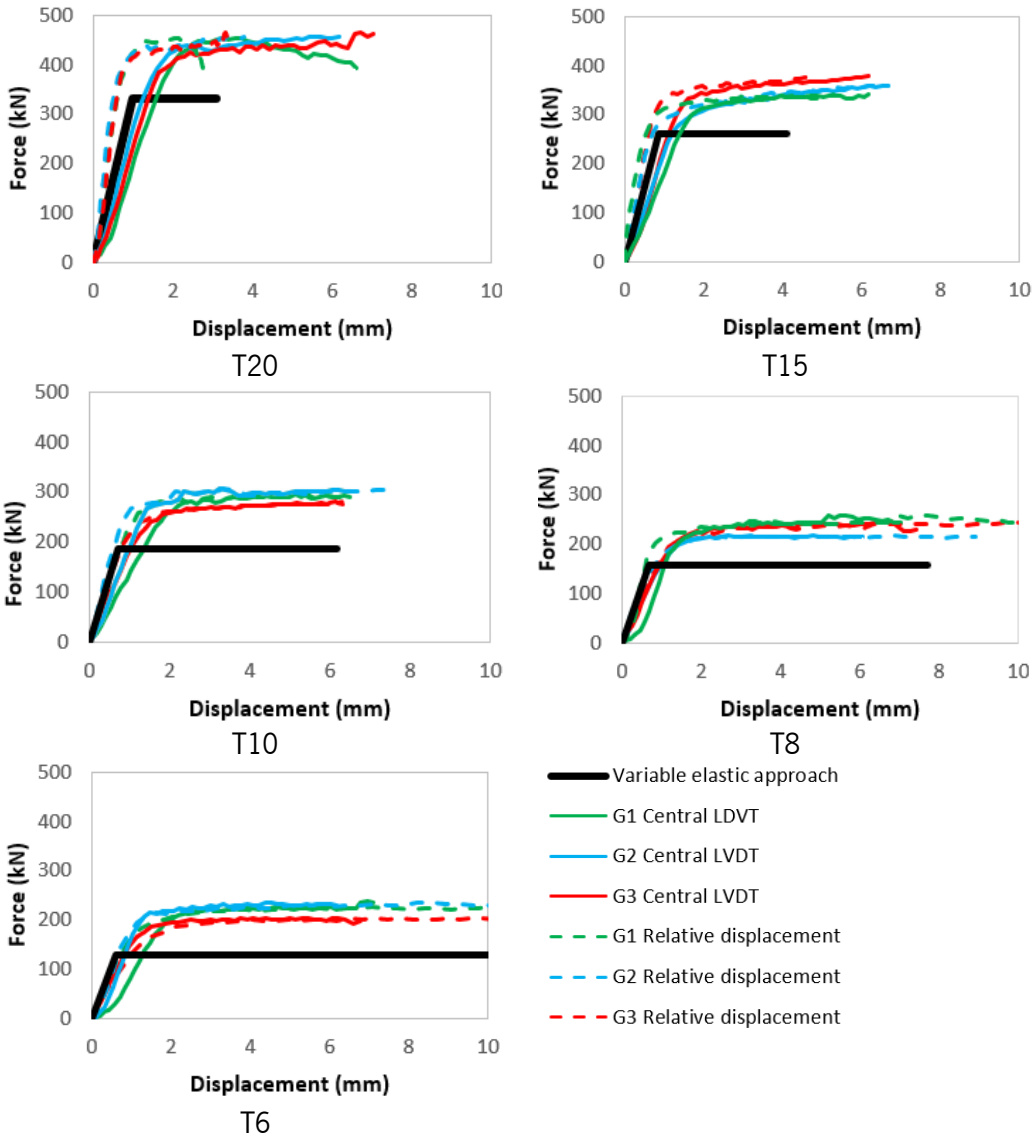


Figure 5.28. Analytical and experimental component load-displacement curve comparison for all series.

5.5.2. Joint results

This Section compares the analytical predictions and moment-rotation trilinear curves based on the component method design methodology proposed with the test results presented in Chapter 4 and with the results obtained by Andreolli *et al.* (2011), named here as P6, P8 and P10. From these results it is possible to evaluate the accuracy of the proposed analytical method for three different moment-resisting joints:

I. Stiffened end-plate with two rows of BiRs
II. Stiffened end-plate with four rows of BiRs
III. Unstiffened end-plate with two rows of BiRs.

When implementing the analytical model, the available experimental results of material strength were utilized. In the absence of these results, the technical documentation was followed.

Table 5.8 provides an overview of the predicted versus experimental failure modes for different joint types. This comparison sheds light on the accuracy of the analytical models in predicting failure behavior, which is critical for ensuring reliable design and safety. For joints P6 and P10, the analytical and experimental results identify failure of the T-stub flange, mode 1 and mode 2 as the failure mode, respectively, indicating that the analytical model accurately predicts the behavior of this joint type. However, for P8, analytical predictions suggested failure of the T-stub flange in mode 1 and the experimental results show mode 2. This difference is due to closely aligned resistances of these two failure modes in this joint. Additionally, the application of mean experimental tensile strength of steel in analytical calculations may have contributed to this difference in predictions.

For G1 and G2 joints, the analytical model accurately represents the behavior of these joints. A specific failure mode was found for G2.t20.d12 and G2.t15.d14, where analytical model predicted tensile failure of the steel threaded rods (mode 3) and the experimental results indicate galling of the threaded rod. As explained in Section 4.2, galling represents a distinct failure mechanism characterized by surface degradation resulting from elevated friction and wear. It is also important to highlight that in the G2.t12.d16, plastic hinge formation on the steel link was the first failure mode that occurred, and it was precisely predicted by the analytical method.

In summary, the analytical procedure successfully predicted all results concerning the occurrence of failure in macro-components. This included the joint type G1.t15.d20, which behaved as an equal-strength connection, with the end-plate yielding almost simultaneously with the steel link. The analysis

correctly indicated that the end-plate would yield first, but that the joint would ultimately fail due to a plastic hinge forming in the link.

Table 5.8. Comparison of failure modes.

Joint Type	Failure mode		
	Analytical	Experimental	Macro-component
G1.t20.d20	Steel link failure	Steel link failure	Full-strength connection
G1.t15.d20	Steel link failure	Steel link failure	Equal-strength connection
G2.t20.d12	Failure of Threaded rods (mode 3)	Galling of threaded rod	Partial-strength connection
G2.t15.d14	Failure of Threaded rods (mode 3)	Galling of threaded rod	Partial-strength connection
G2.t12.d16	Steel link failure	Steel link failure	Full-strength connection
P6	Failure of T-stub flange (mode 1)	Failure of T-stub flange (mode 1)	Partial-strength connection
P8	Failure of T-stub flange (mode 1)	Failure of T-stub flange (mode 2)	Partial-strength connection
P10	Failure of T-stub flange (mode 2)	Failure of T-stub flange (mode 2)	Partial-strength connection

The prediction of prying forces is also important for determining the mechanical response of the joint, since the development of these forces changes the behavior of the tensile region of the connection. The proposition presented in Section 5.2.3.2 provided consistent results, since the development or non-development of prying forces was correctly predicted in all connections tested in this thesis, as well as in those studied by Andreolli *et al.* (2011). A summary of this comparison is presented in Table 5.9.

Table 5.9. Comparison between prediction and experimental development of prying forces.

Joint Type	Development of prying forces	
	Analytical	Experimental
G1.t20.d20	Yes	Yes
G1.t15.d20	Yes	Yes
G2.t20.d12	No	No
G2.t15.d14	No	No
G2.t12.d16	Yes	Yes
P6	Yes	Yes
P8	Yes	Yes
P10	Yes	Yes

The lever arm is a crucial parameter for determining the analytical results of moment resistance and initial rotational stiffness, as it is directly linked to the positions of the connection's center of tension and center of compression. According to experimental test results, in the elastic range, the neutral axis is located near the connection's geometric axis. In the calculation procedure, the position

of the center of tension takes into account the vertical positions of the BiRs relative to the center of compression (h1 and h2), as well as the magnitude of the forces acting on each BiR row.

The analysis of the center of compression is somewhat more complex. As explained in section 5.2.3.3, the load distribution in this region depends on the geometry of all macro-components, which may lead to different suitable active components for compression and, consequently, a different center of compression. Figure 5.29 illustrates the lever arm possibilities considered in the calculation procedure developed in this thesis.

In cases where the compressed region behaves as a T-stub compressing timber parallel to the grain, the effective area (marked in red) is located at the contact region with the link flange, determined by the variable additional bearing width (c_{tv}). The compression region "x" (marked in orange) is proportional to the intensity of tension forces acting on the end-plate and BiRs, starting from the fibers furthest from the neutral axis. The center of compression is positioned in the middle of this region, and the neutral axis is positioned at the end of "x" height, as shown in Figure 5.29 (a).

For situations where the compressed region acts as an end-plate bending under compression (Figure 5.29 (b)), the entire area marked in orange is under compression, with the center of compression located at the geometric center of the triangular load. The distance from the bottom face of the link to this center of gravity is designated as heq.

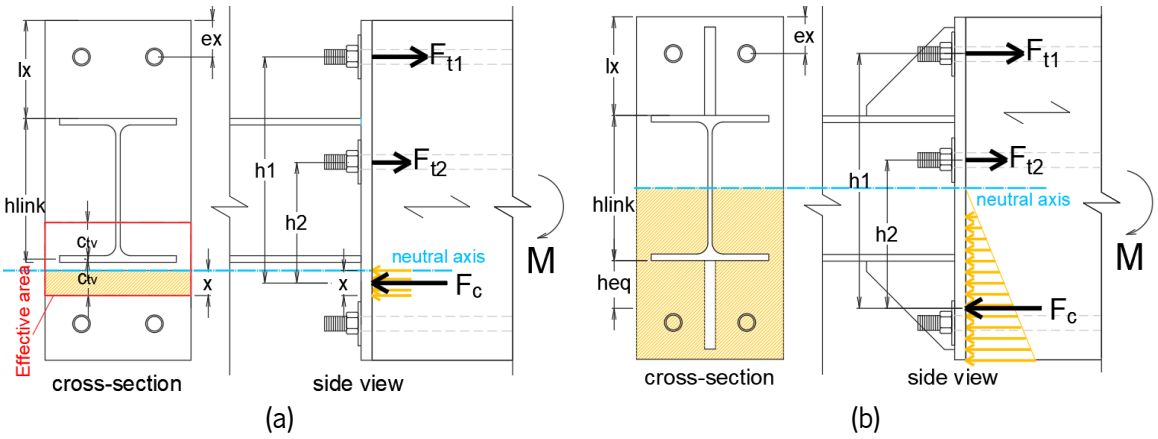


Figure 5.29. Theoretical lever arms for joints with compression side working as (a) T-stub compressing timber parallel to the grain, (b) End-plate in bending under compression.

Considering the two cases mentioned above, the lever arms for the outermost BiRs row can be calculated using Equations (5.76) and (5.77), respectively.

$$h_1 = l_x - e_x + h_{sl} + c_{tv} - \frac{x}{2} \tag{5.76}$$

Where h_{sl} (mm) is the height of the steel link; l_x is the distance between the end-plate edge and steel link upper face.

$$h_1 = l_x - e_x + h_{sl} + h_{eq} \quad (5.77)$$

Tables 5.10, 5.11 and 5.12 present the results of the analytical and experimental yield and ultimate moment resistance, initial rotational stiffness, and rotation capacity, respectively.

Table 5.10. Comparison between predicted and observed joint moment resistance

Joint Type	My (kNm)			Mu (kNm)		
	Analytical	Experimental	Difference	Analytical	Experimental	Difference
G1.t20.d20	53.92	54.30	-0.69%	60.05	61.49	-2.34%
G1.t15.d20	53.92	53.01	1.73%	60.05	55.71	7.79%
G2.t20.d12	19.97	18.59	7.41%	22.75	24.97	-8.90%
G2.t15.d14	27.41	23.45	16.87%	31.22	27.24	14.62%
G2.t12.d16	30.22	32.88	-8.09%	34.44	36.48	-5.58%
P6	5.36	5.72	-6.22%	6.77	8.85	-23.53%
P8	8.12	7.68	5.79%	10.84	14.99	-27.70%
P10	12.47	12.54	-0.58%	16.61	19.85	-16.32%

The comparison between the predicted and experimental results for the yield (My) and ultimate (Mu) moment capacities (Table 5.10) revealed that the analytical method demonstrated generally good accuracy across both groups, with deviations that remained within acceptable limits for most cases.

For G1, the analytical predictions closely matched the experimental results, indicating that the model reliably captures the mechanical response of joints. For the joint G1.t20.d20, the analytical predictions underestimated both the yield and ultimate moments by only 0.69% and 2.34%, respectively, showing excellent agreement with the experiments. Similarly, for G1.t15.d20, the analytical yield moment showed a small overestimation of 1.73%, while the ultimate moment was overpredicted by 7.79%. These results indicate that, for G1, the analytical approach provides a consistent estimation of both My and Mu, with slightly higher deviations.

In G2, which includes joints with smaller beam depths and varying BiR diameters, the discrepancies between analytical and experimental results were more pronounced. The joint G2.t20.d12 showed a modest overestimation of 7.41% for the yield moment and a corresponding underestimation of 8.90% for the ultimate moment. In contrast, G2.t15.d14 presented higher positive deviations, with overestimations of 16.87% for My and 14.62% for Mu. For G2.t12.d16, the analytical model underestimated both yield and ultimate moments by 8.09% and 5.58%, respectively, but these deviations are still within a reasonable margin of accuracy, indicating a balanced performance of the model.

For the joints studied by Andreolli *et al.* (2011), which correspond to smaller-scale connections, the analytical model captured the overall trends but tended to underestimate the ultimate moment resistance more significantly. For instance, in P6, the analytical My differed by -6.22%, while Mu showed a larger underestimation of -23.53%. Similar behavior was observed for P8 and P10, where the underestimation of Mu reached -27.70% and -16.32%, respectively. Despite these differences, the predictions for My remained reasonably close to the experimental results, with deviations between -0.58% and 5.79%. These consistent differences suggest that the analytical model is effective in capturing the yield moment, but it tends to underpredict the joint's capacity in the plastic range, where local deformation and ductility effects become dominant and are not fully represented in the simplified analytical formulation. This underestimation arises from the fact that the component method was formulated based on an elastic-plastic idealization of component behavior, typically characterized by a bilinear post-elastic model for specific steel elements. While this simplification facilitates analytical implementation, it does not fully capture the strain hardening that occurs in steel components after yielding. Moreover, the actual nonlinear moment–rotation response of the joint involves complex interactions, which are not entirely represented in the simplified bilinear model. Consequently, the analytical predictions tend to underestimate both the post-yield stiffness and the ultimate resistance observed experimentally. Nonetheless, the overall agreement between analytical and experimental data confirms the robustness of the analytical approach, with most deviations remaining within acceptable limits for practical design applications.

Table 5.11. Comparison between predicted and observed initial rotational stiffness

Joint type	Initial rotational stiffness (kNm/rad)		
	Analytical	Experimental	Difference
G1.t20.d20	3763.42	4148.47	-9.28%
G1.t15.d20	3188.33	3586.65	-11.11%
G2.t20.d12	3898.22	3879.73	0.48%
G2.t15.d14	3594.37	3476.89	3.38%
G2.t12.d16	3446.00	3280.76	5.04%
P6	796.88	885.66	-10.02%
P8	1324.77	1312.18	0.96%
P10	1773.70	2011.41	-11.82%

In Table 5.11, the experimental values were generally higher than the analytical predictions, with small percentage differences observed (a maximum of 11.82% for P10). For G1 The mean initial rotational stiffnesses obtained experimentally were 4148.47 kNm/rad and 3586.65 kNm/rad, compared to analytical predictions of 3763.42 kNm/rad and 3188.33 kNm/rad, respectively. The

corresponding deviations were −9.28% for the thicker plate (t20) and −11.11% for the thinner plate (t15). These results indicate that while the analytical method captured the general stiffness trend with respect to plate thickness, it systematically underestimated the joint rigidity. Nevertheless, the low deviations demonstrate that the analytical approach provides a reasonably accurate and conservative estimative of the initial stiffness for this group of moment-resisting joints.

For G2, the analytical predictions exhibited excellent agreement with the experimental measurements. The smallest deviation was observed for G2.t20.d12, with a difference of only 0.48%, indicating almost perfect correspondence between the analytical and experimental stiffness values. The configurations G2.t15.d14 and G2.t12.d16 showed slightly higher deviations of 3.38% and 5.04%, respectively, both indicating minor overestimations by the analytical method. The accuracy achieved for G2 demonstrates that the analytical formulation is particularly effective in capturing the stiffness behavior of connections characterized by smaller beam depths and four BiR rows.

For the additional joint configurations P6, P8, and P10, the analytical method also showed consistent behavior. The differences between predicted and experimental stiffnesses ranged from −11.82% to +0.96%, which is comparable to the accuracy achieved for the main groups. The largest deviation (−11.82%) occurred for the P10 configuration, while the smallest (+0.96%) was observed for P8. These results further validate the reliability of the analytical model in predicting stiffness across a wide joint geometries range, from relatively flexible to more rigid ones.

Table 5.12. Comparison between predicted and observed joint rotation capacity

Joint type	Rotation capacity (rad)		
	Analytical	Experimental	Difference
G1.t20.d20	0.1260	0.1173	7.4%
G1.t15.d20	0.1260	0.1070	17.8%
P6	0.1563	0.1500	4.2%
P8	0.1662	0.2100	-20.9%
P10	0.1838	0.1800	2.1%

The comparison between analytically predicted and experimentally observed joint rotation capacities provides valuable insight into the ability of the analytical model to reproduce the ductile behavior of the tested connections. In general, the results of Table 5.12 showed a good correlation between analytical and experimental data, with deviations ranging from approximately 2% to 21%, depending on the joint configuration. This level of accuracy is considered satisfactory given the inherent variability associated with the nonlinear response of steel–timber connections and the complex local effects influencing post-yield

For G1, the analytical predictions slightly overestimated the experimental rotation capacity. The configuration G1.t20.d20 exhibited a predicted capacity of 0.1260 rad, compared to an observed value of 0.1173 rad, resulting in a difference of +7.4%. The thinner plate configuration, G1.t15.d20, showed a larger discrepancy, with the analytical value of 0.1260 rad exceeding the experimental value of 0.1070 rad by 17.8%.

The additional joint configurations P6, P8, and P10 showed a balanced distribution of over- and underestimation. The analytical and experimental results for P6 and P10 were in very close agreement, with differences of +4.2% and +2.1%, respectively, indicating excellent predictive accuracy. In contrast, P8 exhibited an underestimation of −20.9%, with the analytical model predicting a lower rotation capacity (0.1662 rad) than observed experimentally (0.2100 rad). These results indicate that the analytical model tends to overpredict the ultimate rotational capacity for thicker timber beams. This behavior may be attributed to simplifications in the analytical representation of the post-yield deformation mechanisms**.** The analytical approach, being primarily stiffness-based, may not fully capture the progressive damage and localized nonlinearity that occur experimentally, especially in more flexible plate configurations. Nonetheless, the deviations remain within a reasonable range, demonstrating that the analytical method provides a conservative yet realistic approximation of the rotational capacity for design and analysis purposes.

The moment-rotation curves for the entire joint were constructed utilizing the methodology outlined in Chapter 5. The non-linear idealization of the moment-rotation curve is represented in a tri-linear form. The joint moment resistance was determined based on the yield and ultimate moment of the weakest macro-component of the joint. In the moment-rotation curve, the first point is defined by using the calculation procedure proposed using the yield strength, while the second point was obtained using the plastic strength. The obtained analytical moment-rotation curves are depicted and compared to the experimental results in Figures 5.30, 5.31 and 5.32.

In general, the model proposed through the component method demonstrated an effective alignment with the experimental moment-rotation curves. This alignment pertains not only to the initiation of yielding but also to the joint moment resistances, which in these curves are associated with the onset of steel plasticization rather than the ultimate moment of the joint. Moreover, the results regarding initial stiffness were quite satisfactory across all the joint geometries examined.

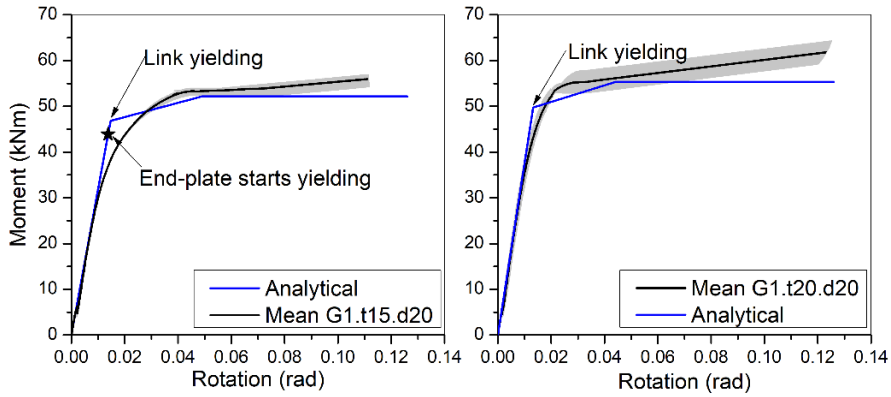


Figure 5.30. Comparison of the moment-rotation curves for G1 joint.

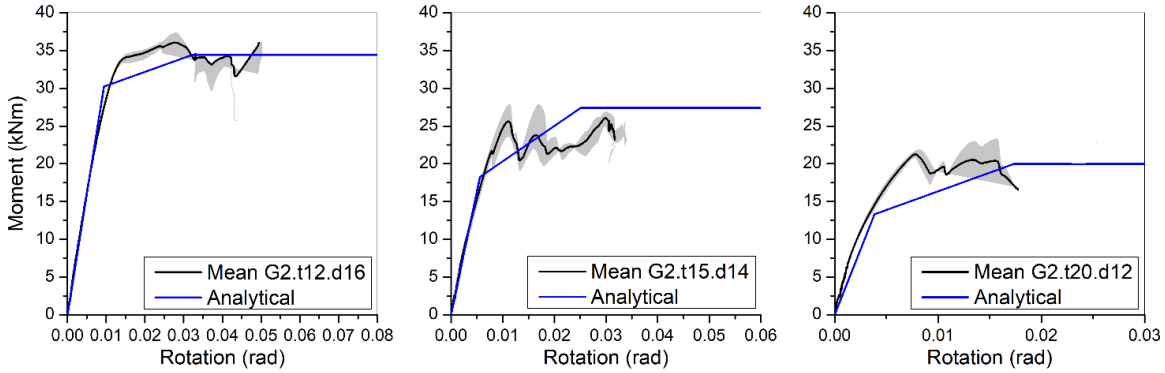


Figure 5.31. Comparison of the moment-rotation curves for G2 joint.

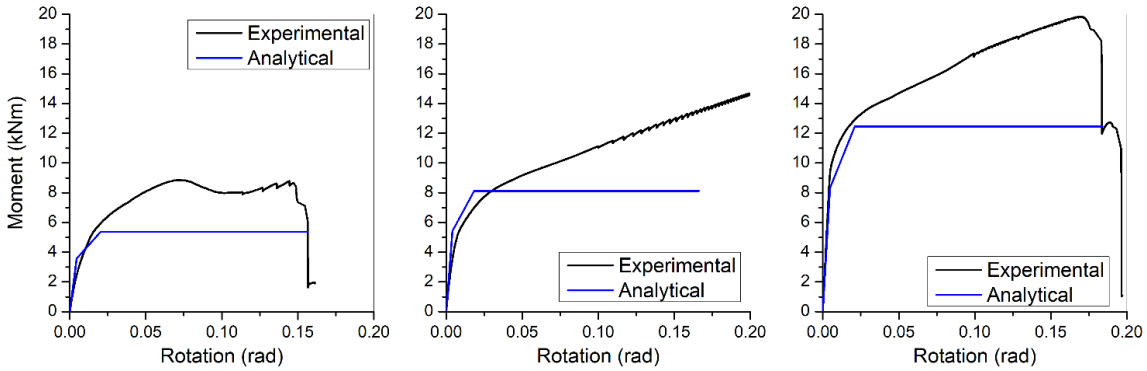


Figure 5.32. Comparison of the moment-rotation curves for joints P6, P8 and P10.

CHAPTER 6

NUMERICAL AND PARAMETRIC ANALYSIS

This chapter outlines the key objectives related to the numerical modelling and parametric analysis of moment-resisting steel-timber joints, focusing on verifying the applicability of the proposed analytical procedure across an extended range of geometries. First, detailed numerical models of these joints were developed using Abaqus® software. Next, the structural behavior predicted by the simulations was verified through a comparative analysis with experimental data. Building on this validated modelling approach, the aim was to investigate critical design parameters that influence joint performance, particularly in achieving high moment capacity and initial rotational stiffness. Finally, the chapter includes a parametric analysis to evaluate the applicability range of the component method, examining both stiffened and unstiffened joint configurations with groups featuring either two or four rows of bonded-in rods.

6.1. Numerical modelling for model validation

Numerical modelling focuses on analyzing moment-resisting steel-timber joints with steel link and BiRs connections, as discussed earlier in this thesis. The objective is to perform a parametric analysis to verify the applicability of the proposed component method design procedure for these joint types, while also exploring geometries that differ from those tested experimentally.

The detailed 3D numerical models for the joint were developed using *Simulia* ABAQUS Finite Element (FE) software (Barbero, 2023). Geometrical features, materials and boundary conditions were assumed according to the experimental test performed and described in Chapter 4. A static non-linear analysis was performed reaching the same imposed displacements values of the tests.

6.1.1. Geometry and boundary conditions

The geometry used matches the dimensions of the test specimens. At this stage, joints were modelled with the geometry of tested specimens of group G1, shown in Figure 6.1, varying only the end-plate thickness (t_{ep}) between 15 and 20 mm, namely t15 and t20. The threaded rods diameter was modelled using the internal dimensions of the rods, according to the Rothoblaas technical sheets.

For illustration purposes, a typical model of the joint is shown in Figure 6.2, which includes the boundary conditions and applied displacements. To replicate the conditions of the experimental tests,

the joint was fixed in three directions at the center of the rigid plate, and a displacement in the Y-direction was applied at the center of the timber beam end.

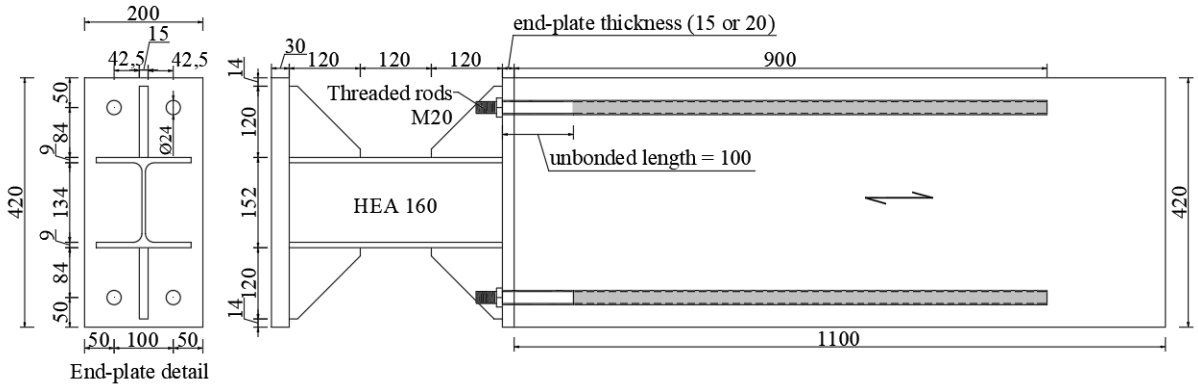


Figure 6.1. Detailed geometry of joints modelled.

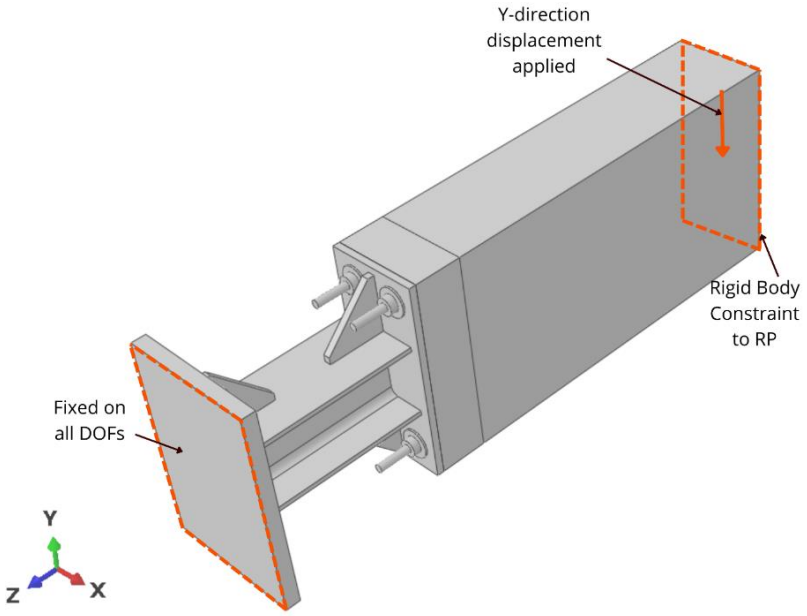


Figure 6.2. Boundary conditions and external constraints of the model.

6.1.2. Mesh definitions

The component parts were modelled through Solid Elements (C3D8RH: 8 nodes, 1 integration point, 3 degrees of freedom per node, Hourglassing problems - zero strain in integration point in bending problems). C3D8RH is an 8-node linear brick element but with reduced integration (normally using a scheme one order less than the full scheme to integrate the element's internal forces and stiffness with only 1 Gauss point), hourglass control using the artificial stiffness method (Flanagan and Belytschko, 1981).

The partition and mesh size varied for each component part. The elements experiencing the greatest deformation in the connection were the end-plate, the link, and the rods, which required a

finer mesh, with additional partitions around the rods. The mesh calibration was performed empirically, initially based on Iovane (2020) and refining the contact regions between the elements.

Initially, the investigation focused on models incorporating both partitioned and non-partitioned components. The implementation of partitioning in Abaqus confers several advantages, facilitating enhanced control over the mesh and allowing for the segmentation of complex parts into simpler regions, thereby enabling techniques such as structured or swept meshing. This approach results in more uniform mesh configurations and can enhance the accuracy and robustness of the analysis, mitigating convergence issues. However, it may also lead to increased processing times in certain scenarios. The primary partitions analyzed in the models included the end-plate, link, and timber beam components, with particular emphasis on delineating the contact regions between components and the areas transitioning from straight to circular geometries.

A comparative analysis of this comparison made on models with the same material properties and similar mesh element dimensions, revealed that the non-partitioned model was processed in slightly less time than its partitioned model. Specifically, the non-partitioned model exhibited a processing time of 93 minutes, while the partitioned model required 113 minutes, resulting in a time differential of 20 minutes, equivalent to a 21.5% increase in processing time for the partitioned model. Despite the shorter processing time associated with the non-partitioned model, the complexity of the component shapes necessitated numerous adjustments to the node organization in Abaqus, a requirement that was absent in the partitioned model. Consequently, in the non-partitioned model, the node arrangement did not adhere to appropriate symmetry, particularly around the openings, as illustrated in the Figure 6.3 depicting the end-plate and timber beam components. Due to these node adjustments, the accuracy of the non-partitioned model was inferior to that of the partitioned model when compared to the results obtained from experimental tests. A difference in initial stiffness and in yield and plastic moment between that model was observed, as shown in Figure 6.4. In light of these findings, the decision was made to utilize the partitioned model for further analyses.

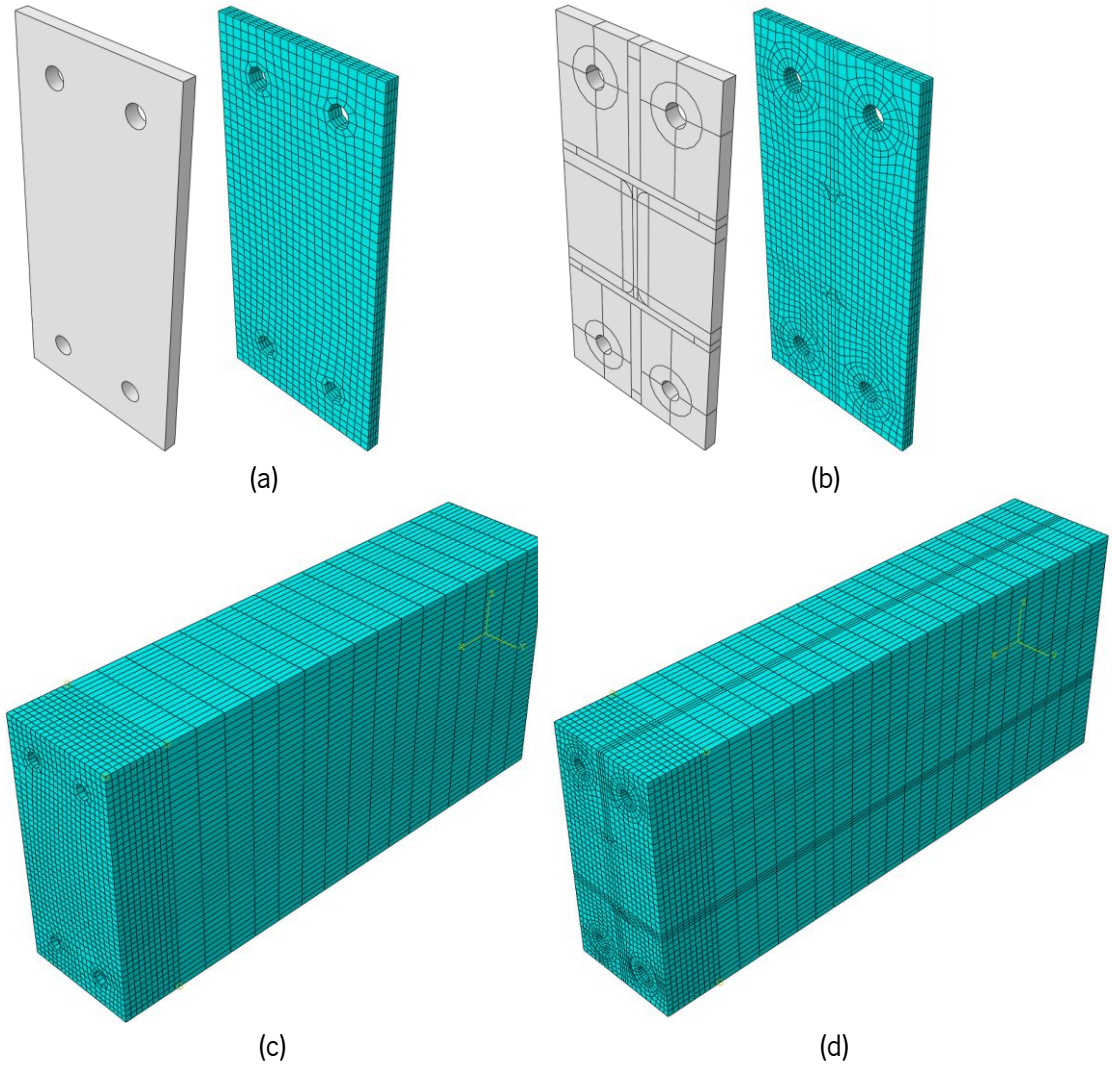


Figure 6.3. Comparison between non-partitioned and partitioned models (a) non-partitioned end-plate, (b) partitioned end-plate, (c) non-partitioned timber beam ,and (d) partitioned timber beam.

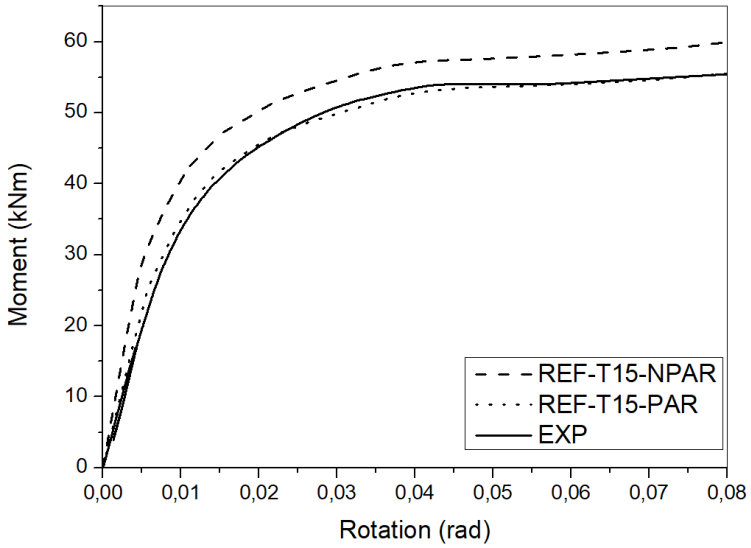


Figure 6.4. Moment-rotation curve for non-partitioned and partitioned models compared with experimental results.

In the investigation of mesh sensitivity in partitioned models, it was initially determined that processing time and accuracy were intricately linked to the mesh density of the contact interfaces of the end-late, link, and timber beam, as well as the thicknesses of the link flange and end-plate. Consequently, the study was concentrated on optimizing the mesh in these critical regions, considering the impact of element size on processing time and the resultant quality of the numerical outputs, as evidenced by the correlation between numerical and experimental results. The results of the analysis conducted on a computer equipped with an 8th generation Core i5 processor (Intel(R) Core(TM) i5-8300H CPU @ 2.30GHz) and 8GB of RAM are presented in Table 6.1 and Figure 6.5.

Table 6.1. Mesh dimensions of the components tested in portioned models.

End-plate		Link		Timber		
Face	Thickness	Face	Flange thickness	Face	Part 1	Part 2
5	2.5	5	1	5	5	50
10	5	10	2.25	10	10	100
20	7.5	20	4.5	20	20	200

Table 6.1 delineates the variations in element dimensions tested within the principal components. In the longitudinal direction of the timber, two distinct element thicknesses were employed: a smaller thickness for the unbonded length region extending up to 50 mm beyond the start of the glued length (designated as part 1), and a different thickness for the remainder of the timber beam (designated as part 2). The same thicknesses applied to the timber were also utilized for the rods. The specifics of the mesh discretization for the end-plate and link are illustrated in Figure.6.6. The mesh discretization of the rods was refined in the zones in contact with the end-plate and timber, employing a reduced element size of 4 mm in these areas.

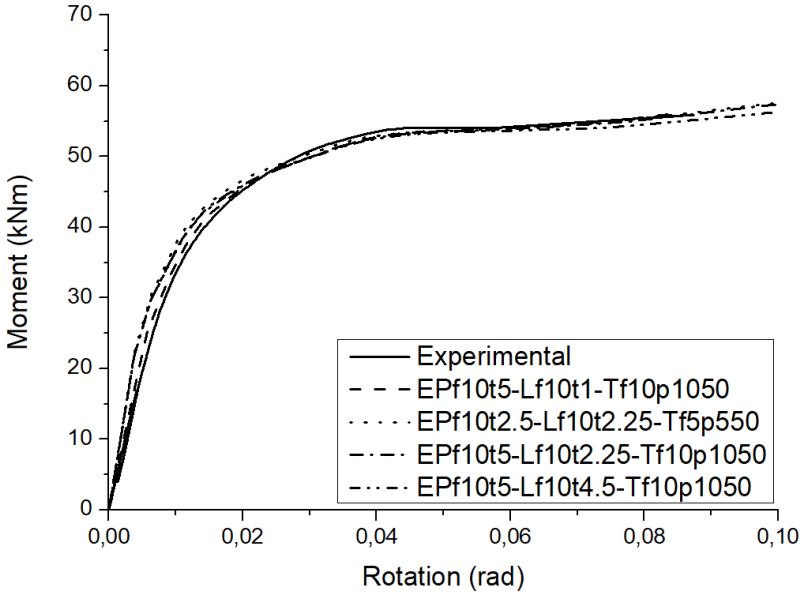


Figure 6.5. Mesh sensitivity analysis for main tested mesh dimensions.

The graph depicted in Figure 6.5 illustrates the outcomes of the main models tested with the mesh configurations outlined in Table 6.1. Models characterized by larger mesh dimensions exhibited shorter processing times, however, they demonstrated variations in accuracy with respect to initial rotational stiffness. Conversely, models with smaller mesh dimensions did not show considerable improvements in accuracy and resulted in extended processing times. The findings with the highest degree of accuracy in relation to experimental results are summarized in Table 6.2, while Figure 6.7 offers a comprehensive representation of the model configurations with the corresponding meshes.

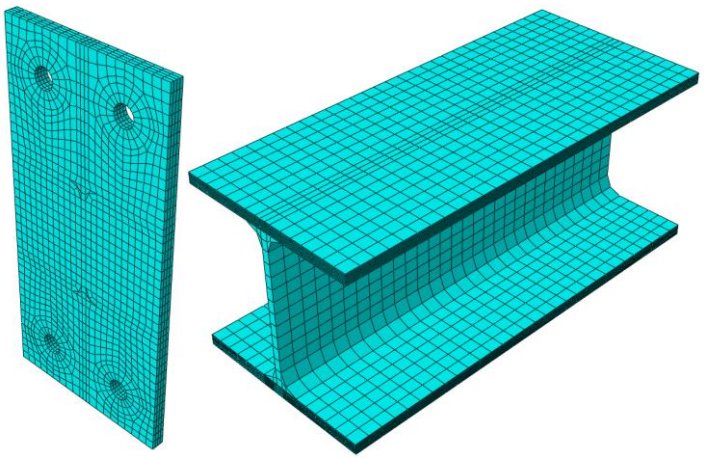


Figure.6.6. Mesh discretization of end-plate and link.

Table 6.2. Summary of mesh sizes of each part in mm.

Part	End-plate	Link	Rod	Timber	Stiffener
Front mesh size	10	10	4	10	10
Thickness mesh size	5	1	4	10	7.5
Length mesh size	10	10	4	50	10

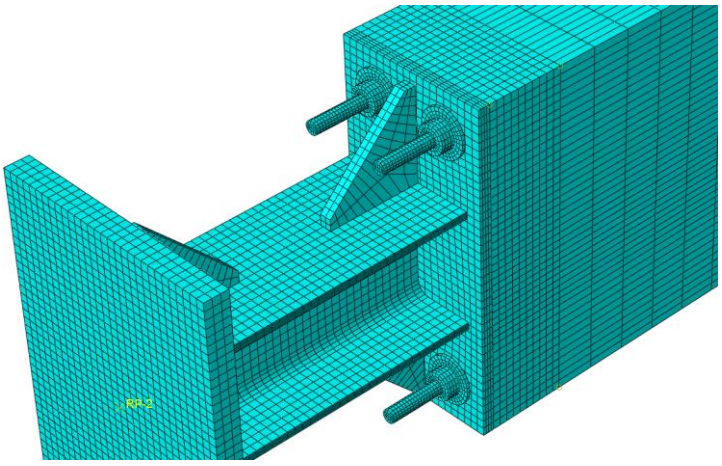


Figure 6.7. Abaqus model with mesh discretization.

6.1.3. Materials

For steel parts (end-plate, BiR, stiffeners and link), an isotropic hardening model was employed. The nonlinear material relationships used general parameters for stiffeners (strength class S235), nuts and washers (grade 8.8), and specific parameters determined through laboratory tests conducted for end-plate, link and threaded rods.

The engineering stress-strain values utilized in the numerical models are presented in Table 6.3, the material properties are calibrated using values close to mean values, and that are in the range of the tensile strengths of the end-plate and steel link samples, as described in Chapter 4. The stress-strain data implemented in Abaqus® was the true stress-strain behavior.

Table 6.3. Properties of steel applied in numerical modelling for model validation

Specimen/Model	Steel component	Young's Modulus (GPa)	Yield Strength (MPa)	Ultimate Strength (MPa)
t20	End-plate	200	367	491
t20	Link	200	258	381
t15	End-plate	200	356	484
t15	Link	200	276	402

The threaded rods applied were metric MGS 1000 from Rothoblaas, with strength class 8.8 for G1 joints and with strength class 4.8 for G2. Coupon tensile tests were conducted on 6 rod specimens extracted from each strength class, following ISO 6892-1:2019. For rods class 8.8, it was found a mean Young's Modulus of 200 GPa, a mean yield strength ($f_{y,mean}$) of 896.07 MPa (CoV 4.51%) and a mean ultimate strength ($f_{u,mean}$) of 1024.52 MPa, CoV 3.05%. The mean values mentioned above were applied in the numerical models. The glued laminated timber was a Norwegian spruce (*Picea abies*) classified with strength class GL24h, according to EN 14080:2013. It was modelled using elastic behavior, considering its anisotropic properties as engineering constants in Abaqus®, from strength class GL24h, as shown in Table 6.4.

Table 6.4. Anisotropic properties of timber beam (EN 14080:2013)

E1 (MPa)	E2 (MPa)	E3 (MPa)	ν_{12}	ν_{13}	ν_{23}	G12 (MPa)	G13 (MPa)	G23 (MPa)
11600	390	390	0.19	0.25	0.253	690	690	69

6.1.4. Interactions

All the components interact with each other through two types of interactions: contact interactions and constraints. In ABAQUS®, contact interactions define how surfaces interact when they come into

contact, including aspects such as friction, rigid contact, and separation. Constraints, on the other hand, impose specific relationships between regions, such as bond constraints, rigid body constraints, or coupling constraints.

Based on Karagiannis *et al.* (2017) and Iovane (2020), the interactions between the rods and the washer, the rods and the end-plate, unbonded length and rods, the end-plate and the washer, the end-plate and the timber beam was defined as a "Surface to Surface Contact", imposed by the general contact algorithm, which uses hard contact formulation, using the penalty method to approximate the hard pressure-overclosure behavior that acts in the normal direction to resist penetration, with a friction coefficient equal to 0,4 for the steel material and 0,3 for the timber material. While the interaction between the link and the end-plate, the rods and the beam, the washer and the nut, the stiffeners with end-plate/link, and the link and the end-plate are "Tie Constraints", schematizing the glue (rod-beam) and the welding (shank-nut and link-end plate) as rigid connections.

These interactions were modelled by utilizing the contact pair option of a "master" and "slave" surfaces in ABAQUS. To this end, the "master" surface was chosen to be the larger or the stiffer surface, whereas the smaller or relatively more flexible surface was defined as "slave". In this FE package, contacts remain normal to the "master" surface at the smallest distances from the nodes. The applied master-slave order (first component as master and second as slave), and general view of these interactions is presented in Figure 6.8.

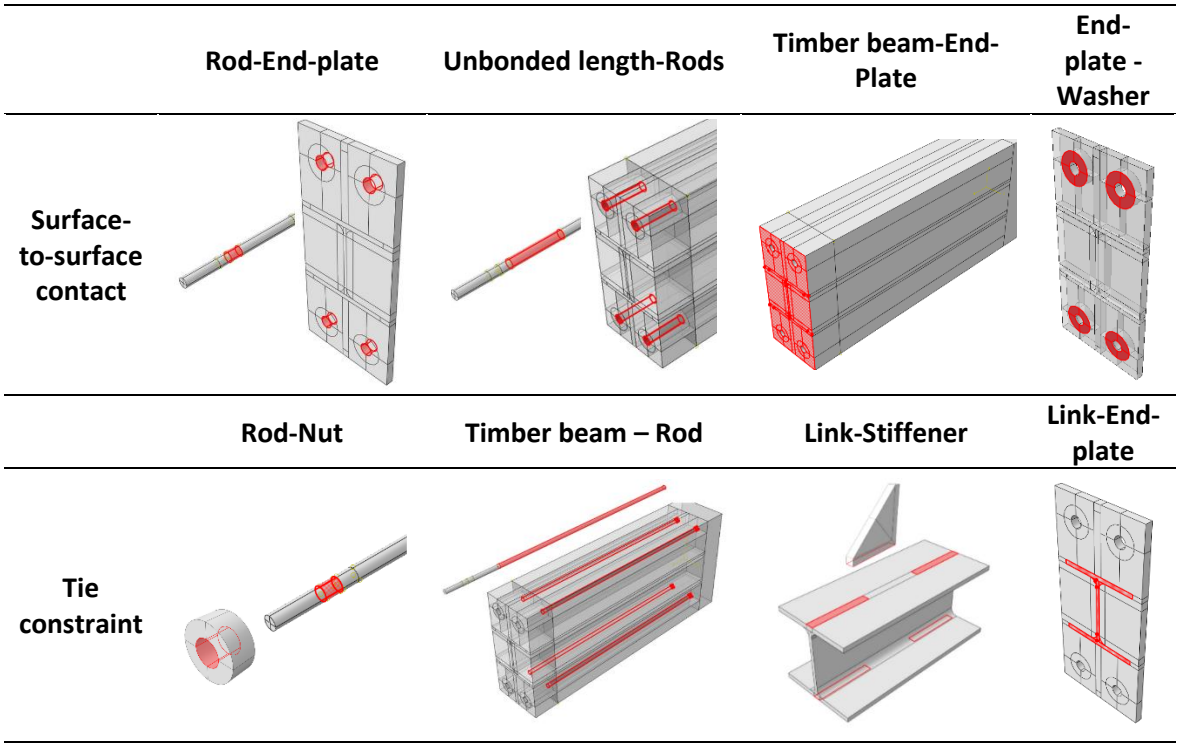


Figure 6.8. Interactions between main components

6.1.5. Model validation

The numerical results using the modelling strategy adopted are compared with the experimental test results. A detailed analysis is performed for the global and components behavior. First, the moment-rotation curves obtained from numerical analysis for the specimens mentioned in Section 6.1.1 were compared with the mean experimental results. For the two models studied, the curves showed a good fit with the experimental results (Figure 6.9), exhibiting an error of 1.22% and 2.05% for specimens t15 and t20, respectively, in the initial rotational stiffness, and 0.25% and 0.14% for the yield moment.

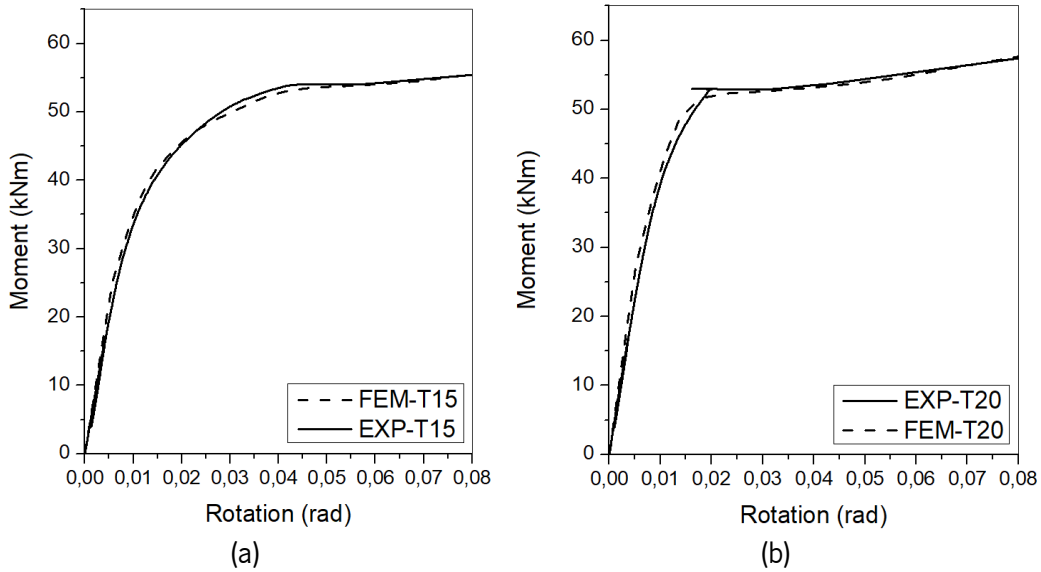


Figure 6.9. Moment-rotation curves comparison for (a) Joint t15 and (b) Joint t20.

The failure hierarchy was defined based on the yield strength (f_y) of each component. The typical engineering stress-strain curve for hot-rolled carbon steel, as illustrated in Figure 6.10, starts in an elastic region characterized by Young's Modulus (E), f_y, and ε_y. This is followed by a horizontal plateau that marks the onset of plasticization until the strain hardening point (ε_{sh}) is reached. Beyond this point, the strain hardening phase begins until the steel reaches its ultimate strength (f_u), at which point failure occurs.

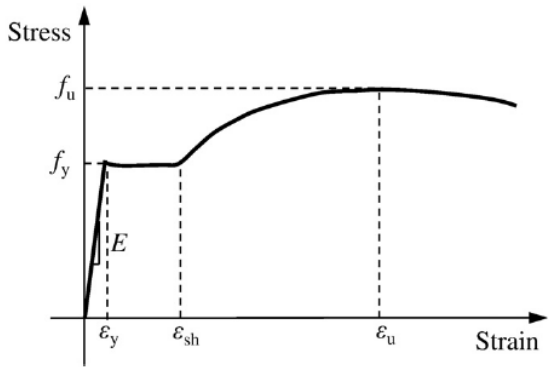


Figure 6.10. Typical engineering stress-strain curve for hot-rolled carbon steel (Yun and Gardner, 2017).

In the type of joint under study, the main failure modes are related to the link, the BiR, and the end-plate. The typical shape of the moment-rotation curves for each of these failures is shown in Figure 6.11. The link exhibits a moment-rotation curve for monotonically increasing moment that closely resembles the shape depicted in Figure 6.10. Since this component is subjected to bending, the outer fiber reaches f_y first. As the moment increases, the remaining regions begin to plasticize, leading to the development of a plastic hinge near the stiffeners. Consequently, this plasticization is represented in the moment-rotation curve of the joint as a horizontal plateau region (Figure 6.11 (a)). When failure occurs first in the BiR, the moment-rotation curve shows a sharper drop, with no significant deformations before ultimate failure (Figure 6.11 (b)). Regarding the end-plate, as bending occurs in the direction transverse to the moment measured in the curve, it is not possible to directly capture the horizontal plateau that demarcates plasticization. However, the start of non-linearity in the moment-rotation curve can be easily identified, corresponding to the onset of yielding in this component. Failure occurs when the ultimate strength is reached (Figure 6.11 (c)). When joint failure occurs due to the failure of this component, there is greater energy dissipation and, consequently, a longer plasticization region between the start of yielding and ultimate failure.

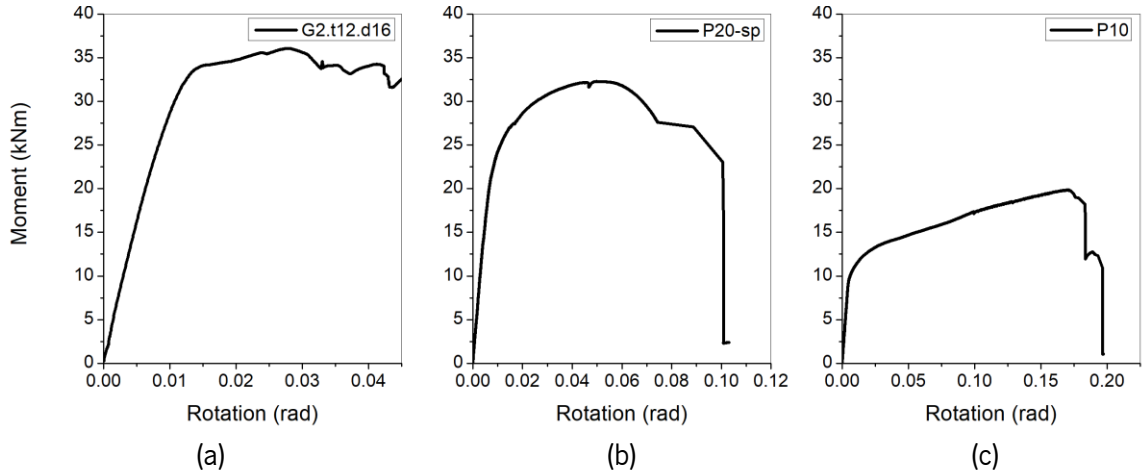


Figure 6.11. Typical moment-rotation curves for failure in different components (a) Link, (b) BiR (Andreolli *et al.*, 2011), and (c) End-plate (Andreolli *et al.*, 2011).

Figure 6.12 shows the moment-rotation curves for the t15 and t20 models, indicating the yielding and plasticization points of the relevant components. In the t15 model, the end-plate begins to yield before the link. In contrast, the t20 model, which features a thicker end-plate, exhibits first the link yielding, this results in less rotation of the joint. It is also important to note that complete plasticization of the link cross-section occurs at the same bending moment magnitude for both models, t15 and t20, since the cross-section and length of the link are identical in both cases.

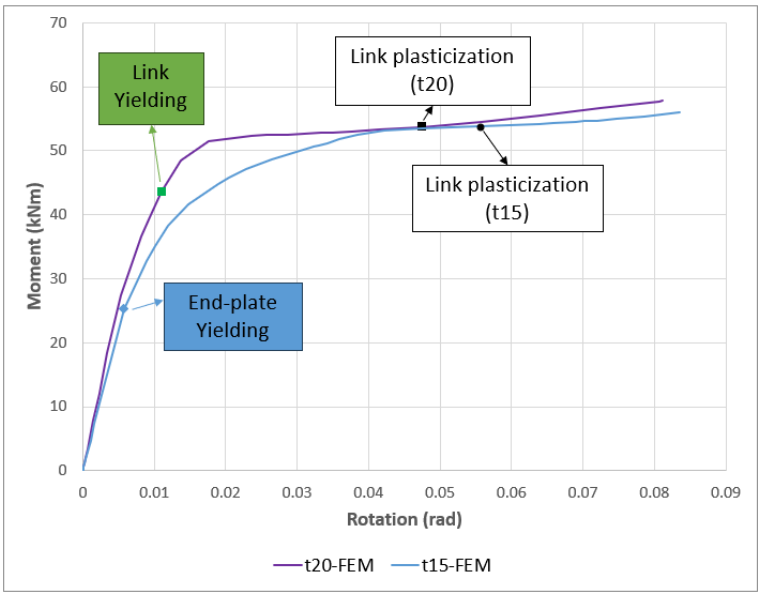


Figure 6.12. Moment-rotation curves and key identifications for relevant components.

The tensile (positive) and compressive (negative) stresses obtained from the FEM at the instant of end-plate yielding in t15 model and link yielding in t20 are presented in Figures 6.13 and 6.14, respectively.

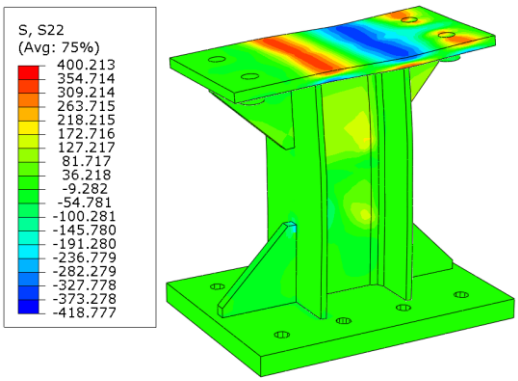


Figure 6.13. Stresses when the end-plate started yielding in t15 model, at Moment of 27.60 kNm and load step 0.024. Stress units in MPa

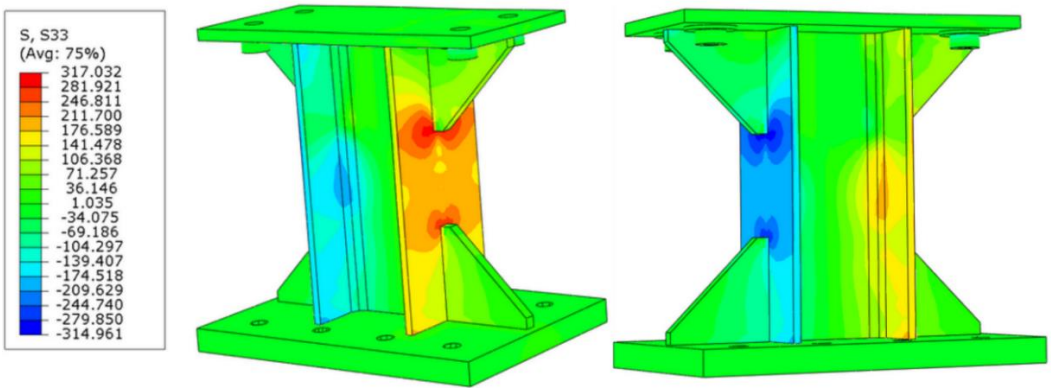


Figure 6.14. Stresses when the link started yielding in t20 model, at Moment of 43.63 kNm and load step 0.150. Stress units in MPa.

The failure mode obtained from the numerical model was consistent with the experimental results, and the failure hierarchy for the studied specimens occurred as expected. Figure 6.15 shows that the failure of joint t15 resulted from the plasticization of the link and the end-plate highlighted in red. It is indicated by the horizontal plateau observed in the moment-rotation curve (see Figure 6.10) and the sharp rotation in the region near the stiffeners. In this case, there was no buckling of the compressed side. While the yielding of the end-plate can be seen from the yield lines (represented by AC YIELD in Abaqus) and the gap between the end-plate and the timber beam.

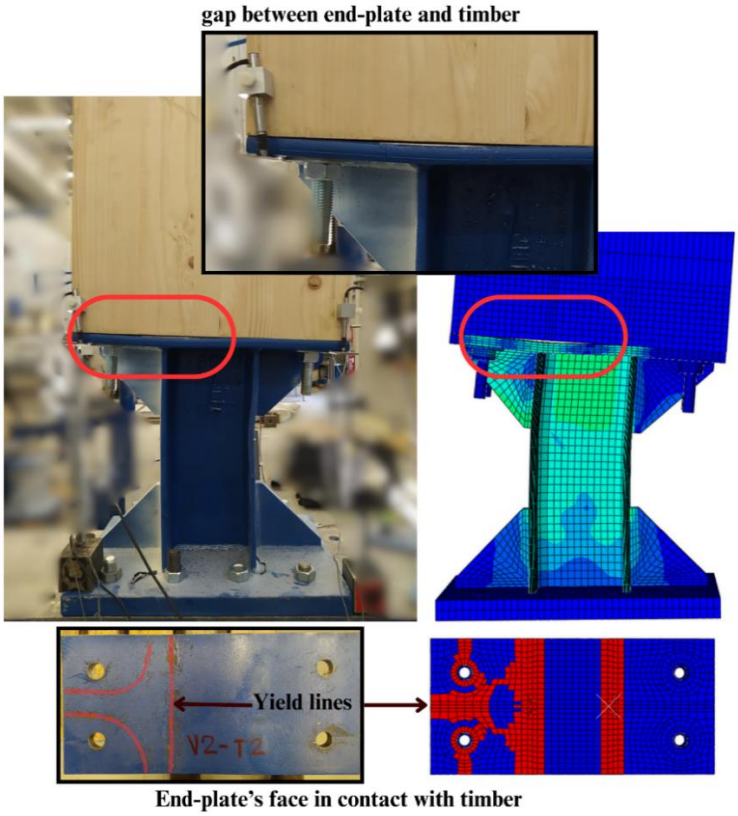


Figure 6.15. Comparison between experimental (left) and numerical (right) failure mode of joint t15.

Figure 6.16 shows the failure mode of joint t20, which is related to the plasticization of the link, as indicated by the plastic hinge formation highlighted in red. Additionally, there was no plasticization of the end-plate, as evidenced by the absence of yield lines. From these comparisons, it can be concluded that this numerical model is suitable for simulating the initial rotational stiffness, yield moment and failure modes of the stiffened end-plate moment-resisting steel-timber joints with bonded-in rods.

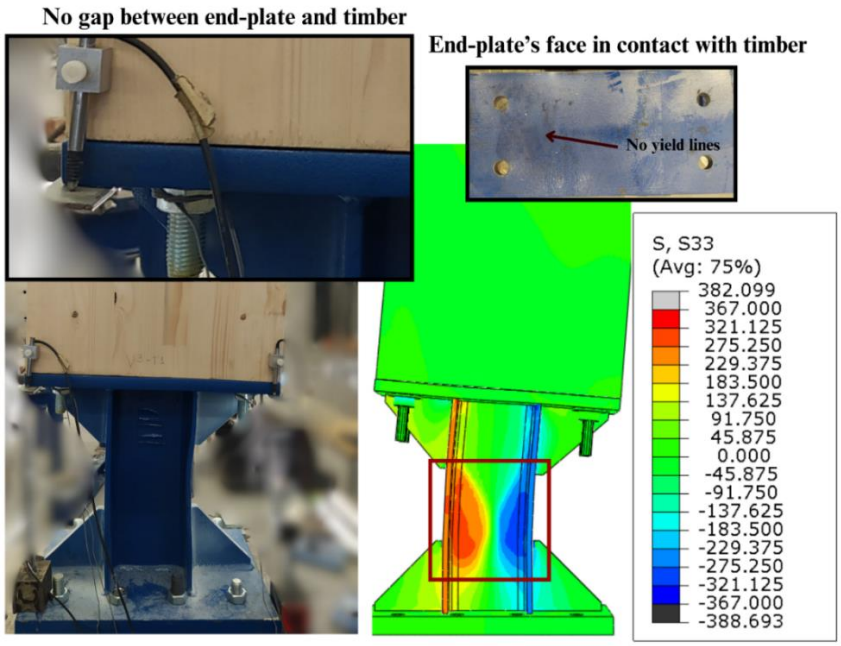


Figure 6.16. Comparison between experimental (left) and numerical (right) failure mode of specimen t20.

6.2. Parametric analysis

Based on the developed FE models, a parametric analysis was conducted to investigate the potential applicability of the analytical procedure developed using the component method, presented in Chapter 5. Specifically, the analysis aimed to determine the parameter ranges in which the method demonstrated the greatest accuracy, using a set of geometries commonly applied in this type of joint. Additionally, the goal was to identify which parameters are critical to initial stiffness, yield moment, and ultimate moment of the joints. To facilitate parametric studies and execute a series of simulations, a Python script for ABAQUS was created. Monotonic analyses were performed on a total of 972 moment-resisting steel-timber joints, varying only one of the following parameters on each model: end-plate thickness, BiR diameter, link cross section, link length, height of the end-plate and timber beam, presence of stiffeners, and number of BiR rows. The dimensions/characteristics applied to the parameters of the joints are summarized in Table 6.5. The nomenclature of the models were defined using the capital letter presented in Table 6.5

Table 6.5. Parameters and dimensions for the joints

End-plate thickness (T) (mm)	BiR diameter (D) (mm)	Link cross section (HEA)	Link length (L)(mm)	Height of the end-plate and timber (H)(mm)	Presence of stiffeners (S)	BiR rows (NBr)
8, 16, 24	M12, M16, M20	HEA120, HEA160, HEA200	300, 400, 500	360, 420, 480	Yes, No	2, 4

It is important to emphasize that while some geometric parameters were maintained, other distances were adjusted due to variations in the main parameters listed in Table 6.5. The position of the link and the stiffeners was consistently centered among all the joints, as was the horizontal distance between the BiRs. The distance between the center of the external BiR and the face of the end-plate was kept at 50 mm in both the vertical and horizontal directions. However, the vertical position and dimension of the stiffeners, as well as the vertical position of the internal BiR varied according to the link cross-section, as shown in Figure 6.17 for models with a height equal to 360 mm (in gray) and BiR M20, changing the link cross section (in blue) from HEA200 to HEA160. These distances were adjusted in order to avoid the plug shear failure of the timber in a region with several BiRs (group failure).

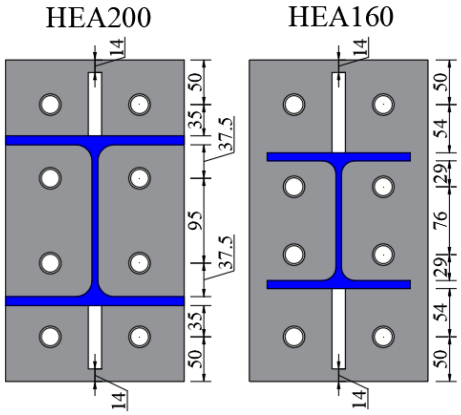


Figure 6.17. Variations on the stiffeners and internal BiR due to the link cross section parameter. Dimensions in mm.

6.2.1. Critical parameters for mechanical behavior

The joint under study consists of three macro-components (link, connection, and timber beam) and several active components. As mentioned in the analytical procedure in Chapter 5, the moment resistance of the joint corresponds to the moment resistance of the weakest macro-component, indicating that the joint follows a hierarchy of failure among the macro-components. Regarding the initial rotational stiffness of the joint ($S_{j,ini}$), there is a simultaneous contribution from all active components. Due to the complexity and versatility of the joint, it is important for the designer to understand which parameters have the greatest influence on the mechanical behavior of the joint to optimize its design.

To determine which input parameters most influence the initial rotational stiffness and ultimate moment results, the relative percentage variation of each output parameter was calculated by changing each input parameter individually while keeping the others constant. Each unique

combination of the other parameters defines a group, within which the variable parameter takes on the available values according to Table 6.5. The means and medians of the relative variation values were then calculated. Based on these values and the identification of outliers, the boxplots shown in Figures 6.18 and 6.19 were constructed.

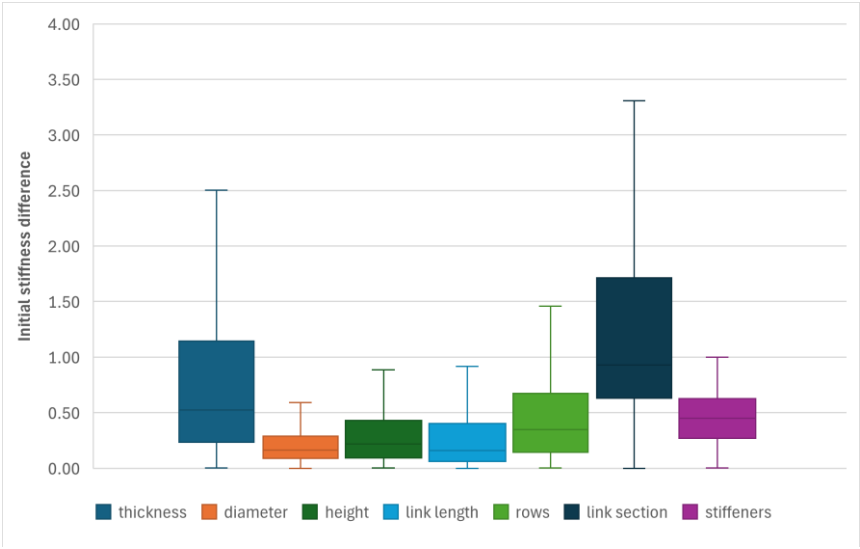


Figure 6.18. Statistical variation of initial rotational stiffness for each input parameter.

Based on Figure 6.18, it can be inferred that the parameters of the link section, end-plate thickness, the presence of stiffeners, and the number of BiR rows exert the most substantial influence on joint initial rotational stiffness. The link section exhibited a maximum variation of 330.79%, with the third quartile recorded at 171.26%, thus establishing it as the critical parameter in initial rotational stiffness. The second most influential parameter was the end-plate thickness, which demonstrated a maximum variation of 250.16%, with the third quartile at 114.56%.

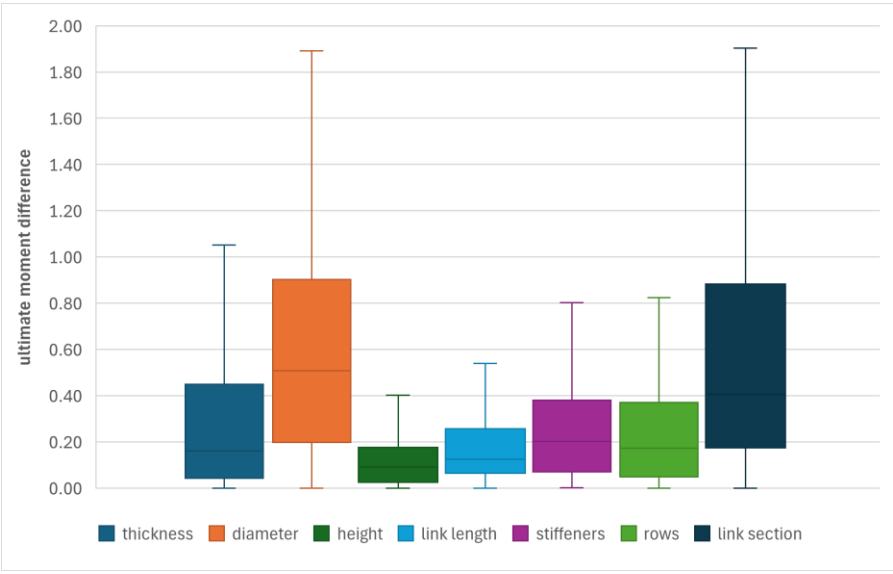
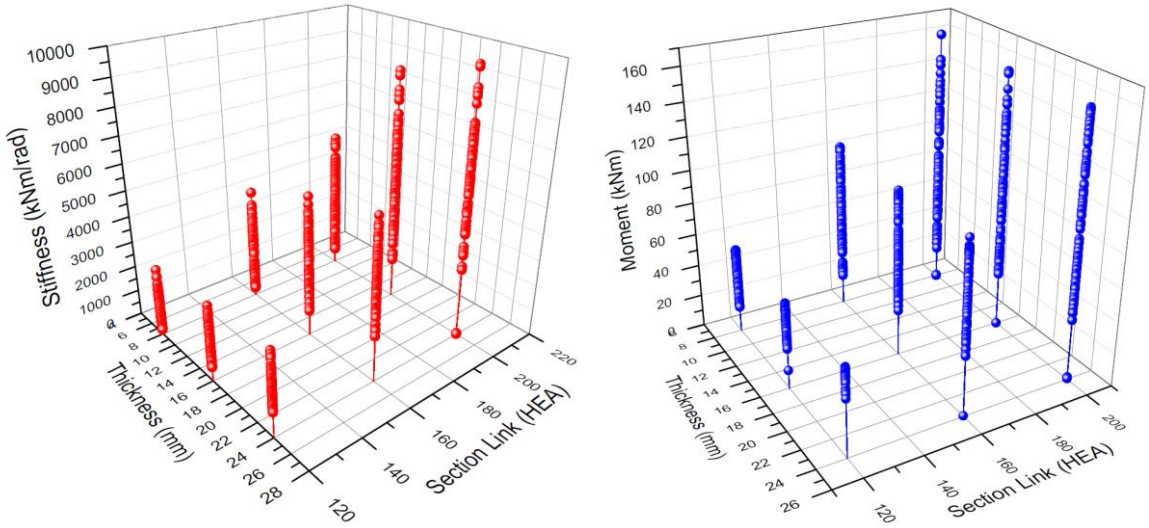


Figure 6.19. Statistical variation of ultimate moment for each input parameter.

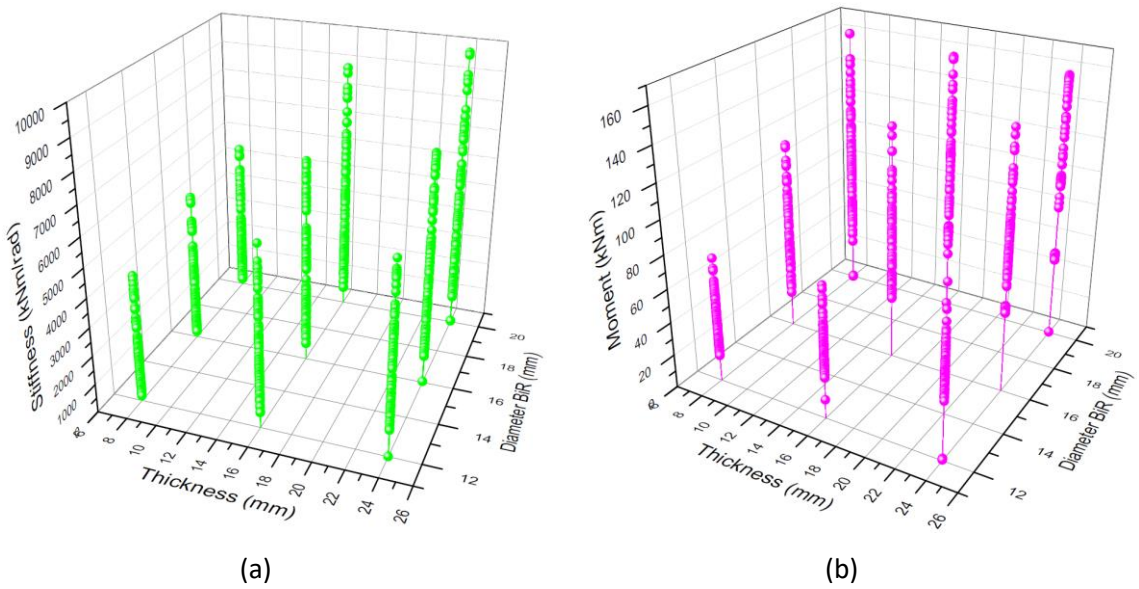
From the data presented in Figure 6.19, it can be inferred that the parameters of link section, BiR diameter, end-plate thickness, the presence of stiffeners, and the number of BiR rows have the most significant influence on joint moment. In this instance, both the link section and BiR diameter had a pronounced impact, reaching a maximum difference of 190.32% and 189.05%, respectively, with the third quartile at 88.27% and 90.13%. In contrast to initial rotational stiffness, BiR represents a critical parameter in joint moment, particularly when combined with larger link sections and thicker end-plates. Furthermore, end-plate thickness also contributed to the overall impact, achieving a maximum variation of 105.20% with a third quartile of 44.80%.

The Figures 6.20 and 6.21 illustrate the combined influence of two parameters on the mechanical response of the connection, based on the organization of results from all the developed parametric models. The graphs can be interpreted by observing the variation of the result along the z-axis in relation to the variations of the parameters on the x-axis and y-axis. When a trend toward constancy appears, it indicates that the corresponding parameter is less relevant to that mechanical response. From this, it is evident that the end-plate thickness significantly impacts the initial rotational stiffness, although its relevance diminishes at this stage. Additionally, the results presented in these figures support the findings related to the link section and diameter parameters.



(a) (b)

Figure 6.20. Influence of end-plate thickness and link section parameters on (a) initial rotational stiffness (b) ultimate moment.



(a) (b)

Figure 6.21. Influence of end-plate thickness and BiR diameter parameters on (a) initial rotational stiffness (b) ultimate moment.

Some characteristics of the joint's mechanical behavior contribute to the link section being the critical parameter in its performance. Firstly, as explained in Chapter 5, the failure hierarchy indicates that joint resistance refers to the yield moment resistance of its weakest component. Therefore, since timber beam failure is always avoided, when there is a connection (macro-component) with high moment resistance, joint resistance depends directly on the link section. Regarding the initial rotational stiffness, the link section has a significant impact for two reasons. First, the height of the link changes with variations in the section, and as the bending stiffness of the joint is assessed, the influence of height becomes extremely significant. Second, this impact is also related to the free distances involved in the interaction with the end-plate. The behavior of the T-stub is closely related to the moment resistance of the plate, which depends on the free distances available for the rotation of the end-plate.

To illustrate the aforementioned aspects, the joints from models M9 and M18 have an end-plate thickness of 24 mm, a BiR diameter of 20 mm, a height of 360 mm, and a link length of 300 mm, yet they exhibit significantly different mechanical behavior simply by changing the link section from HEA120 (M9) to HEA160 (M18). As shown in Figure 6.22, the difference in initial rotational stiffness between the two is 84.7% (M9 = 3045.73 kNm/rad, M18 = 5625.35 kNm/rad), and the difference in ultimate moment is 92.65% (M9 = 49.97 kNm, M18 = 96.26 kNm). Furthermore, at the same level, the axial stress and rotation values for each joint are quite different. At level 1, the M9 link has already reached plasticization with clear plastic hinge formation, while the M18 remains in the elastic

regime. The results for level 2 show that M9 is already in the ultimate limit state (failure), while M18 has only reached yielding at the link flange.

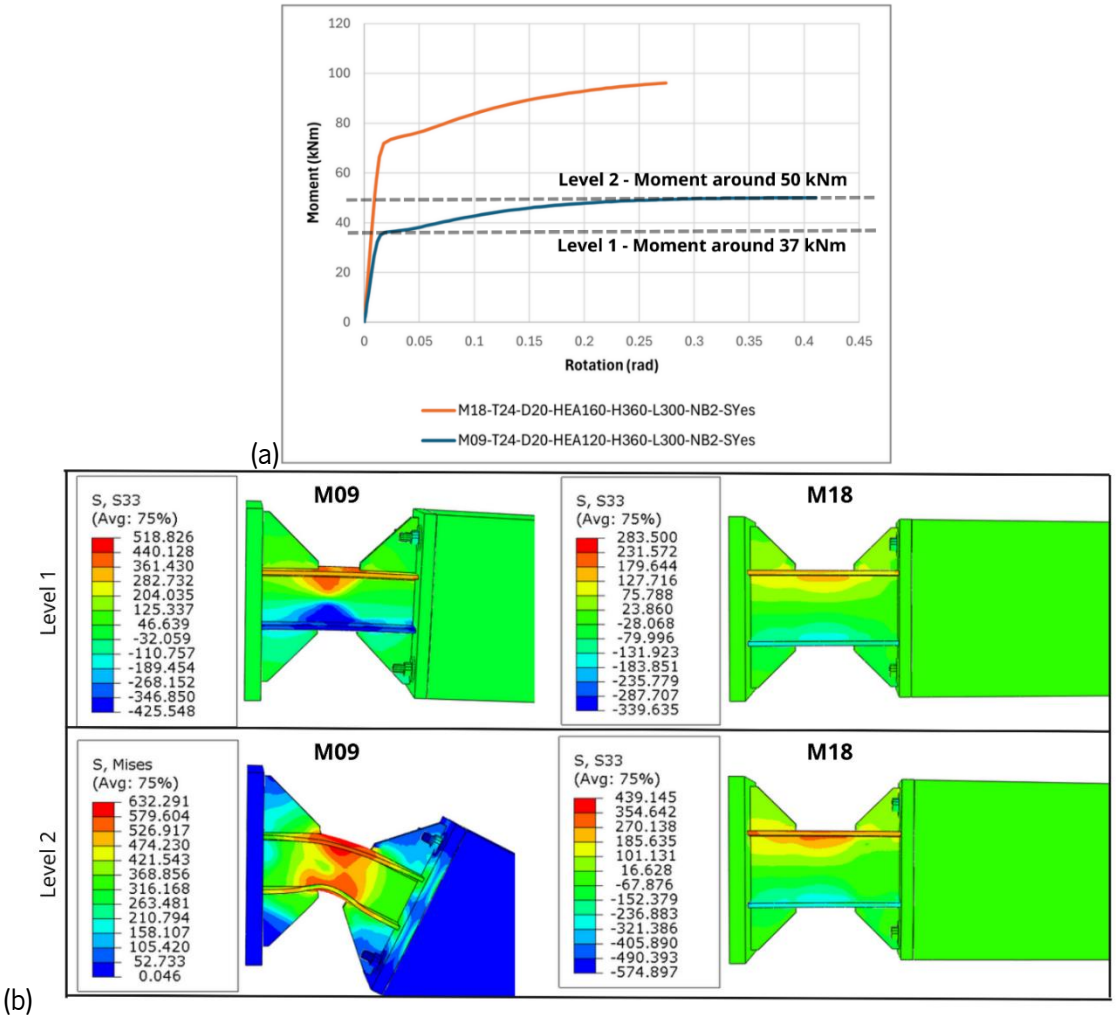


Figure 6.22. Comparative analysis between models M9 and M18 for (a) moment-rotation curves and (b) stress-rotation diagrams.

The conclusion of this analysis indicates that the initial rotational stiffness is more sensitive to factors such as the link section, end-plate thickness, and the presence of stiffeners. Conversely, the ultimate moment exhibits greater sensitivity to the link section, the BiR diameter, and the end-plate thickness. From this parametric study it can be concluded that this joint has the potential to achieve high levels of rotational stiffness and ultimate moment, since a maximum initial rotational stiffness of 9808.49 kNm/rad was obtained in model M513 (T24-D20-HEA200-H360-L300-SYes-NBr4) and a maximum ultimate moment of 157.82 kNm in model M918 (T24-D20-HEA200-H360-L500-SNo-NBr4). Then, it is recommended to prioritize the incorporation of stiffeners, a larger link section, and appropriate thicknesses to optimize stiffness. Additionally, adjustments to the BiR diameter and link section can enhance the moment capacity. Furthermore, it is observed that the link section

significantly influences the mechanical performance of the joint when paired with greater thickness and diameters.

6.2.2. Proposed analytical procedure comparison

Analytical results were generated using the procedure based on the component method (CM) outlined in chapter 5 of this thesis, while maintaining the same characteristics applied in the numerical models.

The comparison between the FE results and the CM results was analyzed using a scatter plot with 1:1 reference line. In this graph, the central dashed line serves as a reference, indicating perfect agreement between the results. Data points situated above this line suggest that CM overestimates the FE results, whereas data points below the line indicate an underestimation. Ideally, in the context of an analytical calculation method, most predictions should fall below the FE results obtained, i.e. below the line. For clarity, the results have been categorized into four groups based on the presence of stiffeners and the number of BiR rows, i.e, stiffened joints with 2 BiR rows (S2BR), unstiffened joints with 2 BiR rows (U2BR), stiffened joints with 4 BiR rows (S4BR), and unstiffened joints with 4 BiR rows (U4BR). The results for the initial rotational stiffness (Sj,ini) are shown in Figure 6.23 for all groups of joint studied.

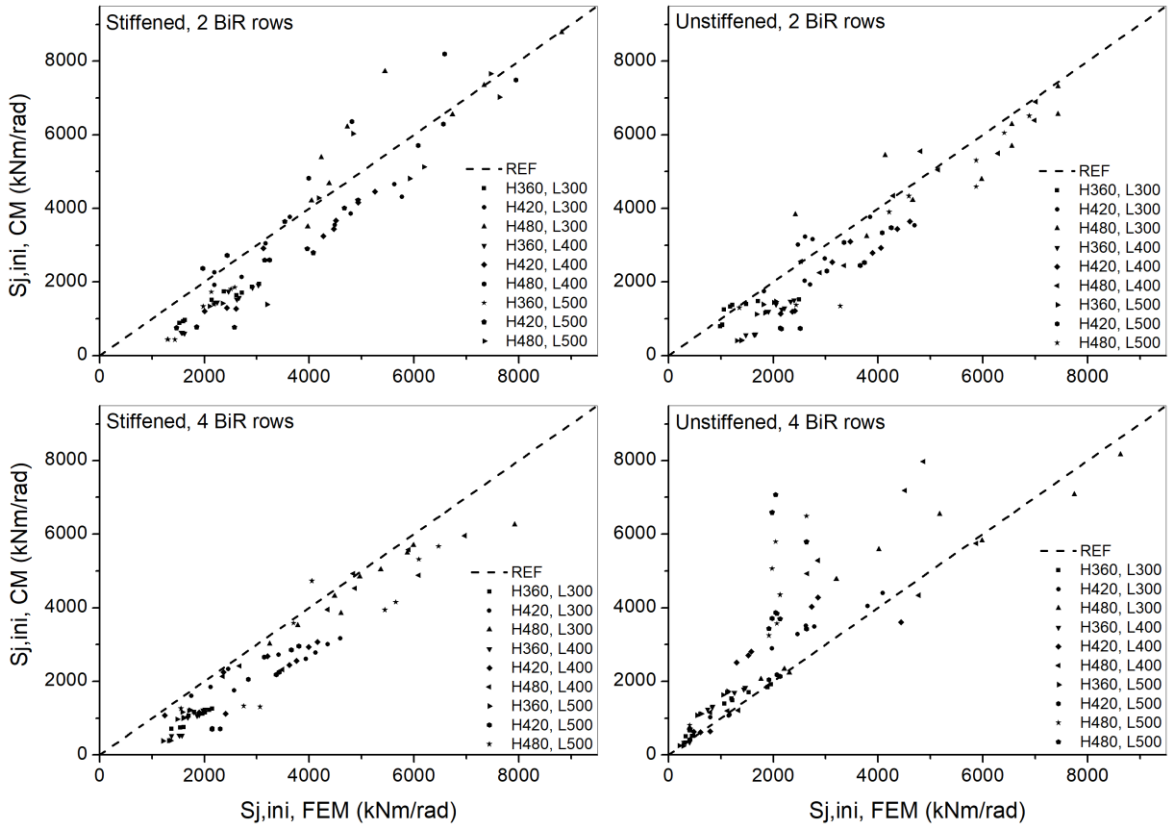


Figure 6.23. Comparison of initial rotational stiffness for S2BR, U2BR, S4BR, U4BR between FE and CM

The results suggest that the proposed calculation procedure accurately predicts the joint initial rotational stiffness across the wide range of geometries studied. Furthermore, for S2BR, U2BR and S4BR joints most results fall below the reference line, demonstrating that CM leans towards a conservative approach. However, for U4BR joints, the predictions derived from the CM exhibited a greater deviation, with a higher number of results situated above the reference line. This overestimation in predictions is observed in joints characterized by an increased end-plate height, which results in a larger free distance between the outermost row of rods and the link flange.

The comparison results illustrated in Figure 6.24 concerning the joint yield moment (My) indicate that the proposed analytical model based on CM demonstrated a high degree of accuracy in predicting outcomes. The majority of the results closely align with the reference line, with only a limited number exhibiting overestimations within the U4BR group.

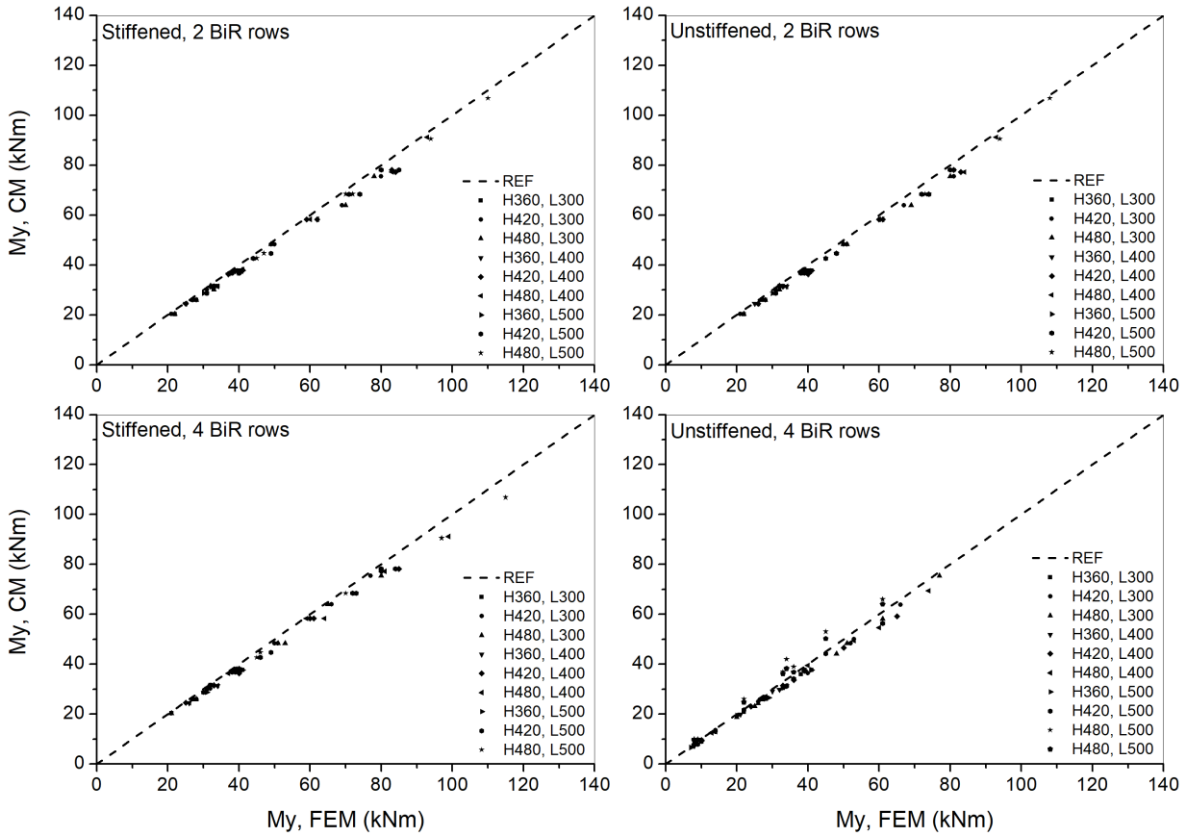


Figure 6.24. Comparison of joint yield moment for S2BR, U2BR, S4BR, U4BR between FE and CM.

Unlike My, the results of the comparison between FE and CM for the joint ultimate moment (Mu) (Figure 6.25) indicate that the analytical method, while prioritizing safety, significantly underestimated the results, particularly for the groups with four BiR rows, S4BR, and U4BR. In this context, the results exhibiting the largest percentage differences from the reference are associated with the longer link lengths and greater link heights, where nonlinear interactions between the steel and timber components are more influential.

This discrepancy primarily arises from the simplified assumptions of the component method that did not fully capture the nonlinear stress redistribution and geometric effects that occurred in the joint under elevated load levels. Specifically, the plastic deformation of the steel link and end-plate, as well as the nonlinear load transfer through the BiR rows, were not accurately represented within the current analytical formulation. As a result, the procedure predicted conservative values of the ultimate moment.

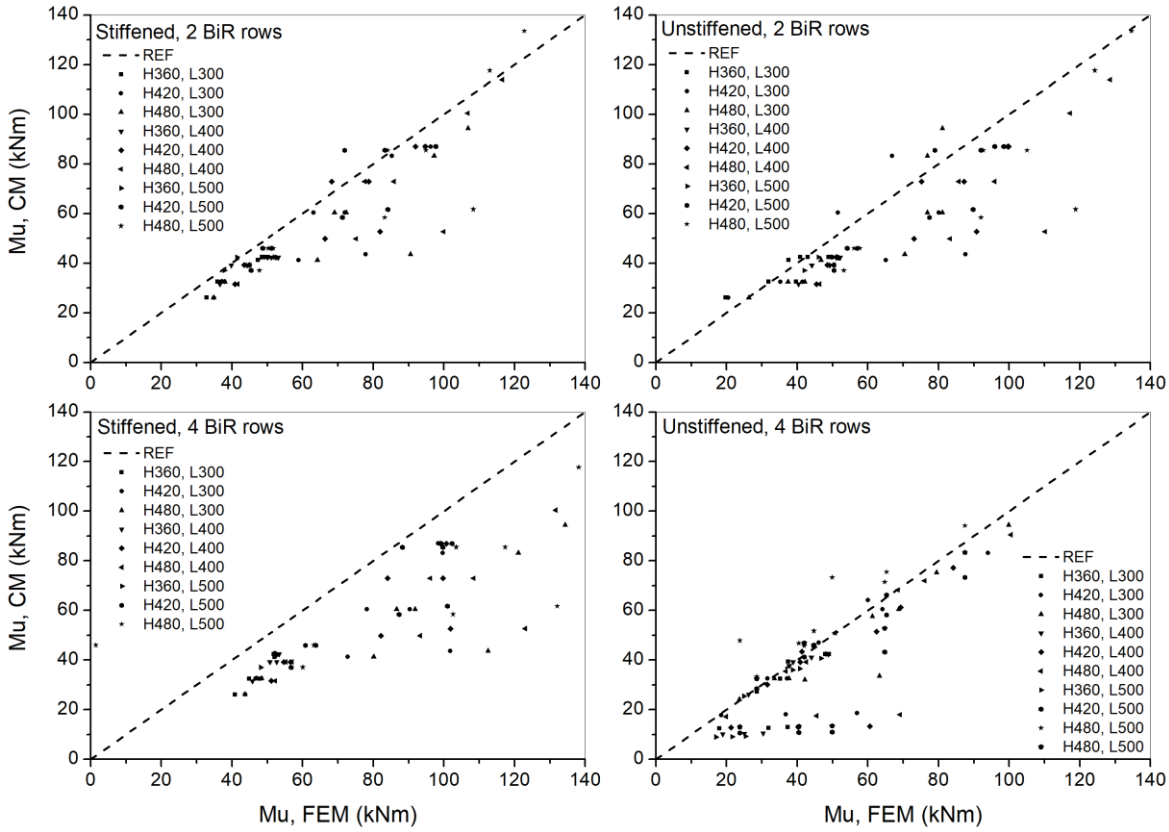


Figure 6.25. Comparison of joint ultimate moment for S2BR, U2BR, S4BR, U4BR between FE and CM.

In conclusion, the parametric analysis conducted on 972 models of moment-resistant steel-timber joints, utilizing a set of proposed joints characterized by geometries commonly employed in engineering projects, has demonstrated that the proposed analytical method based on the component method can accurately predict both the initial rotational stiffness and the yield moment of the joint across a wide range of geometries and for nearly all the groups studied, with the exception of the initial rotational stiffness for U4BR. Furthermore, the method demonstrates a reliable capacity to predict the ultimate moment of the joint, as it tends to underestimate the results in comparison to the models validated by finite element analysis (FE), with less satisfactory accuracy than that observed for the other parameters examined.

CHAPTER 7

CONCLUSIONS AND FUTURE DEVELOPMENTS

This chapter provides a summary of the study conducted in this thesis, highlighting the primary contributions and proposing future developments based on the experiences and results obtained.

7.1. Conclusions

Ductile moment-resisting steel-timber joints are essential in the design of mid- and high-rise timber buildings, as their incorporation facilitates internal forces redistribution, enhances robustness, increases both overall and lateral stiffness, and prevents brittle failures that could jeopardize the structural integrity of the building. To encourage the adoption of these joints, an analysis was conducted on the ductility and mechanical performance of various moment-resisting steel-timber joints, with a particular focus on those utilizing bonded-in rods and dowel-type connections.

In the context of mechanical performance, dowel slotted-in plate joints, which are extensively utilized, have demonstrated commendable rotational capacity and ultimate moment outcomes when reinforced with self-tapping screws (STSs). Nevertheless, these joints frequently exhibit brittle failure modes that adversely affect the timber. Bonded-in rod joints, which employ direct connections with the timber, have been observed to experience brittle and premature failures. However, the integration of steel links or steel boxes with the bonded-in rods significantly enhances the mechanical performance of the joints, achieving elevated values of rotational capacity and moment resistance. Typically, in these types of connections, the steel link or box section yields prior to the failure of the bonded-in rods, resulting in ductile failure modes.

The evaluation of ductility was conducted adopting the equation proposed by EN 12512:2001 and Equation (2.2). The results indicated that joints with bonded-in rods exhibited superior performance, likely attributable to the significant influence of the end-plate and steel link on the joint's plasticization. Conversely, dowel slotted-in plates joints, despite their commendable mechanical behavior, demonstrated average ductility values. This is due to increased rotation at yield, which results in small plastic regions where energy dissipation is more pronounced. Based on these findings, the thesis concentrated the investigation on moment-resistant steel-timber joints with stiffened end-plates and bonded-in rods, as they displayed the highest ductility values and exhibited coupled behavior among

their components. This allowed for the identification of several failure modes that have not yet been thoroughly addressed in the literature.

Previous research has demonstrated that end-plate moment-resisting steel-timber joints, incorporating steel links and bonded-in rods, exhibit significant energy dissipation capacity through the plastic deformation of the end-plate (Tomasi *et al.*, 2008; Andreolli *et al.*, 2011) and the link (Iovane, 2020). Nonetheless, these investigations did not examine the joints under conditions where the end-plate, link, and bonded-in rods undergo simultaneous deformation, as opposed to scenarios where one component fails while the others are oversized. A comprehensive understanding of the structural behavior of the joint in this optimized context would facilitate enhanced utilization of the load-bearing capacity of the most critical components. To this end, a more profound comprehension of the components is required, alongside the development of a more precise calculation procedure. The component method has been identified as the most promising approach for yielding practical and reliable results for the joint. Furthermore, it was imperative to conduct experimental evaluations on specific components as well as the entire joint. In summary, tensile tests were administered on the steel elements, pull-out tests on the bonded-in rods (BiRs), tensile tests on the threaded rods secured with nuts and washers, comprehensive compression tests on GLT, and full or partial compression tests on the T-stub GLT component. Additionally, tests were performed on 15 full-scale joints under monotonic loading, utilizing conventional transducers and Digital Image Correlation (DIC). These experiments, in conjunction with existing knowledge from other studies on the joint, produced results that revealed diverse and versatile structural behaviors for this joint type. The principal findings of the experimental studies include:

— In examining the structural behavior of the T-stub compressing GLT component, it is observed that the T-stub flange compresses the timber in a non-uniform manner, exerting greater pressure in the central region and progressively decreasing towards its ends. The timber's reaction results in the lifting of the T-stub flange edges, leading to a gradual reduction in the contact area. Consequently, the relative edge displacement was found to be greater when the flange thickness (stiffness) was smaller. It was identified that although GLT possesses lower compressive strength and stiffness compared to steel, the predominant failure mode in nearly all specimens studied was the yielding of the T-stub flange, attributed to its limited stiffness and the concentration of stresses in the central region of the GLT.

- For BiRs, the emphasis was placed on the component's strength to prevent brittle failure in the connection. Most of the failure modes discussed are brittle, with the exception of the tensile failure of the rods, which occurs post-yielding. Among the brittle failure modes, shear failure of the wood adjacent to the bondline typically exhibits the highest resistance values, while other modes should be avoided. Experimental tests on the threaded rods (Section 4.2) revealed that the ratio between the experimental ultimate force (Pu,mean) and the theoretical ultimate force (Fu) reached a maximum of 1.30, indicating that the ultimate forces obtained experimentally were 30% greater than those predicted analytically. From this, a Limit Fu was established. To achieve ductile failure modes, a safety factor of at least 1.20 was applied between the resistance of BiRs and the resistance of steel threaded rods only.
- The structural performance of the joint is significantly influenced by the link cross-section, end-plate thickness, bonded-in rod (BiR) diameter, and the distances between the BiR positions in the end-plate. In G1 joints, thicker end-plates enhance moment resistance and initial rotational stiffness. In contrast, in G2 joints, increased end-plate thickness raises rotational stiffness but reduces moment resistance, highlighting BiR diameter as a critical factor.
- Moment-rotation curves were determined for the primary components individually, which makes it possible to identify more precisely which component reached yielding first and which is the correct tendency for the connection to fail, especially for equal joints. These joints can be designed as full-strength, equal-strength, or partial-strength based on the resistance of the link, end-plate, and BiR. In G1.t20.d20 joints, moment resistance is primarily governed by link yielding, maintaining full-strength characteristics. In G1.t15.d20 joints, both the link and end-plate rotate similarly, making classification as equal-strength appropriate. In G2 joints, the moment resistance of the connection is dominated by the BiR, with significant timber rotation due to tensile deformation in the rods. However, in G2.t12.d16 joints, failure occurs in the link while the end-plate and BiR remain elastic. No plastic damage to the timber was observed, confirming its elastic behavior throughout the testing.
- The alignment of the neutral axis in G2 joints depends on end-plate thickness and BiR arrangement. In G2.t15.d14 and G2.t12.d16, it aligns with the centerline of the BiR group (150-160 mm). In G2.t20.d12, a thicker end-plate reduces rotation, shifting the neutral axis to approximately 120 mm.

Despite the extensive body of research on steel-timber joints, the literature lacks a comprehensive calculation procedure encompassing the complete response for this specific type of joint, including moment resistance, initial rotational stiffness, and rotation capacity, which involves multiple macro-components working in conjunction (link, timber beam, and connection). Therefore, this study presented a complete calculation procedure based on component method for three distinct joint geometries: i) the unstiffened extended end-plate with two rows of BiRs, ii) the stiffened extended end-plate with two rows of BiRs, and iii) the stiffened extended end-plate with four rows of BiRs. Moreover, while the structural behavior of the joint under investigation exhibits certain similarities to steel extended end-plate connections, several factors contribute to its heightened complexity, as outlined below:

- The deformations and rotations experienced by the link also contribute to the overall rotation of the joint. Thus, the interpretation of the rotation results of the link becomes more complex and it is necessary to include this coupled behavior of the link and the timber-plate connection in the calculation.
- When timber is in contact with the end-plate, it introduces two distinct interactions: tension arises with the bonded-in rods as opposed to bolts, and compression is confined to the flanges of the end-plate, lacking a supporting column behind it.
- In the context of BiR connections, several conditions were evaluated: the behavior of BiRs is not exclusively contingent upon the failure of the steel component. It is also affected by factors such as bondline resistance, the presence or absence of unbonded lengths, shear resistance at the adhesive-timber interface, and the transverse stresses that may arise on the surface of the timber beam in the absence of unbonded lengths. Additionally, the resistance and stiffness of bonded-in rods are generally lower than those of bolted connections, and the development of prying forces in BiR connections exhibits unique characteristics due to the increased bonded length compared to conventional bolts.

To accomplish the primary aim of presenting a comprehensive calculation procedure for this type of connection, this work introduces several novel proposals:

- The modification of the spring configuration and the formulation of a novel design methodology for determining the initial rotational stiffness of joints are essential. In considering the interdependent behavior of the joint, it is observed that when an equivalent joint is assessed,

the rotations of both the link and the connection occur in near synchrony. Consequently, all active components are integral to the computation of the overall stiffness.

- This study presents the development of a novel equation for determining the elongation length (Lb) of BiRs, which is pertinent for assessing the presence of prying forces within the link. In this context, Lb is conceptualized as the sum of the free length and the effective embedded length.
- The development of novel equations for determining the resistance and stiffness coefficients of timber and end-plate components under compression is presented. In the analysis of this component, two distinct behaviors are observed: either the steel T-stub compresses the timber parallel to the grain, or the end-plate functions as a flat beam undergoing bending due to the presence of the free length between the outer face of the link flange and the edge of the end-plate.

The component-based analytical model demonstrates efficacy in predicting yield behavior, moment resistance, initial stiffness, and rotation capacity. Comparative analysis with experimental data reveals that the model's predictions of moment resistance closely correspond with yield moment variations, initial stiffness predictions are precise for all joints studied. Rotation capacity is consistent for G1 joints. Nonetheless, G2 connections exhibit discrepancies in rotation capacity attributable to thread galling.

The finite element analysis (FEA) yielded consistent results, demonstrating high accuracy in predicting moment-rotation curves, failure modes, initial rotational stiffness, and the behavior of key components. Utilizing these models, a parametric analysis was conducted on 972 moment-resistant steel-timber joint models to evaluate the applicability of the calculation procedure based on the component method across various geometries. The findings indicate that the proposed analytical method can reliably predict both the initial rotational stiffness (Sj,ini) and the yield moment (My) of joints across a wide range of geometries and for nearly all groups studied. Furthermore, the method exhibits a reliable capacity to predict the ultimate moment of the joint, although it tends to underestimate results compared to those validated by finite element analysis, showing less accuracy than for the other parameters examined.

In conclusion, this thesis contributes to the development of a comprehensive and straightforward design procedure based on the component method for predicting structural behavior of unstiffened and stiffened end-plate joints with steel link and multiple bonded-in rod (BiR) rows, identified as a

promising joint configuration suitable for moment-resisting timber frames, due to their high ductility, moment resistance, and rotational stiffness. Through experimental testing and finite element analysis, the study established that the ductile behavior of these joints results from the combined yielding of the steel link, end-plate, and BiRs, which effectively redistributes stresses and prevents brittle timber failures. Detailed component-level analysis was essential to define the governing parameters and failure mechanisms. The analytical model, developed from these findings, refines the component method by incorporating mechanical spring models with coupled behavior of steel link and end-plate-timber connection, novel center of compression and lever arm, and new formulations for steel-timber components. The parametric analysis and comparison between experimental and numerical results confirmed the accuracy of the proposed design model, particularly for yield moment (My) and initial rotational stiffness (Sj,ini) predictions, demonstrating its robustness and applicability to a wide range of geometries.

7.2. Future developments

The research presented in this thesis advances the understanding and reliability of analytical calculations for stiffened moment-resisting timber–steel joints with multiple BiRs. Nonetheless, several areas warrant further investigation to develop a more predictive design and analysis framework for these structural systems. The primary directions for future research are outlined below:

Beam–column joints assemblies: Although this study has concentrated on beam-to-beam configurations, future research should investigate the incorporation of links into comprehensive beam–column assemblies. This approach will enable a realistic assessment of load transfer mechanisms, stress distribution perpendicular to the grain in timber columns, and the interaction between the connection and adjacent structural members.

Full-scale tests on complete joints and timber frames: Comprehensive experimental investigations on complete joint prototypes and timber frames are crucial for validating theoretical and numerical analyses. Such studies provide essential insights into boundary effects and the overall behavior of joints within a structural system. Furthermore, it is imperative to conduct tests on timber frames with joints subjected to both monotonic and cyclic loading conditions.

Joints with short end-plates in compression side: Another valuable area of research involves analyzing connections with short end-plates on the compression side. Investigating whether this design leads to increased stiffness and moment resistance could provide important insights for optimization.

Understanding the mechanical implications of such design choices would help establish guidelines for practical applications.

Cyclic loading and seismic performance: An essential advancement of the component method is its application to cyclic loading conditions, which is vital for evaluating the seismic performance of moment-resisting timber joints. Experimental validation and analytical modeling of timber components, along with their interactions with steel components under cyclic loading, would facilitate predictions of hysteretic behavior, energy dissipation, and the degradation of stiffness and strength.

Extension of the method to the plastic range: The current methodology of the component includes nonlinear behavior but predominantly focuses on the elastic range. Expanding this approach to include the plastic response is essential for accurately predicting the ultimate moment resistance and rotational capacity of joints. This expansion requires a comprehensive analysis of nonlinear interactions among components and the impact of localized plasticity in both steel and timber. Particular attention should be directed towards connections involving timber columns, which may demonstrate distinctive post-elastic mechanisms.

REFERENCES

Abidelah, A., Bouchaïr, A. and Kerdal, D.E. (2012). Experimental and analytical behavior of bolted end-plate connections with or without stiffeners. *Journal of Constructional Steel Research*, 76, pp. 13–27.

Abrahamsen, R. (2017). Mjøstårnet-Construction of an 81 m tall timber building. In *Internationales Holzbau-Forum IHF* (Vol. 2017).

Aicher, S., Gustafsson, P. J., and Wolf, M. (1999). Load displacement and bond strength of glued-in rods in timber influenced by adhesive, wood density, rod slenderness and diameter. Proc., Int. *RILEM Symp. on Timber Engineering, RILEM Publications S.A.R.L.*, Cachan Cedex, France, 369–378.

Andreolli, M., Piazza, M., Tomasi, R., & Zandonini, R. (2011). Ductile moment-resistant steel–timber connections. *Proceedings of the Institution of Civil Engineers-Structures and Buildings*, 164(2), 65-78.

Andreolli, M. (2011) *Giunti semirigidi con barre incollate per strutture lignee*. Doctoral Thesis. Trento, Italy: University of Trento.

Araújo, M. and Castro, J.M. (2014). Deformation capacity of steel members. In Proc., *7th European Conf. on Steel and Composite Structures*. Brussels, Belgium: European Convention for Constructional Steelwork.

Barbero, E.J. (2023). *Finite element analysis of composite materials using Abaqus®*. CRC press.

Beg, D., Zupančič, E. and Vayas, I. (2004). On the rotation capacity of moment connections. *Journal of Constructional Steel Researc*h, 60(3–5), pp. 601–620.

Bengtsson, C. and Johansson, C.-J. (2002) GIROD-Glued in rods for timber structures. SMT4-CT97-2199.

Binck, C. and Frangi, A. (2024). On stiffness and strength of glued-in rods and threaded rods parallel to the grain. In *INTER Proceedings-Meeting 57*. Timber Scientific Publishing, KIT Holzbau und Baukonstruktionen, pp. 111–128.

BlaB, H.J. (1987) Design of timber columns. In *Proc. of the CI BW 18 A Meeting*.

BlaB, H.J. and Laskewitz, B. (1999). Effect of spacing and edge distance on the axial strength of glued-in rods. *Proceedings CIB-W18A*, Graz, Austria, 49.

Borges, L.A.C. (2003). Probabilistic evaluation of the rotation capacity of steel joints. Master dissertation. Coimbra, Portugal: University of Coimbra.

Bouchard, R., Salenikovich, A., Frenette, C., & Bedard-Blanchet, G. (2021). Experimental investigation of joints with multiple glued-in rods in glued-laminated timber under axial tensile loading. *Construction and Building Materials*, 293, 122614.

Broughton, J.G. and Hutchinson, A.R. (2001). Pull-out behaviour of steel rods bonded into timber. *Materials and structures*, 34(2), pp. 100–109.

Brown, D. et al. (2013). *Joints in steel construction: Moment-resisting joints to Eurocode 3*. Vol BCSA/SCI Connections Group. London: The British Constructional Steel work Association Limited.

Brühl, F., Kuhlmann, U., & Jorissen, A. (2011). Consideration of plasticity within the design of timber structures due to connection ductility. *Engineering Structures*, 33(11), 3007-3017.

Buchanan, A., Moss, P. and Wong, N. (2001). Ductile moment-resisting connections in glulam beams. *NZSEE Conference*, (6), pp. 1–9.

Buchanan, A.H. (1990). Bending Strength of Lumber. *Journal of Structural Engineering*, 116(5), pp. 1213–1229.

Buchanan, A.H. and Fairweather, R.H. (1993). Seismic design of glulam structures. *Bulletin of the New Zealand National Society for Earthquake Engineering*, 26(4), pp. 415–436.

Buchanan, A. (2016). The challenges for designers of tall timber buildings. In proceedings: *World Conference in Timber Engineering (WCTE)*. Vienna, Austria.

Buchholz, L., Kuhlmann, U. and Knobloch, M. (2025). Design of Timber Structures in View of Sustainability Based on the Component Method. *Proceedings from the 14th World Conference on Timber Engineering: Advancing Timber for the Future Built Environment, WCTE 2025*, pp. 1742–1751. Available at: https://doi.org/10.52202/080513-0213.

Coelho, A.M.G. and Bijlaard, F.S.K. (2010). Behaviour of high strength steel moment joints. *Heron*, 55(1), pp. 1–32.

COST, C1. (1999). *Control of the semi-rigid behaviour of civil engineering structural connections*. Final Report European Commission EUR, 19244.

D'Aniello, M., Landolfo, R., Piluso, V., & Rizzano, G. (2012). Ultimate behavior of steel beams under non-uniform bending. *Journal of Constructional Steel Research*, 78, 144-158.

DIN 1052:2008-12: Entwurf, Berechnung und Bemessung von Holzbauwerken – Allgemeine Bemessungsregeln und Bemessungsregeln für den Hochbau. Deutsches Institut für Normung. Berlin.

Dong, W., Li, M., He, M., & Li, Z. (2021). Experimental testing and analytical modeling of glulam moment connections with self-drilling dowels. Journal of Structural Engineering, 147(5), 04021047.

Ehrlich, D., Kemper, T., Uhl, J. H., Mari, R. I., Florio, P., Pesaresi, M., ... & Krasnodebska, K. (2024). Atlas of the human planet 2024.

EN 26891:1991: Timber structures – Joints made with mechanical fasteners – General principles for the determination of strength and deformation characteristics. European Committee for Standardization. Brussels, Belgium.

EN 12512:2001: Timber structures – Test methods – Cyclic testing of joints made with mechanical fasteners. European Committee for Standardization. Brussels, Belgium.

EN 13183-2:2005: Moisture Content of a Piece of Sawn Timber - Part 2: Estimation by Electrical Resistance Method. EN 13183-2. European Committee for Standardization. Brussels, Belgium.

EN 1993-1-8:2005: Eurocode 3: Design of steel structures - Part 1-8: Design of joints. European Committee for Standardization. Brussels, Belgium.

DIN EN 1993-1-8:2010-12: Eurocode 3: Design of steel structures - Part 1-8: Design of joints (includes Corrigendum AC:2009). European Committee for Standardization. Brussels, Belgium.

EN 14080:2013: Timber structures – Glued laminated timber and glued solid timber – Requirements. European Committee for Standardization. Brussels, Belgium.

EN 1998-1:2004+A1:2013: Eurocode 8: Design of structures for earthquake resistance – Part 1: General rules, seismic actions and rules for buildings. European Committee for Standardization. Brussels, Belgium.

EN 1993-1-1:2005+A1:2014: Eurocode 3: Design of steel structures – Part 1-1: General rules and rules for buildings. European Committee for Standardization. Brussels, Belgium.

EN 1995-1-1:2004+A2:2014: Eurocode 5: Design of timber structures – Part 1-1: General – Common rules and rules for buildings. European Committee for Standardization. Brussels, Belgium.

EN 338:2016: Structural timber – Strength classes. European Committee for Standardization. Brussels, Belgium.

EN 17334:2021: Glued-in rods in glued structural timber products - Testing, requirements and bond shear strength classification. European Committee for Standardization. Brussels, Belgium.

EN 29816:2021: Wood-based panels – Determination of mechanical properties – Test methods. European Committee for Standardization. Brussels, Belgium.

EN 15048-1:2007+A2:2022: Non-preloaded structural bolting assemblies – Part 1: General requirements. European Committee for Standardization. Brussels, Belgium.

prEN 1995-1-1: Eurocode 5: Design of timber structures - Part 1-1: General rules and rules for buildings. CEN/TC 250/ SC 5 N 1650. European Committee for Standardization. Brussels, Belgium.

Faella, C., Piluso, V. and Rizzano, G. (1999*). Structural steel semirigid connections: theory, design, and software*. CRC press.

Favero, A., Daigneault, A., Sohngen, B., & Baker, J. (2023). A system-wide assessment of forest biomass production, markets, and carbon. *GCB Bioenergy*, 15(2), 154-165.

Feligioni, L. et al. (2003). Influence of glue rheology and joint thickness on the strength of bonded-in rods. *Holz als Roh- und Werkstof*, 61, pp. 281–287.

Fernandez, A., Komp, J., & Peronto, J. (2020). Ascent-challenges and advances of tall mass timber construction. *International Journal of High-Rise Buildings*, 9(3), 235-244.

Flanagan, D.P. and Belytschko (1981). A uniform strain hexahedron and quadrilateral with orthogonal hourglass control. *International journal for numerical methods in engineering*, 17(5), pp. 679–706.

Frese, M., Enders-Comberg, M., Blaß, H. J., & Glos, P. (2012). Compressive strength of spruce glulam. *European Journal of Wood and Wood Products*, 70(6), 801-809.

Gattesco, N., Gubana, A. and Buttazzi, M. (2010). Pull-out strength of bar glued-in-joints. *11th World Conference on Timber Engineering 2010*, WCTE 2010, 2, pp. 1194–1200.

Gehri, E. (2001). Ductile behaviour and group effect of glued-in steel rods. in Proc., Int. *RILEM Symp. on Joints in Timber Structures*, pp. 333–342.

Gehri, E. (2009). Influence of fasteners spacings on joint performance—experimental results and codification. In *proceedings of the 42nd CIB-W18 meeting.* Dübendorf, Switzerland.

Coelho, A. M. G. (2004). *Characterization of the ductility of bolted end plate beam-to-column steel connections.* Doctoral Thesis. Coimbra, Portugal: University of Coimbra.

Global Industry Analysts (2025) Mass Timber Construction - Global Strategic Business Report.

Gohlich, R., Erochko, J. and Woods, J.E. (2018). Experimental testing and numerical modelling of a heavy timber moment-resisting frame with ductile steel links. *Earthquake Engineering and Structural Dynamics*, 47(6), pp. 1460–1477.

Gonzalez, E., Avez, C. and Tannert, T. (2016). Timber joints with multiple glued-in steel rods. *Journal of Adhesion*, 92(7–9), pp. 635–651.

Górszczyk, J., Malicki, K. and Zych, T. (2019). Application of digital image correlation (DIC) method for road material testing. *Materials*, 12(15).

Gu, H., Nepal, P., & Bergman, R. (2023). Carbon credits for mass timber construction. *BioProducts Business*, 1-12.

Guo, H., Xiao, J., Zhang, H., Liu, C., Sheng, X., & Chen, Y. (2024). Component method and numerical investigation on the initial rotational stiffness of fillet welded rectangular hollow sections (RHS) T-joints. *Structures* (Vol. 62, p. 106340).

Habitat, U.N. (2024). *World Cities Report 2024*: Cities and Climate Action.

Hamilton, I., Kennard, H., Rapf, O., Amorocho, J., Steuwer, S., Kockat, J., & Toth, Z. (2024). *Global Status Report for Buildings and Construction-Beyond foundations: Mainstreaming sustainable solutions to cut emissions from the buildings sector*.

He, M. et al. (2020). Rotational behavior of bolted glulam beam-to-column connections with knee brace. *Engineering Structures*, 207, p. 110251.

Hegeir, O. A., Stamatopoulos, H., & Malo, K. A. (2024). Parametric analysis of moment-resisting timber frames combined with cross laminated timber walls and prediction models using nonlinear regression and artificial neural networks. *Buildings*, 14(9), 2975.

ISO 6891:1983: Timber structures — Joints made with mechanical fasteners — General principles for the determination of strength and deformation characteristics. Geneva, Italy.

International Organization for Standardization (2019) ISO 6892-1:2019: Metallic materials — Tensile testing — Part 1: Method of test at room temperature. International Organization for Standardization. Geneva, Italy.

Iovane, G. (2020). *Innovative seismic resistant structural systems for timber*. Doctoral Thesis. Naples, Italy: University of Naples, Federico II.

Iovane, G. and Faggiano, B. (2021). Timber beam-to-column joint with steel link: Design and mechanical characterization through numerical investigation. *COMPDYN Proceedings*, 2021–June, pp. 2359–2365.

Jaspart, J.-P. and Maquoi, R. (1991). Plastic capacity of end-plate and flange cleated connections-prediction and design rules. in *Second international workshop on connections in steel structures: Behaviour, strength and design*.

Jaspart, J. P., & Weynand, K. (2016). *Design of joints in steel and composite structures*. Ernst & Sohn

Jaspart, J.P. (1991). *Study of the semi-rigid behaviour of beam-to-column joints and of its influence on the stability and strength of steel building frames*. Doctoral Thesis. Liège, Belgium: University of Liège.

Jockwer, R., Palma, P., Rebouças, A., & Salenikovich, A. (2023). Development of comprehensive testing procedures for high-performance bonded-in rods. In Conference: *World Conference on Timber Engineering 2023* (WCTE2023), Oslo (pp. 3675-3684).

Jorissen, A., & Fragiacomo, M. (2011). General notes on ductility in timber structures. *Engineering structures*, 33(11), 2987-2997.

Karagiannis, V., Málaga-Chuquitaype, C., & Elghazouli, A. Y. (2017). Behaviour of hybrid timber beam-to-tubular steel column moment connections. *Engineering Structures*, 131, 243-263.

Karacabeyli, E. and Ceccotti, A. (1998). Nailed wood-frame shear walls for seismic loads: Test results and design considerations. *Structural Engineering World Wide*.

Kuhlmann, U., Davison, J. B., & Kattner, M. (1998). Structural systems and rotation capacity. In Proceeding *of COST Conference on Control of the Semi-rigid Behaviour of Civil Engineering Structural Connections*, Liège (pp. 167-176).

Lam, F., Schulte-Wrede, M., Yao, C. C., & Gu, J. J. (2008). Moment resistance of bolted timber connections with perpendicular to grain reinforcements. In *Proceedings of the 10th world conference on timber engineering* (WCTE).

Lam, F., Gehloff, M. and Closen, M. (2010).Moment-resisting bolted timber connections. Proceedings of the Institution of Civil Engineers: *Structures and Buildings*, 163(4), pp. 267–274.

Landolfo, R., D'Aniello, M., Tartaglia, R., Constanzo, S., Demonceau, J. F., Jaspart, J. P., ... & Bompa, D. (2018, December). EQUALJOINTS PLUS: Volume with pre-normative design recommendations for seismically qualified steel joints. In *Proceedings of the ECCS–European Convention for Constructional Steelwork*, Brussels, Belgium (pp. 6-7).

Lee, C.-H. (2002). Seismic design of rib-reinforced steel moment connections based on equivalent strut model. *Journal of Structural Engineering*, 128(9), pp. 1121–1129.

Li, Z., Chen, F., He, M., Long, W., Ou, J., & Li, M. (2023). Experimental investigation on self-centering steel-timber hybrid beam-column connections. *Journal of Structural Engineering*, 149(3), 04022256.

Lu, W.D., Sun, H.F. and Liu, W.Q. (2016). Experimental study on behavior of bolted glulam beam-to-column connections strengthened by self-tapping screws. *Chinese Journal of Building Structures*, 37, pp. 80–86.

Muciaccia, G. (2019). An experimental approach to determine pull-out strength of single and multiple axially loaded steel rods bonded in glulam parallel to the grain. *Wood Material Science & Engineering*, 14(2), pp. 88–98.

Muñoz, W., Mohammad, M., Salenikovich, A., & Quenneville, P. (2008). Need for a harmonized approach for calculations of ductility of timber assemblies. In *Proceedings of the Meeting* (Vol. 41, pp. 307-318).

Murray, T.M. (1983). Design of Lightly Loaded Steel Column Base Plates. *Engineering Journal AISC*, 20(4), pp. 143–152.

Ottenhaus, L. M., Jockwer, R., van Drimmelen, D., & Crews, K. (2021). Designing timber connections for ductility–A review and discussion. *Construction and Building Materials*, 304, 124621.

Pan, B. et al. (2009). Two-dimensional digital image correlation for in-plane displacement and strain measurement: a review. *Measurement science and technology*, 20(6), p. 62001.

Parida, G., Johnsson, H. and Fragiacomo, M. (2013). Provisions for Ductile Behavior of Timber-to-Steel Connections with Multiple Glued-In Rods. *Journal of Structural Engineering*, 139(9), pp. 1468–1477.

Paulay, T. and Priestley, M.J.N. (1992). *Seismic design of reinforced concrete and masonry buildings*. Wiley New York.

Postupka, J., Kuhlmann, U. and Brühl, F. (2016). Ductile behaviour of dowel connections - Application of the component method in timber construction, In *World Conference on Timber Engineering* (WCTE 2016).

Rebouças, A. S., Mehdipour, Z., Branco, J. M., & Lourenço, P. B. (2022). Ductile moment-resisting timber connections: A review. *Buildings*, 12(2), 240.

Rebouças, A. S., Branco, J. M., Lourenço, P. B., & Diógenes, H. J. (2024). Characterization of steel T-stub compressing timber parallel to the grain component. *Engineering Structures*, 314, 118310.

Rebouças, A. S., Branco, J. M., Simões, R., Lourenço, P. B., & Diógenes, H. J. (2025). Design of stiffened end-plate moment-resisting steel-timber joints with multiple bonded-in rods using the component method. *Engineering Structures*, 341, 120793.

Ricerche, C.N. delle (2018) CNR-DT 206 R1/2018: Istruzioni per la progettazione, l'esecuzione ed il controllo delle strutture di legno. Rome.

Richart, F.E., Hall, J.R. and Woods, R.D. (1970). *Vibrations of soils and foundations*..

Safarik, D., Elbrecht, J., & Miranda, W. (2022). *State of tall timber 2022*. CTBUH J, 2022, 22-31.

Sarti, F., Palermo, A. and Pampanin, S. (2016). Experimental calibration of parallel-to-grain strain penetration length for internal epoxied bars. *Construction and Building Materials*, 112, pp. 970–979.

Norm SIA 265:2021: Holzbau. Schweizerischer Ingenieur- und Architektenverein. Zürich, Swiss.

Shen, Y., Christopoulos, C., Mansour, N., & Tremblay, R. (2011). Seismic design and performance of steel moment-resisting frames with nonlinear replaceable links. *Journal of Structural Engineering*, 137(10), 1107-1117.

Shi, Y., Shi, G. and Wang, Y. (2007). Experimental and theoretical analysis of the moment-rotation behaviour of stiffened extended end-plate connections. *Journal of Constructional Steel Research*, 63(9), pp. 1279–1293.

Da Silva, L. S., & Coelho, A. G. (2001). A ductility model for steel connections. *Journal of Constructional Steel Research*, 57(1), 45-70.

Smith, I., Asiz, A., Snow, M., & Chui, I. (2006). Possible Canadian/ISO Approach to Deriving Design Values from Test Data. *The 39th CIB Working Commission W18-Timber Structures*. Italy (August 2006).

Sobra, K., Branco, J. M., & Aranha, C. A. (2014). Application of the component method to traditional dovetail joints of timber trusses. In *Congresso Luso-Brasileiro de Materiais de Construção Sustentáveis*

Solarino, F., Giresini, L., Chang, W. S., & Huang, H. (2017). Experimental tests on a dowel-type timber connection and validation of numerical models. *Buildings*, 7(4), 116.

Stamatopoulos, H., Malo, K.A. and Vilguts, A. (2022). Moment-resisting beam-to-column timber connections with inclined threaded rods: Structural concept and analysis by use of the component method. *Construction and Building Materials*, 322, p. 126481.

EN 408:2010+A1:2012: Timber structures – Structural timber and glued laminated timber – Determination of some physical and mechanical properties. European Committee for Standardization. Brussels, Belgium.

Steenhuis, M., Wald, F. and Stark, J. (2008). Concrete in compression and base plate in bending. *Heron*, 53(1), pp. 51–68.

Steiger, R., Gehri, E. and Widmann, R. (2004). Glued-in steel rods: a design approach for axially loaded single rods set parallel to the grain. in *CIB-W18 meeting thirty-seven*, Edinburgh, UK.

Steiger, R., Gehri, E. and Widmann, R. (2007). Pull-out strength of axially loaded steel rods bonded in glulam parallel to the grain. *Materials and Structures*, 40(1), pp. 69–78.

Steiger, R. (2012). In Brettschichtholz eingeklebte Gewindestangen – Stand des Wissens zu einer leistungsfähigen Verbindungstechnik. *Internationales Holzbau-Forum 2012*, pp. 1–15.

Steiger, R., Serrano, E., Stepinac, M., Rajčić, V., O'Neill, C., McPolin, D., & Widmann, R. (2015). Strengthening of timber structures with glued-in rods. *Construction and building materials*, 97, 90-105.

Stepinac, M. Comparison of design rules for glued in rods. In *COST FP1101 workshop*.

Stockwell, F.W. (1975). Preliminary Base Plate Selection. *Engineering Journal*, 12(3), pp. 92–99.

Sun, X., Qu, Y., Liu, W., Lu, W., & Yuan, S. (2020). Rotational behavior and modeling of bolted glulam beam-to-column connections with slotted-in steel plate. *Advances in Structural Engineering*, 23(9), 1989-2000.

Tao, H., Mao, M., Yang, H., & Liu, W. (2020). Theoretical and experimental behaviour of a hybrid semi-rigid glulam beam-to-column connection with top and seat angles. *Advances in Structural Engineering*, 23(10), 2057-2069.

Tlustochowicz, G., Serrano, E. and Steiger, R. (2011). State-of-the-art review on timber connections with glued-in steel rods. *Materials and Structures*, 44(5), pp. 997–1020.

Tomasi, R., Zandonini, R., Piazza, M., & Andreolli, M. (2008). Ductile end connections for glulam beams. *Structural Engineering International*, 18(3), 290-296.

Totsuka, M., Jockwer, R., Kawahara, H., Aoki, K., & Inayama, M. (2022). Experimental study of compressive properties parallel to grain of glulam. *Journal of Wood Science*, 68(1), 33.

Tschemmernegg, F. and Humer, C. (1988). The Design of Structural Steel Frames under Consideration of the Nonlinear Behaviour of Joints. *Journal of Constructional Steel Research*, 1, pp. 73–103.

Tulebekova, S., Malo, K. A., & Rønnquist, A. (2023). Dynamic identification and model calibration of connection stiffness in multi-storey cross-laminated timber buildings. *Journal of Building Engineering*, 72, 106607.

Vašek, M. and Vyhnálek, R. (2006). Timber semi rigid frame with glued-in-rods joints. *9th World Conference on Timber Engineering 2006*, WCTE 2006, 3, pp. 1825–1832.

Vilguts, A., Nesheim, S. Ø., Stamatopoulos, H., & Malo, K. A. (2022). A study on beam-to-column moment-resisting timber connections under service load, comparing full-scale connection testing and mock-up frame assembly. *European Journal of Wood and Wood Products*, 80(4), 753-770.

Vilguts, A., Stamatopoulos, H., & Malo, K. A. (2021). Parametric analyses and feasibility study of moment-resisting timber frames under service load. *Engineering Structures*, 228, 111583.

Vogel, U. (1985). Some comments on the ECCS publication no. 33: ultimate limit state calculation of sway frames with rigid joints. *Construzioni Metalliche* HI, 37, pp. 35–39.

Wald, F., Gresnigt, A.M., Weynand, K., Jaspart, J.P. (1998). Application of the component method to column bases. *Journal of Constructional Steel Research*, 48 (2-3).

Wald, F., Mareš, J., Sokol, Z., & Drdácký, M. (2000). Component method for historical timber joints. In *The Paramount Role of Joints into the Reliable Response of Structures*: From the Classic Pinned and Rigid Joints to the Notion of Semi-rigidity (pp. 417-424).

Wald, F., Sokol, Z. and Jaspart, J.P. (2008). Base plate in bending and anchor bolts in tension. *Heron*, 53(1–2), pp. 21–50.

Wang, M., Song, X., Gu, X., Zhang, Y., & Luo, L. (2015). Rotational behavior of bolted beam-to-column connections with locally cross-laminated glulam. *Journal of Structural Engineering*, 141(4), 04014121.

Weynand, K., Jaspart, J.-P. and Steenhuis, M. (1995). The stiffness model of revised Annex J of Eurocode 3. In *Proceedings of the3rd International Workshop on Connections*. Trento, Italy.

Yang, H., Liu, W. and Ren, X. (2016). A component method for moment-resistant glulam beam-column connections with glued-in steel rods. *Engineering Structures*, 115, pp. 42–54.

Yasumura, M. (1998). Estimating seismic performance of wood-framed structures. *Proceedings of 5th WCTE*, 2, pp. 564–571.

Yun, X. and Gardner, L. (2017). Stress-strain curves for hot-rolled steels. *Journal of Constructional Steel Research*, 133, pp. 36–46.

Zoetemeijer, P. (1974). A design method for the tension side of statically loaded, bolted beam-to-column connections. *Heron*, 20(1).

Zoetemeijer, P. (1983). *Summary of the research on bolted beam-to-column connections*. Delft University of Technology, Faculty of Civil Engineering,